KINETIC AND SPECTROSCOPIC STUDIES OF ION-PAIR STATES OF IODINE MONOCHLORIDE

by

ELINOR A. KERR

Thesis presented for the Degree of

DOCTOR OF PHILOSOPHY

University of Edinburgh

January 1989

To my Grandmother, my Family and Joe

for all their help and support

A C K N O W L E D G E M E N T S

I would like to thank Professor Robert J. Donovan and Dr. Jeremy P.T. Wilkinson (now of the Shell Research Centre, Thornton) for their joint supervision and encouragement given during this work. Their advice and support were most valuable over the three years.

I am grateful to the SERC for allowing me use of the Synchrotron Radiation Source (SRS) at the SERC Daresbury Laboratory where the majority of the experimental work was carried out. The assistance given by Drs. David Shaw and Andrew Hopkirk at this facility, often during anti-social hours, was invaluable and was much appreciated. I would also like to thank fellow experimenters at the SRS, Mr. Derek I. Austin and Professor Andrew J. Yencha (The State University of New York), for their company and experimental help during the long hours spent sitting on Port 13.

Many thanks are also due to Dr. Trevor Ridley for his expert help in the setting-up and running of the laser experiments carried out at the University of Edinburgh.

I found discussions with Professor Andrew J. Yencha and Dr. Kenneth P. Lawley most useful. The comments of Dr. Michael A. MacDonald were very helpful during the writing of this thesis and I am also grateful to Dr. MacDonald for completing the onerous task of proof-reading the final product. The work of Mr. Derek I. Austin in carrying out computer simulations and producing

a potential cure for the ICl $E(0^+)$ state is acknowledged, where appropriate, in the text. Thanks also to Mr. Austin for interesting and stimulating discussions concerning the ion-pair potentials of the ICl molecule.

I would also like to thank all the members of the Laser Group at Edinburgh who provided moral support and recreational relief over the three years.

Many thanks to Miss Vanessa Ayling for her excellent typing and lay-out of the text and also to Dr. Nick Price who assembled most of the figures.

Finally, I am grateful to the SERC for providing me with a research studentship to carry out this work.

DECLARATION

I hereby declare that this thesis has been composed by me, and that the work described in it is my own and was carried out at the University of Edinburgh, except where due acknowledgement is made.

Signed:

Date: 12/2/89.

A B S T R A C T

Highly excited electronic states of iodine monochloride, ICl, have been studied using single and two-photon absorption techniques. Single photon, vacuum ultraviolet (VUV) radiation was supplied by the Synchrotron Radiation Source (Daresbury Laboratory) and ultraviolet/visible photons by an excimer pumped dye laser system.

Fluorescence excitation, absorption and dispersed fluorescence spectra of ICl were collected following single photon, VUV excitation. ICl has a rich, VUV absorption spectrum but the corresponding fluorescence excitation spectrum shows that not all populated states fluoresce. Below 158 nm ICl absorption occurs to many Rydberg states but direct fluorescence was not observed from any of these states. However, fluorescence assigned to the D'(2) → A'(2) (ion-pair → valence) transition was observed to the blue of 140 nm, as a result of collisions between excited I atoms and ground-state ICl molecules.

Between 158 nm and 195 nm, excitation to both Rydberg and ion-pair states is observed. Ion-pair absorption occurs mainly to the $E(0^+)$ state, the lowest ion-pair state of this symmetry. No evidence was found for a $\Delta\Omega = 1$ transition from the ground state, in agreement with an empirical rule for valence → ion-pair transitions. Weak fluorescence from the $f(0^+)$ state, the next highest (0^+) ion-pair state, was observed although it is not known whether this state is populated directly by absorption or by interaction with the $E(0^+)$ state. Both $\Omega = 0^+$ and 1 Rydberg states lie in the same energy region as the $E(0^+)$ state. Consideration of the absorption and fluorescence

excitation spectra in this region suggests the existence of interaction, or mixing, between the $E(0^+)$ and neighbouring Rydberg states. Two types of perturbation are proposed; heterogeneous mixing between the $E(0^+)$ state and an $\Omega = 1$ Rydberg state and homogeneous mixing between the $E(0^+)$ state and a previously unreported $\Omega = 0^+$ Rydberg state. Both types of perturbation lead to loss of $E(0^+)$ fluorescence through coupling with the Rydberg states which appear to be predissociated. The interaction between ion-pair and Rydberg states is more severe for the homogeneous perturbation. However, even in this case the diabatic (curve-crossing) model of the $E(0^+)$ ion-pair and $\Omega = 0^+$ Rydberg potentials is found to best describe the experimental results.

Time resolved studies were also carried out in the 158 - 195 nm regions and support the theory of interaction between the $E(0^+)$ ion-pair and $\Omega = 0^+$, 1 Rydberg states. A radiative lifetime of approximately 50 ns was found independent of excitation wavelength and was attributed to fluorescence from unperturbed ion-pair levels. However, the number of exponentials (lifetimes) required to fit the experimental decays varied with excitation wavelength. Two decays were necessary in areas of heterogeneous perturbation while three decays were needed in the region of strong homogeneous interaction. The additional lifetimes obtained were shorter, reflecting the opening of predissociation pathways through Rydberg/ion-pair interactions.

The reaction of ICl with Xe and Kr was studied following VUV excitation of static cell mixtures. Reaction with Xe was found to proceed via the ICl^* ion-pair states producing both $XeCl^*$ and XeI^* in the $B(^1/_2)$ excited states. XeI^* formation was observed from its

thermodynamic threshold (174.4 nm) but no reaction was observed between ICl and Kr since the $KrCl^*$ threshold lies on the high energy border of ICl ion-pair absorption.

Optical-optical double resonance excitation employing two UV-VIS laser photons was employed to study the $E(0^+)$ ion-pair state from $v' = 3$-116. Dispersed fluorescence from several known $E(0^+)$ rovibrational levels was collected and, along with data from synchrotron radiation experiments, was used to construct an $E(0^+)$ potential curve.

CONTENTS

Continued .....

Continued .....

CONTENTS (Continued)

CHAPTER ONE

INTRODUCTION

1.1 Introduction

This thesis is concerned primarily with the ion-pair and Rydberg states of ICl. Spectroscopic observations on these states together with observations on their collisional and chemical behaviour will be presented. Ion-pair states, as their name implies, possess a strong degree of ionic character which greatly influences the form of the potential curves and their behaviour. As early as 1934, it was proposed [1] that the $I_2(D\ ^1\Sigma_u^+)$ state dissociated to ions rather than atoms, as deduced for the $B(^1\Sigma_u^+)$ state of H_2 [2]. Over the years several absorption and emission systems were assigned to ionic states, not only of iodine but also of other halogen/interhalogen molecules. However, information on these states was sparse. In Mulliken's review paper of 1971 [3] only three of the twenty I_2 ion-pair states had been observed experimentally. This is due, in part, to the high vertical excitation energies of the halogen/interhalogen ion-pair states which consequently require highly energetic photons ($\lambda < 200$ nm) for single photon excitation.

The availability of tuneable vacuum ultraviolet (VUV) radiation, such as synchrotron radiation (SR), and the development of optical-optical double resonance (OODR) excitation techniques have since combined to allow a more comprehensive study of ion-pair states to take place.

In this chapter, the fundamental differences between Rydberg, ion-pair and valence states will be considered together with the effect that these differences have on the shape and location of the potential curves. Previous work on valence and ion-pair states will be reviewed as much new data has accumulated since publication of the monograph of Huber and Herzberg in 1979 [4].

1.2 Classification of Electronic States

The electronic states of a diatomic molecule may be subdivided into three categories; valence, ion-pair and Rydberg states, dependent on the diabatic dissociation limits of the state. All three categories arise as a consequence of excitation of a valence electron, ie. an electron occupying a molecular orbital formed by a linear combination of the atomic orbitals of the relevant ground-state atoms. Excitation of lower shell (core) electrons requires significantly higher energies (ie. X-ray excitation) and will not be discussed here.

Consider the different classes of electronic states using the ICl molecule as an example. These are:

(i) Valence states, which correlate with ground-state iodine and chlorine atoms ($^2P_{3/2}$, $_{1/2}$) with outer electron configurations of $5s^25p^5$ and $3s^23p^5$ respectively.

(ii) Rydberg states, which dissociate to one ground-state atom and one Rydberg atom. For example, the lowest Rydberg dissociation limit for the ICl molecule is I^* ($5s^25p^46s$, $^4P_{5/2}$) and Cl ($3s^23p^5$, $^2P_{3/2}$).

(iii) Ion-pair states which correlate with ionic rather than atomic dissociation products, eg. I^+ ($5s^25p^4$, $^3P_{2,1,0}$, ^1D and ^1S) with Cl^- ($3s^23p^6$, ^1S).

The three types of states are shown in Figure 1.1.

The Rydberg potentials of Figure 1.1 are approximations only since little spectroscopic information is available for these states - only the ω_e and $\omega_e x_e$ values [4]. The equilibrium internuclear bondlengths of these states (the r_e values) are not known and in Figure 1.1 the $a_6(1)$ and $b_6(1)$ Rydberg states have been positioned at the r_e of the ground state, X $^1\Sigma^+$. This approximation can be justified by considering the change in molecular orbital (MO) electron configuration on excitation from the ground to a Rydberg state.

The outer electron configuration of the ICl ground state can be expressed as $\sigma^2\pi^4\pi^{*4}\sigma^{*0}$ where the σ,σ^* and π,π^* molecular orbitals are formed by linear combination of the $np\sigma$ and $np\pi$ atomic orbitals respectively (with n = 3 for Cl atoms and n = 5 for I atoms). Hereafter the electron configurations will be denoted in terms of the $\sigma\pi\pi^*\sigma^*$ orbital occupancy, ie. 2440 for the ground state, X $^1\Sigma^+$.

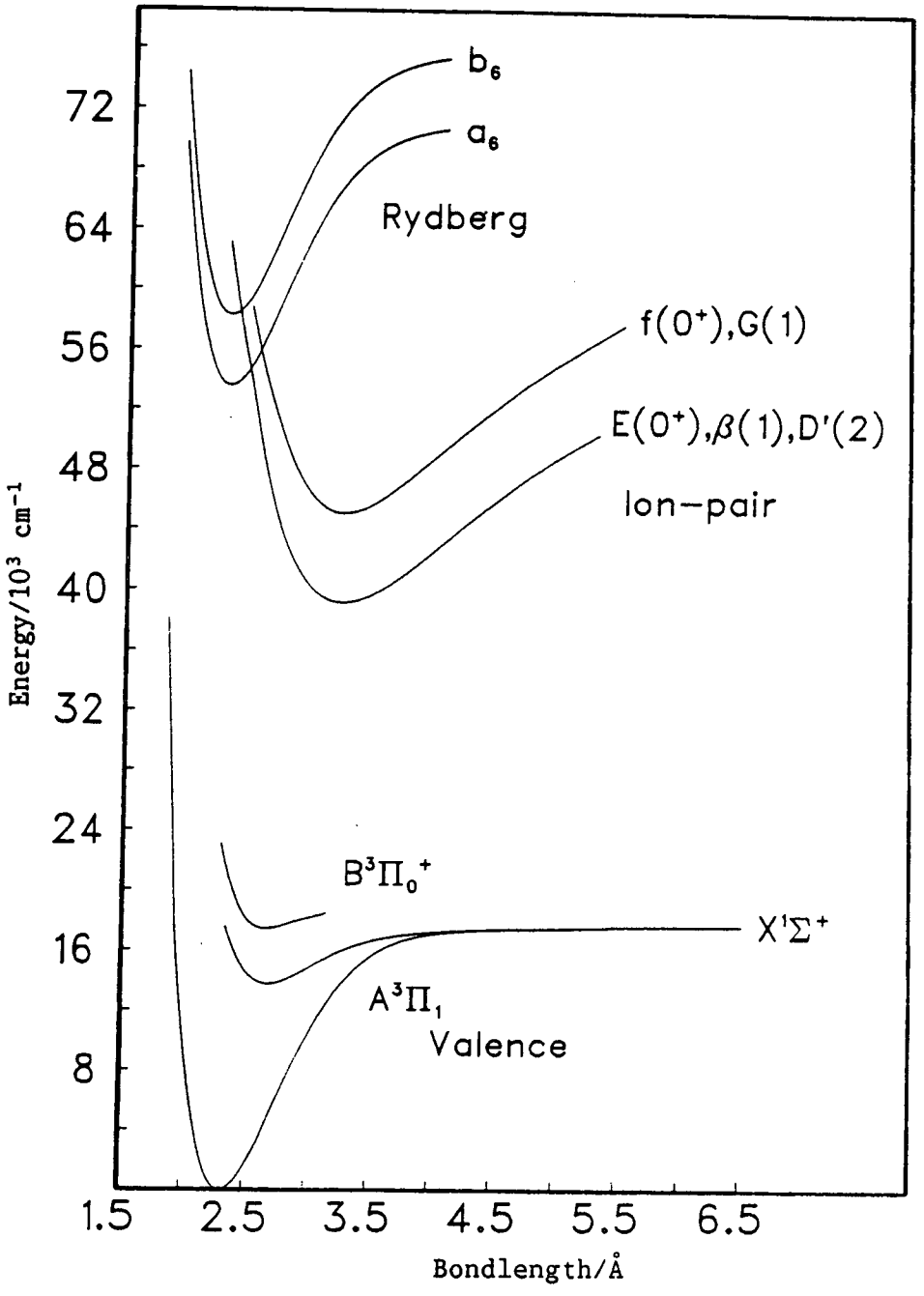

Figure 1.1 - Some known valence, ion-pair and Rydberg states of ICl. Several states are listed beside each ion-pair potential since the ion-pair states lie in clusters (see text).

Excitation to the lowest energy Rydberg state occurs by promotion of a π^* electron to a 6sσ iodine atom-like orbital giving a resultant electron configuration of 2430 6sσ [5]. Since the π^* orbitals are mainly atomic (non-bonding) orbitals centred on the iodine atom this excitation has little effect on the bonding properties of the molecule. The Rydberg state so formed has similar molecular constants to the ground state (and also the ICl^+ ion) [1] but is translated to higher energy by the $\pi^* \rightarrow 6s\sigma$ excitation energy.

By contrast, Figure 1.1 shows that the ion-pair states differ radically from the ground state. Ion-pair states are characterised by:

(i) The width of the states. Ion-pair states possess a soft attractive limb resulting in a wide potential and thus large amplitudes of vibration for the higher vibrational levels.

(ii) Large equilibrium internuclear bondlengths; compare an r_e of 2.321 Å for the ICl $X\ ^1\Sigma^+$ ground state [6] with that of the $E(0^+)$ ion-pair state, 3.258 Å (see Table 1.3).

(iii) The large dissociation energies (D_e) of the states; <u>eg</u>. for ICl D_e ($X\ ^1\Sigma^+$) = 17,558 cm^{-1} [7] while D_e ($E(0^+)$) = 33,700 cm^{-1} (see Table 1.3).

(iv) The tendency of ion-pair states to cluster together dependent on their diabatic dissociation products. The three ICl ion-pair states from the I^+ ($^3P_2$) and Cl^-(^1S) dissociation limit all lie within 50 cm^{-1} of one another [8].

The above properties are all a consequence of ion-pair states dissociating to ions rather than atoms. The medium and long-range attractive potential of an ion-pair state is dominated by an r^{-1} Coulombic attraction term rather than the r^{-6} term which describes the attraction at large r between valence state atoms. Thus, ion-pair states which correlate with the same dissociation limit possess similar attractive limbs and are found at approximately equal T_e values.

The $V(r) \propto e^2/r$ attractive limb is also responsible for the width and depth of the ion-pair states since the r^{-1} term produces an extremely long range, gently sloping potential extending to large r.

Until recently the ion-pair states had been studied less extensively than valence states for several reasons, one being that valence states are readily accessible by UV/VIS radiation whilst the ion-pair states are not. Although the lowest ion-pair state of ICl, the $E(0^+)$ state, has a T_e of 39,059 cm^{-1} (~ 256 nm) and lies in the UV region, low vibrational levels cannot be populated in a single photon transition. From Figure 1.1 it is apparent that a vertical, Franck-Condon allowed transition from the ground state populates high vibrational levels of the $E(0^+)$ state requiring energies in the vacuum ultraviolet (VUV) spectral region. This is a consequence of the large

shift in r_e between the ion-pair and ground states and is typical of all single photon, ground to ion-pair state transitions.

The study of ion-pair states has also been inhibited by a poor understanding of the nature of these states. While halogen/interhalogen Rydberg states can be regarded as the ground state translated to higher energies no such analogy exists for ion-pair states. Early research on ICl ion-pair states (pre the 1970's) was performed mainly by discharge excitation techniques, sometimes in the presence of a foreign gas (see Section 1.4). The emission systems from the populated ion-pair states were then analysed. Such excitation methods were non-state selective and also depended on good characterisation of the lower states in the emission systems for extraction of ion-pair molecular constants.

Ultraviolet/visible fluorescence from high vibrational levels of ion-pair states generally terminates on repulsive states or unbound portions of bound valence states - another consequence of the large shift in equilibrium internuclear bondlengths between the ion-pair and bound valence states. A theoretical explanation of such bound-free transitions, which result in complex, structured continuum emission systems, was not reported until 1971 [9] further hindering the comprehension of the halogen/interhalogen ion-pair states.

1.3 The Valence States of ICl

Twenty-three valence states correlate diabatically with ground state ($^2P_{3/2,\ 1/2}$) iodine and chlorine atoms. Very few of

these states are bound to any great extent [3] making characterisation difficult. However, to date, molecular constants for eight of the twenty-three valence states have been reported (see below). Knowledge of the valence states and their interactions has been important in the study of the ion-pair states since several groups (principally Brand and coworkers) have employed various valence states as intermediates in optical-optical double resonance excitation to the ion-pair states [10]. In turn, emission from ion-pair states at large r has probed the van der Waals minima of otherwise repulsive valence states [11].

Figure 1.2 shows a schematic correlation diagram of the valence states of ICl. On the left the electron configurations and the Hund's case (a) through Hund's case (c) signatures of the electronic states are shown with correlations to the separated atoms on the right. The letter codes of the characterised states are also shown, excepting the b(1) state which correlates with one of the two $\Omega = 1$ states dissociating to $I(^2P_{3/2})$ and Cl^* $(^2P_{1/2})$ [11].

Of the 23 valence states only three states, excluding the ground state, are bound significantly. These three states; the $A(^3\Pi_1)$, $B(^3\Pi_{0^+})$ and $A'(^3\Pi_2)$ states, all possess the 2431 electron configuration which has a net bonding effect [3]. The molecular constants of the known valence states and their diabatic dissociation limits are summarised in Table 1.1.

The UV/VIS absorption spectrum of ICl has been studied extensively over the years [19]. Seery and Britton have reported the extinction coefficient, ε, over the range 220 - 600 nm [20]. In this

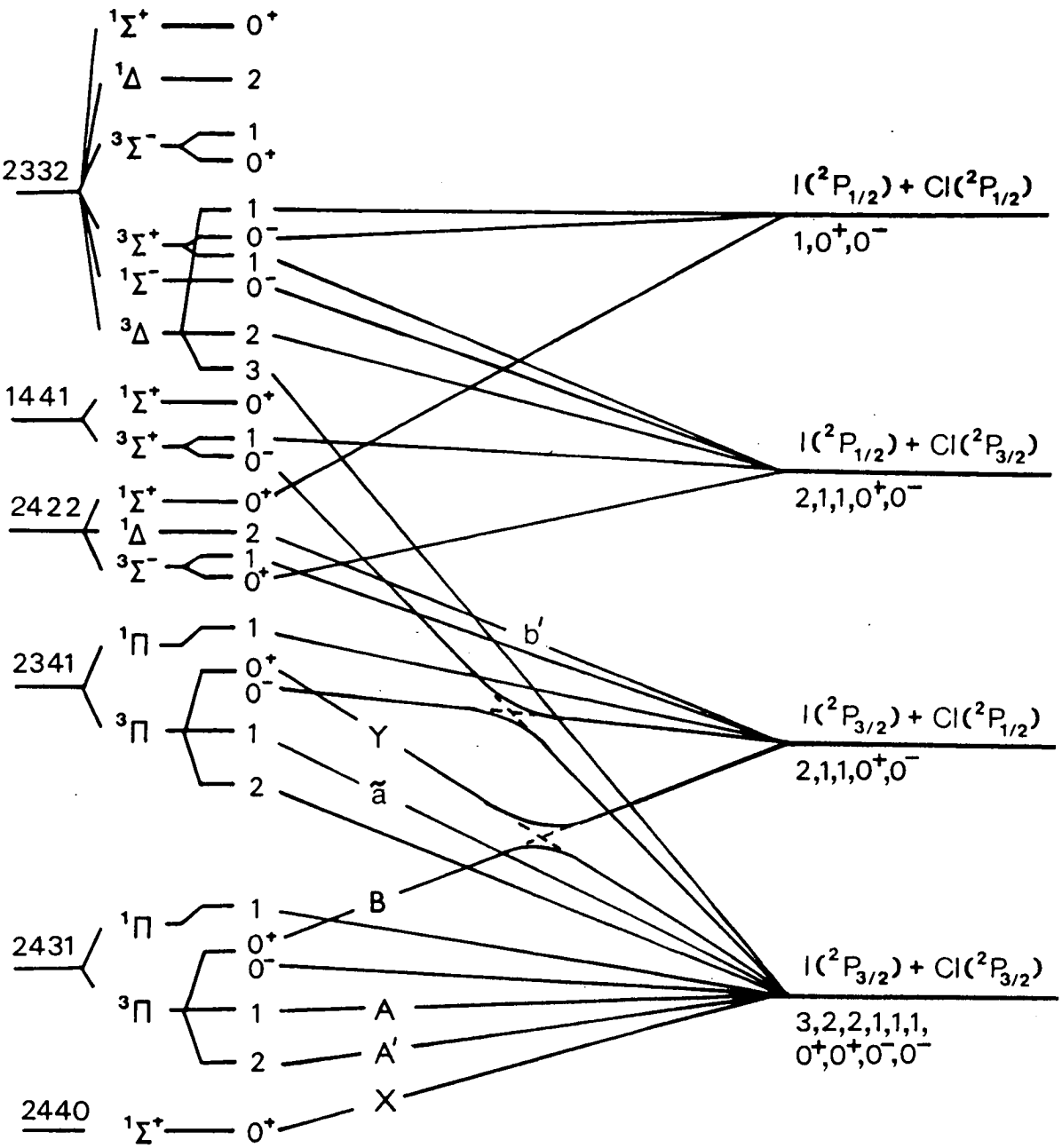

Figure 1.2 - Schematic correlation diagram for the valence states of ICl. The dashed lines indicate diabatic crossings for states of the same symmetry (see Chapter Three). All states, apart from $\Omega = 0$ states are doubly degenerate.

TABLE 1.1 - PRINCIPAL CONSTANTS OF THE KNOWN ICl VALENCE STATES

	$X(^1\Sigma^+)$	$A'(^3\Pi_2)$	$A(^3\Pi_1)$	$B(^3\Pi_{0^+})$	$\tilde{a}(^3\Pi_1)$	$a'(0^+)$ [a]	b(1)	b'(2)
Diabatic Dissociation Limit I + Cl	$^2P_{3/2} + {}^2P_{3/2}$	$^2P_{3/2} + {}^2P_{3/2}$	$^2P_{3/2} + {}^2P_{3/2}$	$^2P_{3/2} + {}^2P_{1/2}$	$^2P_{3/2} + {}^2P_{3/2}$	$^2P_{3/2} + {}^2P_{3/2}$	$^2P_{3/2} + {}^2P_{1/2}$	$^2P_{3/2} + {}^2P_{1/2}$
Electron Configuration	2440	2431	2431	2431	2341	2341	2341 or 2422	2422
T_e	0	12,682.05	13,742.9	17,375.58	17,338.0	< 17,370	18,273.30	18,275.84
ω_e	384.324	224.57	211.0	204.271	32.85	-	26.75	31.093
$\omega_e x_e$	1.5149	1.882	2.12	2.493	1.272	-	0.882	1.672
$\omega_e y_e$	-8.679×10^{-4}	-0.0107	-0.0024	-0.949	-	-	-	0.0070
B_e	0.1141546	0.08653	0.08529	0.086523	0.0382	-	0.03579	0.034834
$10^4\alpha_e$	5.229	6.75	7.4	14.0	8.89	-	-	15.87
$10^6\gamma_e$	-6.981	-2.7	-	223.0	-81.1	-	-	-
D_e	17,557.57	4875.52	3814.7	1064.35	219.6	$\geq$ 185	166.63	164.09
r_e/Å	2.321	2.665	2.685	2.666	4.01	-	~ 4.2	~ 4.2
References	6, 7, 12	13	14, 15	16	17	8, 18	11	11

All units in cm^{-1} unless stated otherwise

[a] The Y(0^+) state of Gordon and Innes [18]

region, two maxima in absorption are observed, one at 470 nm and the other in the ultraviolet region at 240 nm. Both maxima correspond to absorption to repulsive portions of valence potential curves.

Structured absorption, attributed mainly to the $A(^3\Pi_1) \leftarrow X(^1\Sigma^+)$ system, occurs below the first dissociation limit at 17,558 cm^{-1} (569.5 nm). The $A'(^3\Pi_2)$ state is not observed in absorption, even though it is the most deeply bound of the 2431 states, since a $\Delta\Omega = 2$ transition is disallowed in single photon absorption. Bound levels of the $B(^3\Pi_0+)$ state extend to shorter wavelengths as the $B(^3\Pi_0+)$ state correlates diabatically with a ground state ($^2P_{3/2}$) iodine atom and an excited ($^2P_{1/2}$) chlorine atom at large r. However, the $B(^3\Pi_0+)$ state is interrupted above the v = 3 level by an unbound state of the same symmetry, the $Y(0^+)$ state, resulting in a well-documented avoided crossing [18,21-22]. The so-formed lower adiabatic $B(0^+)$ state then correlates with ground state ($^2P_{3/2}$) iodine and chlorine atoms (as shown in Figure 1.2) via a potential maximum at ~ 3.6 A [18]. A new, weakly bound state, the $B'(0^+)$ state, correlating with $I(^2P_{3/2}) + Cl(^2P_{1/2})$ atoms is also formed. The maximum in the lower adiabatic $B(0^+)$ state occurs at ~ 18,140 cm^{-1} (relative to the minimum of the ground state). Thus, structured absorption bands are observed to the blue of the first dissociation limit at 17,558 cm^{-1} corresponding to absorption to the $B(^3\Pi_0+)$ state.

The absorption system with a maximum at 470 nm is assigned mainly to the repulsive limb of the $B(^3\Pi_0+)$ 2431 state, with small contributions from $^{1,3}\Pi_1$ (2431) $\leftarrow {}^1\Sigma^+$ (2440) transitions. The lower system peaking at 240 nm is attributed to absorption to the corresponding $^{1,3}\Pi$ states of the 2341 electron configuration with the $^3\Pi_0+$, $Y(0^+)$, absorption again dominant [1].

The two, excited valence states which are of prime importance to this work are the $A(^3\Pi_1)$ [14-15, 23-24] and $B(^3\Pi_{o^+})$ [16,18,25] states, since these states were employed as intermediates in the OODR excitation study of the $E(0^+)$ ion-pair state. Both states have been studied extensively and their molecular constants are well known.

1.4 The Ion-Pair States of ICl

Twenty ion-pair states correlate diabatically with ionic dissociation limits; ten to I^+ and Cl^- and ten to Cl^+ and I^- ions. Figure 1.3 shows the various ion-pair and Rydberg dissociation limits alongside the ionisation potentials to the two lowest ICl^+ states. All energies are relative to the minimum of the ICl ground state. The Ω values and designated letter codes of the lower lying ion-pair states are listed beside the appropriate dissociation limit in Table 1.2. The ion-pair dissociation limits were calculated with an iodine ionisation potential of 10.454 eV [26] and a chlorine electron affinity of 3.613 eV [27]. A D_e value of 17,558 cm^{-1} for the ICl ground state was employed [7]. The energies of excited atoms and ions are listed in Moore [26,28].

Ionisation potentials to the ground-state ICl^+ $(^2\Pi_{3/2})$ ion and the spin-orbit excited ICl^+ $(^2\Pi_{1/2})$ ion have been reported by Venkateswarlu [5] as 81,362 cm^{-1} and 85,996 cm^{-1} respectively.

The ion-pair states correlating with the lower I^+ and Cl^- ions are reasonably well characterised around their potential minima. Of the six ion-pair states which comprise the two lowest clusters,

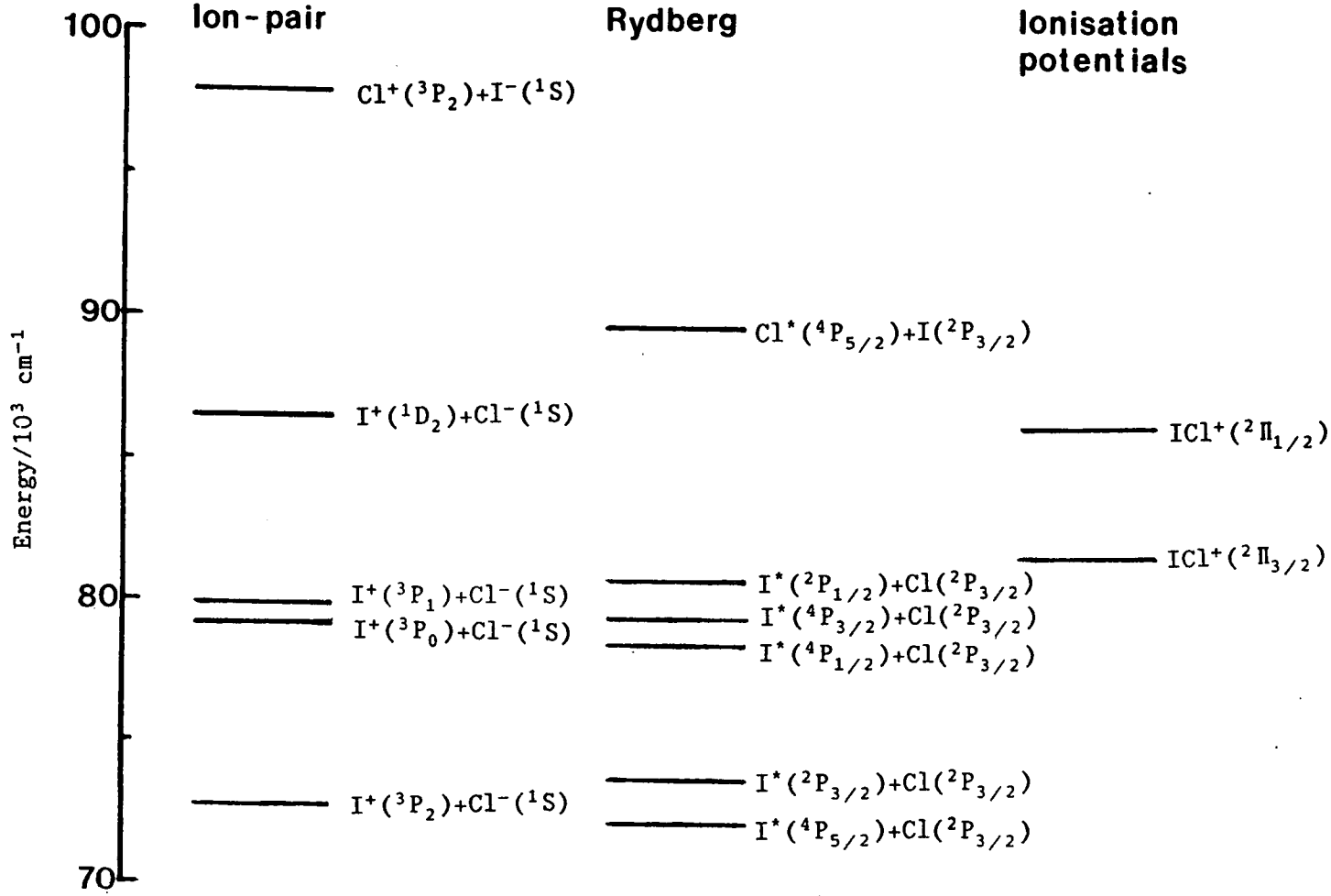

Figure 1.3 - The dissociation limits of the ICl ion-pair and Rydberg states. The two lowest ionisation potentials of ICl are also shown. All energies are relative to T_e of the $X(^1\Sigma^+)$ state.

TABLE 1.2

THE DISSOCIATION LIMITS AND PRODUCTS OF SOME ICl ION-PAIR STATES

Dissociation Products	Dissociation Limit/cm^{-1}	Correlating States
$I^+(^3P_2) + Cl^-(^1S)$	72,759	$E(0^+)$, $\beta(1)$, $D'(2)$
$I^+(^3P_0) + Cl^-(^1S)$	79,210	$f(0^+)$
$I^+(^3P_1) + Cl^-(^1S)$	79,849	$\Omega = 0^-$, $G(1)$
$I^+(^1D) + Cl^-(^1S)$	86,490	$\Omega = 0^+, 1, 2$
$I^+(^1S) + Cl^-(^1S)$	105,388	$\Omega = 0^+$
$I^-(^1S) + Cl^+(^3P_2)$	97,844	$\Omega = 0^+, 1, 2$

molecular constants have been reported for five (see below). The states dissociating to the I^+ ($^3P_1$) and ($^3P_0$) ions are classed as a cluster since the two dissociation limits are separated by only 639 cm^{-1} with a resultant ΔT_e of 629 cm^{-1} between the $\Omega = 1$ ($^3P_1$) and $\Omega = 0^+$ ($^3P_0$) states [29-30]. The only state in this group of six which has yet to be identified is the $\Omega = 0^-$ ($^3P_1$) state. This state is difficult to access due to its negative parity since $+ \leftrightarrow -$ transitions are disallowed, limiting the possible excitation pathways.

The T_e values of the 0^+ states of the $^3P_2$ and $^3P_0$ clusters are separated by 5,864 cm^{-1} while the $^3P_2$ and $^3P_1$ $\Omega = 1$ state separation is 6,449 cm^{-1} (see Table 1.3). Since the energy differences between the relevant dissociation limits are 6,451 cm^{-1} and 7,090 cm^{-1} respectively [26], it is reasonable to assume that all ion-pair states follow approximately similar paths, with location determined mainly by the energy of the dissociation limits. Thus, the ion-pair manifold can be considered as a stack of parallel states which lie at energies dependent on the state of the pertinent I^+ (or Cl^+) ion.

The four states correlating with I^+ (^1D, ^1S) ions lie above the ICl ionisation potential as do all states which dissociate to Cl^+ and I^- (see Figure 1.3). Consequently, none of these states have been observed experimentally.

Figure 1.3 shows that the ion-pair and Rydberg dissociation limits lie in the same energy range. Many ion-pair states must therefore undergo avoided crossings with Rydberg states of the same symmetry and dissociate to atomic rather than ionic species at large r [3].

The ion-pair states of ICl were first observed in emission following non-selective discharge excitation. As early as 1928, Filippov [31] reported an emission system from an ICl/N_2 mixture with a maximum at 435.0 nm. With hindsight this is assigned as the emission spectrum analysed in detail by Tellinghuisen et al [32], with contributions from both $D'(2) \rightarrow A'(2)$ and $\beta(1) \rightarrow A(1)$ transitions. In 1947 Asundi and Venkateswarlu [33] observed several emission systems in the ultraviolet/visible region, tentatively assigning the upper states as two previously reported by Cordes and Sponer to lie in the vacuum ultraviolet region [34]. However, these states have subsequently been identified as the $a_6(1)$ and $b_6(1)$ Rydberg states [5] with scant evidence for emission in the ultraviolet/visible regions. The fluorescence observed by Asundi and Venkateswarlu must also be attributed to the ion-pair states.

Haranath and Rao completed a detailed investigation of emission in the 380 - 440 nm region [35], assigning this system as fluorescence from an ion-pair state to the $A(^3\Pi_1)$ valence state. The ω_e' value of 173.2 cm^{-1} and the implied T_e' of 37,740 cm^{-1} obtained from their analysis is in reasonable agreement with the accepted constants of the lowest ion-pair states [36], although the T_e value is rather low. Tellinghuisen's analysis again suggests that $D'(2) \rightarrow A'(2)$ fluorescence is also present in this region. State selective studies of the $\beta(1)$ and $D'(2)$ states are required to clarify this situation.

Selective excitation of the ICl ion-pair states was first achieved by optical-optical double resonance excitation. This

technique allows access to low vibrational levels of ion-pair states by utilising the outer turning points of real intermediate states, as shown in Figure 1.4. OODR excitation has several advantages over single photon excitation:

(i) UV or VIS radiation is suitable for both excitation steps.

(ii) A two step process circumvents the Franck-Condon restrictions of single photon absorption.

In 1974, Barnes et al [37] reported two-step excitation to an ICl state lying at ~ 4.8 eV (38,700 cm^{-1}). Spectroscopic analysis of this state was not carried out but its location and the intermediate state employed, the $A(^3\Pi_1)$ state, suggests that it is the $\Omega = 1$ state of the lowest cluster. King et al subsequently excited the same $\Omega = 1$ state and reported a T_e of 38,916.0 cm^{-1} [38]. King designated this the E(1) state but it is more commonly known as the $\beta(1)$ $(^3P_2)$ state, after the notation of Brand et al [8]. Since 1983 Brand and coworkers have reported a comprehensive OODR study of the ion-pair states of ICl, providing spectroscopic constants for five of these states. The molecular constants of the known ion-pair states are given in Table 1.3.

Table 1.3 shows that the known molecular constants are valid only around the potential minima. The lowest cluster is the most extensively characterised with constants extending to $v \simeq 30$ for all three states. Such constants are valid only within the stated

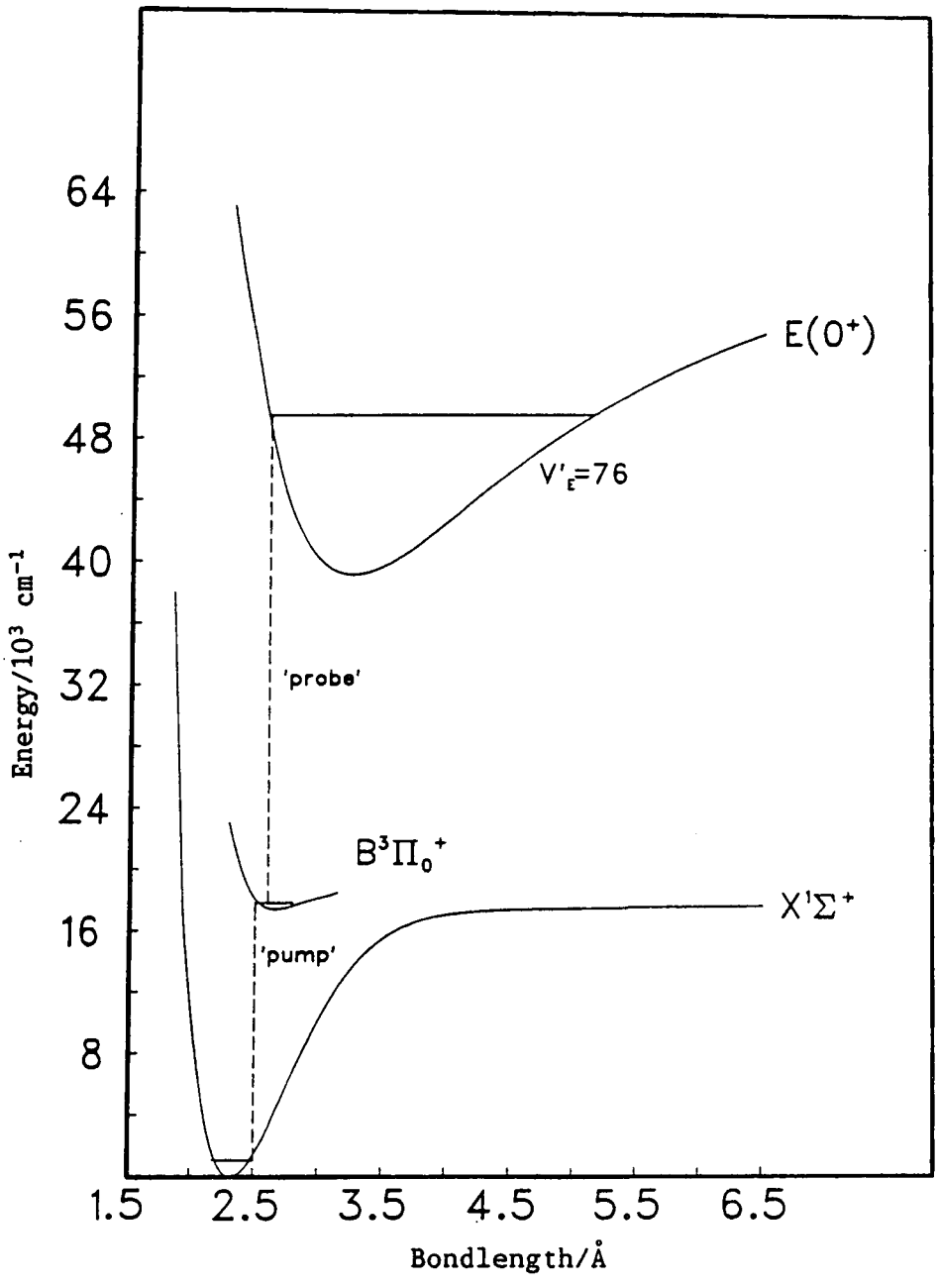

Figure 1.4 - Scheme for OODR excitation to the E(0^+) state of ICl. By utilising the B($^3\Pi_{0^+}$) state as an intermediate, E-state vibrational levels from v′ = 0 to v′ = 116 were accessed (see Chapter Four).

TABLE 1.3 – PRINCIPAL CONSTANTS OF THE KNOWN ICl ION-PAIR STATES [a]

State	Dissociation Limits $I^+ + Cl^-$	Vibrational [b] Range	T_e	ω_e	$\omega_e x_e$	$10^4 \omega_e y_e$	$10^2 B_e$	$10^4 \alpha_e$	D_e [c]	r_e/Å [d]	Ref
E(0^+)	$^3P_2 + {}^1S$	0 – 2, 5, 7, 9 – 15, 26 – 29	39,059.485	165.676	0.2891	-36.5	5.8029	2.274	33,700	3.258	36
β(1)	$^3P_2 + {}^1S$	0 – 12, 24 – 28	39,103.666	170.310	0.4679	0.87	5.6707	1.899	33,655	3.295	36
D′(2)	$^3P_2 + {}^1S$	0 – 2, 21 – 27	39,061.830	173.627	0.5572	9.17	5.4782	2.019	33,697	3.353	36
$f(0^+)$	$^3P_0 + {}^1S$	3 – 5, 7 – 10, 12 – 14	44,923.79	184.40	0.771	35.9	5.777	2.13	34,286	–	30
G(1)	$^3P_1 + {}^1S$	1 – 7	45,552.805	184.854	0.6737	–	5.8898	2.485	34,296	3.231	29

(a) All units are cm^{-1} unless stated otherwise.

(b) Vibrational ranges from which molecular constants are derived.

(c) Calculated assuming the dissociation limits given in Table 1.2.

(d) The r_e values of the three states in the lowest cluster are not given explicitly in Reference 36. The values quoted are means of the RKR turning points for the v = 0 levels.

range since heterogeneous perturbation occurs between the three states. Consequently simultaneous analysis of all three states is necessary to obtain molecular constants which fit the experimental data [36]. Extrapolation to higher v is therefore meaningless. The occurence of heterogeneous perturbation between ion-pair states of the same cluster is not surprising since the states lie superimposed on one another.

Brand and coworkers limited their investigation to low ion-pair vibrational levels but in this work levels of the $E(0^+)$ state up to v = 116 were excited by the OODR technique (see Chapter Four). Excitation to yet higher levels was achieved by single photon absorption of VUV synchrotron radiation.

The two excitation techniques, absorption of single photon synchrotron radiation and laser OODR excitation, should be regarded as complimentary to one another. Double resonance experiments are ideally suited to sample the ion-pair states around their potential minima while the shift in r_e between the ground and ion-pair states dictates that single photon absorption accesses high vibrational levels only. Both techniques are state selective, given the $\Delta\Omega = 0, \pm 1$ selection rule for each photon absorbed. However, the degree of selectivity is quite different for each technique. Employing narrow bandwith laser excitation ($\Delta\lambda \sim 0.2$ cm^{-1}), single rovibrational levels can be populated whilst broad bandpass synchrotron radiation (typically $\Delta\lambda \sim 0.1$ nm) populates several vibrational levels.

The ability to excite single rovibrational levels by laser OODR has been used extensively by Brand and coworkers, and also in this work, as a diagnostic tool. $\Delta\Omega = 0$ electronic transitions are characterised by $P(\Delta J = -1)$ and $R(\Delta J = +1)$ rotational lines, where J is the rotational quantum number, while $\Delta\Omega = \pm 1$ transitions possess P, $Q(\Delta J = 0)$ and R branches. Since the spectroscopy of the common intermediate valence states is well known (see Table 1.1) the term values of the upper state can be found accurately and its Ω value determined. Although both $\Delta\Omega = 0, \pm 1$ electronic transitions are allowed, Brand et al have noted an empirical rule limiting valence $\rightarrow$ ion-pair transitions to those between states with the same Ω value [17]. Brand and coworkers have only observed exceptions to this rule when perturbation or collisional population pathways are involved. Excitation to known rovibrational levels also facilitates extraction of data for the determination of molecular constants.

By comparison, synchrotron radiation excitation is a rather less selective technique. At best several vibrational levels are excited simultaneously. This is, in part, due to the high density of states in the upper regions of the ion-pair states but is mainly due to the low photon flux of synchrotron compared to laser radiation which limits the excitation bandwidth. Although synchrotron radiation excitation is second to laser excitation in terms of selectivity it is superior in other respects. For example, synchrotron radiation can easily be scanned over a range of several hundred nanometers, the wavelength limits being restricted only by the dispersive and optical elements employed. Synchrotron radiation also possesses a quite unique temporal profile with the SRS at the Daresbury Laboratory

providing pulses of ~ 160 ps duration at a repetition rate of 500 MHZ in multi-bunch mode. When operating in single bunch mode these short pulses are produced at intervals of 320 ns, providing an ideal source for 'real time' lifetime measurements [39].

Finally, synchrotron radiation not only supplies tuneable radiation over a large energy range but also in regions where other tuneable sources are scarce or unknown, ie. the X-ray, VUV and near-IR regions. Tuneable VUV radiation allows access to high vibrational levels of the $E(0^+)$ ion-pair state of ICl, the lowest $\Omega = 0^+$ ion-pair state, in single photon transitions.

In this study, due to the relative positions of the ground, excited valence and ion-pair states, it transpires that single photon absorption populates the $E(0^+)$ ion-pair state at vibrational levels above $v \simeq 104$ slightly below the maximum level ($v = 116$) accessed by OODR excitation. The $E(0^+)$ ion-pair state is thus well characterised by combination of these two techniques. However, when homonuclear, rather than heteronuclear diatomic molecules are excited the two techniques populate different electronic states. This is a consequence of homonuclear g, u selection rules which allow $g \leftrightarrow u$ transitions but forbid $g \leftrightarrow g$ or $u \leftrightarrow u$ transitions. In homonuclear spectroscopy, single and double resonance excitation techniques offer choice not only in the region of the ion-pair state excited but, also, in selection of the state itself.

Synchrotron radiation studies of the $E(0^+)$ state of ICl form the bulk of this thesis. Since absorption to ICl Rydberg states

also occurs in single photon excitation from the ground state (see Figure 1.1) these experiments provide a good opportunity for study of Rydberg - ion-pair interactions. Such interactions occur when Rydberg and ion-pair states lie in the same energy region and it has been found that an adequate description of the experimental results presented here cannot be achieved without invoking some form of coupling between the two types of states.

The $E(0^+)$ ion-pair state of ICl is the analogue of the $D(^1\Sigma_u^+)$ state of iodine, both being the lowest $0_{(u)}^+$ state in the ion-pair manifold. The I_2 $D(^1\Sigma_u^+)$ state has a MO electron configuration of 1441 and has been likened to the $^1\Sigma_u^+$ $1s\sigma_g 1s\sigma_u$ ionic state of H_2 [40] as the filled I_2 $p\pi$ orbitals make little contribution to bonding. Intense $\sigma_u \leftarrow \sigma_g$ transitions are predicted theoretically [3] and indeed an extensive banded system peaking at 182.5 nm, designated the Cordes system, is attributed to the $I_2(D(^1\Sigma_u^+) \leftarrow X(^1\Sigma_g^+))$ transition. The $1441 \leftarrow 2440$ absorption is intense since it involves a one electron - one photon transition. Figure 1.2 shows that only one ICl state from the 1441 electron configuration does not correlate with ^2P ground-state iodine and chlorine atoms. This is the aforementioned $E(0^+)$ state. The other ion-pair states are based on the 2332 or higher electron configurations. Absorption to these states from the 2440 $^1\Sigma^+$ ground-state involves a two electron jump and accordingly weaker, single photon transitions are expected.

Although the description of an ion-pair state by its MO electron configuration applies well around the ground-state r_e of a molecule, as the internuclear separation increases this approximation

breaks down. It is well established that the outer limb of an ion-pair state is characterised by Coulombic attraction between the two dissociative ions. It therefore follows that neither description applies across the entire width of an ion-pair state and care must be taken when applying either of these simple models in interpretation of experimental results.

Much progress in the study of ion-pair states has been made since 1971 when Mulliken [3] showed the important role that ion-pair states possess in the spectroscopy of halogen/interhalogen molecules. These states are of interest both fundamentally - as a third class of electronic state - and practically. For example, an optically pumped I_2 laser system has been developed operating on an ion-pair → valence state transition [41]; the analogue of the commercially available F_2 laser which lases on the D'(2) → A'(2) transition at 158 nm. The coexistance of Rydberg and ion-pair states at the same energies results in interaction between the two types of states, providing an interesting theoretical problem whilst greatly affecting the spectroscopy of the molecule.

The ion-pair states of a diatomic molecule may be likened to charge-transfer excited states of polyatomic molecules as each is dominated by the Coulombic attraction between oppositely charged ions. Further parallels between the ion-pair states of diatomic molecules and polyatomic species may be drawn if one considers the high density of rovibrational levels in an ion-pair state. This is due not only to the width of the ion-pair states but also because ion-pair states lie together in clusters. In the lowest ion-pair cluster of ICl, three

sets of rovibrational levels are superimposed on one another with this number increasing as one proceeds up the ion-pair manifold. Thus, studies of the ion-pair states of halogen/interhalogen molecules may also shed some light on processes which occur in polyatomic molecules.

REFERENCES

1. R.S. Mulliken, Phys. Rev., **46**, 549 (1934).
2. L. Pauling, Chem. Rev., **5**, 204 (1928).
3. R.S. Mulliken, J. Chem. Phys., **55**, 288 (1971).
4. K.P. Huber and G. Herzberg, "Molecular Spectra and Molecular Structure", Vol. IV, Van Nostrand - Reinhold, New York, 1979.
5. P. Venkateswarlu, Can. J. Phys., **53**, 812 (1975).
6. E. Herbst and W. Steinmetz, J. Chem. Phys., **56**, 5342 (1972).
7. G.W. King and R.G. McFadden, Chem. Phys. Lett., **58**, 119 (1978).
8. J.C.D. Brand, D. Bussieres, A.R. Hoy, S.M. Jaywant and D.B. Miller, Opt. Commun., **48**, 195, (1983).
9. R.S. Mulliken, J. Chem. Phys., **55**, 309 (1971).
10. J.C.D. Brand, U.D. Deshpande, A.R. Hoy and S.M. Jaywant, J. Mol. Spectrosc., **100**, 416 (1983).
11. J.C.D. Brand and A.R. Hoy, J. Mol. Spectrosc., **114**, 219 (1985).
12. J.C.D. Brand, D. Bussieres and A.R. Hoy, Mol. Phys., **53**, 525 (1984).
13. J.C.D. Brand, D. Bussieres and A.R. Hoy, J. Mol. Spectrosc., **113**, 388 (1985).
14. J.A. Coxon, R.M. Gordon and M.A. Wickramaaratchi, J. Mol. Spectrosc., **79**, 363 (1980).
15. J.A. Coxon and M.A. Wickramaaratchi, J. Mol. Spectrosc. **79**, 380 (1980).
16. S.G. Hansen, J.D. Thompson, R.A. Kennedy and B. J. Howard, J. Chem. Soc. Faraday Trans., 2, **78**, 1293 (1982).
17. J.C.D. Brand, D. Bussieres, A.R. Hoy and S.M. Jaywant, Can. J. Phys., **62**, 1947 (1984).

18. R.D. Gordon and K.K. Innes, J. Chem. Phys., **71**, 2824 (1979).

19. J.A. Coxon, "Chemical Society Special Report on Molecular Spectroscopy", Vol. 1, p. 177, The Chemical Society, London, 1972.

20. D.J. Seery and D. Britton, J. Phys. Chem., **68**, 2263 (1964).

21. C.D. Olson and K.K. Innes, J. Chem. Phys., **64**, 2405 (1976).

22. M.S. Child and R. Bernstein, J. Chem. Phys., **59**, 5916 (1973).

23. E. Hulthen, N. Johansson and U. Pilsater, Ark. Fys., **14**, 31 (1958).

24. E. Hulthen, N. Jarlsater and L. Koffman, Ark. Fys., **18**, 479 (1960).

25. M.A.A. Clyne and I.S. McDermid, J. Chem. Soc. Faraday Trans. II, **72**, 2252 (1976).

26. C.E. Moore, "Atomic Energy Levels", NBS Circular 467, Vol. III, U.S. Bureau of Commerce, Washington, D.C., 1958.

27. R.S. Berry and C.W. Reimann, J. Chem. Phys., **38**, 1540 (1963).

28. C.E. Moore, "Atomic Energy Levels", NBS Circular 467, Vol. II, U.S. Bureau of Commerce, Washington, D.C., 1952.

29. J.C.D. Brand, U.D. Deshpande, A.R. Hoy and E.J. Woods, Can. J. Chem., **61**, 846 (1983).

30. J.C.D. Brand, A.R. Hoy and S.M. Jaywant, J. Mol. Spectrosc., **106**, 388 (1984).

31. A. Filippov, Z. Physik, **50**, 861 (1928).

32. J.D. Spivey, J.G. Ashmore and J. Tellinghuisen, Chem. Phys. Lett., **109**, 456 (1984).

33. R.K. Asundi and P. Venkateswarlu, Indian. J. Phys., **21**, 76 (1947).

34. H. Cordes and H. Sponer, Z. Phys., **79**, 170 (1932).

35. P.B.V. Haranath and P.T. Rao, Indian J. Phys., 21, 76 (1947).

36. D. Bussieres and A.R. Hoy, Can. J. Phys., 62, 1941 (1984).

37. R.H. Barnes, C.E. Moeller, J.F. Kircher and C.M. Verber, Appl. Phys. Lett., 24, 610 (1974).

38. G.W. King, I.M. Littlewood, R.G. McFadden and J.R. Robins, Chem. Phys., 41, 379 (1979).

39. I.H. Munro and N. Schwentner, Nucl. Instr. and Meth., 208, 819 (1983).

40. R.S. Mulliken, J. Chem. Phys., 7, 20 (1939).

41. M.J. Shaw, C.B. Edwards, F.O'Neill, C. Fotakis and R.J. Donovan, Appl. Phys. Lett., 37, 346 (1980).

CHAPTER TWO

EXPERIMENTAL DETAILS

2.1 Introduction

Experimental work was carried out employing either synchrotron radiation or laser radiation as the excitation source. Synchrotron radiation studies were performed on three stations at the Synchrotron Radiation Source (SRS) of the SERC Daresbury Laboratory; stations FS13.2, HA12 and VUV3.2. The majority of the results presented here were obtained on beamline FS13.2. Higher resolution absorption and fluorescence excitation studies were recorded on VUV3.2 while some preliminary studies employed station HA12.

A detailed account of the system on beamline 13.2 will be given together with more concise descriptions of the other two stations, highlighting differences between the three beamlines.

Optical - optical double resonance (OODR) laser experiments were conducted at the University of Edinburgh utilising two Lambda Physik dye lasers pumped by an excimer laser operating on the XeCl ($B(^1/_2) \rightarrow X(^1/_2)$) transition.

2.2.1 The Synchrotron Radiation Source (SRS)

From classical mechanics it is well known that an accelerating electron emits a continuum of radiation [1]. This

property was noted in the use of early particle accelerators, such as synchrotrons, and was developed until today storage rings are dedicated exclusively to production of this type of radiation.

Synchrotron radiation is valuable and unique since it consists of a continuum extending from the X-ray region, through ultraviolet (UV) and visible wavelengths to the infra-red region. The emitted light possesses extremely good vertical collimation, as a result of electrons travelling at relativistic velocities, and is highly polarised.

Synchrotrons and storage rings operate on the same basic principle, each utilising an oscillating electric field to accelerate electrons through a fixed orbit as defined by a periodic arrangement of magnets. They differ, however, in the method of control of the orbiting electrons.

Synchrotrons utilise a varying magnetic field to maintain electron orbit as the electric field energy is increased. Storage rings are designed to be more stable and maintain a constant particle energy, thus requiring a constant magnetic field. Energy lost as radiated light is compensated for by periodic injection of radio frequency (rf) power.

Figure 2.1 shows a plan of the Synchrotron Radiation Source (SRS) at Daresbury Laboratory. Electrons are initially accelerated by the linear accelerator (linac) to an energy of 10-15 MeV ($I \leq 20$ mA). Injection into the booster synchrotron follows with subsequent

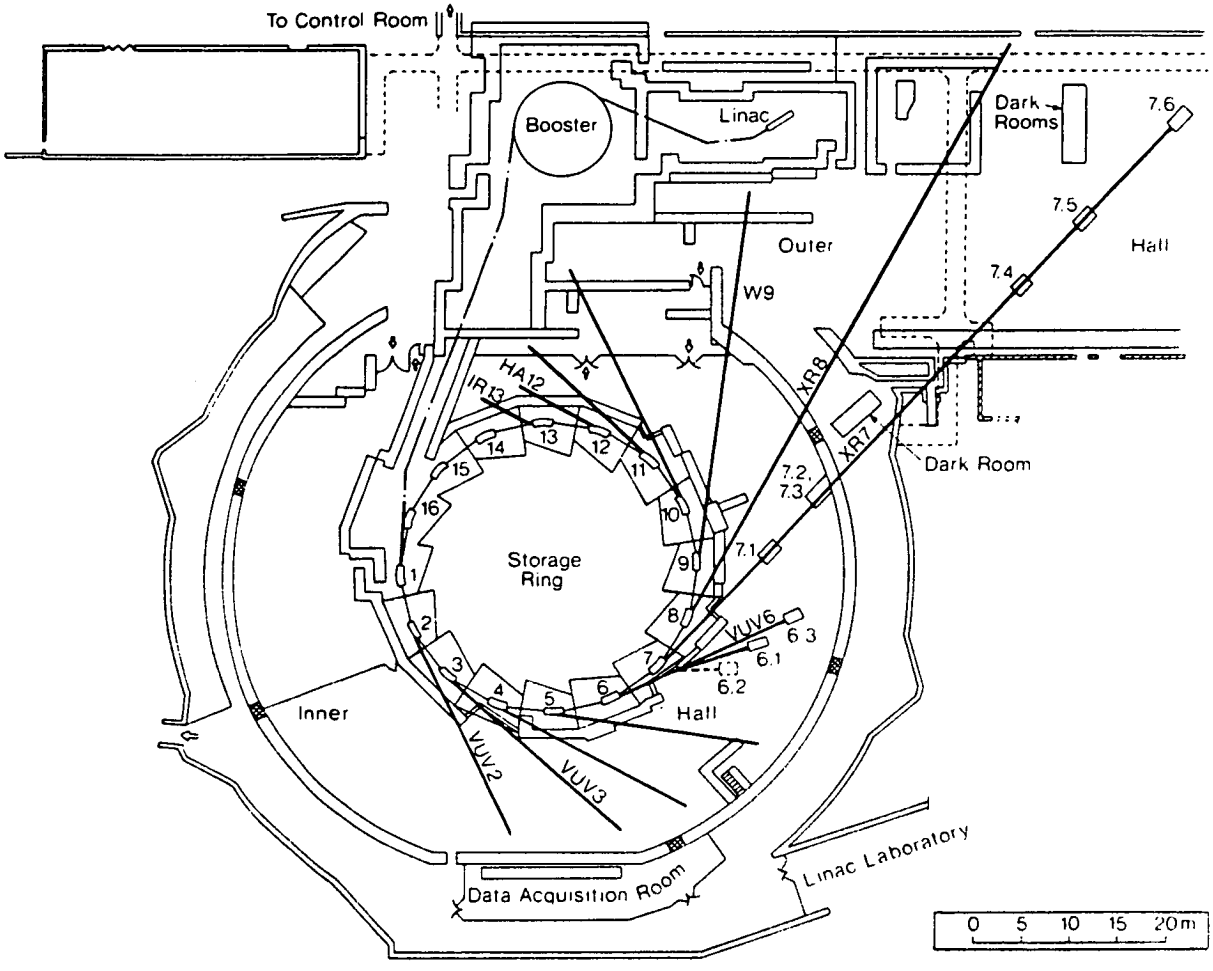

Figure 2.1 - The Synchrotron Radiation Source at the SERC Daresbury Laboratory.

acceleration to 0.6 GeV (I = 20 mA). At this energy injection into the storage ring occurs and final acceleration to 2 GeV takes place with typical injection currents of around 300 mA.

Rf power is transferred to the storage ring by a resonant cavity operating at a frequency of 500 MHz. Since electrons can only be accelerated when they are in phase with the accelerating rf field synchrotron radiation possesses an interesting time structure. Electrons circulate in bunches separated by the period of the rf field, in this case 2.0 ns. The number of bunches contained in the storage ring is dependent on the diameter of the ring and the period of the rf field. For the SRS, the ring circulation period is 320 ns and thus in multi-bunch mode 160 bunches of electrons, each with a bunch length of 160 ps, circulate separated by 2 ns.

Storage rings are also designed to function in single-bunch mode with only one electron bunch circulating. This mode is ideal for "real time" lifetime studies since it provides a succession of 160 ps pulses separated by the ring period of 320 ns. Lifetimes in the ns to μs range can be successfully measured employing the time-correlated single photon counting technique as detailed in Chapter Five. An injection current of ~ 15 mA is typical for single bunch operation.

Synchrotron radiation is emitted tangentially from each bending magnet (see Figure 2.1) with the wavelength range of a work station defined by the dispersive element employed. The three stations employed in this study all transmit radiation in the vacuum ultraviolet (VUV) spectral region.

Further details of the characteristics of synchrotron radiation and its use in fields such as time resolved spectroscopy can be found in References 2 and 3.

2.2.2 Station FS13.2

The experimental set-up on 13.2 was versatile allowing collection of simultaneous absorption and fluorescence excitation spectra, dispersed fluorescence spectra (both in the UV/VIS and VUV/UV regions) and time-resolved data.

Incoming white light radiation from the SRS was dispersed by a 0.5 m normal incidence Seya monochromator, manufactured by Bird and Tole, which provided radiation in the vacuum ultraviolet (VUV) region. After the incident beam was focussed into the centre of the absorption/fluorescence cell by a CaF_2 lens (d = 25 mm, f = 250 mm), the cross-section of the exciting radiation was 2.5 mm by 10 mm, the Seya entrance and exit slits being fully open (3 mm).

The bandpass of radiation with 3 mm slits is 4.5 nm (FWHM). A resolution of ~ 0.1 nm was the highest obtainable from the 0.5 m Seya.

A schematic diagram of the experimental lay-out on station FS13.2 is shown in Figure 2.2.

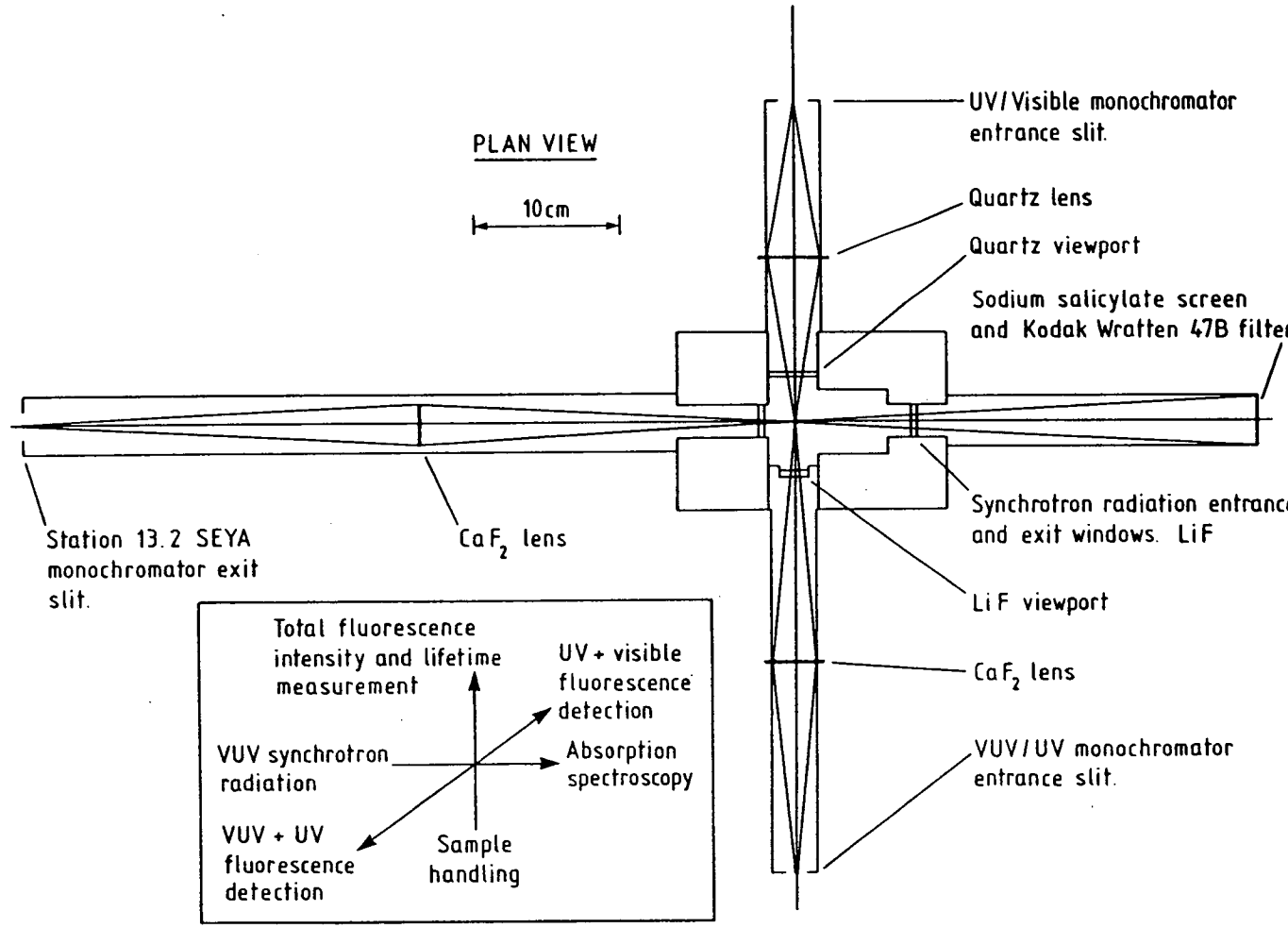

Figure 2.2 - Experimental arrangement of station FS13.2 at the Synchrotron Radiation Source (SRS), Daresbury Laboratory.

The sample cell consisted of a 3-way aluminium cross. The entrance and exit windows were separated by 100 mm, with the fluorescence observation zone situated ~ 20 mm along the beam axis from the entrance viewport. LiF or Spectrosil quartz windows were used, dependent on the transmission characteristics required.

Sample absorption was recorded by converting VUV synchrotron radiation to visible light with an external coating of sodium salicylate on the LiF window of the evacuated extension arm. To isolate the sodium salicylate fluorescence from scattered light a Kodak Wratten filter (47B) was placed between the phosphor coating and photomultiplier tube.

The fluorescence excitation photomultiplier is mounted in the vertical plane of the excitation beam. Total fluorescence within the sensitivity range of the photomultiplier was collected or a portion defined by the bandpass of a filter.

In the horizontal plane of the beam path two secondary monochromators were sited, coupled to the cell via adaptors containing lenses which focuss the sample fluorescence onto the monochromator entrance slits. Both monochromators were mounted on their sides to match the horizontal cross-section of the SRS beam passing through the cell and thus the area of the sample which is excited.

Two secondary monochromators were employed as the first, a 0.25 m Spex (Model Minimate), operates in the UV/VIS region while the second, a 0.2 m Acton (Model VM-502), is a VUV/UV monochromator. A

CaF_2 lens (d = 38 mm, f = 100 mm) was the focussing element for VUV/UV fluorescence while a Spectrosil quartz lens (d = 50 mm, f = 50 mm) was placed in the coupling arm to the Minimate.

The grating in the Minimate was a 2400 grooves mm^{-1} aberration-corrected concave holographic grating with a linear dispersion of 2 nm mm^{-1} while the Acton possessed a 1200 grooves mm^{-1} aberration-corrected concave holographic grating which gave a linear dispersion of 4 nm mm^{-1}. Both dispersion figures quoted apply for operation in the first order.

On the underside of the cell, the pumping port and the sample inlet were situated. Samples were prepared in pyrex bulbs on a conventional glass vacuum line and were then transferred to the cell.

MKS Baratron pressure transducers were employed as pressure gauges, both on the vacuum line and in the sample chamber. Throughout this work pressures are quoted in Torr (1 Torr = 133 Nm^{-2}).

A variety of photomultipliers was used during the course of experimental work. EMI 9883QKA photomultipliers were employed on the absorption and fluorescence excitation axes and also for dispersed fluorescence measurements with the Minimate UV/VIS monochromator. This tube has a bialkali photocathode with wavelength sensitivity in the range ~ 200 - 600 nm.

Two solar blind photomultipliers were used. An EMI G26K314LF fitted with a bialkali photocathode and a LiF window which extends the photomultiplier range down to ~ 110 nm giving a wavelength sensitivity

of ~ 110 - 600 nm. Both fluorescence excitation and dispersed fluorescence spectra (in conjunction with the Acton VUV/UV monochromator) were collected with this tube.

VUV fluorescence excitation spectra were, also, recorded with an EMI G26E314LF photomultiplier having a CsI photocathode and a LiF window. The spectral response of this photomultiplier was ~ 115 - 195 nm.

For lifetime studies a Mullard XP2020Q photomultiplier, cooled to -30°C, was mounted in the fluorescence excitation configuration, collecting UV/VIS fluorescence. A broad bandpass filter was generally in use when collecting time-resolved data.

Wavelength calibration of the three spectrometers on station 13.2 (the Seya, Minimate and Acton) was carried out by sending the monochromator to zero order and adjusting the grating position until maximum zero-order light flux was observed. This was then the true zero-order position of the instrument. Further calibration of the Seya was achieved by observation of the Schumann-Runge absorption bands of O_2 and internal calibration with known positions of ICl Rydberg transitions [4].

The Acton monochromator was cross-calibrated by the appearance of atomic iodine fluorescence lines which were observed following excitation at short wavelengths.

Data acquisition was achieved by digitising the absorption/fluorescence photomultiplier signals via a Camac interface and the station PDP11/04 microcomputer. Digitised data was subsequently transferred to the mainframe computer, a NAS (AS7000) for data processing. All absorption and fluorescence signals were collected by conventional single-photon counting techniques.

The signal output in the time-resolved work was processed using a time-to-amplitude converter (TAC), a fast A-to-D converter and a multichannel analyser, as discussed more fully in Chapter 5. This data was also transferred to the NAS (AS7000) for storage and analysis.

2.2.3 Station HA12

Early experimental work was carried out on beamline HA12 with an experimental set-up which transmitted synchrotron radiation of wavelengths above ~ 160 nm. The low wavelength limit was imposed by the sample cell which consisted of a 1 cm^2 Spectrosil cuvette fitted with a fused 'Young's greaseless' PTFE tap. This cell was then placed in the centre of a large evacuable chamber.

A Spex 1500 SP Czerny-Turner monochromator (1m) dispersed the white light synchrotron radiation giving a linear dispersion of 1 nm mm^{-1}.

The configuration of the assembly was simple with two experimental axes; the absorption axis collinear with the synchrotron

radiation beam and a perpendicular fluorescence axis where either fluorescence excitation or dispersed fluorescence spectra were collected. Dispersed spectra in the UV/VIS region only were recorded by the Spex (Model Minimate) monochromator with a 1200 grooves mm^{-1} grating resulting in a linear dispersion of 4 nm mm^{-1}.

VUV radiation was converted into visible light on the absorption channel by a sodium salicylate screen as described for station FS13.

Absorption and fluorescence signals were detected by photomultiplier tubes bolted directly onto the metal chamber. A filter was placed before the fluorescence photomultiplier tube to further specify the range of observed fluorescence in the excitation spectra.

The data acquisition system on HA12 was as that for FS13 with the photomultiplier signals stored initially on a PDP11/04 microcomputer via a Camac interface and then transferred to the NAS (AS7000) mainframe computer.

2.2.4 Station VUV3.2

Higher resolution absorption and fluorescence excitation studies were performed on beamline 3.2. The dispersing element of this station is a 5m normal incidence MacPherson monochromator which has a 1500 grooves mm^{-1} concave grating resulting in a linear dispersion of 0.17 nm mm^{-1}. The highest resolution of spectrum

presented here is 0.03 nm, a marked increase over the maximum attainable resolution on station FS13.2.

The experimental apparatus employed was that of FS13 transferred to the higher resolution monochromator but neither dispersed fluorescence spectra nor time-resolved data were collected.

EMI 9883QKA photomultipliers, as described previously, were employed on the absorption and fluorescence excitation channels. The data acquisition system was identical to that on FS13.2.

2.3 Optical-Optical Double Resonance Experiments

The experimental arrangement for optical-optical double resonance (OODR) laser excitation is shown schematically in Figure 2.3. The basic components of the system were two dye lasers pumped by one excimer laser, the sample cell, fluorescence collection and signal processing equipment.

Pump and probe photons were supplied by Lambda Physik FL3002E and FL2002 pulsed dye lasers respectively. Both dye lasers were pumped simultaneously by a Lambda Physik EMG 201 MSC excimer laser operating on the XeCl ($B(^1/_2) \rightarrow X(^1/_2)$) transition at 308 nm. The emergent excimer beam, which had a typical energy of 400 mJ per pulse, was passed through a beamsplitter with 50% of the excimer radiation entering each dye laser. The length of the excimer, and thus the dye laser, pulses was approximately 20ns FWHM.

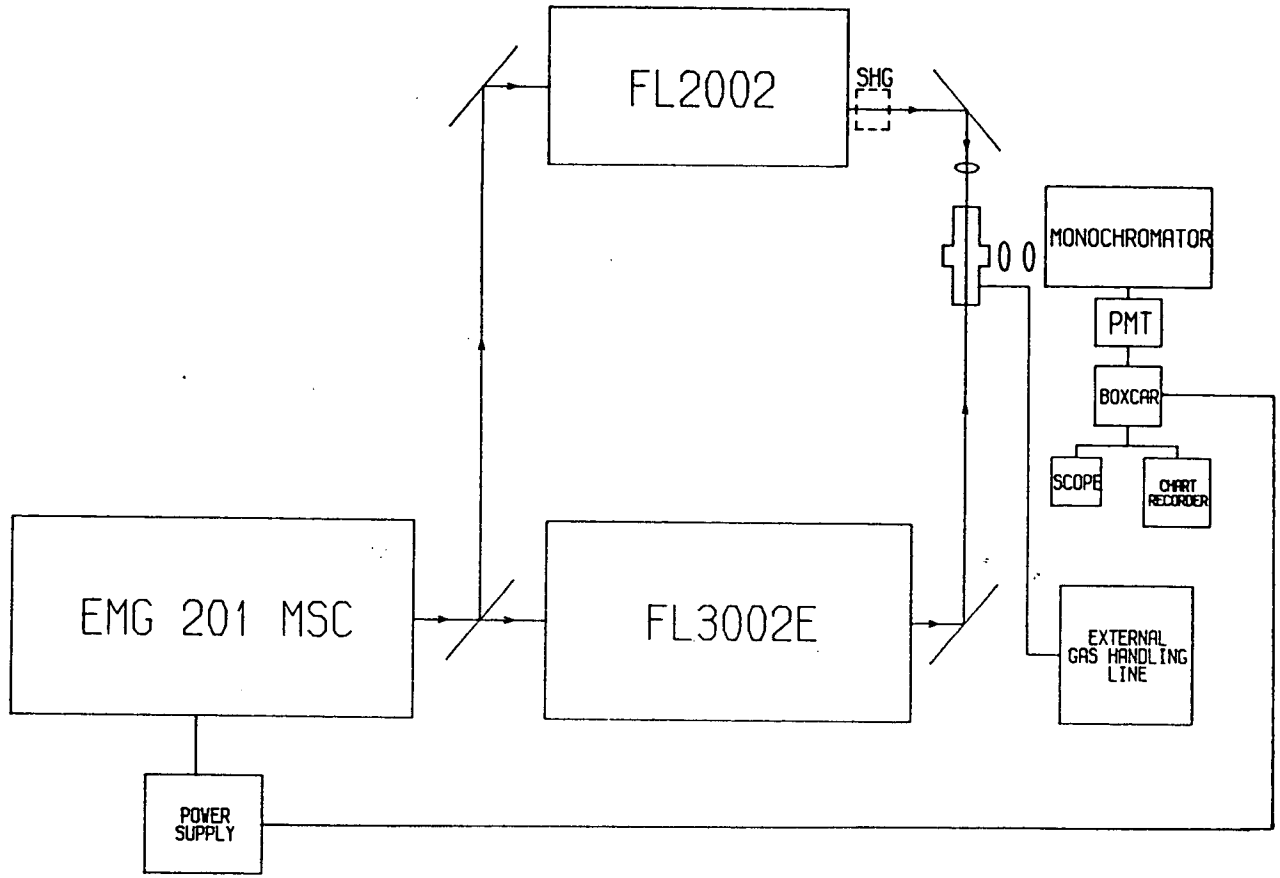

Figure 2.3 - Experimental arrangement for optical-optical double resonance (OODR) laser excitation to the $E(0^+)$ ion-pair state of ICl.

Rhodamine 6G in methanol (569 - 608 nm) was the lasing medium in the FL3002E laser, providing the first photon and consequently access to the intermediate state in the two-photon process. During OODR experiments the first photon wavelength was held constant while the second dye laser, the FL2002, was scanned using several dyes to populate different regions of the upper state. The laser dyes employed are detailed in Chapter 4. Frequency doubled dye laser output was generated by a FL30 KDP crystal providing probe photons below 333 nm. The second harmonic generation (SHG) light was separated from the fundamental dye laser beam by a UG5 filter.

The output energy of the FL3002E using Rhodamine 6G dye was ~ 25 mJ per pulse, while the efficiencies of the other dyes varied from 8 to 15% of the input excimer energy.

Excitation to single rovibrational levels was achieved with a dye laser bandwidth of 0.2 cm^{-1} at 584 nm (5th order) for both the FL3002E and the FL2002.

The laser light pathlengths from the excimer beamsplitter were adjusted such that the two dye laser pulses arrived simultaneously at the sample cell.

The sample chamber consisted of a cylindrical pyrex cross (diameter 25 mm, length 220 mm, width 50 mm) fitted with a 'Young's greaseless' tap and a small cold finger. All windows were Spectrosil allowing transmission of UV light. Fluorescence was collected perpendicular to the direction of the collinear laser beams as shown in Figure 2.3.

Two lenses were employed to maximise the detection of sample fluorescence. The first is a collection lens with a 5 cm (f/1.5) focal length and has two functions:

(i) Increasing the acceptance angle of the fluorescence.

(ii) Focussing the fluorescence onto the entrance slit of the monochromator.

The second lens (f = 15 cm) acts as a magnification element and was placed in such a position as to try and fill the first monochromator mirror with fluorescence.

The monochromator employed was a Jobin-Yvon HRS2 (f/7, 0.6 m) monochromator with a 1500 grooves mm^{-1} grating mounted in a Czerny - Turner configuration.

An EMI 9661B photomultiplier (sensitivity range 200 - 650 nm) or a Hamamatsu R928 tube (sensitivity range 185 - 930 nm) was used to detect fluorescence - dependent on the $E(0^+)$ vibrational level excited.

The photomultiplier signal was processed by a Stanford Research Systems (Model SR250) gated integrator with boxcar averager. Adjustment of the delay and width of the gate to give a maximum signal to noise (S/N) ratio was achieved by displaying the signal and gate on a four channel oscilloscope (Tektronix model 2445). The output, averaged over three or ten laser shots, was routed to a Kipp and Zonen

BD9 two-channel chart recorder and an IBM PC-XT 286 microcomputer. The boxcar was triggered from the synchronous output of the excimer laser.

To calibrate the frequency of the pump laser a small fraction of the beam was passed through an I_2 cell by a glass plate. The I_2 fluorescence excitation spectrum was recorded by a Hamamatsu R928 photomultiplier (wavelength sensitivity 185 - 930 nm) employing a Hoya R64 filter (which transmits wavelengths above 620 nm only) to protect the photomultiplier from scattered laser light.

Calibration was achieved by comparison of the I_2 fluorescence excitation spectrum with an atlas of iodine line frequencies [5].

2.4 Disproportionation of ICl

In all experiments excess Cl_2 was added to ICl to suppress disproportionation of ICl into its constituent elements,

$$\underline{ie}. \quad 2\ ICl \rightleftharpoons I_2 + Cl_2.$$

Calder and Giauque [6] studied ICl disproportionation and reported a disproportionation constant,

$$K = \frac{[Cl_2]\ [I_2]}{[ICl]^2}\ , \text{ of } 4.9 \times 10^{-6}.$$

It is necessary to suppress contamination of ICl with I_2 since I_2 has a very rich VUV absorption spectrum [7] distorting the spectra obtained of ICl. Single photon absorption of Cl_2 in the VUV occurs to the blue of 140 nm [8] and does not interfere with absorption to the ICl ion-pair states. Samples contained either equal

pressures of ICl and Cl_2 or ICl:Cl_2 in the ratio of 1:2. Either mix was sufficient to suppress I_2 formation.

2.5 Materials

ICl used in all experiments was obtained from BDH Chemicals Limited and had a minimum purity of 98%. Liquid ICl was decanted and degassed at 0°C and -196°C (liquid N_2 temperature) until an ICl vapour pressure of ~ 4.2 Torr was observed at ice temperature.

The excess Cl_2 added to the ICl sample to suppress I_2 formation via disproportionation was either BOC Chemically Pure Grade (99.5% minimum purity) or Mathieson Ultra-high purity Cl_2.

Xe and Kr, both BOC research grade, and BOC white spot grade N_2 were employed in reactive and quenching experiments.

All gases condensable at liquid N_2 temperature were thoroughly degassed before use.

REFERENCES

1. J.A.R. Samson, "Techniques of Vacuum Ultraviolet Spectroscopy", Wiley, New York, 1967.

2. I.H. Munro and A.P. Sabersky, "Synchrotron Radiation Research", Chapter 9, H. Winick and S. Doniach, Eds., Plenum Press, New York, 1980.

3. I.H. Munro and N. Schwentner, Nucl. Instr. and Meth., **208**, 819 (1983).

4. P. Venkateswarlu, Can. J. Phys., **53**, 812 (1975).

5. S. Gerstenkorn and P. Luc, "Atlas du spectre d'absorption de la molecule d'iode", CNRS, Paris, 1978.

6. G.V. Calder and W.F. Giauque, J. Phys. Chem., **69**, 2443 (1965).

7. J.A. Myer and J.A.R. Samson, J. Chem. Phys., **52**, 716 (1970).

8. T. Moeller, B. Jordon, P. Gurtler, G. Zimmerer, D. Haaks, J. Le Calve and M.C. Castex, Chem. Phys., **76**, 295 (1983).

CHAPTER 3

VACUUM ULTRAVIOLET ABSORPTION AND FLUORESCENCE EXCITATION SPECTRA OF ICl

3.1 Introduction

Much work on characterising the ion-pair states of ICl around their potential minima has been performed by Brand and co-workers [1-3], employing the optical-optical double resonance (OODR) technique. However, little is known about the ion-pair states further up their vibrational manifold.

Single photon absorption from the gound state is ideally suited to probe these levels as the shift in equilibrium internuclear bondlength between the ground and ion-pair states is sufficiently large that only high vibrational levels can be accessed in a Franck-Condon transition. Such studies have, to date, been sparse due to the scarcity of tuneable vacuum ultraviolet (VUV) radiation sources.

The use of synchrotrons as radiation sources has given an experimental tool which provides tuneable VUV light, thus opening up the study of highly excited states by single photon experiments. The state selectivity of laser excitation cannot be matched but the wavelength range available more than compensates for loss of specificity. A further advantage of synchrotron radiation is that VUV excitation energies are accessible without utilising multiphoton absorption techniques which alter the selection rules for allowed electronic transitions.

Theoretical and synchrotron studies of Cl_2 [4,5] have shown that mixing of isoenergetic Rydberg and ion-pair states is prominent, leading to anomalies in the absorption and fluorescence processes of the molecule. This phenomenon is a general one for molecules in which the Rydberg states are situated at similar energies to the ion-pair or other excited states.

Absorption to the inner limb of the ion-pair potential can, therefore, provide information on the interaction between the two states. When such interactions are present the potential curves may deviate strongly from their expected courses; deduced by the spectroscopic constants applicable at the potential minima.

The vacuum ultraviolet spectrum of ICl has been studied on a few occasions only, with attention focussed mainly on Rydberg absorptions. Cordes and Sponer [6] reported two Rydberg band systems in 1932 and other systems have subsequently been observed by Venkateswarlu [7] who carried out a comprehensive study of ICl absorption in the 122 - 190 nm region, including all Rydberg bands previously identified.

The observed bands were fitted to 23 Rydberg series, 12 converging to the ICl^+ ($^2\Pi_{3/2}$) ion and the remainder to the spin-orbit excited ion, ICl^+ ($^2\Pi_{1/2}$). In addition to the Rydberg absorptions, a band system extending from 158 - 166 nm was reported and identified as being analogous to the Cordes bands in I_2. The I_2 ($D\ ^1\Sigma_u^+ \leftarrow X\ ^1\Sigma_g^+$) transition has previously been assigned as the major component of the Cordes system [8], where the $D\ ^1\Sigma_u^+$ state is the lowest 0_u^+

(case (c)) symmetry ion-pair state. By analogy, Venkateswarlu implies that the observed ICl system is absorption from the ground to the lowest 0^+ ion-pair state, the $E(0^+)$ state. Analysis of this system was not attempted by Venkateswarlu and has yet to be published.

Little is known of the emission systems of the ICl excited states which lie in the vacuum ultraviolet. Haranath and Rao [9] reported in emission the two band systems first observed in absorption by Cordes and Sponer [6] and designated the a_6 and b_6 Rydberg levels by Venkateswarlu [7]. ICl was excited in a condensed transformer discharge with fluorescence observed from the initially excited Rydberg levels to the ground state.

Bibinov and Vinogradov [10] recorded a low resolution (0.3 nm) absorption spectrum of ICl between 120 and 190 nm as part of a study on the quenching and reactions of ICl with rare gases following excitation in this spectral region. Standard electronic detection techniques were used in contrast to the photographic recording employed by Venkateswarlu and earlier workers. The Rydberg and ion-pair systems previously reported were observed and the absorption cross-section was measured for the first time.

In this work, ICl absorption spectra were collected and subsequently corrected for the incident synchrotron radiation intensity in the VUV spectral region. In addition, the fluorescence processes of the ICl molecule were simultaneously monitored by recording fluorescence excitation spectra. Emission over a range, specified by various filter-photomultiplier combinations, was collected perpendicular to the synchrotron beam axis as the excitation wavelength was scanned.

Consideration of the absorption and fluorescence excitation spectra and the correlation between the two gives information on the excited states which fluoresce and the wavelength region of the fluorescence. Interactions between states and competition between radiative and non-radiative processes can be deduced by comparison of the spectra.

Recording of fluorescence excitation spectra in conjunction with absorption therefore provides another handle to the understanding of the spectroscopy of the molecule in question.

3.2 Experimental

Absorption and fluorescence excitation spectra were recorded on three stations at the Synchrotron Radiation Source (SRS), Daresbury Laboratory : Stations FS13, VUV 3.2 and HA12. On beamline 13.2 the highest attainable resolution consistent with a resonable photon flux was 0.1 nm while higher resolution spectra, commonly 0.03 nm, were collected on VUV 3.2. In addition, a low resolution ($\Delta\lambda$ = 0.3 nm) pressure dependence study of the fluorescence excitation above 159 nm was carried out on HA12. The resolution of each spectrum is listed in the figure captions.

On Station 13.2 a CaF_2 lens was employed to focuss the incident beam into the sample chamber resulting in transmission of radiation above 128 nm only. The limiting elements of transmission on beamline 3.2 were the LiF windows of the cell with a cut-off around 105 nm.

The ICl absorption spectrum was corrected for the variation of incident light intensity with wavelength. Three factors contribute to this variation:-

(i) The synchrotron radiation output.

(ii) The transmission function of the dispersing monochromator coupled with that of any optical elements present.

(iii) The decay of beam current, and thus intensity, with time.

The monochromator output was determined as a function of incident wavelength by collecting the synchrotron radiation intensity at a sodium salicylate screen situated at the rear of the evacuated sample chamber. This function was then corrected for ring current decay monitored directly at the storage ring.

The absorption spectrum is displayed, unless otherwise stated, in arbitrary cross-section units (ie. the absorption path length and sample number density have not been taken into account and are embedded in the cross-section) while the fluorescence excitation spectrum was corrected for beam decay only.

Three photomultipliers were employed on the fluorescence excitation channel to cover different spectral regions: an EMI 9883QKA for the UV-VUV region (200 - 600 nm); an EMI G26K314LF (110 - 600 nm) and an EMI G26E314LF solar blind tube (115 - 195 nm).

Two coloured glass Melles Griot filters were used in conjunction with the UV-VIS photomultiplier tube; a UG3 filter which transmits in the 320 - 460 nm range and a BG1 filter with bandpass extending from 280 - 480 nm.

Spectra collected on HA12 were recorded at low resolution ($\Delta\lambda$ = 0.3 nm) and have not been corrected for the variation of incident light intensity with wavelength or for beam current decay. The fluorescence excitation axis was situated perpendicular to that of the beam as on station FS13 and VUV 3.2, however only the Mullard XP2020Q photomultiplier, covering the UV-VIS region, was employed.

Excess Cl_2 was present in all experiments to avoid sample contamination by I_2 formed via an ICl disproportionation reaction.

Further experimental details can be found in Chapter 2.

3.3 ICl Absorption in the Vacuum Ultraviolet

The corrected absorption spectrum of ICl in the 125 - 195 nm spectral range, recorded on beamline FS13, is displayed in Figure 3.1. At wavelengths above 165 nm the two most prominent features are absorption to the a_6 and b_6 Rydberg states mentioned earlier. The a_6 system extends from 179 - 190 nm while absorption to the b_6 Rydberg levels occurs between 165 and 174 nm. In each case, the band structure corresponds to a vibrational progression of the upper state with additional hot bands.

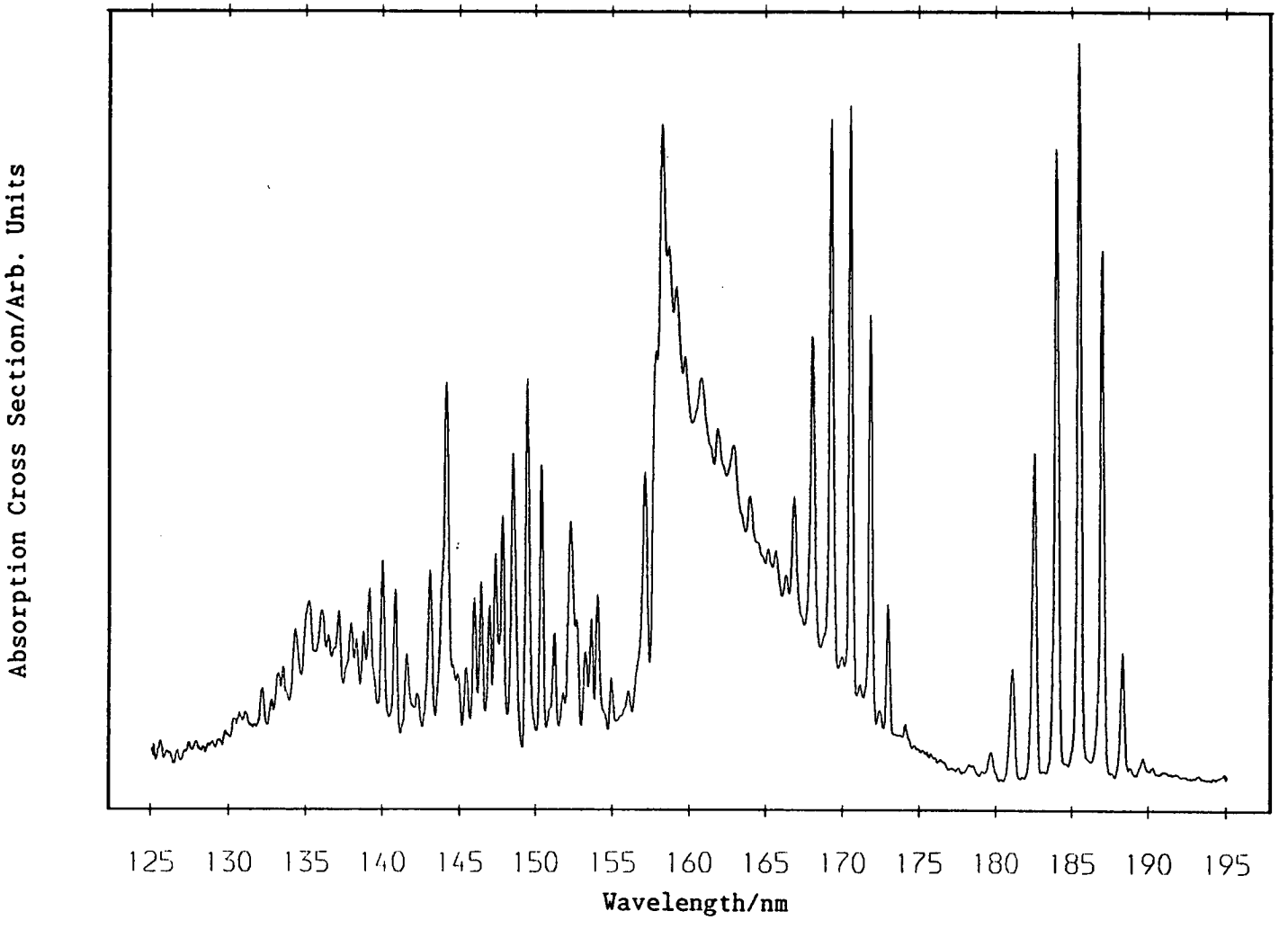

Figure 3.1 - Absorption cross section of ICl and Cl_2. ICl pressure = 25 mTorr, Cl_2 pressure = 50 mTorr. Spectral resolution, $\Delta\lambda$ = 0.1 nm.

The absorption between 158 - 177 nm appears to be a "continuum" which rises to a maximum at 158 nm. Overlapping absorption to the b_6 (1) Rydberg state is observed superimposed on this "continuum". Included in the 158 - 177 nm wavelength range is the extensive band system observed by Venkateswarlu [7] between 166 nm and 158 nm. To shorter wavelengths, discrete structure is again observed which corresponds to fragmentary vibrational progressions of many Rydberg states. Below 140 nm, radiation is absorbed not only by ICl but also by the Cl_2 vapour present which has a well-known absorption system at these wavelengths [4,11].

The absorption "continuum" has been assigned by analogy [7] as excitation to the lowest 0^+ ion-pair state of ICl. Bibinov and Vinogradov [10] designate this the D $^1\Sigma^+$ ion-pair state, more commonly known as the E(0^+) state of Brand et al [3,12] whose notation is used throughout this work. Single photon absorption to the lowest ion-pair state of 0^+ (case (c)) symmetry is expected to be strong. In case (c) coupling the main selection rule governing electronic transitions is ($\Delta\Omega = 0, \pm 1$), although experimentally it has been found [3] that parallel transitions ($\Delta\Omega = 0$) are much stronger than perpendicular transitions ($\Delta\Omega = \pm 1$). This preference is especially the case in charge-transfer transitions between valence and ion-pair states. Assignment of the absorption continuum to the E(0^+) $\leftarrow$ X $^1\Sigma(0^+)$ system is therefore reasonable.

No structure corresponding to ion-pair vibrational spacing is observed in Figure 3.1, nor in the spectrum published by Bibinov et al, due to insufficient resolution. Additional structure between the "continuum" maximum at 158 nm and the last band in the b_6 Rydberg

series is observed which was not reported by Bibinov [10]. The spacing of these bands, approximately 400 cm^{-1}, is too large to correspond to the vibrational separation of an ion-pair state.

Figure 3.2 shows a higher resolution absorption spectrum recorded on station VUV 3.2. Ion-pair vibrational spacing can just be observed between 158 nm and 166 nm in Figure 3.3. Unfortunately the spectra from beamline VUV 3.2 also show contributions from BrCl absorption. BrCl molecules were formed by the reaction of Cl_2 with Br_2 which had adhered to the aluminium cell during previous experiments. This impurity proved very difficult to remove, giving subsequent contamination of some spectra. The peaks in Figures 3.2 and 3.3 which have some or total contribution from BrCl absorption are marked with an asterisk. In Figure 3.4, both the BrCl and BrCl - contaminated, ICl absorption spectra are displayed in order that the degree of contamination may be gauged. The BrCl absorption bands comprise of transitions to two Rydberg states which are presumably analogous to the a_6 and b_6 systems of ICl. These states have been reported previously [6,13].

On closer examination of Figures 3.1 and 3.2 several additional absorption peaks, not reported by Venkateswarlu, were observed between the b_6 Rydberg bands. The positions of these bands and the b_6 absorption system are listed in Table 3.1. From comparison of the spacing between vibrational levels of the Rydberg state and the unidentified bands it appears that the second band series is also Rydberg in origin.

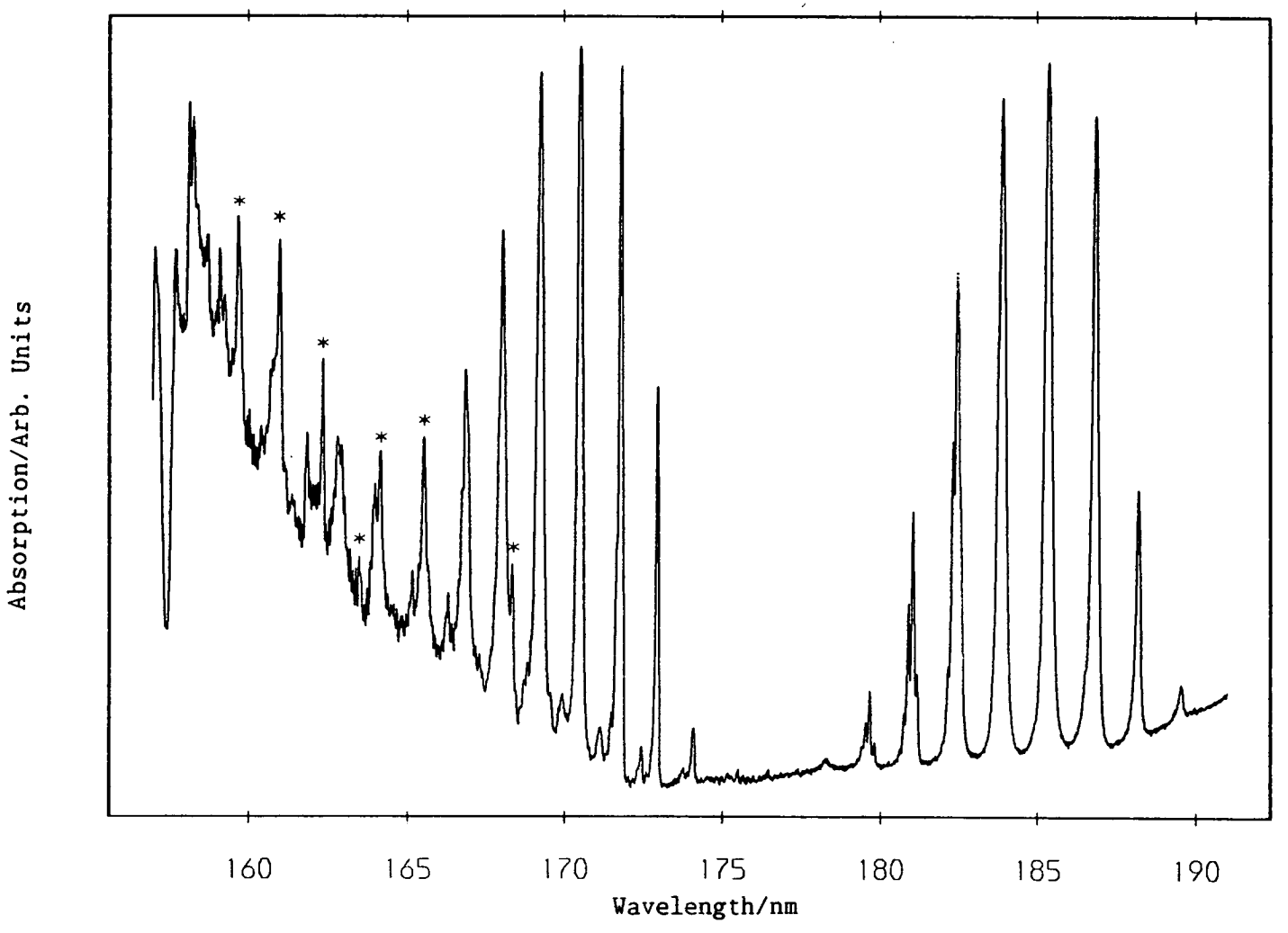

Figure 3.2 - ICl absorption above 157 nm recorded at higher resolution ($\Delta\lambda$ = 0.03 nm). Asterisks mark the peaks which contain a significant degree of BrCl contamination. Spectrum is not corrected for variation of excitation light intensity with wavelength. ICl pressure = 70 mTorr, Cl_2 pressure = 130 mTorr.

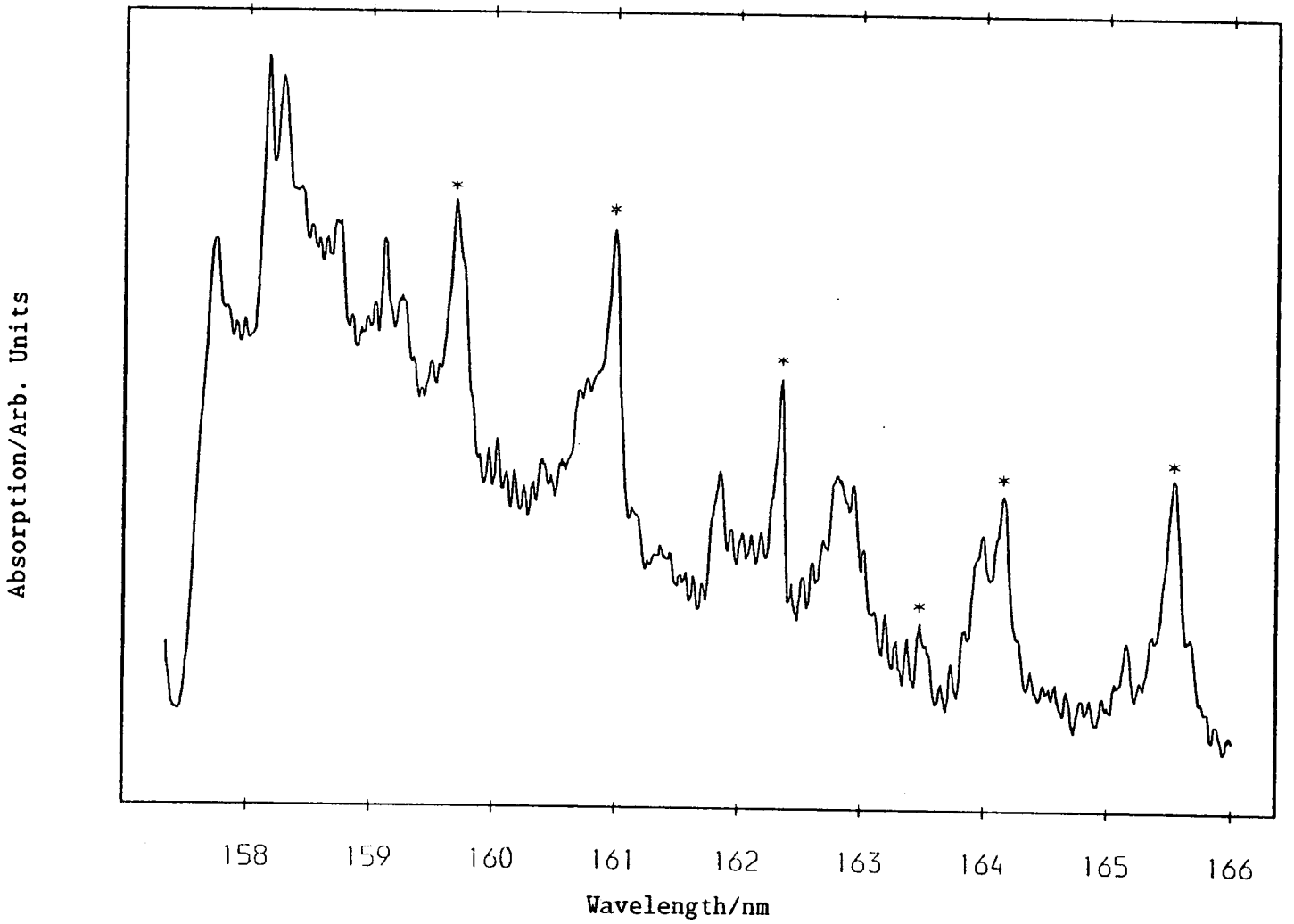

Figure 3.3 - ICl absorption exhibiting ion-pair vibrational structure ($\Delta\lambda$ = 0.03 nm, ICl pressure = 70 mTorr, Cl_2 pressure = 130 mTorr). BrCl contaminant peaks are marked with an asterisk. Spectrum is not corrected for the excitation function of the incident radiation.

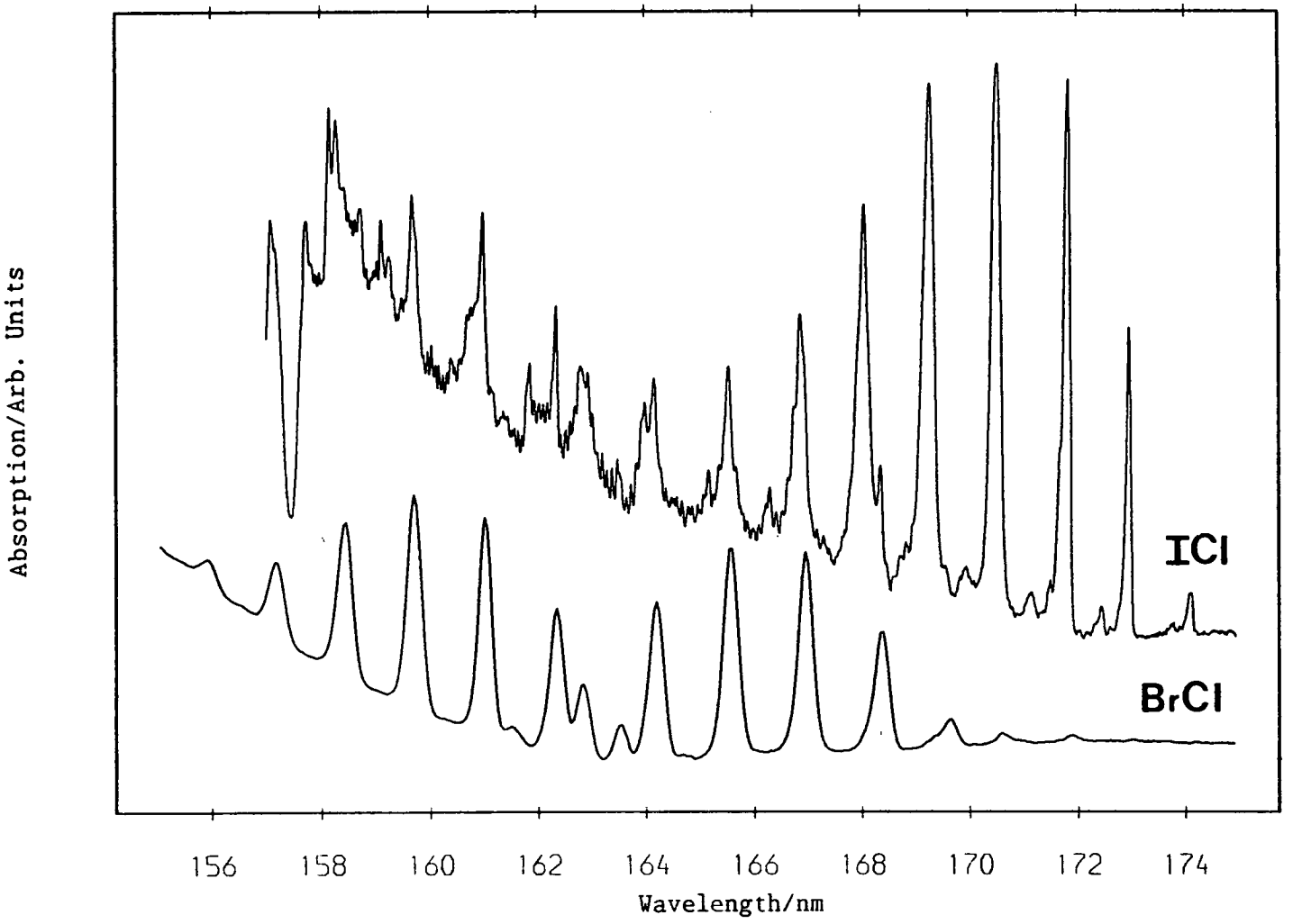

Figure 3.4 - Upper trace - ICl absorption spectrum containing BrCl contaminant. $\Delta\lambda$ = 0.03 nm, ICl pressure = 70 mTorr, Cl_2 pressure = 130 mTorr. Lower trace - BrCl absorption in the same region. $\Delta\lambda$ = 0.3 nm, BrCl pressure = 80 mTorr, Cl_2 pressure = 160 mTorr. Neither trace is corrected for the excitation function of the incident radiation.

TABLE 3.1

POSITIONS OF THE $b_6'(0^+) \leftarrow X(0^+)$ AND $b_6(1) \leftarrow X(0^+)$ ABSORPTION BANDHEADS

System	v', v''	λ_{vac}/nm [a]	ν/cm^{-1}	$\Delta\nu$/cm^{-1} [b]
$b_6(1) \leftarrow X(0^+)$	0,2	174.08	57 445	
				378
	0,1	172.96	57 817	
				374
	0,0	171.83	58 197	
				447
	1,0	170.52	58 644	
				437
	2,0	169.26	59 081	
				429
	3,0	168.04	59 510	
				431
	4,0	166.84	59 938	
				434
	5,0	165.64	60 372	
$b_6'(0^+) \leftarrow X(0^+)$	0,0	173.74	57 557	
				434
	1,0	172.44	57 991	
				447
	2,0	171.12	58 438	
				417
	3,0	169.91	58 855	

[a] Bandhead positions accurate to ± 0.03 nm (± 11 cm^{-1}).

[b] Bandhead separations accurate to ± 16 cm^{-1}.

The a_6 Rydberg state has a molecular core of ICl^+ ($^2\Pi_{3/2}$) with the Rydberg electron occupying a 6sσ orbital. The interaction between an ICl^+ core and a Rydberg electron is best described by (Ω_c, ω) coupling [14]. In this type of coupling, the outer Rydberg electron is so little coupled to the core of the molecule that the spin and orbital motions of the electron couple to form a resultant ω which then combines with the total electronic angular momentum, Ω_c, of the core to give Ω for the molecular Rydberg state. (Ω_c, ω) coupling between a $^2\Pi_{3/2}$ core and an electron in a 6sσ orbital gives two states with Ω values of 1 and 2. The b_6 Rydberg state is the spin-orbit excited counterpart of the a_6 state, with an ICl^+ ($^2\Pi_{1/2}$) core and the Rydberg electron again occupying a 6sσ orbital. (Ω_c, ω) coupling produces three states with $\Omega = 0^-$, 0^+ and 1.

The only "good" quantum number under (Ω_c, ω) coupling is the resultant Ω value of the molecule. Allowed single photon transitions from the ground electronic state are therefore $0^+ \leftarrow 0^+$ and $1 \leftarrow 0^+$. The a_6 Rydberg levels observed are assigned to the $\Omega = 1$ component of the ($^2\Pi_{3/2}$) 6sσ configuration while both the $\Omega = 0^+$ and 1 components of the ($^2\Pi_{1/2}$) 6sσ configuration are accessible. Venkateswarlu assigned the b_6 Rydberg bands as superpositions of absorption to both the $\Omega = 0^+$ and 1 states. It is now proposed that the second series of bands, previously unidentified, corresponds to absorption to the 0^+ component of the ($^2\Pi_{1/2}$) 6sσ coupling. The two components of this configuration shall henceforth be referred to as the b_6 (1) and $b_6'(0^+)$ states.

The $b_6'(0^+)$ bands have not been previously reported. The resolution of the spectrum recorded by Bibinov et al was too low for the bands to be distinguished from the b_6 (1) Rydberg bands while the weak absorptions were not detected on photographic plates by Venkateswarlu. Several additional bands, such as hot bands and higher members of vibrational series, have been observed in the course of this work which were not detected using photographic detection methods.

The weaker b_6 system has been assigned to the 0^+ state mainly because of correlations which exist between the fluorescence excitation and absorption spectra. These will be discussed in the following section. It is not, however, unreasonable that the strong b_6 system has an Ω value of 1 as the a_6 and b_6 absorptions are of similar intensities and there is no ambiguity in the assignment of the a_6 (1) system. The $\Omega = 1$ component of the $(^2\Pi_{3/2})$ $6s\sigma$ configuration is the only accessible state in a single photon transition.

The new band series ($b_6'(0^+)$) cannot be attributed to additional hot bands. If this were the case a second progression should also be observed in the a_6 Rydberg system as both states have similar vibrational intensity envelopes and hence lie at approximately equal r_e values. In addition, the vibrational spacing observed (see Table 3.1) is typically Rydberg, indicating that the progression is from $v = 0$ in the ground state to increasing values of v in an upper Rydberg state.

Assuming that the lowest band, observed at 173.74 nm, is the (0, 0) band of the system $b_6'(0^+) \leftarrow X\ ^1\Sigma^+$, the term value ($T_e$) of the b_6' (0^+) state is estimated to be 57,517 ± 10 cm^{-1}. This term value was determined by calculating the mean of the differences between the b_6 (1) and $b_6'(0^+)$ absorption bands and subtracting this mean from the known T_e value, 58,167 cm^{-1}, of the b_6 (1) state [15].

Although absorption to the $b_6'(0^+)$ state is relatively weak, in the following section it will be shown that this state plays a major role in the intramolecular dynamics of the ICl molecule.

3.4 Comparison of Absorption and Fluorescence Excitation Spectra Above 155nm

From comparison of the ICl absorption and fluorescence excitation spectra it has been deduced that mixing between Rydberg and ion-pair states is occurring at wavelengths above 155 nm. Examples of Rydberg - valence mixing have previously been reported for diatomic molecules such as H_2, Na_2, Cl_2, F_2, HCl and O_2 [4,5,16-20] (the term 'valence' here describes states which dissociate to either ions or ground state atoms). ICl spectroscopy thus falls naturally into two sections. The first, above 155 nm, where absorption to both Rydberg and ion-pair states is observed with interactions between the states playing a dominant role and the second, to shorter wavelengths, with absorption confined mainly to Rydberg states. Below 140 nm both ICl and Cl_2 absorption and fluorescence systems are present.

The majority of this section will be concerned with the Rydberg - ion-pair mixing in the region above 155 nm and the resulting effect on the ICl spectra.

In Figure 3.5 ICl absorption and fluorescence excitation spectra in the 155 - 195 nm region are displayed. Fluorescence from the excited states was collected in the range 280 - 480 nm. It is obvious from Figure 3.5 that the fluorescence excitation structure does not mirror that of the absorption as expected. There is neither a "continuum" rising to a maximum at 158 nm nor strong fluorescence at the positions of the Rydberg bands. The latter observation is not surprising since fluorescence was reported by Haranath and Rao [9] from the a_6 (1) and b_6 (1) states to low vibrational levels of the ground state only. Such fluorescence lies in the VUV region and would not be detected by the filter-photomultiplier combination in use. Venkateswarlu's photographic plates [7] show that both the a_6 (1) and b_6 (1) absorption bands displayed are diffuse, indicating that a predissociation channel competes with fluorescence in the depopulation of these states. Indeed in a previous work [21], before the emission spectrum of Haranath and Rao was considered, it was reported that the a_6 (1) Rydberg levels, and probably the b_6 (1) levels, were completely predissociated.

Minima are, therefore, observed in the fluorescence excitation spectrum at positions of absorption to the a_6 (1) and b_6 (1) Rydberg states as these levels either predissociate or fluoresce outside the range of the detection equipment. The sample appears optically thick at such wavelengths since absorption to a Rydberg level diminishes the number of photons available to populate the fluorescent state(s). Fluorescence excitation spectra, run at varying ICl pressures, show the minima deepening with increasing ICl pressure.

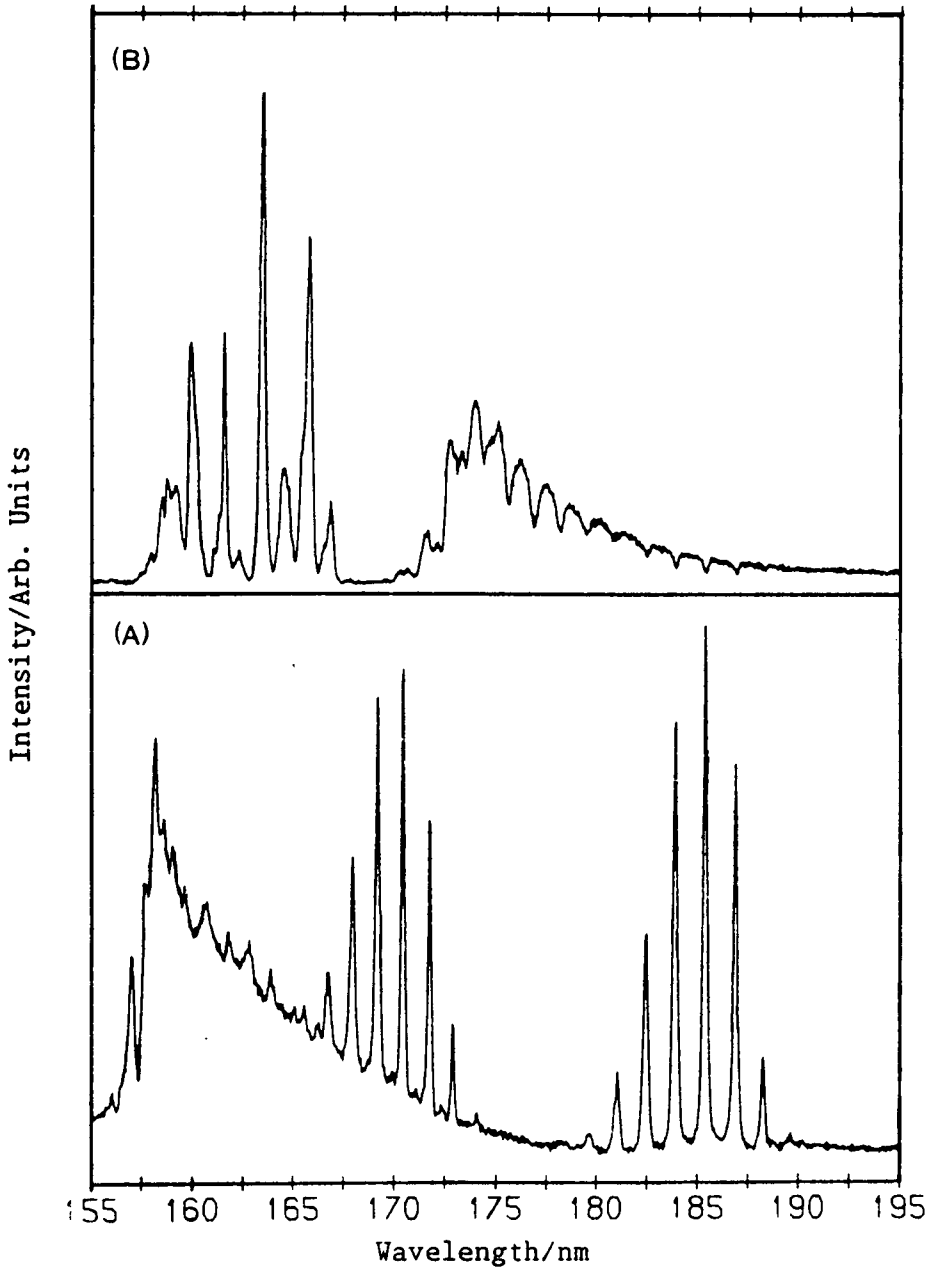

Figure 3.5 - Absorption cross-section (A) and fluorescence excitation spectrum (B) of ICl above 155 nm. Fluorescence was detected in the 280 - 480 nm region. Both spectra are normalised to the most intense peak. Ratio of ICl : Cl_2 = 1:2 in both spectra. P (absorption) = 75 mTorr, P (fluor.) = 135 mTorr. $\Delta\lambda$ = 0.1 nm.

To the blue of the a_6 (1) Rydberg system much structure unaccounted for by the absorption spectrum is observed. The fluorescence excitation rises to a maximum around 174 nm and then falls rapidly to total loss of fluorescence at 170 nm. Below 167 nm fluorescence from the excited states again commences but now in a highly structured form. Figure 3.6 shows the fluorescence excitation and absorption from 168 - 192 nm in greater detail.

Several series of minima are observed at wavelengths above 170 nm. The first, marked by filled circles in Figure 3.6, corresponds to the positions of the a_6 (1) Rydberg bands and the optically thick regions discussed earlier. Between the a_6 (1) and b_6 (1) Rydberg states, pronounced minima appear in the fluorescence excitation with no corresponding structure in the ICl absorption. The effect of optical thickness is again observed with the b_6 (1) system but does not account for the number of minima present or the decrease in fluorescence quantum yield to higher energies.

The minima between 174 and 180 nm appear to be an extension of the a_6 (1) series with slightly irregular spacing and increased depth. The optical density effect cannot account for these minima as no corresponding Rydberg absorptions are present. To the blue of 174 nm, further members of the series are found. Indeed, in the 170 - 174 nm region, three different interactions combine to produce the resultant structure in the fluorescence excitation spectrum:-

(i) The b_6 (1) Rydberg minima resulting from optical thickness of the sample (marked by open triangles in Figure 3.6).

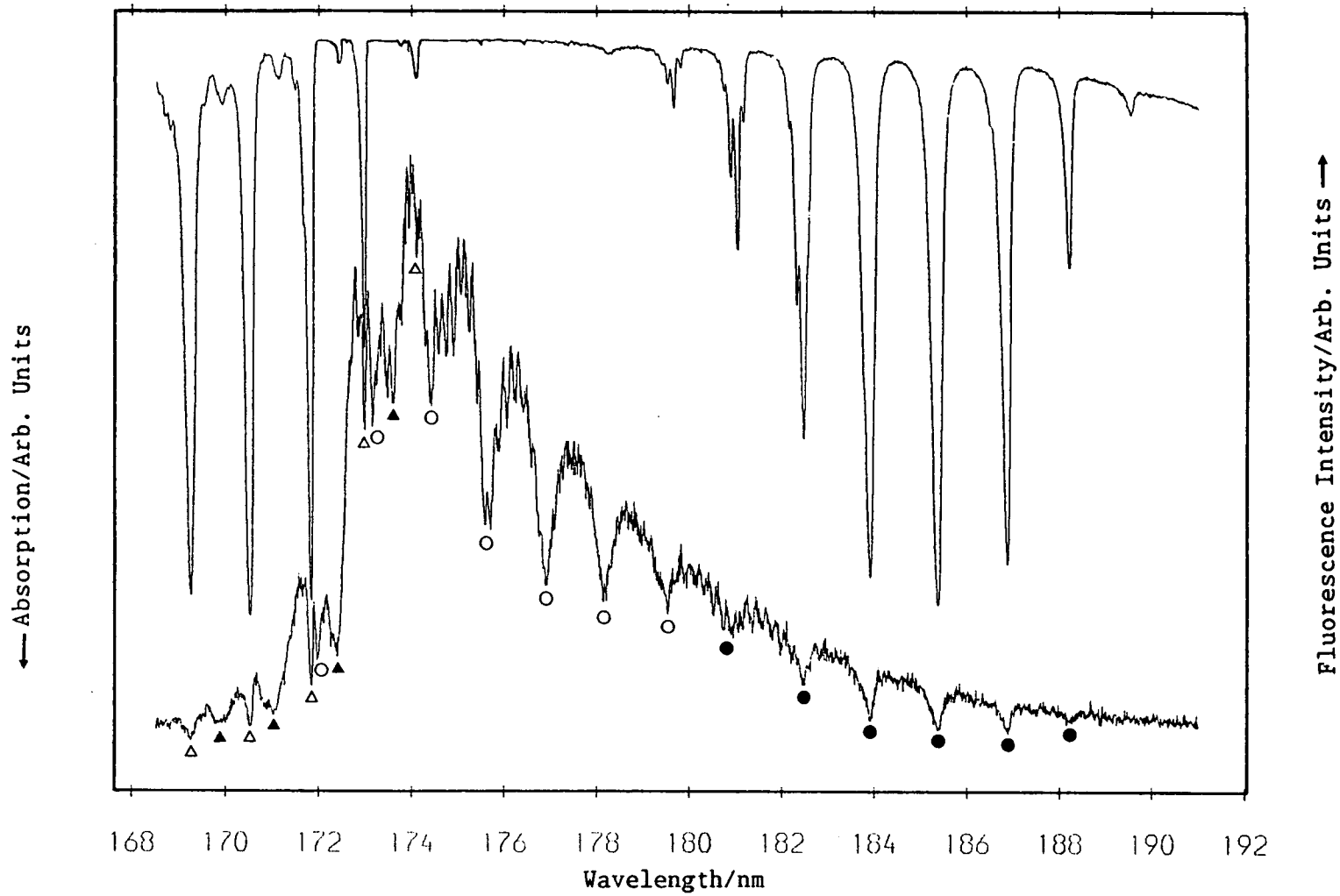

Figure 3.6 - ICl absorption (upper trace) and fluorescence excitation (lower trace) spectra in the region 168 - 192 nm. The absorption spectrum is not corrected for the excitation function of the incident radiation and is inverted for ease of comparison between maxima in absorption and minima in fluorescence excitation. $\Delta\lambda$ = 0.03 nm, ICl pressure = 70 mTorr, Cl_2 pressure = 130 mTorr. For explanation of symbols see text.

(ii) The continuation of the minima linked to the a_6 (1) Rydberg series (shown by open circles).

(iii) A third series, as yet unidentified (marked by filled triangles in Figure 3.6).

The effect of $b_6'(0^+)$ Rydberg absorption on the fluorescence excitation has still to be considered. Figure 3.6 shows that the positions of the third series of minima correspond with those of the $b_6'(0^+)$ absorption bands. The loss of fluorescence following absorption to a $b_6'(0^+)$ level is too large to be attributed to the optical density of the sample. From the comparitive strengths of absorption to the $b_6'(0^+)$ and b_6 (1) states, it is predicted that such an effect should be minimal. Indeed, as absorption occurs to higher vibrational levels of the 0^+ state the intensity of fluorescence decreases until, at 170 nm, no fluorescence is observed in the 280 - 480 nm range. The $b_6'(0^+)$ state appears to be intimately coupled with the fluorescence levels, providing an efficient pathway for non-radiative decay.

The positions and separations of the a_6 (1) minima and the minima proposed to be a continuation of this series are listed in Table 3.2. The wavenumbers of the Rydberg absorption bands observed in this work and by Venkateswarlu [7] are also included. Predicted band positions, relative to the (0,0) band at 53,502 cm^{-1}, were calculated with ω_e and $\omega_e x_e$ values obtained from a Birge-Sponer plot of Venkateswarlu's absorption data; the most accurate to date. Values of 435 ± 1 cm^{-1} and 0.6 ± 0.1 cm^{-1} were found for ω_e and $\omega_e x_e$ respectively.

TABLE 3.2

COMPARISON BETWEEN THE POSITIONS OF MINIMA IN THE FLUORESCENCE EXCITATION AND OBSERVED AND CALCULATED POSITIONS OF $a_6(1) \leftarrow X(0^+)$ BANDHEADS

v', v''	$\lambda_{minimum}$/nm	$\nu_{minimum}$/cm^{-1}	ν_{calc}/cm^{-1} (a)	ν_{abs}/cm^{-1} (b)	ν_{abs}/cm^{-1} (c)
0,0	186.88	53 510	53 502	53 504	53 502
1,0	185.38	53 943	53 936	53 937	53 936
2,0	183.95	54 363	54 369	54 371	54 369
3,0	182.46	54 806	54 800	54 799	54 800
4,0	180.93	55 270	55 230	55 230	55 231
5,0	179.53	55 701	55 659	55 654	55 660
6,0	178.19	56 120	56 087	56 101	-
7,0	176.90	56 529	56 514	-	-
8,0	175.66	56 928	56 939	-	-
9,0	174.41	57 336	57 363	-	-
10,0	173.18	57 743	57 786	-	-
11,0	172.00	58 139	58 208	-	-

(a) Positions of the a_6 (1) $\leftarrow X(0^+)$ absorption bandheads calculated with respect to a (0,0) band at 53 502 cm^{-1}, employing ω_e = 435 cm^{-1} and $\omega_e x_e$ = 0.6 cm^{-1}.

(b) Positions of the $a_6(1) \leftarrow X(0^+)$ absorption bandheads observed experimentally.

(c) Positions of the $a_6(1) \leftarrow X(0^+)$ absorption bandheads reported by Venkateswarlu [7].

Good agreement occurs between the observed absorption bands and minima in fluorescence excitation up to the (3,0) band. The position of the minimum at the (4,0) band is unclear as the optical density of the sample is a function of the decreasing absorption cross-section to the Rydberg levels. However, the minimum corresponding to the (5,0) band is markedly deeper (Figure 3.6), moreso than is expected from the corresponding absorption strength. To the blue of, and including, the (5,0) band the depth of the minima suggests the opening of a non-radiative pathway at intervals consistent with the separation of Rydberg vibrational levels. From the predicted vibrational levels of the a_6 (1) state and the positions of the observed minima it is concluded that this pathway proceeds via the a_6 (1) Rydberg state. The "non-radiative" pathway may include channels such as predissociation or fluorescence in a region outside the filter band-pass, as proposed for lower vibrational levels of the a_6 (1) Rydberg state.

The crucial difference between the two sets of minima, those attributed to the optical density and those at and above the position of the (5,0) band, is that the former arise purely from a physical effect while the latter must result from interaction between the a_6 (1) Rydberg and the fluorescing state. Optical density can play no part in production of these minima as direct absorption to the higher Rydberg levels is precluded by the Franck-Condon factors. The behaviour of the two sets of minima in varying pressure studies (Section 3.9) further highlights the different pathways which lead to the appearance of minima in the fluorescence excitation.

Table 3.3 lists the positions of the b_6 (1) and $b_6'(0^+)$ Rydberg bands and the corresponding minima in the fluorescence excitation. Good agreement is again found between the b_6 (1) absorptions and the observed minima. The $b_6'(0^+)$ minima are slightly blue shifted from the corresponding absorption bands but as the separations of both series are typically Rydberg and the observed shifts are small, the decrease in fluorescence yield has been attributed to a strong interaction between the $b_6'(0^+)$ Rydberg state and the fluorescing levels. The discrepancies between positions of maximum absorption and minimum fluorescence may indeed be a result of such an interaction.

Below 170 nm very little correlation exists between absorption and fluorescence excitation spectra. The fluorescence excitation is no longer a "continuum" but consists of discrete bands while irregularly spaced absorptions are superimposed on the ion-pair vibrational spacing. The absorption "continuum" rises to a maximum around 158 nm where absorption also occurs to the c_6 Rydberg state which has a $(^2\Pi_{3/2})$ 6pσ configuration with an Ω value of 1 [7]. The region 155 - 170 nm is shown in greater detail in Figure 3.7. The b_6 (1) and c_6 (1) absorption bands are marked but the resolution is insufficient to resolve ion-pair vibrational separations. In Table 3.4 the positions of maxima in the absorption and fluorescence excitation are given for comparison. From Figure 3.7 and Table 3.4 it is observed that maxima in the fluorescence excitation occur between maxima in absorption. However, correlation between the maxima in absorption and minima in fluoresence is not as clear-cut as that observed in the excitation region above 170 nm.

TABLE 3.3

COMPARISON BETWEEN THE POSITIONS OF RYDBERG ABSORPTION BANDS AND FLUORESCENCE EXCITATION MINIMA IN THE 169.0 - 174.5 nm REGION

System	v', v''	λ_{abs}/nm	ν_{abs}/cm^{-1}	λ_{minima}/nm[a]	ν_{minima}/cm^{-1}	$\Delta\nu_{minima}$/cm^{-1}
$b_6(1)\leftarrow X(0^+)$	0,2	174.08	57 445	174.10	57 438	
						375
	0,1	172.96	57 817	172.97	57 813	
						381
	0,0	171.83	58 197	171.84	58 194	
						443
	1,0	170.52	58 644	170.54	58 637	
						440
	2,0	169.26	59 081	169.27	59 077	
$b_6'(0^+)\leftarrow X(0^+)$	0,0	173.74	57 557	173.60	57 604	
						404
	1,0	172.44	57 991	172.39	58 008	
						465
	2,0	171.12	58 438	171.02	58 473	
						378
	3,0	169.91	58 855	169.92	58 851	

[a] The positions of minima correlating with $b_6(1)$ absorption bands are accurate to ± 0.03 nm (± 11 cm^{-1}). The minima correlating with $b_6'(0^+)$ absorption bands are less well defined and have an estimated error of $\Delta\lambda$ = ± 0.05 nm (± 18 cm^{-1}).

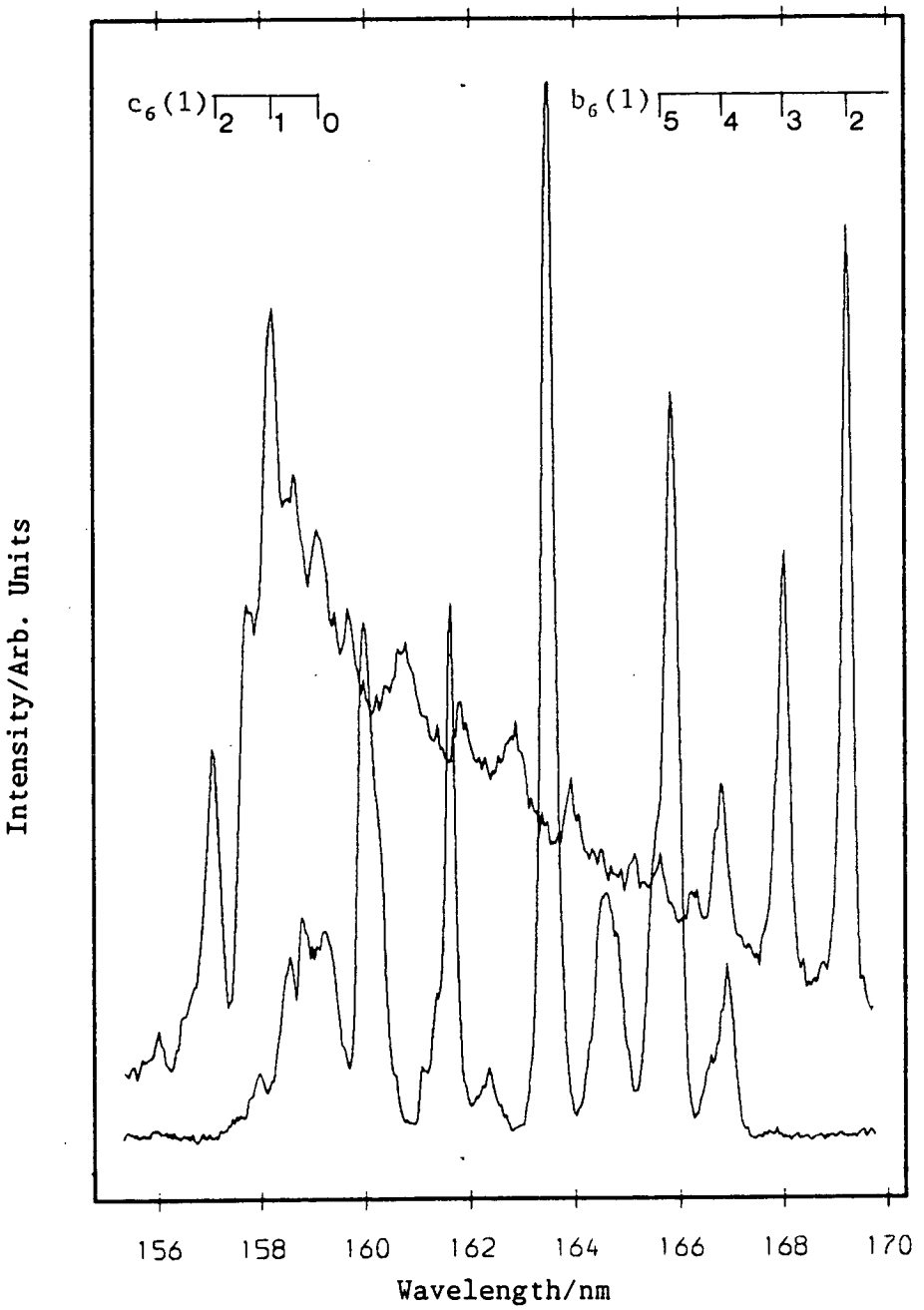

Figure 3.7 - Fluorescence excitation (lower trace, ICl pressure = 45 mTorr, Cl_2 pressure = 90 mTorr) and absorption (upper trace, ICl pressure = 25 mTorr, Cl_2 pressure = 50 mTorr) in the 155 - 170 nm region. $\Delta\lambda$ = 0.1 nm.

TABLE 3.4

ABSORPTION AND FLUORESCENCE EXCITATION MAXIMA IN THE 156 - 170 nm REGION

Fluorescence Excitation Maxima [a]		Absorption Maxima [b]			
		System	v', v''	λ/nm	ν/cm^{-1}
		$b_6(1) \leftarrow X(0^+)$	2,0	169.26	59 081
			3,0	168.04	59 510
			4,0	166.84	59 938
			5,0	165.64	60 372
λ/nm	ν/cm^{-1}				
166.92	59 909				
165.87	60 288	Unknown		166.28	60 139
164.57	60 764			165.14	60 555
163.51	61 158			163.95	60 994
162.40	61 576			162.87	61 399
161.64	61 866			161.83	61 793
159.96	62 516			160.74	62 212
158.80	62 912			159.70	62 617
				158.64	63 036
				157.72	63 403
		$c_6(1) \leftarrow X(0^+)$	0,0	159.10	62 853
			1,0	158.18	63 219
			2,0	157.08	63 661

[a] Fluorescence excitation maxima determined to ± 0.03 nm (± 12 cm^{-1}).

[b] $b_6(1)$ absorptions accurate to ± 0.03 nm (± 12 cm^{-1}) while the unknown and $c_6(1)$ systems are determined to ± 0.05 nm (± 20 cm^{-1}).

Bibinov and Vinogradov [10] also reported the band structure in the 159 - 167 nm region of the fluorescence excitation; a region in which they were unable to resolve any distinct structure in absorption. It was proposed that the minima observed in the fluorescence excitation correlated satisfactorily with positions of the b_6 (1) vibrational levels extrapolated beyond $v' = 4$ and were a result of interactions between the fluorescing state and the b_6 (1) Rydberg state. The higher resolution absorption studies reported in this work do exhibit structure in the region of interest but it is obvious (see Figure 3.7) that the additional absorption bands are not sited at positions of higher b_6 (1) vibrational levels.

In Table 3.5, the positions of absorption bands observed in this work and by Venkateswarlu [7] are listed alongside the predicted positions for the vibrational levels of the b_6 (1) state. The b_6 (1) vibrational constants were also obtained from a Birge-Sponer plot of Venkateswarlu's data which gave values of 451 ± 8 cm^{-1} for ω_e and 3.0 ± 1.5 cm^{-1} for $\omega_e x_e$. Good agreement is found between the predicted values and observed positions up to the (5,0) band of the b_6 (1) $\leftarrow X\ ^1\Sigma^+$ system (this is the first time that the (5,0) absorption band has been reported). To shorter wavelengths, the predicted and observed values no longer coincide and it is concluded that the absorption bands in this region are not a "continuation" of the b_6 (1) Rydberg state.

Bibinov's theory that loss of fluorescence occurs via the b_6 (1) state is too simplistic. Above 170 nm, it has been shown that minima in the fluorescence excitation occur at positions of the b_6 (1) Rydberg absorption bands as a result of a purely physical effect. There is no indication of electronic coupling between the fluorescing and b_6 (1)

TABLE 3.5

COMPARISON OF THE $b_6(1) \leftarrow X(0^+)$ AND UNASSIGNED ABSORPTION BANDS IN THE 157 - 172 nm REGION WITH CALCULATED POSITIONS OF THE $b_6(1) \leftarrow X(0^+)$ SYSTEM

System	v', v''	λ/nm	ν/cm^{-1}	ν_{venk}/cm^{-1} [a]	ν_{calc}/cm^{-1} [b]
$b_6(1) \leftarrow X(0^+)$	0,0	171.83	58 197	58 198	58 198
	1,0	170.52	58 644	58 643	58 643
	2,0	169.26	59 081	59 087	59 082
	3,0	168.04	59 510	59 513	59 515
	4,0	166.84	59 938	59 944	59 942
	5,0	165.64	60 372	-	60 363

			System	v', v''	ν_{calc}/cm^{-1} [b]
Unassigned	166.28	60 139			
	165.14	60 555	$b_6(1) \leftarrow X(0^+)$	6,0	60 778
	163.95	60 994		7,0	61 187
	162.87	61 399		8,0	61 590
	161.83	61 793		9,0	61 987
	160.74	62 212		10,0	62 378
	159.70	62 617		11,0	62 763
	158.64	63 036		12,0	63 142
	157.72	63 403		13,0	63 515

(a) Positions of the $b_6(1) \leftarrow X(0^+)$ absorption bandheads reported by Venkateswarlu [7].

(b) Positions of $b_6(1) \leftarrow X(0^+)$ bandheads calculated with respect to a (0,0) band at 58 198 cm^{-1} and employing ω_e = 451 cm^{-1} and $\omega_e x_e$ = 3.0 cm^{-1}.

states. It seems unlikely therefore that at higher vibrational levels the b_6 (1) state should be responsible for the periodic, total loss of fluorescence which is observed experimentally. In addition, absorption bands in the 158 - 166 nm region have been reported here which were not observed by Bibinov et al. From comparison of the absorption and fluorescence excitation spectra (see Figure 3.7) it appears that it is these bands which affect the fluorescence processes of the excited ICl molecule rather than high vibrational levels ($v'>4$) of the b_6 (1) state, as proposed by Bibinov.

No mention has, as yet, been made of the nature of the fluorescing state(s). It has already been noted that the Rydberg states; the a_6 (1), b_6 (1) and $b_6'(0^+)$ either predissociate or fluoresce in the vacuum ultraviolet and, in some cases, provide efficient pathways for non-radiative decay by coupling with fluorescing levels. The majority of the fluorescence must, therefore, originate from the $E(0^+)$ state, which was earlier assigned as the upper state of the absorption "continuum" observed between 158 and 178 nm. Dispersed fluorescence spectra collected following excitation at various wavelengths across the 155 - 190 nm range have confirmed this. Indeed, from the fluorescence excitation spectrum it appears that ion-pair absorption continues weakly out to ~ 190 nm underlying the a_6 (1) absorptions.

The dominant emission system is the $E(0^+) \rightarrow X\ (^1\Sigma^+)$ which extends from a red extremum at 404 nm to shorter wavelengths. Several other systems are present to the red of 404 nm and one, with an extremum at 325 nm, is observed to the blue. The dispersed fluorescence will be discussed in greater detail in Chapter 4.

Filters were employed in combination with the UV-VIS photomultiplier to minimise the contribution made by states other than the $E(0^+)$ to fluorescence excitation spectra. The UV-VIS fluorescence excitation can be regarded as the fluorescence cross-section of the $E(0^+)$ ion-pair state.

The situation at energies where ion-pair and Rydberg states co-exist is complex, as has been observed from comparison of absorption and fluorescence excitation spectra. The data obtained experimentally is currently insufficient to offer a full explanation and understanding is further hindered by the lack of ab initio potential curves which are available for lighter diatomic molecules such as H_2 and Cl_2 [5,16]. It is, however, obvious that interactions between states play a crucial role at these energies and such interactions will be discussed in the following sections. Several possible explanations for the experimental data will be put forward and although incomplete should, hopefully, provide some illumination on the types of processes which are occurring.

3.5 Interactions Between Rydberg and Ion-Pair States

There are two main types of perturbations which can occur between electronic states: homogeneous and heterogeneous perturbations [14]. A homogeneous perturbation takes place when both states possess the same multiplicity ($\Delta S = 0$) and the same Λ value, while a heterogeneous perturbation occurs if the Λ values differ by one. For electronic states best described by Hund's case (c), the above selection rules are reduced to $\Delta\Omega = 0$ and $\Delta\Omega = \pm 1$ for homogeneous and heterogeneous perturbations respectively as the multiplicities and Λ values are not defined.

All ICl ion-pair states are coupled under Hund's case (c) while the symmetries of the Rydberg states are derived from (Ω_c, ω) coupling. In both cases, the Ω value is the only well defined quantum number and thus the $\Delta\Omega$ selection rules for perturbations apply.

Interaction between two states is not only dependent on their Ω values but, also, on a Franck-Condon type principle [14] stating that:-

> 'Two vibrational levels belonging to two different electronic states and lying at approximately the same energy will influence each other strongly only if classically the system can go over from one state to the other without a large alteration of position and momentum'.

It follows that the point of maximum perturbation occurs at the intersection of the potential curves, providing that the energy difference between interacting levels is small.

For a strong, homogeneous perturbation the interaction (repulsion) at this point is sufficiently large that the non-crossing rule applies. The non-crossing rule was first formulated by von Neumann and Wigner [22] and stipulates that:-

> 'The potential curves of two electronic states of the same species cannot cross each other'.

(The species of the state, in the case of ICl ion-pair and Rydberg states, refers to the Ω value). As a result of such a perturbation, an

avoided crossing takes place and two "new" potential curves are formed. This situation is illustrated in Figure 3.8. The diabatic (original) potentials are represented by curves AA′ and BB′ while the adiabatic (resultant) potentials are shown by AB′ and BA′. The solid curves around the point of intersection indicate the avoided crossing.

The diabatic and adiabatic approximations represent extreme cases and the best description of a perturbed system is usually found to lie somewhere between the two; the position dependent on the interaction strength.

A consequence of the mixing of two states is that the resultant adiabatic states possess properties of both diabatic states. Consider two diabats with wavefunctions ψ_1 and ψ_2. The adiabatic wavefunctions, ψ_a and ψ_b, of the states formed by an avoided crossing can be expressed as linear combinations of the diabatic wavefunctions, ie:-

$$\psi_a = c_1 \psi_1 - c_2 \psi_2$$

and (3.1)

$$\psi_b = c_2 \psi_1 + c_1 \psi_2,$$

where c_1 and c_2 are constants.

The magnitudes of constants c_1 and c_2 are a function of both the energy differences between unperturbed levels and the Franck-Condon overlap. It is these constants which determine the extent of mixing between the original states.

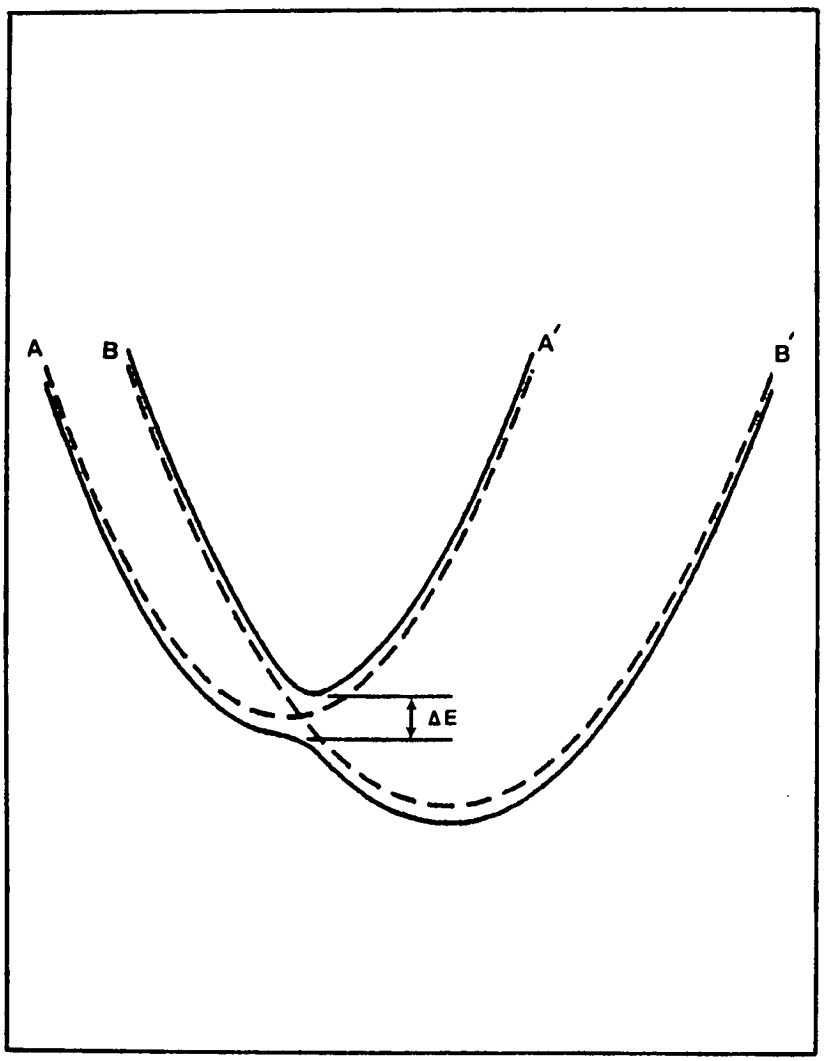

Figure 3.8 - An avoided crossing. Curves AA′ and BB′ represent the diabatic potentials while AB′ and BA′ represent the adiabatic potentials. $\Delta E = 2W_{12}$, see text.

The interaction strength, $W_{12}(r_x)$, is defined as the matrix element of the perturbation function, W, which describes the coupling between two states at their crossing point, r_x, ie:-

$$W_{12} = \langle \psi_1^* \, W \, \psi_2 \rangle . \qquad (3.2)$$

$W_{12}(r_x)$, also, has a physical significance as $\Delta E = 2W_{12}(r_x)$ (Figure 3.8), where ΔE is the energy gap between the adiabatic curves at the point of intersection, r(x). The larger the value of $W_{12}(r_x)$, the stronger the perturbation and hence the greater the justification for treating the electronically coupled states by an adiabatic approximation.

It has been shown by Child and Bernstein [23] that, around r_x, the adiabats can be expressed in terms of the diabats as:-

$$V_{\pm}(r) = {}^1/_2 \, [V_1(r) + V_2(r)] \pm {}^1/_2 \, \{[V_1(r) - V_2(r)]^2 + 4W^2{}_{12}(r)\}^{1/2} \qquad (3.3)$$

The adiabats differ from the diabats only in the vicinity of r_x, where $|V_1 - V_2| \ll W_{12}$. At r_x, $V_1(r_x) = V_2(r_x)$ and equation (3.3) reduces to:-

$$V_+(r_x) = E(r_x) + W_{12}(r_x)$$

and

$$V_-(r_x) = E(r_x) - W_{12}(r_x)$$

giving the relationship:-

$$V_+ (r_x) - V_- (r_x) = \Delta E (r_x) = 2W_{12} (r_x)$$

mentioned above.

Homogeneous and heterogeneous perturbations can also be classified by the effect which they have on the perturbed states. A homogeneous interaction between states perturbs the vibrational levels of the states involved. This is not surprising as in the case of an avoided crossing the shape of the potential curve changes and thus the vibrational spacing must alter. A good example of perturbation in vibrational levels is found in the Cl_2 ($1\ ^1\Sigma_u^+$) state [4] which is a mixed Rydberg/ion-pair state. Below the region of perturbation regular ion-pair spacing is observed. However, as the perturbed area is approached the vibrational spacing becomes irregular and for some levels, consecutive vibrational wavefunctions differ dramatically.

A heterogeneous interaction between states does not affect the vibrational levels but perturbs the rotational levels. This type of interaction is again strongest at the crossing point of the states, as indicated by the Franck-Condon principle for perturbations. The resolution employed in this work is insufficient to resolve rotational structure but the effect of heterogeneous interactions is observed in the fluorescence excitation.

Due to the nature of the interactions, homogeneous and heterogeneous perturbations are sometimes referred to as electronic-vibrational and electronic-rotational perturbations respectively.

3.6 Analysis of the Spectroscopy of ICl in the 155 - 190 nm Region

Sections 3.3 and 3.4 show that at least four states play an important role in ICl spectroscopy following excitation between 155 and 195 nm:- the a_6 (1), b_6 (1), $b_6'(0^+)$ Rydberg states and the $E(0^+)$ ion-pair state. Several other states are found in close proximity:- the $\Omega = 2$ $(^2\Pi_{3/2})6s\sigma$ and $\Omega = 0^-$ $(^2\Pi_{1/2})6s\sigma$ Rydberg states and the β (1) and $D'(2)$ ion-pair states. The $\Omega = 2$ and $\Omega = 0^-$ Rydberg states share the same electronic configuration as the $a_6(1)$ and $b_6(1)$ states respectively while the $E(0^+)$, β (1) and $D'(2)$ states form the lowest ion-pair cluster. The energy separation between Rydberg states with identical configurations is expected to be small [24] and was only resolved in one case by Venkateswarlu [7] where a separation of 23 cm^{-1} was observed. Due to the essentially non-bonding role of the Rydberg electron, Rydberg states lie parallel to one another at energies dependent on the occupied Rydberg orbital. The three close-lying ion-pair potentials also follow similar paths, as discussed in Chapter 1. Absorption to the second cluster of ion-pair states is another possibility in this region as the second cluster lies approximately 6,000 cm^{-1} above the first [3].

Although many states lie in the excitation region, electronic selection rules limit absorption to states with $\Delta\Omega = 0, \pm 1$ relative to the ground state. This rule is observed for Rydberg states but for absorption to ion-pair states, only a $\Delta\Omega = 0$ selection rule appears to apply. There is no evidence, either in absorption or dispersed fluorescence, to suggest that the β (1) state is populated. This empirical observation also applies to other halogen and interhalogen

molecules [4, 25-28] although Gedanken has proposed a contribution from an $\Omega = 1$ ion-pair state in the molecular circular dichroism spectrum of I_2 [29].

Dispersed fluorescence studies of ICl (see Chapter 4) show emission not only from the $E(0^+)$ state but also from the $f(0^+)$ state, the $\Omega = 0^+$ state of the second, ion-pair cluster. The question of whether the $f(0^+)$ state is populated directly by absorption or by coupling with the $E(0^+)$ state will be considered within this section.

Figure 3.9 shows the fluorescence excitation and absorption spectra between 51,000 and 64,000 cm^{-1} plotted alongside a schematic diagram of the potential curves in the same region. Only the potentials which are thought to play a major role in the spectroscopy are shown.

In Figure 3.9 the Rydberg states are represented by the ground-state transposed to higher energies and shorter bondlength. As the electron which is promoted is slightly anti-bonding a reduction in the equilibrium internuclear bondlength of the Rydberg state is expected. Venkateswarlu's data [7] is in agreement since both the $a_6(1)$ and $b_6(1)$ absorption bands are degraded to the blue. The Rydberg states are expected to lie between the r_e of the ground-state molecule (2.321 Å [30]) and the ICl^+ ion (2.233 Å [31]). The Rydberg states displayed here have slightly shorter bondlengths (r_e = 2.2 Å) to conform with the features observed in the fluorescence excitation and absorption spectra. The shift is small enough to give no cause for concern. The position of the Rydberg states is in agreement with the strong absorption profiles of the $a_6(1)$ and $b_6(1)$ states with the ground-state r_e lying between the

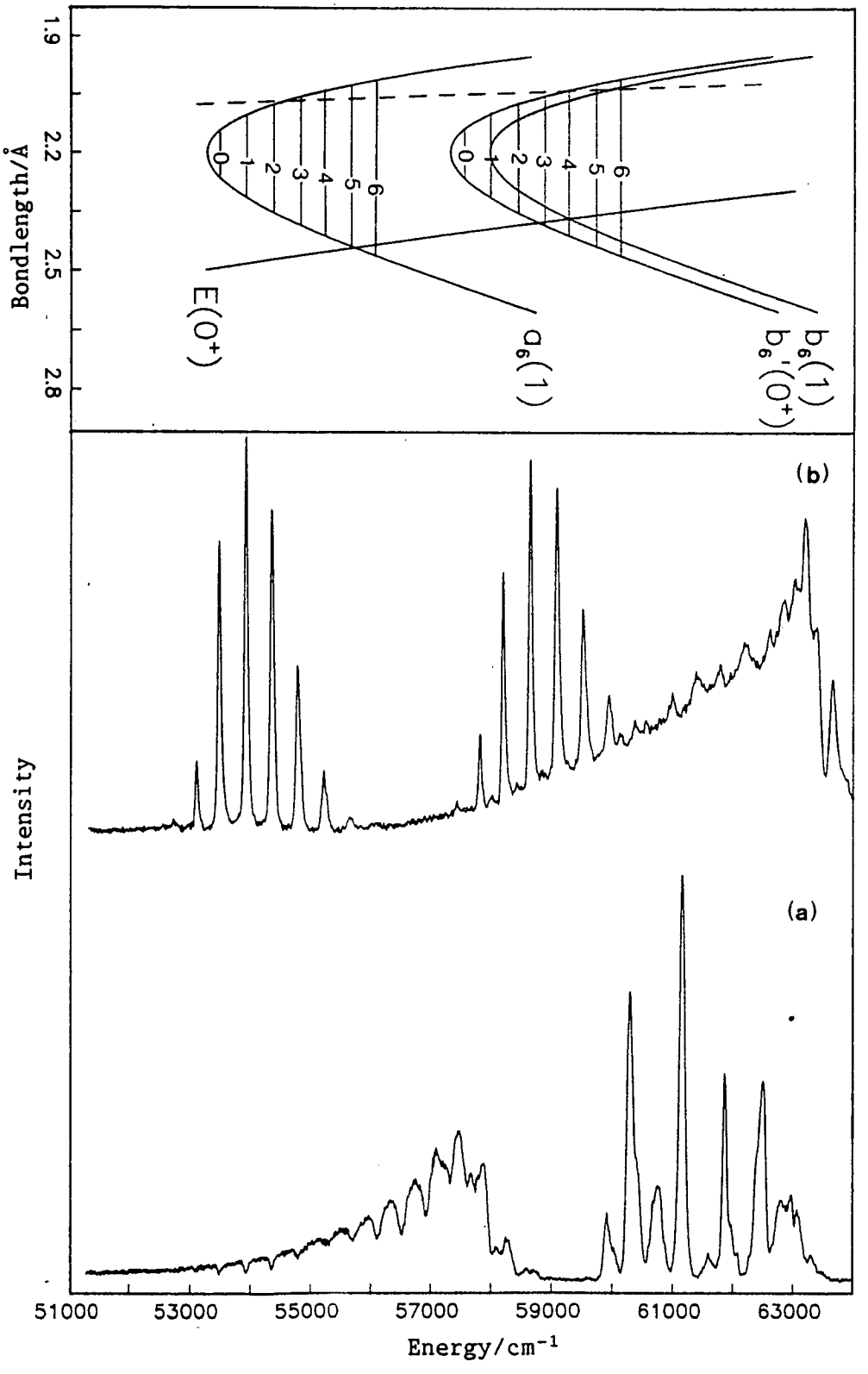

Figure 3.9 - Schemetic diagram of the relevant ICl potential curves plotted alongside the ICl fluorescence excitation (a) and absorption spectra (b) in the 51,000 - 64,000 cm^{-1} region. The predissociating $\Omega = 0^+$ repulsive state is represented by the dashed line. The vibrational levels from 0 - 6 are shown for the a_6 (1) and $b_6'(0^+)$ Rydberg states.

outer turning points of the v' = 1 and 2 vibrational levels. The repulsive limb of the $E(0^+)$ ion-pair state is that proposed by Austin (see Chapter 4 and Reference 35).

The potentials in Figure 3.9 are drawn in the diabatic limit, ie. the $E(0^+)$ ion-pair and $b_6'(0^+)$ Rydberg states do not avoid one another.

Consider the electronic interaction between the a_6 (1) and $E(0^+)$ states. In Section 3.4 it was proposed that the fluorescence excitation minima in the 55,500 - 57,500 cm^{-1} region arose from coupling between the $E(0^+)$ and a_6 (1) states which opened up a non-radiative pathway at positions of the $v' \geq 5$ a_6 (1) Rydberg levels. As the Ω values of the two states differ by one the coupling must be of the heterogeneous variety. At energies where coincidence between the Rydberg and ion-pair levels is observed, the ion-pair population may be depleted via the predissociated a_6 (1) Rydberg state. Due to the high density of states in the $E(0^+)$ ion-pair manifold, especially at high v, coincidence occurs at every Rydberg vibrational level with the extent of interaction governed by the Franck-Condon rule for perturbations. As the heterogeneous perturbation does not manifest itself in the fluorescence excitation until the a_6 v' = 5 level, the Franck-Condon overlap between states is poor below this position. The repulsive limb of the ion-pair potential must therefore cross the a_6 (1) Rydberg state around v = 5, as shown in Figure 3.9. Minima formed via electronic-rotational coupling between two states will henceforth be termed dip-resonances.

The major interaction in the 51,000 - 64,000 cm^{-1} energy region is expected to occur between the $E(0^+)$ and $b_6'(0^+)$ states as both have Ω values of 0. Although the non-crossing rule suggests that an avoided crossing should take place, in the following discussion the two states are treated in the diabatic approximation, ie. it is assumed that the interaction matrix element W_{12} is small and that the potentials intersect. This approximation has been adopted as it best describes the experimental observations. The strength of the coupling between the two states is not sufficient to produce shifts in the energy levels which are large enough to be observable with the available experimental resolution but is sufficient to cause a substantial reduction in the fluorescence quantum yield.

In Section 3.4, it was shown that at positions of the $b_6'(0^+)$ absorption bands sudden sharp losses occurred in fluorescence. It was subsequently concluded that the $b_6'(0^+)$ state acted as a gateway to non-radiative decay for the $E(0^+)$ ion-pair state. Around 59,000 cm^{-1}, total loss of fluorescence is observed in the fluorescence excitation with band structure appearing at higher energies. These observations have also been attributed to an $E(0^+)$ - $b_6'(0^+)$ interaction.

As one proceeds up the $b_6'(0^+)$ vibrational manifold it is observed (Figure 3.6 and Figure 3.8) that the corresponding fluorescence loss increases with v', until at v' = 3 (~ 58,850 cm^{-1}) the fluorescence quantum yield drops to zero. At energies below v' = 3, ion-pair fluorescence appears between the positions of the Rydberg bands where the coupling between Rydberg and ion-pair states is less strong. However, between 58,850 and 59,740 cm^{-1} (v' = 3 and 5 of the $b_6'(0^+)$ state) there is a complete absence of fluorescence. Above 59,740 cm^{-1}, fluorescence again commences but periodically the fluorescence level drops to the baseline. Figure 3.7 shows that the fluorescence

excitation maxima are positioned between the irregularly shaped absorption bands in this region. It is now proposed that these absorption bands correspond to higher vibrational levels of the $b_6'(0^+)$ state. Absorption does not occur directly to these Rydberg levels but rather to the ion-pair state. At energies where Rydberg and ion-pair vibrational levels coincide a build-up in the absorption cross-section is observed, due to the coupling between the two states. At these levels, the non-radiative pathway opens and the level of observed fluorescence is again depleted.

The positions of $b_6'(0^+) \leftarrow X(0^+)$ vibrational bands were calculated employing the b_6 (1) vibrational constants extracted from Venkatesarlu's data [7] (ω_e = 451 ± 8 cm^{-1}, $\omega_e x_e$ = 3.0 ± 1.5 cm^{-1}). The calculated values are listed with positions of experimentally observed bands in Table 3.6. Good agreement is found up to the (7,0) band but divergence is observed to shorter wavelengths. Extrapolation of the $b_6'(0^+) \leftarrow X(0^+)$ series using the b_6 (1) vibrational constants reported by Bibinov et al [10] (ω_e = 445 cm^{-1}, $\omega_x x_e \simeq$ 1.7 cm^{-1}) is also listed in Table 3.6. Reasonable agreement is observed not only with the four bands assigned to the $b_6'(0^+) \leftarrow X(0^+)$ transition but also with the unassigned system to shorter wavelengths. The differences in the two calculated series highlight the pitfalls in extraction of vibrational constants from a few data points. The vibrational spacing of the b_6 (1) Rydberg state is irregular compared with that of the a_6 (1) state resulting in large standard deviations and making accurate extrapolation difficult.

TABLE 3.6

CALCULATED POSITIONS OF THE $b_6'(0^+) \leftarrow X(0^+)$ BANDHEADS FOR COMPARISON WITH EXPERIMENTALLY OBSERVED BANDS

System	v', v''	λ\nm	ν/cm^{-1}	ν_{calc}/cm^{-1} (a)	ν_{calc}/cm^{-1} (b)
$b_6'(0^+) \leftarrow X(0^+)$	0,0	173.74	57 557	57 551	57 548
	1,0	172.44	57 991	57 996	57 988
	2,0	171.12	58 438	58 435	58 428
	3,0	169.91	58 855	58 868	58 863
	4,0	-	-	59 295	59 294
	5,0	-	-	59 716	59 722
	6,0	166.28	60 139	60 131	60 147
	7,0	165.14	60 555	60 540	60 568
	8,0	163.95	60 994	60 943	60 986
	9,0	162.87	61 399	61 340	61 400
	10,0	161.83	61 793	61 731	61 811
	11,0	160.74	62 212	62 116	62 219
	12,0	159.70	62 617	62 495	62 623
	13,0	158.64	63 036	62 868	63 024
	14,0	157.72	63 403	63 235	63 421

(a) $b_6'(0^+) \leftarrow X(0^+)$ band positions calculated employing a $b_6'(0^+)$ T_e of 57 326 cm^{-1} and the vibrational constants extracted from Venkateswarlu's data [7], ω_e = 451 cm^{-1}, $\omega_e x_e$ = 3.0 cm^{-1}.

(b) $b_6'(0^+) \leftarrow X(0^+)$ band positions calculated using the vibrational constants reported by Bibinov et al [10], ω_e = 445 cm^{-1}, $\omega_e x_e$ = 1.7 cm^{-1}. T_e of the $b_6'(0^+)$ state = 57 326 cm^{-1}.

However, assuming that b_6 (1) vibrational constants also apply to the $b_6'(0^+)$ state, the agreement between observed and calculated absorption bands is sufficient to suggest that the resonance type absorption structure in the 60,000 - 63,000 cm^{-1} region arises as a consequence of coupling between the $b_6'(0^+)$ and $E(0^+)$ states.

The slightly irregular vibrational spacing observed for the $v' = 0$-3 levels may be a result of shifts in the vibrational levels due to perturbation. However, more accurate determination of the band positions is necessary to confirm this.

The shapes and separations of the resonance-type absorption structure are irregular as this structure is a result of coupling with the $E(0^+)$ state and not of direct absorption to the $b_6'(0^+)$ Rydberg state. The strength of the coupling will depend on the energy separation between Rydberg and ion-pair levels and also on the Franck-Condon overlap between the two wavefunctions.

A surprising aspect of the absorption spectrum is the intensities of the two types of absorption structure : structure due to:-

(i) Direct absorption to $v' = 0 - 3$ of the $b_6'(0^+)$ state.

(ii) Resonances between $v' = 6 - 13$ of the $b_6'(0^+)$ Rydberg state and vibrational levels of the $E(0^+)$ state.

The $b_6'(0^+)$ absorption bands are expected to be of at least equal intensity as the b_6 (1) bands since both states possess the same electron configuration, 2430 6sσ, and the same core symmetry, $^2\Pi_{1/2}$.

However, the $b_6'(0^+)$ bands with $v' = 0$-3 are much weaker than the b_6 (1) bands. The absorptions observed at the positions of $v' = 6 - 13$ in the $b_6'(0^+)$ Rydberg state are strong by comparison.

The reason for these rather strange intensity effects is not known. It appears that mixing between the $E(0^+)$ and $b_6'(0^+)$ states "steals" intensity from the direct absorption process but "lends" intensity to the indirect resonance absorptions.

In this section it has been shown that the $b_6'(0^+)$ state is strongly coupled to the $E(0^+)$ and acts as a gateway for non-radiative decay of the ion-pair state. To fulfil such experimental observations the $b_6'(0^+)$ state must be predissociated. Two criteria by which predissocation is diagnosed are the broadening of absorption and the weakening of emission lines [14]. Line broadening cannot be detected in this work as the resolution is too poor. Such analysis would also be hindered by the low intensity of the $b_6'(0^+)$ absorption bands.

No evidence for emission from the $b_6'(0^+)$ state has been observed experimentally. At positions of the $b_6'(0^+)$ Rydberg absorptions minima occur in fluorescence excitation, both in the UV/VIS region (see Figure 3.8) and the VUV (Section 3.11). Further proof that the $b_6'(0^+)$ state is predissociated lies in the behaviour of fluorescence from the $E(0^+)$ state which couples to the predissociating state via the $b_6'(0^+)$ state. Between ~ 58,850 and 59,740 cm^{-1} (a region corresponding to $v' = 3$ to $v' = 5$ of the $b_6'(0^+)$ state) total loss of fluorescence occurs. This region must correspond to the energies at which the repulsive curve crosses the inner limb of the $b_6'(0^+)$ Rydberg potential. At these energies the Rydberg levels would be extremely

diffuse and predissociation pathways would open for the $E(0^+)$ state over the same energy range, resulting in the complete loss of fluorescence observed. To higher energies, predissociation again occurs only when resonance between Rydberg and ion-pair levels is achieved.

Selection rules for predissociation are very similar to those for perturbation [14]. Thus in Hund's case (c) a repulsive state which strongly predissociates the $b_6'(0^+)$ Rydberg must also have an Ω value of 0^+. The repulsive state will have an extremely steep inner limb and must correlate with ground or spin-orbit excited iodine and chlorine atoms. The same repulsive state will cut through the inner limbs of the a_6 (1) and b_6 (1) Rydberg potentials and may be responsible for the predissociation channel in these states. However, many repulsive states must lie in this area and the predissociation of the a_6 (1) and b_6 (1) states could equally well occur via some other state.

3.7 The Diabatic versus Adiabatic Model

Either the diabatic or adiabatic picture can be chosen to represent a perturbation between two states of the same symmetry. The vibrational eigenfunctions of potentials from either approximation do not exactly represent the observed levels. Interaction matrix elements between these zero-order levels must be added in order to reproduce the levels observed experimentally [33]. The electronically coupled states may be described either in:-

(i) the diabatic mode:-

$$\Psi = \sum_{v1} a_{v1} \Phi_1^{\,d} \chi_{v1}^{\,d} + \sum_{v2} b_{v2} \Phi_2^{\,d} \chi_{v2}^{\,d}$$

or (ii) the adiabatic mode:-

$$\Psi = \sum_{v1} c_{v1} \Phi_1^{\,ad} \chi_{v1}^{\,ad} + \sum_{v2} d_{v2} \Phi_2^{\,ad} \chi_{v2}^{\,ad}$$

where 1 and 2 refer to the interacting electronic states and Φ and χ to the electronic and vibrational eigenfunctions respectively. The non-crossing rule, referred to earlier, applies only for exact solutions of the electronic Hamiltonion [33]. In the present case, the experimental results can best be described by the diabatic (curve crossing) model.

There are several reasons why the diabatic model is preferred over the adiabatic. A schematic diagram of the two approximations, adiabatic and diabatic, is displayed in Figure 3.10 for the present case of Rydberg/ion-pair mixing.

In the adiabatic limit the lower potential has a point of inflection in the region of the avoided crossing while a second tightly-bound state is formed at higher energies. The newly formed state has an ion-pair inner wall and an attractive Rydberg limb. The adiabatic model has not been adopted mainly because such potentials are inconsistent with the experimental absorption data.

Figure 3.3 shows $E(0^+)$ ion-pair absorption extending from 158 - 166 nm, in the same region as first reported by Venkateswarlu [7]. From the fluorescence excitation it can be see that ion-pair absorption, although weak, extends as far red as ~190 nm (Figure 3.6). Such long ranging absorptions are typical of ion-pair states [34]. Absorption to the inner limb of the lower, adiabatic potential is not expected to continue down to 158 nm. Around r_x of the avoided crossing the inner limb of the lower adiabat swings out to shorter r to become essentially that of the $b_6'(0^+)$ diabatic Rydberg state. Since r_e of the Rydberg state is less than the ground state r_e the adiabat quickly moves out of the Franck-Condon region as the excitation energy is increased.

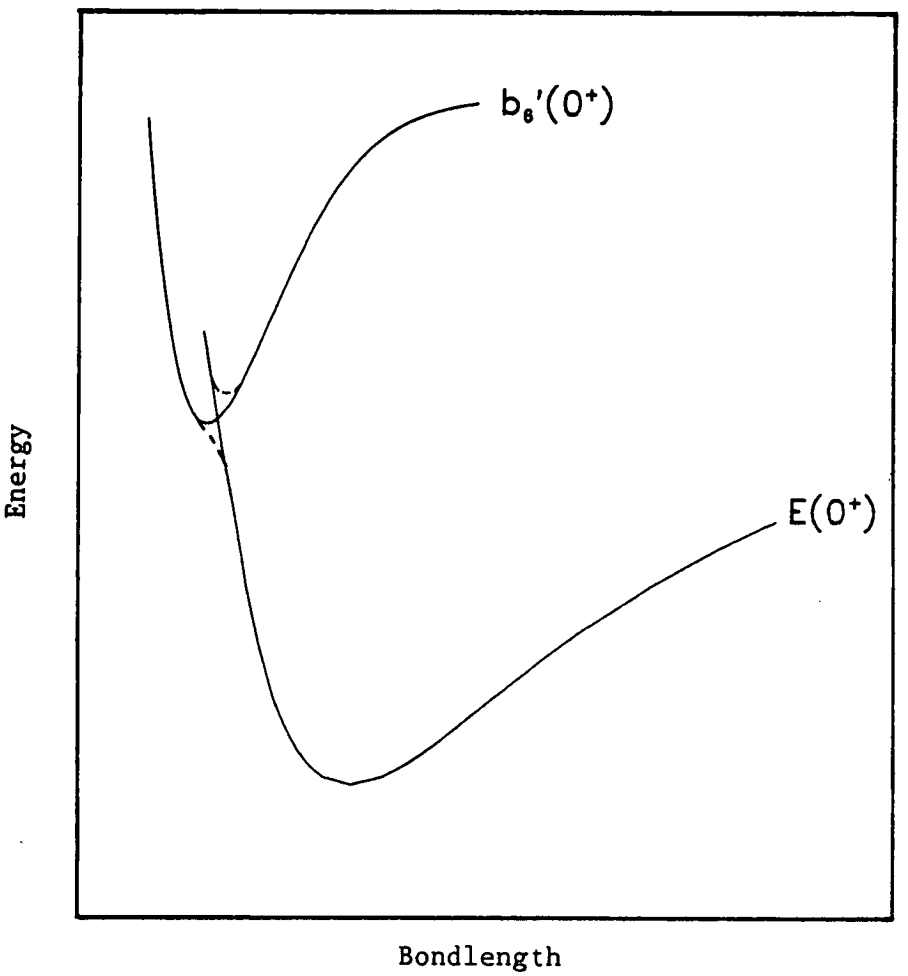

Figure 3.10 - Diabatic representation of the $b_6'(0^+)$ and $E(0^+)$ potentials (solid curves). An avoided crossing (adiabatic model) between the two states is shown by the dashed curves around the crossing point.

Assuming that the $b_6'(0^+)$ Rydberg state lies at the same r_e as the b_6 (1) state (see Figure 3.9), the probability that absorption continues up the $b_6'(0^+)$ inner limb to the $v' = 13$ level at ~ 63,000 cm^{-1} (~159 nm) is extremely low.

In the adiabatic limit the "new" tightly bound state (the upper adiabat) lies in the Franck-Condon region. Absorption to this state should be observed if the adiabatic model is a good approximation. This situation was reported experimentally for Cl_2 [4], where $^1\Sigma_u^+$ Rydberg and ion-pair states avoid each other strongly. The upper adiabat is narrow in comparison to a normal Rydberg state and subsequently has widely spaced vibrational levels. No absorption bands fitting this description were found in the ICl absorption. A possible vibrational progression of the upper adiabat is observed in the fluorescence excitation band system between 59,700 and 63,500 cm^{-1} (167.5 - 157.5 nm) but as no corresponding absorption bands exist, the observation of an appropriate progression appears coincidental only.

Ion-pair vibrational spacings measured from the absorption spectrum in the 158-166 nm region (Figure 3.3) and the fluorescence excitation in the 174.5 - 177.0 nm region (Figure 3.6) agree, within experimental error limits, with the vibrational spacings of a basically unperturbed ion-pair potential as reported by Austin [35].

3.8 A Detailed Analysis of the Absorption Profile

From the absorption and fluorescence excitation spectra it has been deduced that ion-pair absorption to the $E(0^+)$ state extends from 158 nm to approximately 190. Bibinov and Vinogradov [10] assigned the absorption "continuum" rising to a maximum around 158 nm to the $E(0^+) \leftarrow X(^1\Sigma^+)$ transition. However, from the $E(0^+)$ ion-pair potential derived by Austin (see Reference 35 and Section 4.6), which reproduces the observed vibrational spacings and dispersed fluorescence of the $E(0^+)$ state, it is predicted that $E(0^+)$ absorption is strongest around 167 nm (59,880 cm^{-1}). Absorption to an ion-pair state is expected to be roughly gaussian in shape, as observed for the $I_2(D(^1\Sigma_u^+))$ state [36], due to reflection of the probability distribution of the v = 0 ground-state vibrational level. Therefore, the observed absorption profile of a "continuum" rising to a maximum followed by an almost immediate cut-off, suggests that contributions from other absorbing states are present. c_6 (1) Rydberg absorptions do occur around 158 nm (63, 290 cm^{-1}) (Figure 3.7) but should not add markedly to the "continuum". Similar absorption profiles have been observed for Br_2 [27] and IBr [37].

A possible candidate for absorption in this region is the $f(0^+)$ ion-pair state which correlates with $I^+(^3P_0)$ and $Cl^-(^1S)$ ions. The $f(0^+)$ state belongs to the second cluster of ion-pair states and has a T_e roughly 6000 cm^{-1} above that of the $E(0^+)$ state [3]. Absorption to the $f(0^+)$ state lies to the blue of $E(0^+)$ absorption. From the dispersed fluorescence it is known that the $f(0^+)$ state is populated. A system attributed to the $f(0^+) \rightarrow X(^1\Sigma^+)$ transition has been observed

following excitation at both 176.0 nm and 164.0 nm (see Chapter 4). Population of the $f(0^+)$ state may occur by either direct absorption or via homogeneous coupling with the $E(0^+)$ state.

The observation that the intensity of $f(0^+)$ fluorescence is constant relative to the $E(0^+) \rightarrow X(^1\Sigma^+)$ system, following excitation at either wavelength, favours the latter process of population. If direct absorption to the $f(0^+)$ state did occur, the relative intensity of $f(0^+)$ to $E(0^+)$ fluorescence should increase as the excitation wavelength decreases. No significant increase has been observed experimentally. In addition, the ion-pair vibrational spacing found in absorption (Figure 3.3) and fluorescence excitation (Figure 3.6) shows the presence of one vibrational progression only.

By analogy with the corresponding states of I_2 [25], it is predicted that single photon absorption to the $f(0^+)$ state is much weaker than to the $E(0^+)$. This can be rationalised by considering the molecular orbital configurations of the relevant states. The $E(0^+)$ state has an electron configuration of 1441 while the $f(0^+)$ correlates with a configuration of 2332. Only the $E(0^+)$ state is accessible from the ground state (2440) by a single electron transition. Absorption to the $f(0^+)$ state may underlie the stronger $E(0^+) \leftarrow X(^1\Sigma^+)$ transition but be sufficiently weak that $f(0^+)$ vibrational separations are not observed.

The question concerning the method of population of the $f(0^+)$ state remains unanswered. Evidence from dispersed fluorescence suggests that population of the $f(0^+)$ state occurs via coupling with the $E(0^+)$

state. However, an underlying contribution to absorption from the $f(0^+)$ state in the "continuum" region is not unexpected. A repulsive state, most likely correlating with ground state atoms, could also contribute to absorption in this region. The facts remain that fluorescence from the $f(0^+)$ state is observed and that the absorption profile between 158 and 166 nm is unusually shaped. The irregularily shaped absorption profile has been attributed to the presence of absorbing states other than the $E(0^+)$ state and two possible modes for $f(0^+)$ state population have been proposed.

3.9 Pressure Dependence of Fluorescence Excitation Spectra

A pressure dependence study of the fluorescence excitation above 158 nm was carried out on station HA12. As the sample chamber consisted of a Spectrosil cell the intensities of the banded system in the 158 - 167 nm region were affected by the cell transmission function. This is illustrated by the differing intensities of spectra recorded on stations HA12 and FS13.

Figure 3.11 shows the fluorescence excitation between 158 and 195 nm recorded over a range of N_2 pressures varying from 0 to 92 Torr. The ICl and Cl_2 pressures were held constant throughout at 1 Torr of each. As the pressure of N_2 is increased several changes are observed, the most dramatic being the loss of structure to the red of 174 nm. In Section 3.4 the formation of minima in this region was attributed to two effects:-

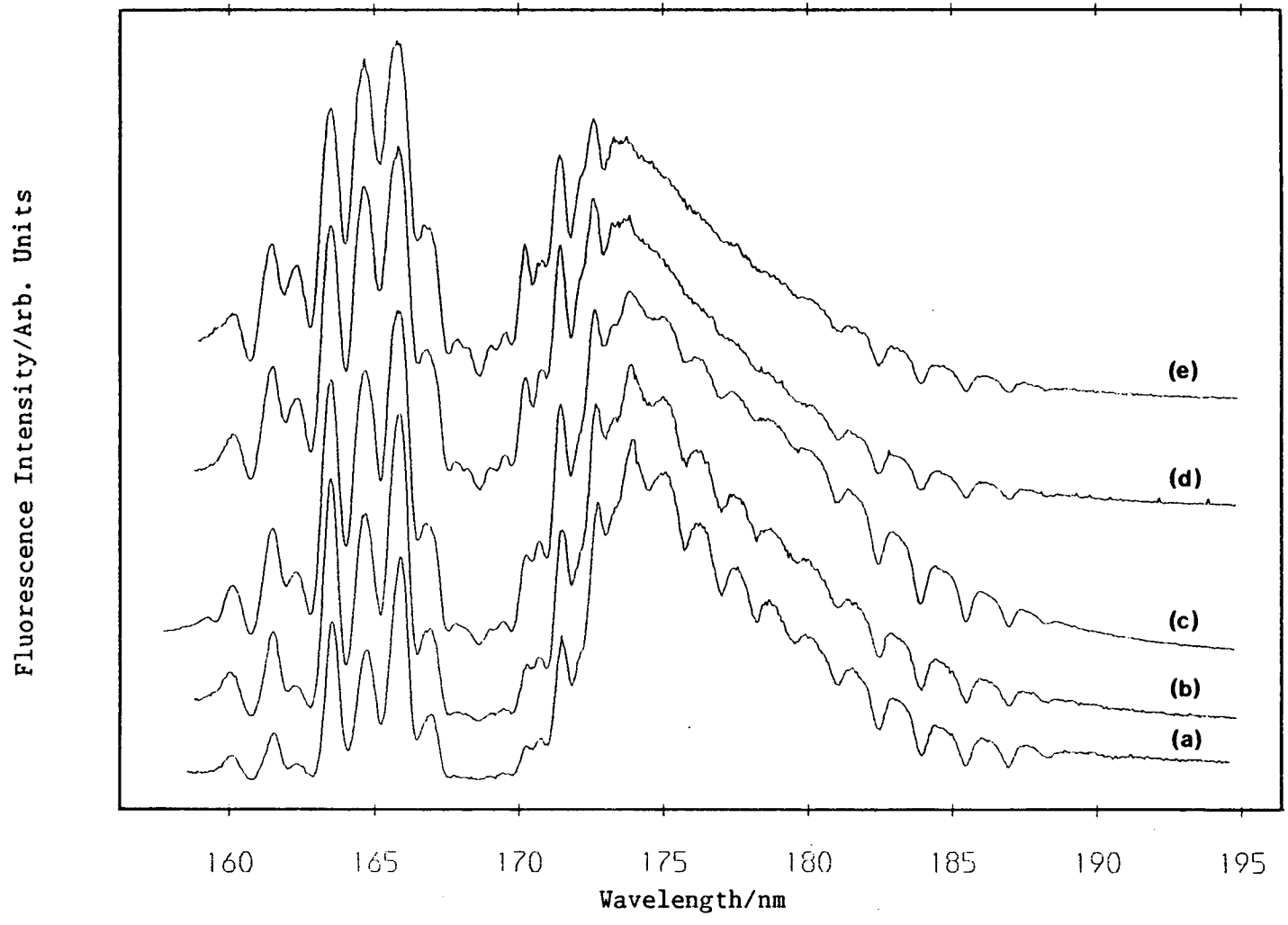

Figure 3.11 - Fluorescence excitation spectra of ICl recorded employing varying N_2 pressures: (a) 0 Torr (b) 8.5 Torr (c) 29 Torr (d) 60 Torr and (e) 92 Torr. ICl pressure = Cl_2 pressure = 1 Torr. $\Delta\lambda$ = 0.3 nm.

(i) The optical thickness of the sample.

(ii) Electronic - rotational coupling between the $E(0^+)$ and a_6 (1) states.

From Figure 3.11 it is observed that the five minima between 174 nm and 180 nm disappear as N_2 pressure increases. These minima lie at positions of the (5,0) → (9,0) bands in the a_6 (1) ← $X(^1\Sigma^+)$ transition. Only the (5,0) band appears in absorption, and then only weakly. The minima to the red of, and including, the (4,0) band at 181 nm remain irrespective of sample pressure. The behaviour of the minima under increasing pressure has helped identify the boundary between the two different series and thus to estimate the point at which the a_6 (1) and $E(0^+)$ states intersect.

Minima formed as a result of the optical density of the sample correlate with the a_6 (1) absorption bands as at these wavelengths the Rydberg absorption cross-section is much greater than that of the fluorescing ion-pair state. The dominant process in formation of these minima is absorption to the a_6 (1) state, a process uneffected by N_2 pressure. The Rydberg levels may broaden slightly but the effect is basically pressure independent.

By contrast, the dip-resonances arise through coupling between the $E(0^+)$ ion-pair and the a_6 (1) Rydberg states and these minima <u>are</u> pressure dependent. As the N_2 pressure increases quenching of the initially populated ion-pair levels occurs. This has been observed for

other halogen and interhalogen molecules [38-40] with cascading taking place from the initial, high vibrational levels down through the ion-pair manifold to the foot of the lowest ion-pair cluster. ICl is no exception as can be seen in Chapter 4 where the dispersed fluorescence in the presence of foreign gas shows strong emission from low vibrational levels of the D', $\Omega = 2$, ion-pair state which lies in the lowest cluster. The quenching process competes with the loss mechanism, opened up by coupling between the $E(0^+)$ and a_6 (1) states, until at relatively high pressures (~ 60 Torr N_2)interstate transfer becomes dominant. The filling-in of the dip-resonances shows that the loss mechanism active at positions of $v' = 5 - 9$ in the a_6 (1) state does not take effect instantaneously. Vibrational levels at these wavelengths are sufficiently long lived that collisions with an inert gas can quench the excited ICl molecules out of the interaction zone.

Such an effect is also observed for the homogeneous interaction between the $E(0^+)$ and $b_6'(0^+)$ states. This is most obvious in the banded system between 159 nm and 167 nm. As N_2 pressure increases the ratio between fluorescence excitation maxima and minima decreases, although loss of fluorescence is still observed especially around 169 nm. Minima in the fluorescence excitation do not disappear completely, as is observed in the case of the heterogeneous perturbation, illustrating the strength of interaction between the two $\Omega = 0^+$ states. At N_2 pressures $\geq$30 Torr fluorescence is even observed between 167 nm and 170 nm; the region where it is proposed that the predissociating state crosses the $b_6'(0^+)$ inner wall (see Section 3.6).

A similar effect has been reported by Bibinov and Vinogradov [10] with Ar pressures ranging from 20 Torr to 760 Torr.

Finally, it should be noted that the lower band system increases in intensity with respect to the system above 170 nm as the N_2 pressure is increased. The spectra presented in Figure 3.11 are not corrected for beam current decay, however as each spectrum was recorded over the same time interval this should not affect the above observation.

3.10 The Spectroscopy of ICl Following Excitation in the 125 - 155 nm Region

The region to the blue of 155 nm has not been studied as extensively as that to longer wavelengths. One of the reasons being that ion-pair/Rydberg interactions are predominant above 155 nm whereas transitions below this wavelength occur mainly to Rydberg states. Figure 3.12 shows the UV/VIS fluorescence excitation and absorption spectra in the low wavelength region. Although intense absorptions are observed over the entire range of excitation wavelengths, fluorescence only occurs following excitation at or below 140 nm. (The weak system around 147 nm is due to slight contamination by BrCl). Analysis is further complicated by the presence of excess chlorine in the sample as chlorine absorption systems are present in the region $\lambda \leq 140$ nm [4]. However, little contribution from Cl_2 excited states appears in the fluorescence excitation of Figure 3.12 since fluorescence from these states occurs mainly to the blue of 280 nm, the low wavelength limit of the BG1 filter in use.

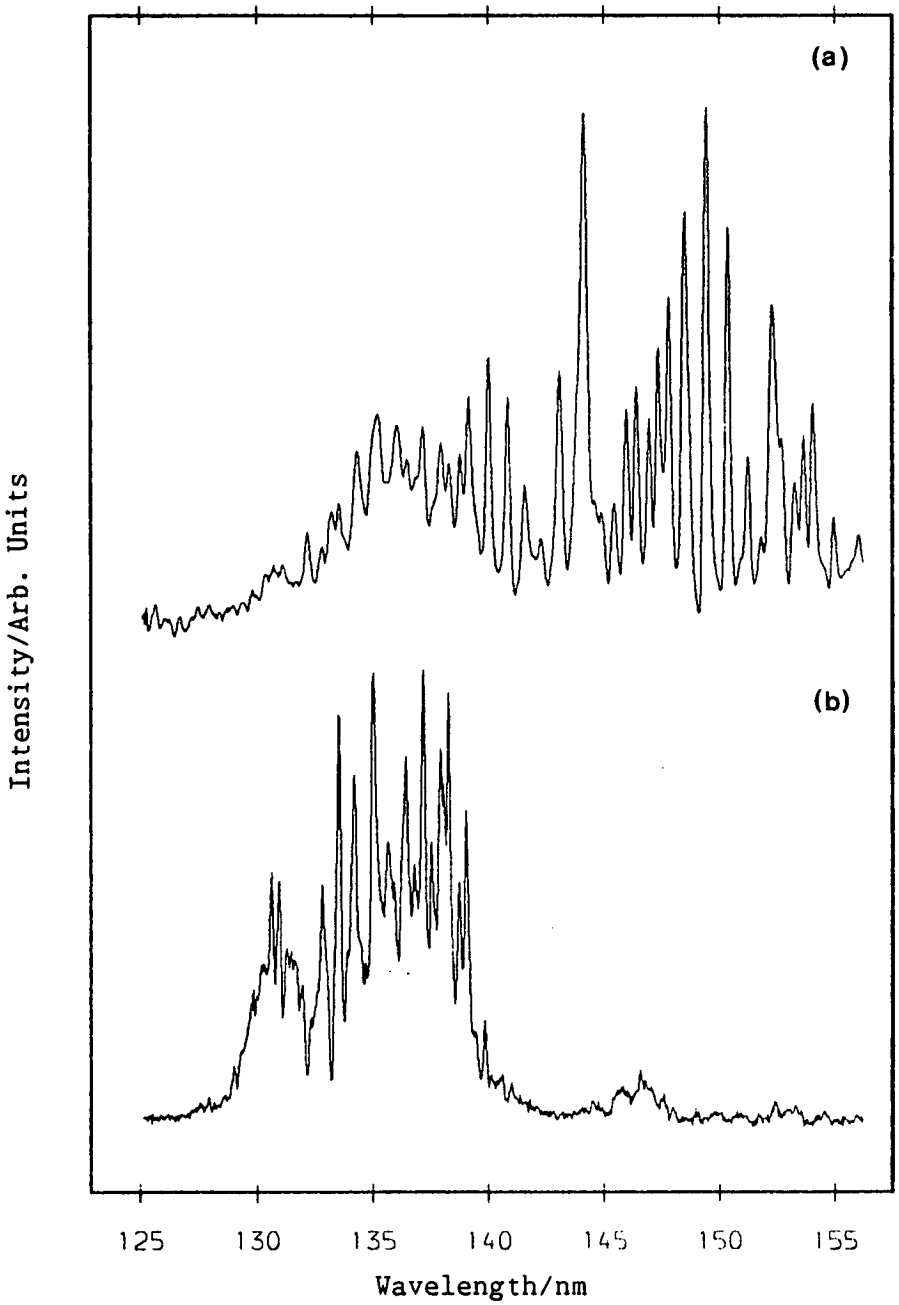

Figure 3.12 - (a) Absorption cross section (ICl pressure = 25 mTorr, Cl_2 pressure = 50 mTorr) and (b) fluorescence excitation (ICl pressure = 45 mTorr, Cl_2 pressure = 90 mTorr) of ICl and Cl_2 in the 125 - 155 nm region. $\Delta\lambda$ = 0.1 nm.

Venkateswarlu [7] has assigned the majority of observed bands in the region below 155 nm as absorptions to Rydberg states which lie below the vertical ionization limit of ICl at ~ 123 nm. It has already been noted that fluorescence is only observed in the VIS/UV region following excitation to the blue of 140 nm. This is also the case for fluorescence in the VUV (see Section 3.12) indicating that the Rydberg states populated by radiation in the 140 - 155 nm region are predissociated.

VUV dispersed fluorescence spectra following excitation at 137.0 nm and 130.5 nm are shown in Figure 3.13. The main emission occurs from excited (Rydberg) iodine atoms with the two intense lines at 178.3 nm and 183.0 nm corresponding to $^2P_{3/2}$ (6s) → $^2P°_{3/2}$ (5p) and $^4P_{5/2}$ (6s) → $^2P°_{3/2}$ (5p) atomic iodine transitions respectively. Following excitation at 137.0 nm a third more extensive system is observed extending to the blue from a red extremum around 200 nm. This emission is identified as the 1 $^1\Sigma_u^+$ → X ^{1} Σ_g^+ transition of molecular chlorine which has been extensively studied by Moeller et al [4]. Absorption to the 1 $^1\Sigma_u^+$ state does not take place at an excitation wavelength of 130.5 nm.

From the fluorescence excitation of the two atomic lines shown in Figure 3.14 it is observed that formation of excited iodine atoms commences around 146.6 nm (excitation bandwidth $\Delta\lambda$ = 4.5 nm) whereas the theoretical threshold for formation of I* (6s $^4P_{5/2}$) atoms lies at 138.9 nm. The two bands observed above 155 nm are due to bound-bound fluorescence of ICl and scattered excitation light. The onset observed experimentally is slightly misleading as the I* fluorescence excitation is convoluted with that of Cl_2 (1 $^1\Sigma_u^+$ → X $^1\Sigma_g^+$) emission which, also,

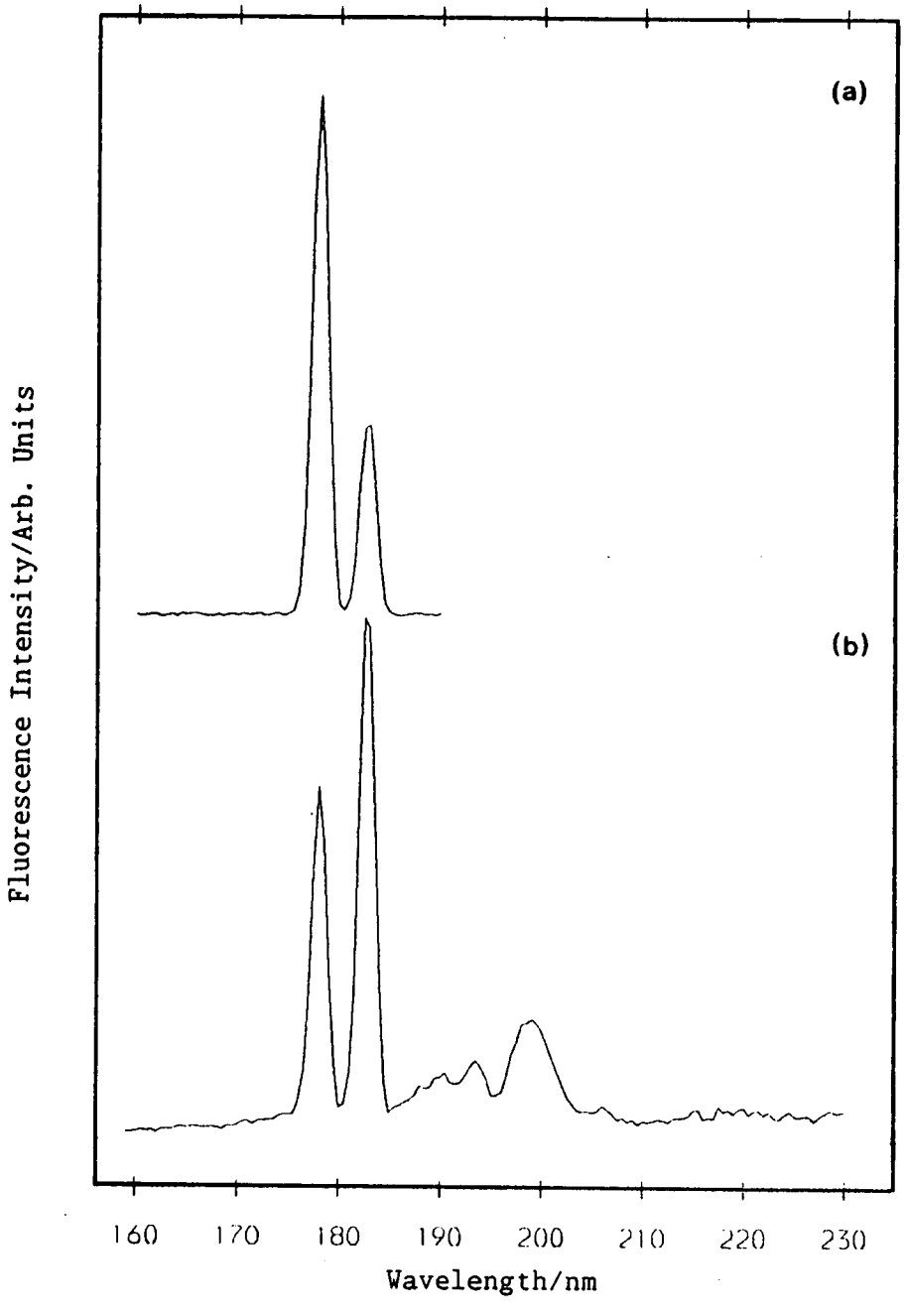

Figure 3.13 - Dispersed fluorescence spectra of ICl and Cl_2 excited at (a) 130.5 nm and (b) 137.0 nm. Fluorescence was excited with a bandpass of 4.5 nm and analysed with 2.0 nm resolution. ICl pressure = 200 mTorr, Cl_2 pressure = 400 mTorr.

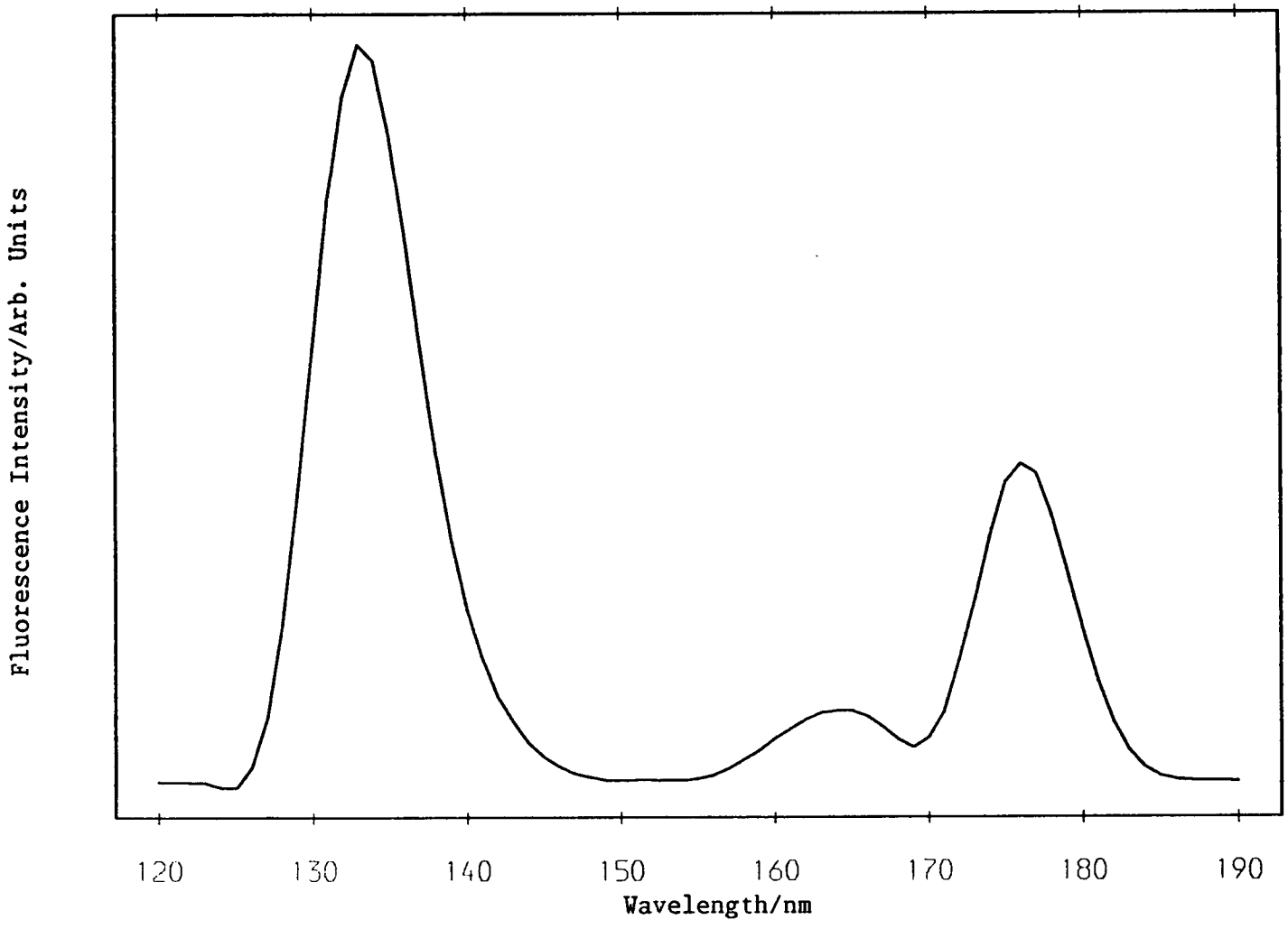

Figure 3.14 - Fluorescence excitation spectrum of the I^* $^2P_{3/2}$ and $^4P_{3/2}$ atomic lines. Fluorescence was excited with a bandpass of 4.5 nm and detected at 177 nm ($\Delta\lambda$ = 6.0 nm). ICl pressure = 133 mTorr, Cl_2 pressure = 266 mTorr.

has a component around 177 nm, the detection wavelength (detection bandwidth $\Delta\lambda$ = 6.0 nm). However, as Cl_2 fluorescence is weak in comparison with the iodine atomic lines it is believed that I^* (6s $^4P_{5/2}$) atoms are formed close to threshold. The thermodynamic threshold for I^* (6s $^2P_{3/2}$) formation lies at 136.1 nm but as the two atomic transitions are so close-lying their excitation functions cannot be differentiated at a resolution of 6.0 nm. The calculated threshold for formation of the next I^* excited atom, I^* (6s, $^4P_{1/2}$), is 127.7 nm and lies below the cut-off wavelength of the CaF_2 focussing lens.

Production of I^* (6s $^4P_{5/2}$) and I^* (6s $^2P_{3/2}$) atoms at excitation wavelengths below 140 nm must occur via predissociation of the initially populated Rydberg states. At excitation wavelengths above 140 nm no fluorescence is observed as the predissociating states correlate with ground-state $^2P_{3/2,\ 1/2}$ atoms but to lower wavelengths the excitation photons contain sufficient energy for the predissociating states to correlate with I^* atoms.

In the UV/VIS fluorescence excitation (Figure 3.12) I^* formation is not monitored directly by $I^* \rightarrow I$ fluorescence but rather by emission from the ICl D'(2) ion-pair state which is formed in a secondary collision process. Figure 3.15 shows dispersed fluorescence in the UV/VIS and VUV regions following excitation at 139.0 nm. The region below 200 nm is as for excitation at 137.0 nm with Cl_2 ($1\ ^1\Sigma_u^+ \rightarrow X\ ^1\Sigma_g^+$) bound-free fluorescence extending to the blue from 199 nm and the two I^* atomic lines just resolved around 178 nm. Fluorescence from the Cl_2 ($1\ ^1\Sigma_u^+$) state to bound levels of the ground state is observed at and to the red of the excitation wavelength. The weak emission in the UV-VIS region above 280 nm is responsible for the fluorescence excitation spectrum of Figure 3.12.

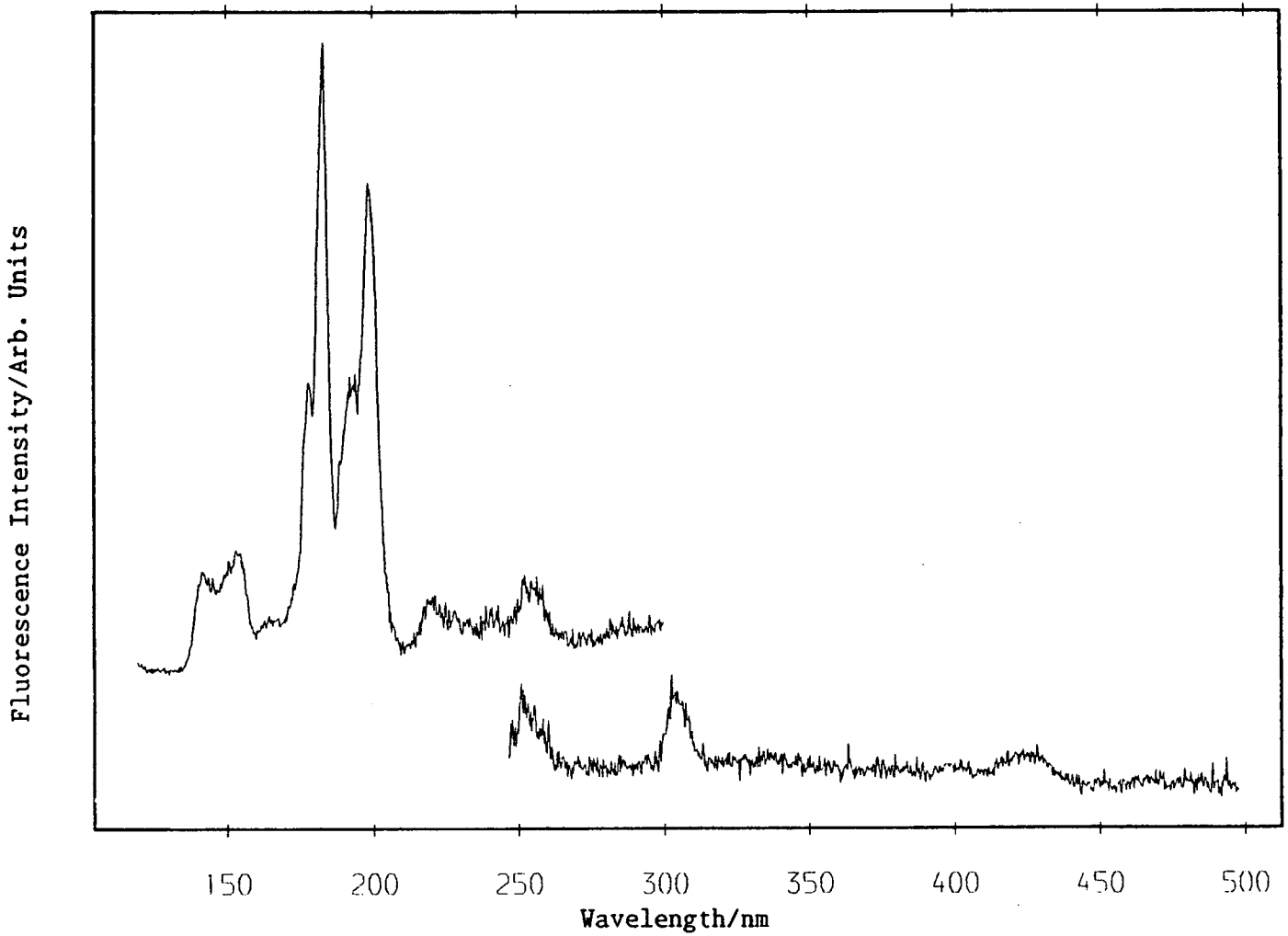

Figure 3.15 - Dispersed fluorescence spectra of ICl and Cl_2 excited at 139.0 nm with a bandpass of 4.5 nm. VUV/UV fluorescence was analysed with 4.0 nm resolution and the UV/VIS fluorescence with 1.7 nm resolution. ICl pressure = 283 mTorr, Cl_2 pressure = 567 mTorr.

Several systems in emission are identified above 200 nm. The fluorescence bands between 200 and 310 nm are attributed to emission from excited Cl_2 states, although the origin of these bands is still speculative [41]. The fluorescence system with maximum around 430 nm extending to the blue corresponds to the ICl D'(2) → A'(2) ion-pair → valence transition. However, in the absence of buffer gas the D'(2) state cannot be populated by collisional quenching of an initially excited ion-pair state as discussed in Section 3.9. Furthermore, at these excitation wavelengths absorption has been assigned to Rydberg rather than ion-pair states.

This phenomenon has been reported previously for ICl by Bibinov et al [10] and also for I_2 [42]. The proposed mechanism being that the ICl D'(2) state is formed via collisions with excited I^* ($6s\ ^4P_{5/2}$) atoms ie:-

$$ICl\ (X\ ^1\Sigma^+) + h\nu \rightarrow I^*\ (^4P_{5/2}) + Cl$$

and

$$I^*\ (^4P_{5/2}) + ICl\ (X\ ^1\Sigma^+) \rightarrow ICl\ (D'(2)) + I$$

The UV/VIS fluorescence excitation (Figure 3.12) can be considered the fluorescence excitation spectrum of this secondary process since the D'(2) → A'(2) emission is the main system within the detection filter bandpass. From Figure 3.12 the observed threshold for D'(2) → A'(2) fluorescence and thus for I^* ($6s\ ^4P_{5/2}$) formation is 140 ± 0.5 nm which corresponds well with the thermodynamic threshold of 138.9 nm.

From a similar study it was concluded that $I^* \ ^4P_{5/2}$ atoms play the major role in I_2 $D'(2_g)$ formation [43]. Further studies on ICl are necessary to determine the contribution made by the I^* $(6s \ ^2P_{3/2})$ atom. It has also been found that for I_2 the yield of excited atomic product follows the absorption spectrum closely [34]. Such an observation cannot be made with ICl due to the superposition of ICl and Cl_2 absorption bands in the energy region above threshold.

Following excitation at wavelengths below 140 nm it is observed that molecular ICl is predissociated to form $I^* \ ^4P_{5/2}$ and $^2P_{3/2}$ excited atoms which subsequently collide with ground state ICl to form the D'(2) ion-pair state. This reaction occurs from the thermodynamic threshold for formation of the $I^* \ ^4P_{5/2}$ atom and continues down to the CaF_2 cut-off at 128 nm. Further studies in this region are necessary to determine the exact mechanism for formation of the D'(2) state and the contributions that the different I^* excited atoms make to this process. Additional questions such as why the D'(2) state is populated preferentially to the $\beta(1)$ and $E(0^+)$ states in the same ion-pair cluster should also be considered.

3.11 Fluorescence Excitation in Three Spectral Regions

Fluorescence excitation spectra were recorded employing three filter - photomultiplier combinations to cover the wavelength range from 128 - 600 nm. The resulting spectra are displayed in Figure 3.16 : the detection ranges being 128 - 600 nm, 128 - 195 nm and 280 - 480 nm for the top, middle and bottom traces respectively. The photomultiplier response curves are shown in Figure 3.17. A BG1 filter (bandpass 280 - 480 nm) was employed in conjunction with the EMI 9883QKA tube. For ease

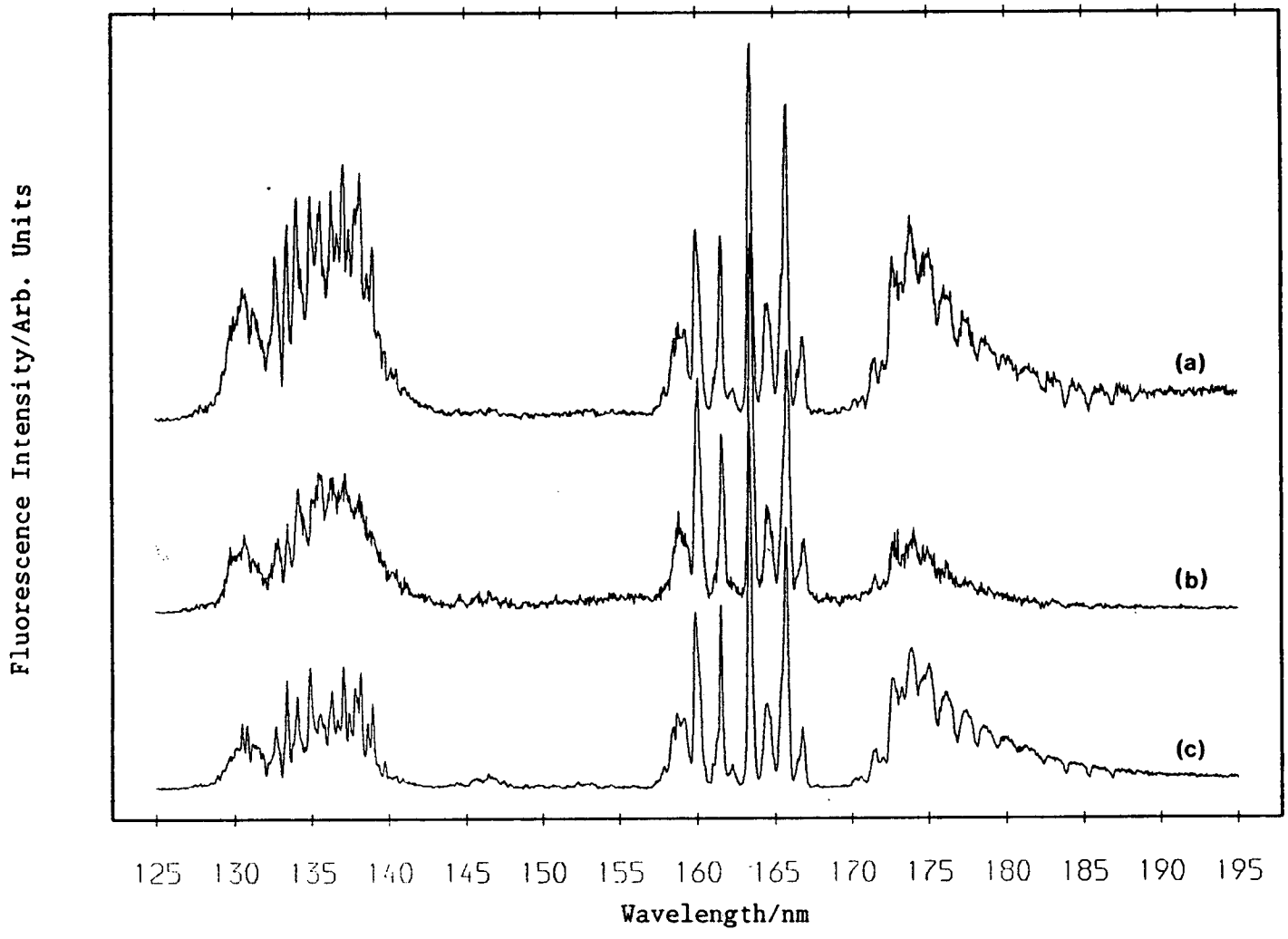

Figure 3.16 - Fluorescence excitation spectra of ICl and Cl_2 (1 : 2 mixture) showing fluorescence collected in 3 spectral regions. (a) 128 - 600 nm, $\Delta\lambda$ = 0.2 nm, P = 120 mTorr, (b) 128 - 195 nm, $\Delta\lambda$ = 0.3 nm, P = 110 mTorr and (c) 280 - 480 nm, $\Delta\lambda$ = 0.1 nm, P = 135 mTorr. All spectra are normalised to the most intense peak.

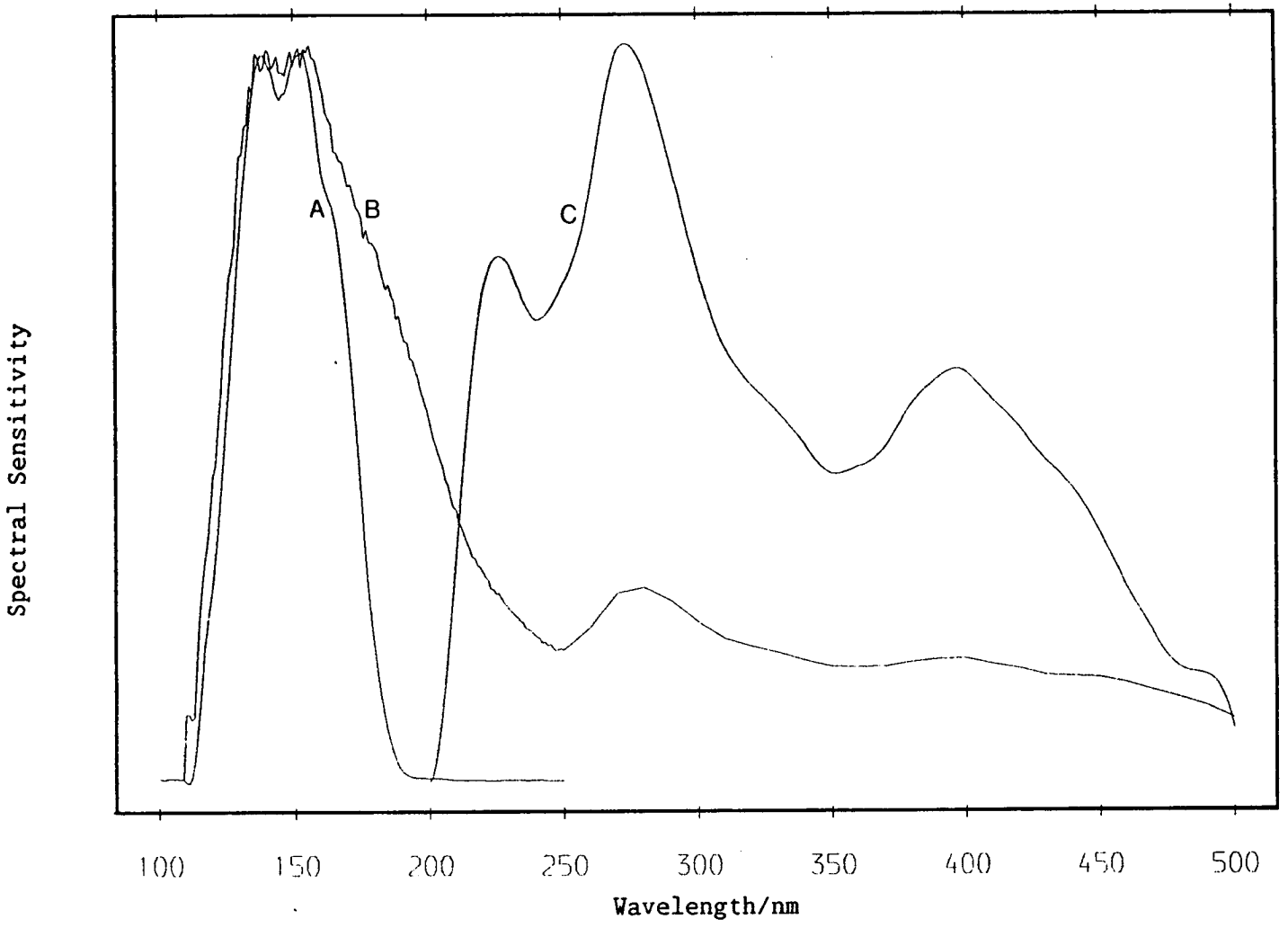

Figure 3.17 - Photomultiplier response curves. A - EMI G26E314LF solar blind tube, B - EMI G26K314LF tube with a bialkali photocathode and C - EMI 9883QKA tube. Response curves are all normalised to the most intense peak.

of comparison each spectrum has been normalised to the most intense peak.

There is little difference in the fluorescence excitation spectra following excitation at wavelengths above 155 nm; apart from the loss of sensitivity in the VUV only spectrum above 170 nm which is a function of the photomultiplier response curve. To shorter wavelengths the fluorescence excitation spectra are again similar, the differences between the three spectra being due partly to differing resolutions and partly to contributions from the VUV Cl_2 systems which are detected in the VUV only (top trace) and the VUV/UV/VIS (middle) trace.

Figure 3.16 shows that the emitting states excited by radiation of $\lambda \geq 155$ nm have extensive fluorescence systems ranging from the VUV through the UV to the visible region. For $\lambda_{exc} < 143$ nm two separate processes occur as discussed in the previous section.

(i) $^4P_{5/2}$ and $^2P_{3/2}$ formation and fluorescence, detected in the VUV.

(ii) Formation of the D'(2) ion-pair state by collisions of excited iodine atoms with ground state ICl molecules. This process is detected in the UV/VIS region.

As both processes depend on production of I^* excited atoms, the ICl fluorescence excitation spectra of the different spectral regions are similar (allowing for the afore-mentioned contributions from Cl_2 fluorescence). No fluorescence is observed following 143 - 158 nm

excitation indicating that states populated by radiation in this region are predissociated.

Finally, no evidence for fluorescence from the a_6 (1) and b_6 (1) states is observed although fluorescence from these states has been reported by Haranath and Rao [9]. Even in the VUV sensitive fluorescence excitation spectrum, minima appear at the positions of a_6 (1) and b_6 (1) Rydberg absorptions. The experiments of Haranath and Rao were conducted in a condensed transformer discharge and it is possible that inverse predissociation of I^* and Cl atoms occurs to form a_6 (1) and b_6 (1) Rydberg states which subsequently fluoresce, as observed for the AlH free radical [44]. From this work it can only be concluded that a_6 (1) and b_6 (1) fluorescence is weak, if present at all, and that a predissociation channel for these states must also exist.

REFERENCES

1. J.C.D. Brand, U.D. Deshpande, A.R. Hoy and E.J. Woods, Can. J. Chem., **61**, 846 (1983).
2. J.C.D. Brand, D. Bussieres, A.R. Hoy, S.M. Jaywant and D.B. Miller, Opt. Commun., **48**, 195 (1983).
3. J.C.D. Brand, A.R. Hoy and S.M. Jaywant, J. Mol. Spectrosc., **106**, 388 (1984).
4. T. Moeller, B. Jordan, P. Gurtler, G. Zimmerer, D. Haaks, J. Le Calve and M.-C. Castex, Chem. Phys., **76**, 295 (1983).
5. S.D. Peyerimhoff and R.J. Buenker, Chem. Phys., **57**, 279 (1981).
6. H. Cordes and H. Sponer, Z. Phys., **79**, 170 (1932).
7. P. Venkateswarlu, Can. J. Phys., **53**, 812 (1975).
8. R.S. Mulliken, J. Chem. Phys., **55**, 288 (1971).
9. P.B.V. Haranath and P.T. Rao, Indian J. Phys., **31**, 156 (1957).
10. N.K. Bibinov and I.P. Vinogradov, Opt. Spectrosc. (USSR), **59**, 191 (1985).
11. L.C. Lee, M. Suto and K.Y. Tang, J. Chem. Phys., **84**, 5277 (1986).
12. D. Bussieres and A.R. Hoy, Can. J. Phys., **62**, 1941 (1984).
13. P.B.V. Haranath and P.T. Rao, Indian J. Phys., **31**, 368 (1957).
14. G. Herzberg, "Spectra of Diatomic Molecules", Van Nostrand, New York, 1950.
15. K.P. Huber and G. Herzberg, "Molecular Spectra and Molecular Structure", Vol. IV, Van Nostrand-Reinhold, New York, 1979.
16. K. Dressler, R. Gallusser, T. Quadrelli and L. Wolneiwicz, J. Mol. Spectrosc., **75**, 205 (1979).
17. G. Delacretaz and L. Woste, Chem. Phys. Lett., **120**, 342 (1985).
18. P.J. Hay and D.C. Cartwright, Chem. Phys. Letters, **41**, 80 (1976).
19. M. Bettendorff, S.D. Peyerimhoff and R.J. Buenker, **66**, 261 (1982).

20. R.J. Buenker and S.D. Peyerimhoff, Chem. Phys. Lett., **36**, 415 (1975).

21. E.A. Kerr, M.A. MacDonald, R.J. Donovan, J.P.T. Wilkinson, D. Shaw and I. Munro, J. Photochem., **31**, 149 (1985).

22. J.V. Neumann and E. Wigner, Z. Physik, **30**, 467 (1929).

23. M.S. Child and R.B. Bernstein, J. Chem. Phys., **59**, 5916 (1973).

24. R.S. Mulliken, Phys. Rev., **46**, 549 (1934).

25. R.J. Donovan, M.A. MacDonald, K.P. Lawley, A.J. Yencha and A. Hopkirk, Chem. Phys. Lett., **138**, 571 (1987).

26. M.A. MacDonald, Ph.D. Thesis, University of Edinburgh, 1984.

27. D.I. Austin, R.J. Donovan, A. Hopkirk, K.P. Lawley, D. Shaw and A.J. Yencha, Chem. Phys., **118**, 91 (1987).

28. M.A. MacDonald, J.P.T. Wilkinson, C. Fotakis, M. Martin and R.J. Donovan, Chem. Phys. Lett., **99**, 250 (1983).

29. A. Gedanken, Chem. Phys. Lett., **110**, 626 (1984).

30. E. Herbst and W. Steinmetz, J. Chem. Phys., **56**, 5342 (1972).

31. R.P. Tuckett, Private Communication.

32. J.C.D. Brand and A.R. Hoy, J. Mol. Spectrosc., **114**, 197 (1985).

33. H. Lefebvre-Brion and R.W. Field, "Perturbations in the Spectra of Diatomic Molecules", Academic Press, London, 1986.

34. R.J. Donovan, B.V. O'Grady, K. Shobatake and A. Hiraya, Chem. Phys. Lett., **122**, 612 (1985).

35. D.I. Austin, Ph.D. Thesis, University of Edinburgh, 1987.

36. J.A. Myer and J.A.R. Samson, J. Chem. Phys., **52**, 716 (1970).

37. A.J. Yencha, R.J. Donovan, A. Hopkirk and D. Shaw, J. Phys. Chem., **92**, 5523 (1988).

38. R.J. Donovan, B.V. O'Grady, L. Lain and C. Fotakis, J. Chem. Phys., **78**, 3727 (1983).

39. J.P.T. Wilkinson, M.A. MacDonald and R.J. Donovan, Chem. Phys. Lett., **101**, 284 (1983).

40. J. Le Calve, M.C. Castex, D. Haaks, B. Jordan, G. Zimmerer, Nuovo Cimento, 63 B., 265 (1981).

41. T. Moeller, B. Jordan, P. Gurtler, G. Zimmerer, D. Haaks, J. Le Calve and M.C. Castex, "Spectral Line Shapes, Vol. 2," edited by K. Burnett (Walter de Gruyter, Berlin, 1983), p. 597.

42. N.K. Bibinov and I.P. Vinogradov, Khim. Fiz., 3, 836 (1984).

43. N.K. Bibinov and I.P Vinogradov, Sov. J. Chem. Phys., 3, 1284 (1985).

44. G. Herzberg, "The Spectra and Structures of Simple Free Radicals. An Introduction to Molecular Spectroscopy", Cornell University Press, USA, 1971.

CHAPTER FOUR

DISPERSED FLUORESCENCE FROM THE ION-PAIR STATES OF ICl FOLLOWING LASER AND SYNCHROTRON RADIATION EXCITATION

4.1 Introduction

Dispersing fluorescence from initially populated upper levels serves two purposes as it assists in identification of the emitting state(s) and also aids characterisation of potential curves. Fluorescence from an ion-pair state is generally recognisable by the distinctive oscillatory continua which result from transitions between high vibrational levels of ion-pair states and unbound portions of valence states, hence the term bound-free fluorescence. Such emission is a consequence of the difference in r_e between the ion-pair and ground state and also the application of the Franck-Condon principle, especially the often neglected conservation of momentum tenet.

It was only as recently as 1971 that Mulliken introduced a semi-classical treatment to interpret so called "structured continua" emission and applied this method of analysis to the I_2 McLennan bands [1, 2]. Since that date many bound-free systems have been identified and analysed not only in halogen spectroscopy [3 - 6] but also in emission from other species such as the rare gas halides [7, 8]. The theory and methods for simulation of bound-free fluorescence have been dealt with extensively elsewhere [9 - 11] and will only be described briefly in this work.

Population of the $E(0^+)$ ion-pair state was achieved by two methods. Firstly by single photon excitation to high vibrational levels, $v' > 104$, employing broad bandpass synctrotron radiation (SR) and secondly by the optical-optical double resonance (OODR) technique which allowed excitation to single rovibrational levels in the $v' = 3 - 116$ range. Initially, it was hoped that the energy regions accessed by the two techniques would overlap considerably allowing a more detailed study to be made of the higher vibrational levels of the $E(0^+)$ state. However, OODR excitation was limited to an upper v' value of 116 mainly because of poor Franck-Condon factors for the transition from the intermediate to final state.

Dispersed fluorescence spectra were recorded over a broad wavelength range incorporating both the short wavelength bound-bound limit and the long wavelength extremum of the bound-free system. For SR excited levels two monochromators, one a vacuum ultraviolet (VUV) and the other an ultraviolet/visible (UV/VIS) instrument, were necessary to cover the range of ion-pair fluorescence, while at lower excitation energies one was sufficient. Bound-bound fluorescence is important in the determination of the repulsive wall of the ion-pair state providing that the lower state, in this case the X ($^1\Sigma^+$) ground state, is well known.

Preliminary quenching experiments in the presence of foreign gas were also carried out.

Further details of the spectral simulations and the construction of the $E(0^+)$ potential curve can be found in Reference 9.

4.2 Experimental

4.2.1 Synchrotron Radiation Excitation

Dispersed fluorescence spectra were recorded on two stations at the SRS; stations FS13.2 and HA12. On station FS13.2 VUV/UV and UV/VIS dispersed fluorescence spectra were collected simultaneously utilising a 0.2 m Acton (Model VM - 502) and a 0.25 m Spex (Model Minimate) monochromator respectively. The Minimate monochromator was equipped with a 2400 groove mm^{-1} aberration corrected concave grating with a linear dispersion of 2 nm mm^{-1} while the Acton had a 1200 groove mm^{-1} aberration corrected concave holographic grating with a linear dispersion of 4 nm mm^{-1}. An EMI 9883QKA photomultiplier (response ~ 200 - 600 nm) detected UV/VIS dispersed fluorescence while on EMI G26K314LF tube (response ~ 110 - 600 nm) was employed in conjunction with the Acton monochromator. Combined photomultiplier - monochromator response functions, determined by Dr P Greenhill, are displayed in Figure 4.1. The dispersed fluorescence spectra recorded on station FS13.2 are corrected for the relevant response functions unless otherwise stated.

Preliminary dispersed fluorescence experiments were carried out on HA12 with the Spex Minimate monochromator. For these experiments the grating in use had 1200 groove mm^{-1} giving a linear dispersion of 4 nm mm^{-1} and was blazed at 500 nm. A cooled Mullard XP2020Q photomultiplier was employed to detect UV/VIS fluorescence.

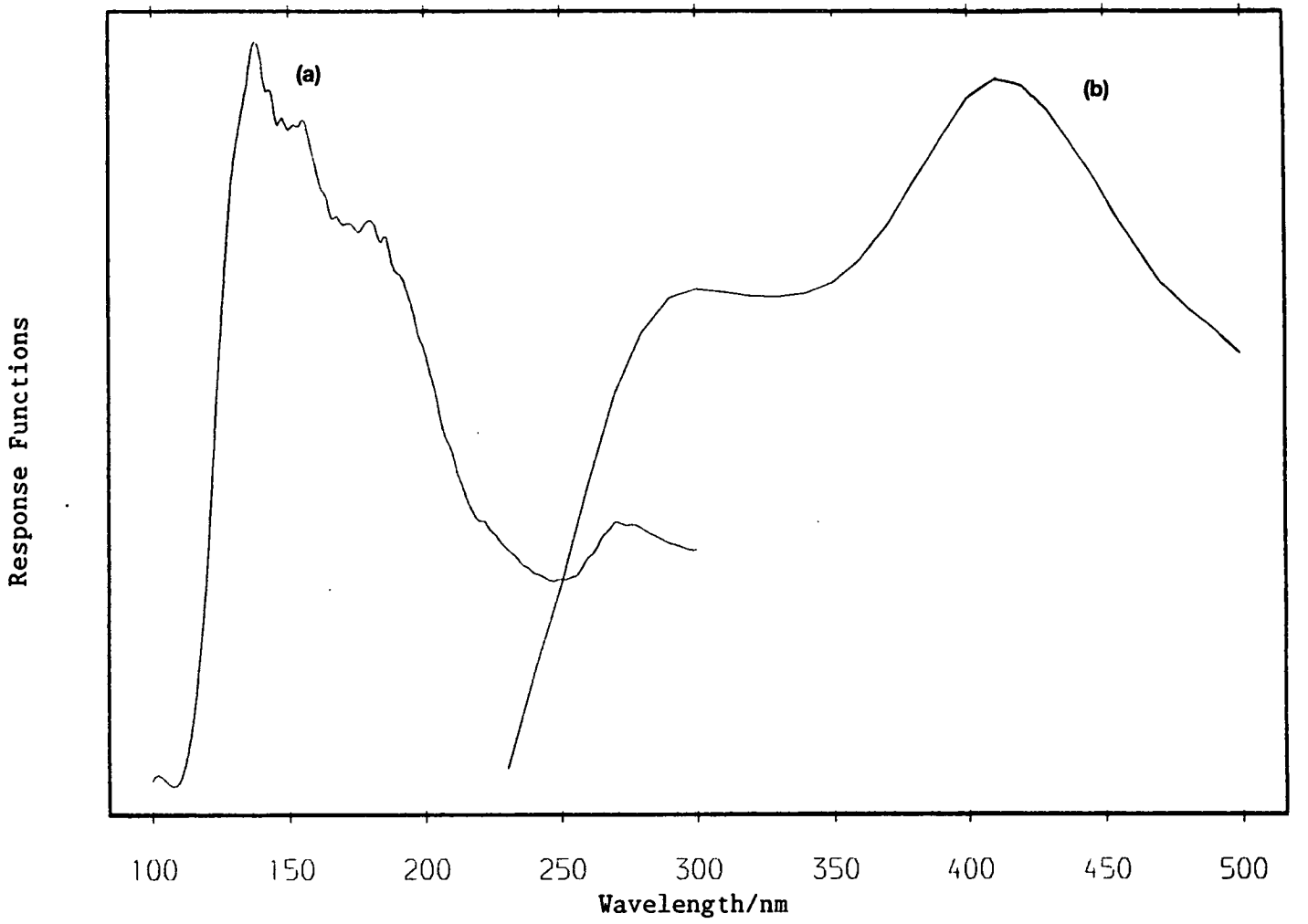

Figure 4.1 - Photomultiplier - monochromator response functions for (a) EMI G26K314LF - Acton VUV monochromator and (b) EMI 9883QKA-Minimate UV/VIS monochromator combinations. Both traces are normalised to the most intense peak.

4.2.2 Optical - Optical Double Resonance Excitation

Lambda Physik 3002E and 2002 dye lasers were pumped simultaneously by a Lambda Physik 201 MSC XeCl excimer laser to provide the pump and probe photons respectively for double resonance excitation to the $E(0^+)$ state. Rhodamine 6G and Rhodamine B laser dyes were used in the pump laser while various dyes (Coumarin 47, Bis-MSB, QUI, DMQ and PTP) were employed to probe the $E(0^+)$ $v' = 3 - 60$ region. To access vibrational levels above $v' = 60$ the output from Rhodamine 101, Rhodamine B, Rhodamine 6G and Coumarin 153 dyes was frequency doubled with a FL30 KDP crystal. The fluorescence signal was collected perpendicular to the axis of the collinear laser beams, dispersed by a Jobin Yvon *f*/7 monochromator and detected by either an R166 or R928 Hamamatsu photomultiplier tube. The Jobin Yvon monochromator was situated on the blue extremum of the $E(0^+) \rightarrow X(^1\Sigma^+)$ fluorescence to minimise contributions from other fluorescence systems. The signal was processed by a Stanford Research SR 250 boxcar and recorded simultaneously on a chart recorder and an IBM PC. Scanning the probe laser and tracking of the frequency doubling crystal was also controlled from the IBM PC.

The pump laser frequency was calibrated by simultaneously recording ICl and I_2 fluorescence excitation spectra on a two-channel chart recorder (Kipp and Zonen BD9) and comparing the I_2 spectrum with an atlas of iodine line frequencies [12]. Calibration of the probe photons proved more complex as several energy regions were involved. Frequency doubled photons could be calibrated accurately by comparison of the undoubled dye laser output with I_2 fluorescence excitation, as

above. However, probe photons of wavelength less than 400 nm had to be calibrated less satisfactorily; using various hollow cathode lamps to produce an offset value for the dye laser counter reading. The different calibration methods led to varying errors in the term values of $E(0^+)$ rovibrational levels populated, typically ± 0.8 cm^{-1}, or better. All laser experiments were carried out at pressures of 1 Torr ICl and 1 Torr Cl_2.

Further experimental details are given in Chapter 2.

4.3 Oscillatory Continuum Emission

Oscillatory continuum emission occurs from a bound upper state to either unbound portions of a lower bound state or to a purely repulsive state. Such continua are observed extensively in emission from ion-pair states as fluorescence from vibrationally excited ion-pair levels samples many unbound lower levels. Such bound-free emission can only be interpreted by close consideration of the Franck-Condon principle.

The classical Franck-Condon principle states that in an electronic transition the positions and momenta of the nuclei tend strongly to remain the same. Thus transitions from a vibrationally excited upper level cannot terminate on the classical turning points of the lower potential where the molecule possesses no kinetic energy, with the exception of transitions from the upper state turning points. Instead, electronic transistions terminate on a difference potential, termed a Mulliken difference potential, the locus of points where nuclear position and kinetic energy are conserved ie. points of

stationary phase. In Figure 4.2 the Mulliken difference potential for ICl $E(0^+) \rightarrow X(^1\Sigma^+)$ emission from $v' = 173$ of the $E(0^+)$ state is represented by the dashed curve.

Classically, a smooth continuum of fluorescence frequencies is expected but as the term oscillatory continuum implies this is not observed. In the case of an extremum in the difference potential, as shown here, two oscillation frequencies occurring as a result of quantum mechanical diffraction effects are superimposed upon the classical continuum. Such emission is referred to as a double frequency or interference type oscillatory continuum [10]. The two oscillation frequencies arise from separate effects:-

(i) Phase matching of the upper and lower wavefunctions, $\psi'(r)$ and $\psi''(r)$, as a function of r.

(ii) Interference between transitions which have the same $E'-E''$ value but which terminate on different branches of the difference potential.

Consider the phase matching of the upper and lower wavefunctions. Due to the Franck-Condon principle the two wavefunctions, $\psi'(r)$ and $\psi''(r)$, must possess the same de Broglie wavelength at a given r as:-

$$\lambda = \frac{h}{(2\mu K)^{1/2}}$$

, where μ is the reduced mass of the molecule and K is the kinetic energy of the molecule at internuclear separation, r.

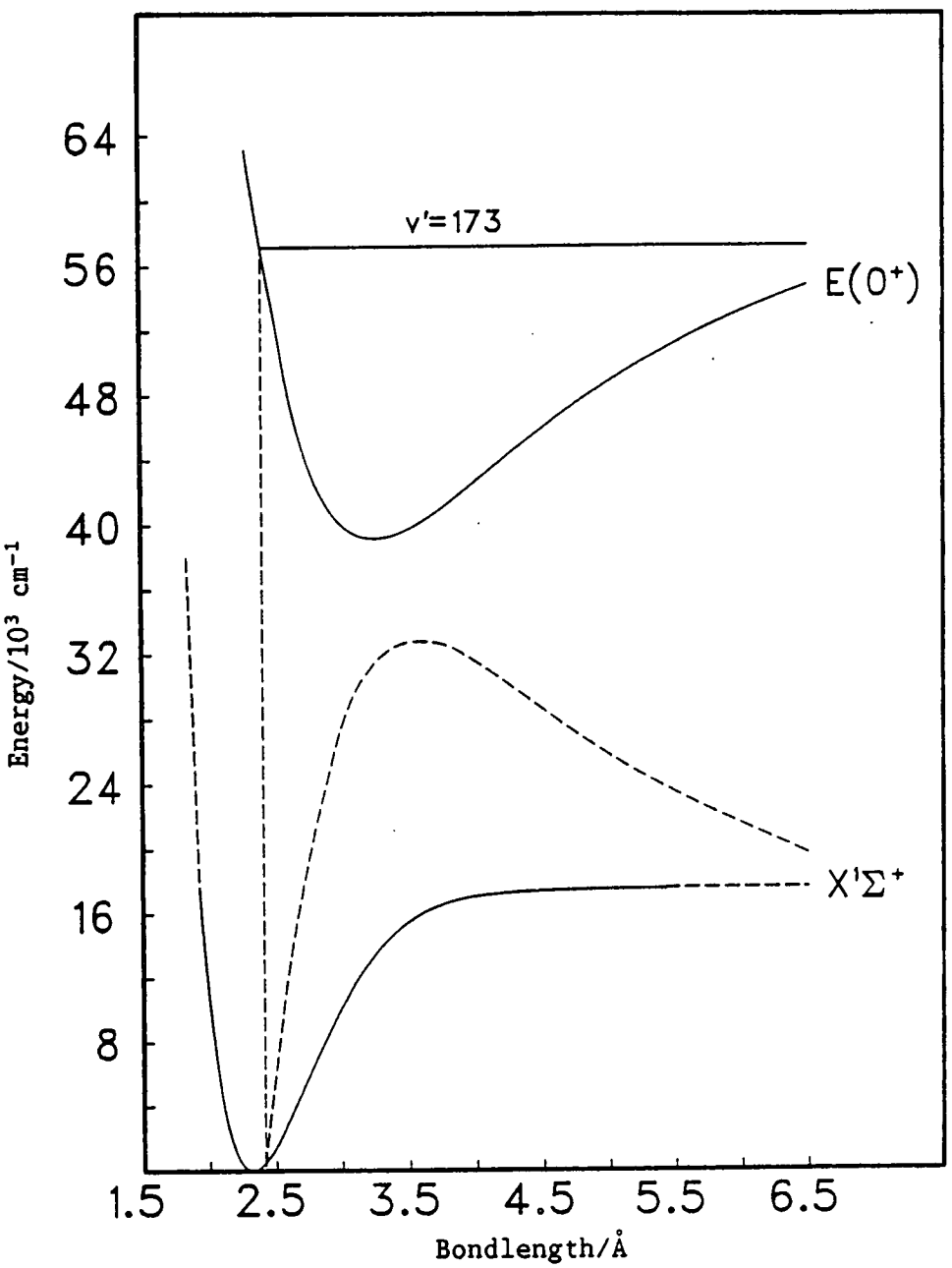

Figure 4.2 - The $E(0^+)$ and $X(^1\Sigma^+)$ states of ICl. The Mulliken difference potential for $E(v' = 173) \rightarrow X(^1\Sigma^+)$ is shown by the dashed curve. Extrapolation of the known portion of the $X(^1\Sigma^+)$ potential is also represented by dashes.

However, the two wavefunctions are not necessarily in phase. The high frequency oscillation observed is a result of interference between the $\psi'(r)$ and $\psi''(r)$ wavefunctions.

The second interference effect, between the overlap integrals $\int\psi'(r)\psi''(r)dr$ at the two points of stationary phase with common E", is responsible for the lower oscillation frequency.

On consideration of Figure 4.2 one expects three intensity maxima to occur in the fluorescence. One at both ν_{max} and ν_{med} corresponding to the left and right turning points respectively and one at ν_{min} which correlates with transitions to the maximum of the Mulliken difference potential. This third intensity maximum is observed since the Mulliken difference potential is relatively flat around this point, allowing transitions to occur at frequency ν_{min} over a large range of r.

A second class of oscillatory continuum emission, referred to as single frequency or reflection type emission [10], is observed if the difference potential is monotonic (ie. there is one point of stationary phase at each emission wavelength). In this case, only $\psi'(r)$ and $\psi''(r)$ phase matching takes place and two intensity maxima are observed.

Oscillatory continuum emission is a good example of a quantum mechanical interference effect. The shape and frequency of the observed oscillations provides information on the two potential curves involved in the transition and thus is most valuable if one is already well characterised [3].

4.4 Dispersed Fluorescence Following Synchrotron Radiation Excitation

Figure 4.3 shows the UV/VIS dispersed fluorescence following single photon excitation at 176.0 and 164.0 nm. Several fluorescence systems are observed in the 280 - 500 nm range. An extensive oscillatory continuum is observed with red extremum at ~ 410 nm while a second, less intense red extremum is sited around 325 nm. To the red of 420 nm a range of less structured bands is observed which may belong to one or more emission systems.

The majority of fluorescence in the 280 - 420 nm range has been assigned to the $E(0^+) \rightarrow X\ (^1\Sigma(0^+))$ oscillatory continuum. This system belongs to the double frequency or interference category of bound-free emission. Here two oscillation frequencies are superimposed upon the continuum predicted by classical mechanics, indicating that the difference potential has a maximum. In Figure 4.4 the computer simulated and observed fluorescence spectra are displayed for 176.0 nm excitation. Computer simultations of the dispersed fluorescence were carried out using the well characterised ground-state potential [13, 14] and a variable potential for the upper $E(0^+)$ state. The parameters of the $E(0^+)$ potential were adjusted until the simulated fluorescence agreed well with that observed experimentally. The functional form of the ion-pair potential and the final $E(0^+)$ potential curve are discussed in Section 4.6.

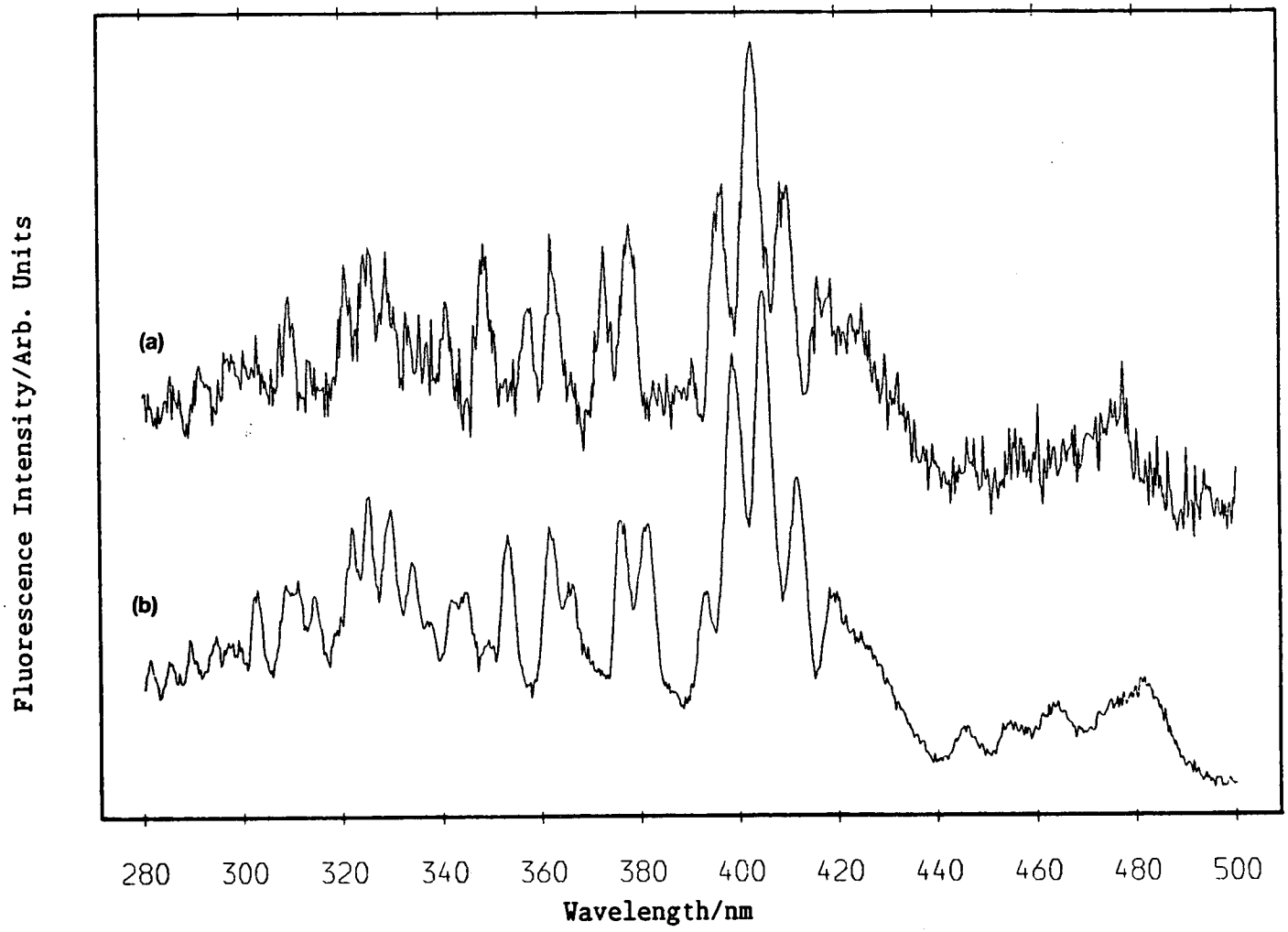

Figure 4.3 - Dispersed fluorescence spectra of ICl and Cl_2 excited at (a) 164.0 nm and (b) 176.0 nm. Fluorescence was excited with a bandpass of 4.5 nm and analysed with 1.7 nm resolution. (a) ICl pressure = 337 mTorr, Cl_2 pressure = 675 mTorr. (b) ICl pressure = 320 mTorr, Cl_2 pressure = 640 mTorr. Both

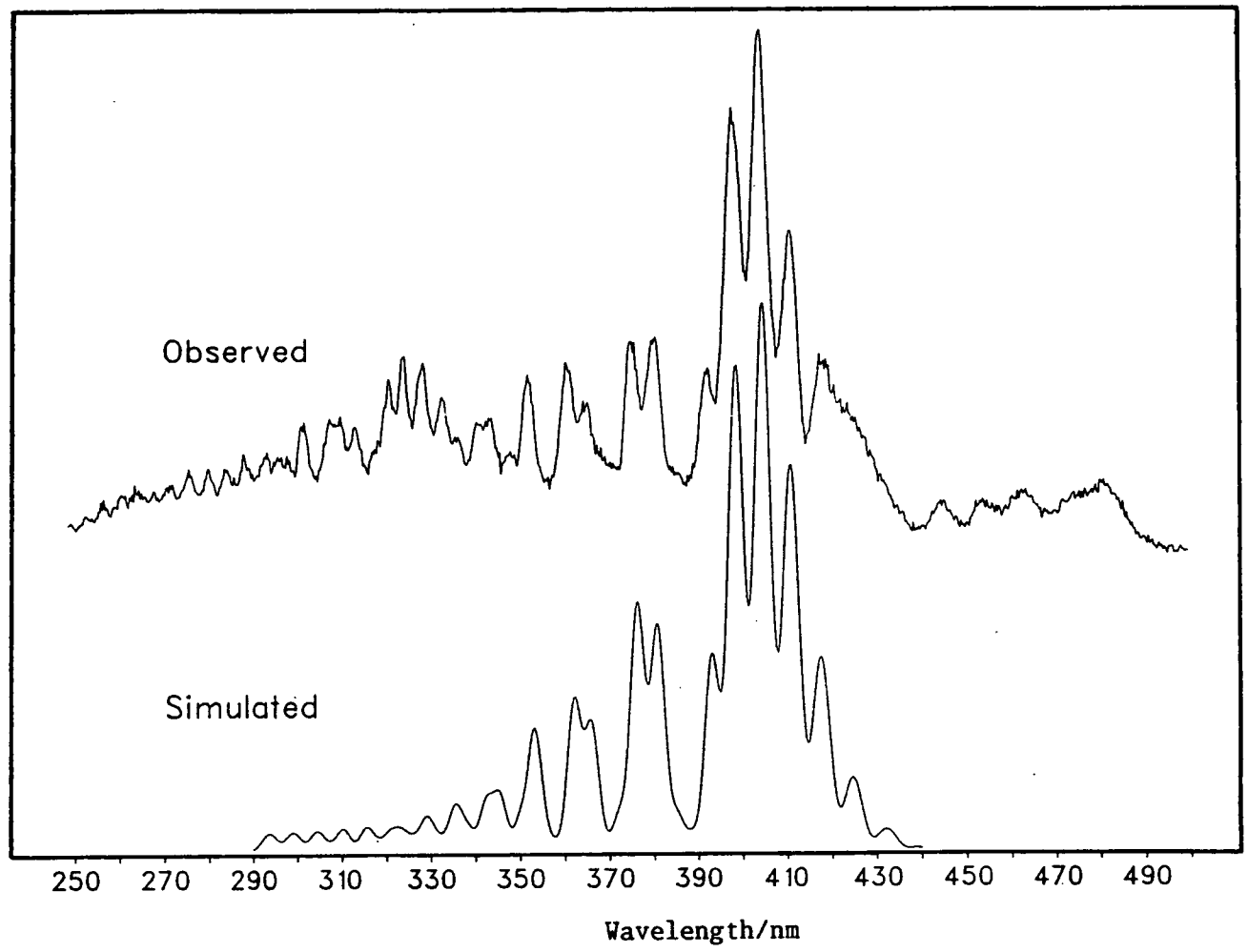

Figure 4.4 - Observed and simulated dispersed fluorescence of ICl excited by synchrotron radiation at 176 nm. Fluorescence was excited with a bandpass of 4.5 nm and analysed with 1.7 nm resolution. Ratio of ICl:Cl_2 pressure employed is 1:2 with P_{ICl} = 320 mTorr. Fluorescence is not corrected for the response function of the analysing system.

As the SRS is a less intense source than a laser system a broad excitation bandpass was necessary for detection of dispersed fluorescence. The excitation bandpass for the spectra in Figures 4.3 and 4.4 was 4.5 nm (FWHM) which populated approximately 25 vibrational levels at 176.0 nm excitation. The large number of emitting vibrational levels was accounted for in the simulations by including contributions from 20 vibrational levels selected from a range of 30 centred around the excitation energy. All simulations were carried out for the natural isotopic mix of ICl.

The dispersed fluorescence spectra following excitation at 176.0 nm and 164.0 nm are very similar. From Figure 4.3 it is observed that, within the accuracy of the experiment, the position of the $E(0^+) \rightarrow X(^1\Sigma^+)$ long wavelength extremum is independent of excitation wavelength. This is a general property of double frequency oscillatory spectra since as the excitation wavelength increases so too does the energy of the Mulliken difference potential maximum. The computer simulation of the ICl $E(0^+) \rightarrow X(^1\Sigma^+)$ oscillatory continuum following 176.0 nm excitation has verified that this is, as expected, the main emission system in the UV/VIS region. Owing to the spectral similarities and behaviour of the fluorescence system with varying excitation energy, it is concluded that the $E(0^+) \rightarrow X(^1\Sigma^+)$ transition is the main fluorescence process following excitation at wavelengths above 155 nm.

It is noted that the second maximum observed around 325 nm also remains invariant with excitation wavelength. This system has sufficient structure to suggest that it too is the long wavelength

extremum of a second, double frequency oscillatory continuum. An obvious candidate for the upper state is the $f(0^+)$ ion-pair state belonging to the second ion-pair cluster and correlating with I^+ ($^3P_0$) and Cl^- (^1S) ions at dissociation.

The $f(0^+)$ state lies 5,864 cm^{-1} above the $E(0^+)$ state at 44,924 cm^{-1} [15] and from Austin's RKR analysis [9] is also known to lie at a similar r_e. Assuming that the shape of the $f(0^+)$ potential mirrors that of the $E(0^+)$ state, it is estimated that the long wavelength limit of the $f(0^+) \rightarrow X(^1\Sigma^+)$ oscillatory continuum lies 5,864 cm^{-1} to the blue of the $E(0^+) \rightarrow X(^1\Sigma^+)$ red extremum, ie. around 326.6 nm. This is very close to the position of the observed bandhead and thus the second system has been assigned to the $f(0^+) \rightarrow X(^1\Sigma^+)$ oscillatory continuum.

Several diffuse bands are observed beyond 420 nm. From comparison of the experimental and simulated spectra in Figure 4.4 it is obvious that an additional system underlies the red end of the $E(0^+) \rightarrow X(^1\Sigma^+)$ emission. This system and the bands in the 440 - 490 nm region are broad and lack structure indicating that these bands either belong to a single frequency type oscillatory continuum or are part of unresolved bound-bound systems. The $B(^3\Pi_{0^+})$ state with T_e at 17,376 cm^{-1} [16] is the only $\Omega = 0^+$ valence state, apart from the ground state, which is bound to any significant degree and must be a likely candidate for the lower state in an $E(0^+) \rightarrow$ valence state transition. However, at present there is insufficient data to assign the fluorescence systems at wavelengths longer than 420 nm and further experimental work is required.

Figure 4.5 shows the VUV/UV dispersed fluorescence for the 176.0 nm and 164.0 nm excitation wavelengths. It was hoped that analysis of the bound-bound fluorescence from the inner turning point of the upper state could provide information on the nature of the state, ie. whether there was significant Rydberg character present after excitation at the lower wavelength. However, due to the poor resolution of both the excitation and dispersion monochromators, necessary to detect VUV fluorescence, no pertinent information was obtained.

The dispersed fluorescence spectra obtained following SR excitation at wavelengths above 155 nm have identified the $E(0^+)$ state as the major emitting state. Two fluorescence systems have been assigned; the $E(0^+) \rightarrow X(^1\Sigma^+)$ and $f(0^+) \rightarrow X(^1\Sigma^+)$ systems. Both these transitions are parallel in nature, $\Delta\Omega = 0$, upholding the propensity rule noted by Brand et al [17] for excitation between valence and ion-pair states.

4.5 Optical-Optical Double Resonance Excitation

4.5.1 Excitation Scheme

OODR excitation offers various advantages over excitation by synchrotron radiation, the main one being population of a single rovibronic level as opposed to many vibrational levels. Previous to this work the $E(0^+)$ state had been probed up to $v' = 40$ via several intermediate valence states and a set of Dunham parameters produced which characterised the potential up to $v' = 30$ [18]. The aim of the

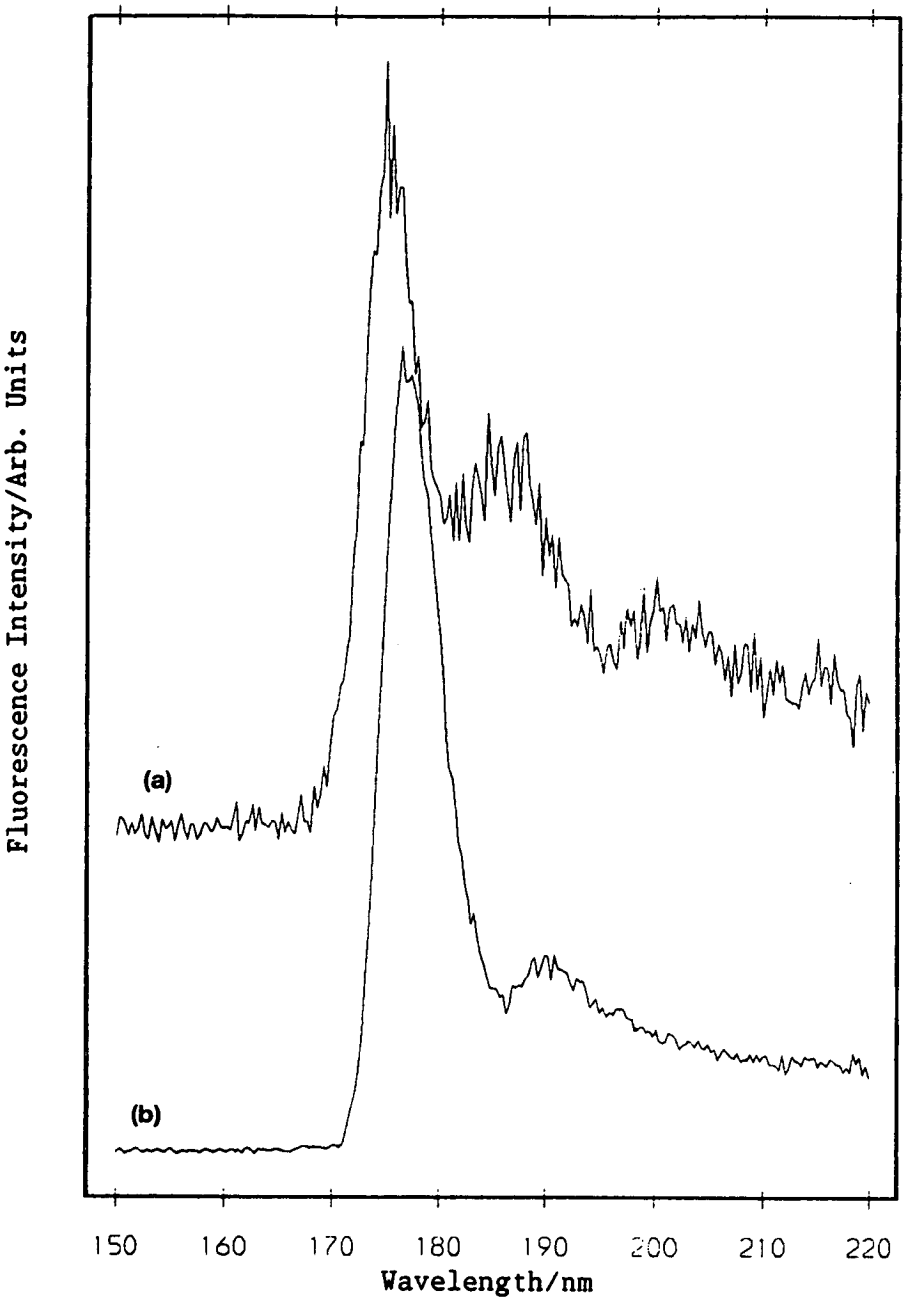

Figure 4.5 - VUV/UV dispersed fluorescence of ICl and Cl_2 excited at (a) 164.0 nm and (b) 176.0 nm. Fluorescence was excited with a bandpass of 4.5 nm and analysed with 2.0 nm resolution. (a) ICl pressure = 337 mTorr, Cl_2 pressure = 675 mTorr. (b) ICl pressure = 320 mTorr, Cl_2 pressure = 640 mTorr. Both spectra normalised to the most intense peak.

present double resonance experiments was to extend the known portion of the $E(0^+)$ state as far up the vibrational manifold as possible.

Three valence states present themselves as possible intermediates in the pump-probe sequence, the $B(^3\Pi_{0^+})$, $A(^3\Pi_1)$ and $A'(^3\Pi_2)$ states which all belong to the 2431 molecular orbital (MO) configuration. These are the only three valence states, apart from the ground state, which are bound to any considerable extent. The $A'(^3\Pi_2)$ state can be discounted immediately as the $\Delta\Omega = 2$ transition, $A'(^3\Pi_2) \leftarrow X(^1\Sigma^+)$, is not allowed. Theoretically, either the $A(^3\Pi_1)$ or $B(^3\Pi_{0^+})$ states can be used as the intermediate in the $E(0^+) \leftarrow ? \leftarrow X(^1\Sigma^+)$ excitation sequence.

The $A(^3\Pi_1)$ state is lower lying (T_e = 13,742.9 cm^{-1} [19]) and is relatively unperturbed whereas the $B(^3\Pi_{0^+})$ state lies at higher energy (T_e = 17,375.6 cm^{-1}) and interacts strongly with the repulsive $Y'(0^+)$ state to form an avoided crossing [20]. The result of this, and other interactions, is that the $B(^3\Pi_{0^+})$ state is only bound up to, and including, $v' = 2$ and has a considerably shorter radiative lifetime than the $A(^3\Pi_1)$ state. The lifetime of the $A(^3\Pi_1)$ state lies in the 405 - 460 μs range, dependent on the excitation wavelength, [21] while the reported $B(^3\Pi_{0^+})$ lifetime is 4.88 μs for $v' \leq 2$ [22] decreasing to less than a nanosecond for the predissociated $v' = 3$ level [20]. As T_e of the $B(^3\Pi_{0^+})$ state lies below the dissociation limit of the $A(^3\Pi_1)$ state, overlap between the $A(^3\Pi_1) \leftarrow X(^1\Sigma^+)$ and $B(^3\Pi_{0^+}) \leftarrow X(^1\Sigma^+)$ absorption bands is observed (see Table 1.1).

The $A(^3\Pi_1)$ state appears the more attractive intermediate as it is more stable. However, there is no record of an $E(0^+) \leftarrow A(^3\Pi_1)$ transition which is not perturbation aided. Bussieres and Hoy [18] have reported excitation to the $E(0^+)$ state via the $A(^3\Pi_1)$ state but only through $E(0^+)$ - $\beta(1)$ and $A(1)$ - (0^+) perturbations, where the unknown (0^+) state is probably the $a'(0^+)$ state of Brand et al [23].

Initially, an attempt was made to use the $A(^3\Pi_1)$ state as the intermediate, pumping mainly through the Q39 rotational line of the $I^{35}Cl(19,0)$ vibrational band. In theory, the $E(0^+) \leftarrow A(^3\Pi_1)$ $\Delta\Omega = 1$ transition is allowed, although Brand's $\Delta\Omega = 0$ propensity rule for ion-pair $\leftarrow$ valence excitation is noted. Brand and coworkers employed photographic detection in their experiments and this is probably the reason why $\Delta\Omega = 1$ transitions were not observed as analogous transitions have been reported for I_2 using fluorescence excitation techniques [24]. In this work, three ion-pair states were accessed from the $A(^3\Pi_1)$ state and were assigned as the $\beta(1)(^3P_2)$, $G(1)(^3P_1)$ and $f(0^+)(^3P_o)$ states, where the (^3P) term is the state of the I^+ ion with which the ion-pair state correlates diabatically. These assignments were made on the basis of preliminary dispersed fluorescence studies and the rotational structure observed in the fluorescence excitation. Following a $\Delta\Omega = 0$ excitation, P and R branch transitions are observed in the upper state fluorescence excitation while P, Q and R branches, with the Q branch predominant, are found in a perpendicular ($\Delta\Omega = 1$) excitation step. The excitation of these states will not be pursued further as this work is mainly concerned with the $E(0^+)$ ion-pair state. No evidence for population

of the $E(0^+)$ state was observed. However, by population of the $f(0^+)$ state the $\Delta\Omega = 0$ propensity rule for valence - ion-pair transitions appears to have been broken. Further investigation is necessary to determine why the $f(0^+)$ but not the $E(0^+)$ state can be populated via the $A(^3\Pi_1)$ intermediate. This observation presents an interesting theoretical problem, while limiting the choice of intermediate state for unperturbed access to the $E(0^+)$ state to the $B(^3\Pi_{0^+})$ state.

Figure 4.6 shows the fluorescence excitation of the ICl $B(^3\Pi_{0^+}) \leftarrow X\ (^1\Sigma^+)$ (1,2) vibrational band alongside the fluorescence excitation of I_2 in the same spectral region. The I_2 spectrum provided calibration by comparison with an atlas of I_2 line frequencies [12] while the populated rotational levels were calculated using the constants of Hansen et al [16] for both the ICl $B(^3\Pi_{0^+})$ and $X(^1\Sigma^+)$ states. Little contribution from the $A(^3\Pi_1) \rightarrow X(^1\Sigma^+)$ fluorescence excitation is observed due to the long radiative lifetime of this state [21] compared to that of the $B(^3\Pi_{0^+})$ state [22] and the relatively high pressure of 2 Torr employed in the experiment.

As the $B(^3\Pi_{0^+}) \leftarrow X(^1\Sigma^+)$ transition is parallel in nature, $\Delta\Omega = 0$, P and R branches only are expected. The ICl spectrum in Figure 4.6 is deceptively simple since superposition of $I^{35}Cl$ P and R branches occurs from the R7 and P1 rotational lines to higher J. The pump line employed in the majority of double resonance experiments is marked by a diamond in Figure 4.6 and corresponds to the coincidental P25 and R31 transitions.

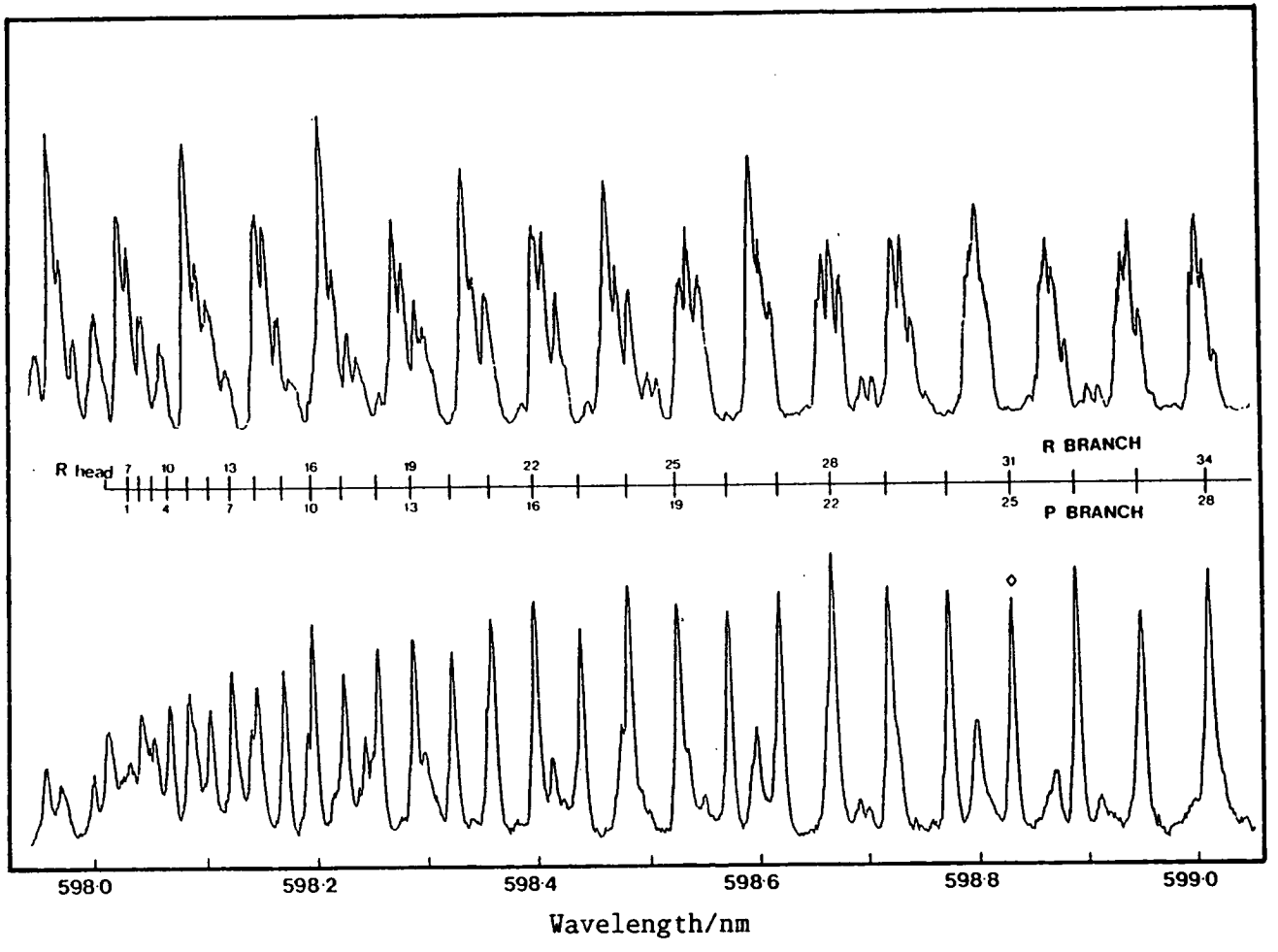

Figure 4.6 - Fluorescence excitation spectrum of the ICl $B(^3\Pi_0+)v' = 1 \leftarrow X(^1\Sigma^+)$ $v'' = 2$ transition (lower trace) calibrated by simultaneous collection of I_2 fluorescence (upper trace). ICl fluorescence was collected by a UG5 filter and EMI 9661B PMT, and I_2 fluorescence by a HOYA R64 filter and Hamamatsu R928 PMT. I_2 pressure = 300 m Torr; ICl pressure = Cl_2 pressure = 1 Torr. Laser light was generated employing Rhodamine 6G dye, $\Delta\lambda \simeq 0.2$ cm^{-1}.

With the pump laser fixed on a known rotational transition, fluorescence excitation spectra with the probe laser were run. The detection monochromator was situated at the low wavelength limit of the $E(0^+) \rightarrow X(^1\Sigma^+)$ system to minimise contributions from other excited states. An example of the fluorescence excitation of the $E(0^+)$ state which covers the E_v = 74-77 vibrational range is shown in Figure 4.7. P and R doublets are observed from each of the two rotational levels populated in the $B(^3\Pi_o+)$ state as expected for a parallel transition.

The combined P25 and R31 pump line to v = 1 of the $B(^3\Pi_o+)$ state from v" = 2 in the ground state was employed to populate the $E(0^+)$ state up to v = 100. Above this level the Franck-Condon factors from v' = 1 became too poor to probe higher vibrational levels. A second pump line, the P12 line of the $B(^3\Pi_o+) \leftarrow X\ (^1\Sigma^+)$ (2,0) band, was employed to populate higher vibrational levels. However, no transitions were observed to v' > 116 due to the blue extremum of the $E(0^+) \rightarrow X\ (^1\Sigma^+)$ system entering the VUV and also the recurring problem of decreasing Franck-Condon factors.

4.5.2 Dispersed Fluorescence

Figures 4.8 and 4.9 show the observed and simulated $E(0^+) \rightarrow X(^1\Sigma^+)$ fluorescence system following excitation to the $E_{v,J}$ = 53, 23 and $E_{v,J}$ = 76, 23 levels respectively. Assuming no significant collisional energy transfer, the dispersed fluorescence originates from a single rovibrational level. This greatly simplifies the fluorescence, especially in the bound-bound region, in comparison with that obtained following synchrotron radiation excitation.

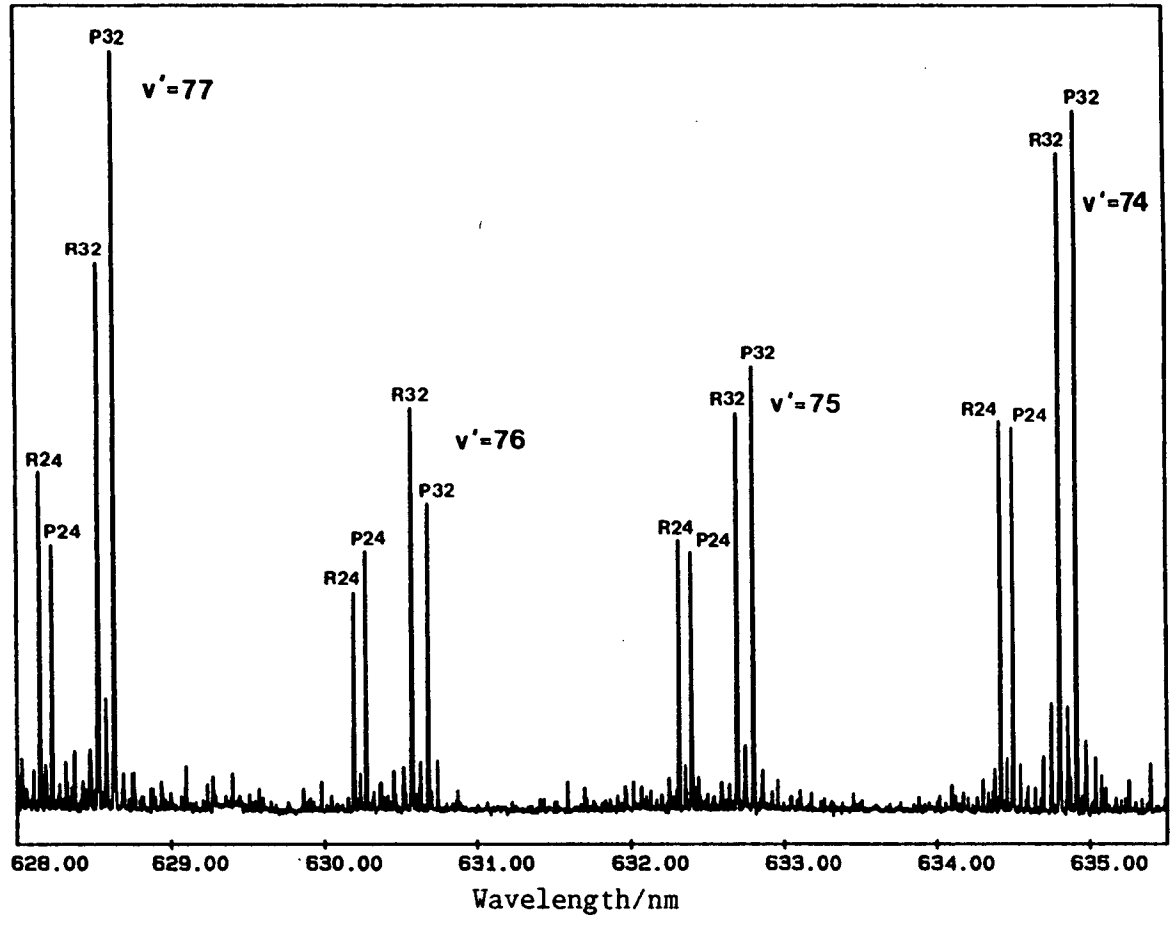

Figure 4.7 - Fluorescence excitation of the $E(0^+)$ $v' = 74 - 77$ vibrational levels, pumped via the P25 and R31 rotational lines of the $B(^3\Pi_{0^+}) \leftarrow X(^1\Sigma^+)$ (1, 2) vibrational band. Fluorescence was collected from the blue extremum of the $E(0^+) \rightarrow X(^1\Sigma^+)$ system utilising an EMI 9661B photomultiplier. Rhodamine 101 dye was employed in conjunction with a FL30 KDP doubling crystal. Probe laser resolution, $\Delta\lambda \simeq 0.2$ cm^{-1}. The wavelength scale shows the fundamental probe laser wavelength.

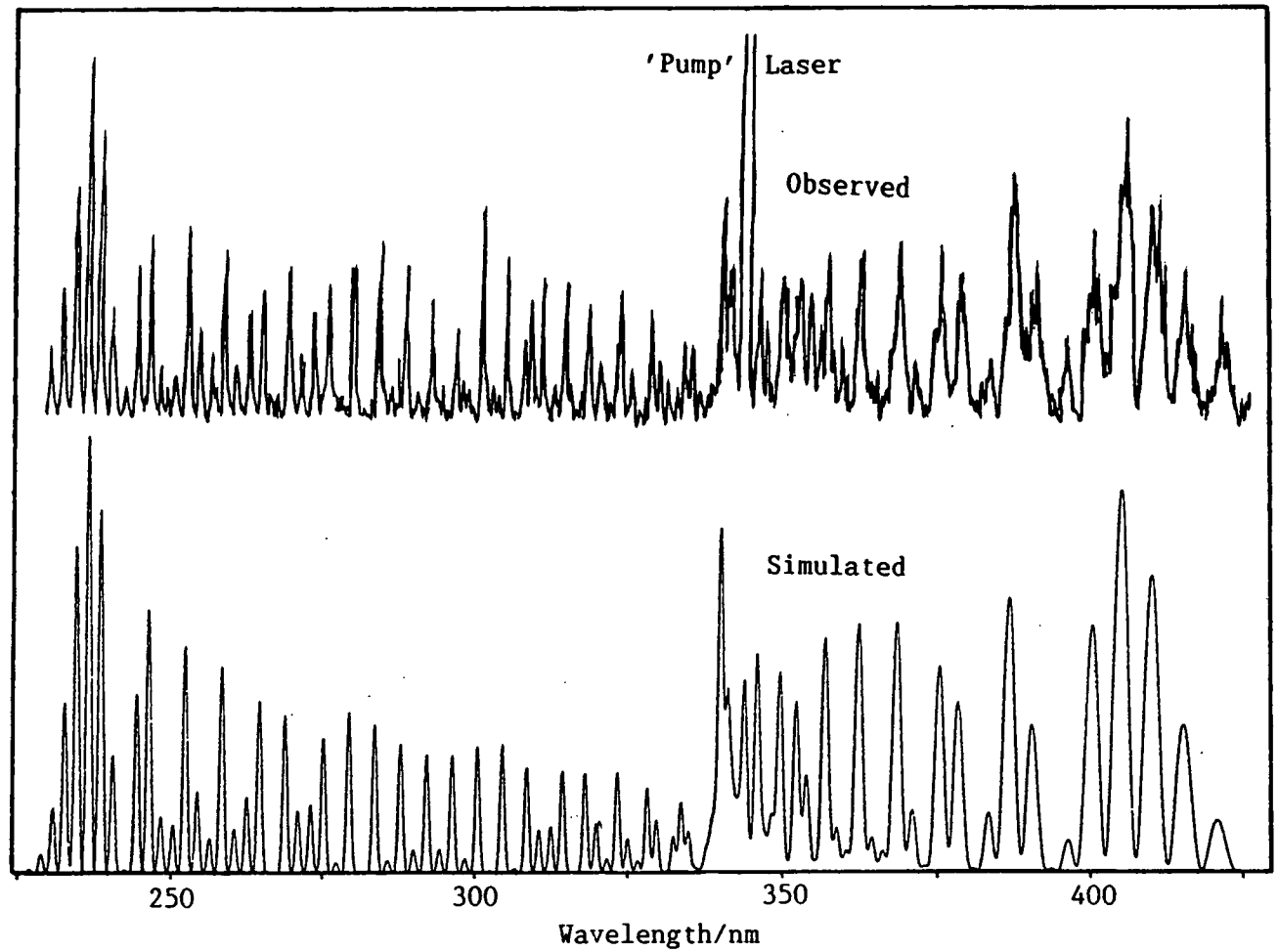

Figure 4.8 - Simulated and observed dispersed fluorescence of $I^{35}Cl$, $E_{v,J}$ = 53,23 → X, excited by OODR. ICl pressure = Cl_2 pressure = 1 Torr. Fluorescence was analysed with a resolution of 0.75 nm.

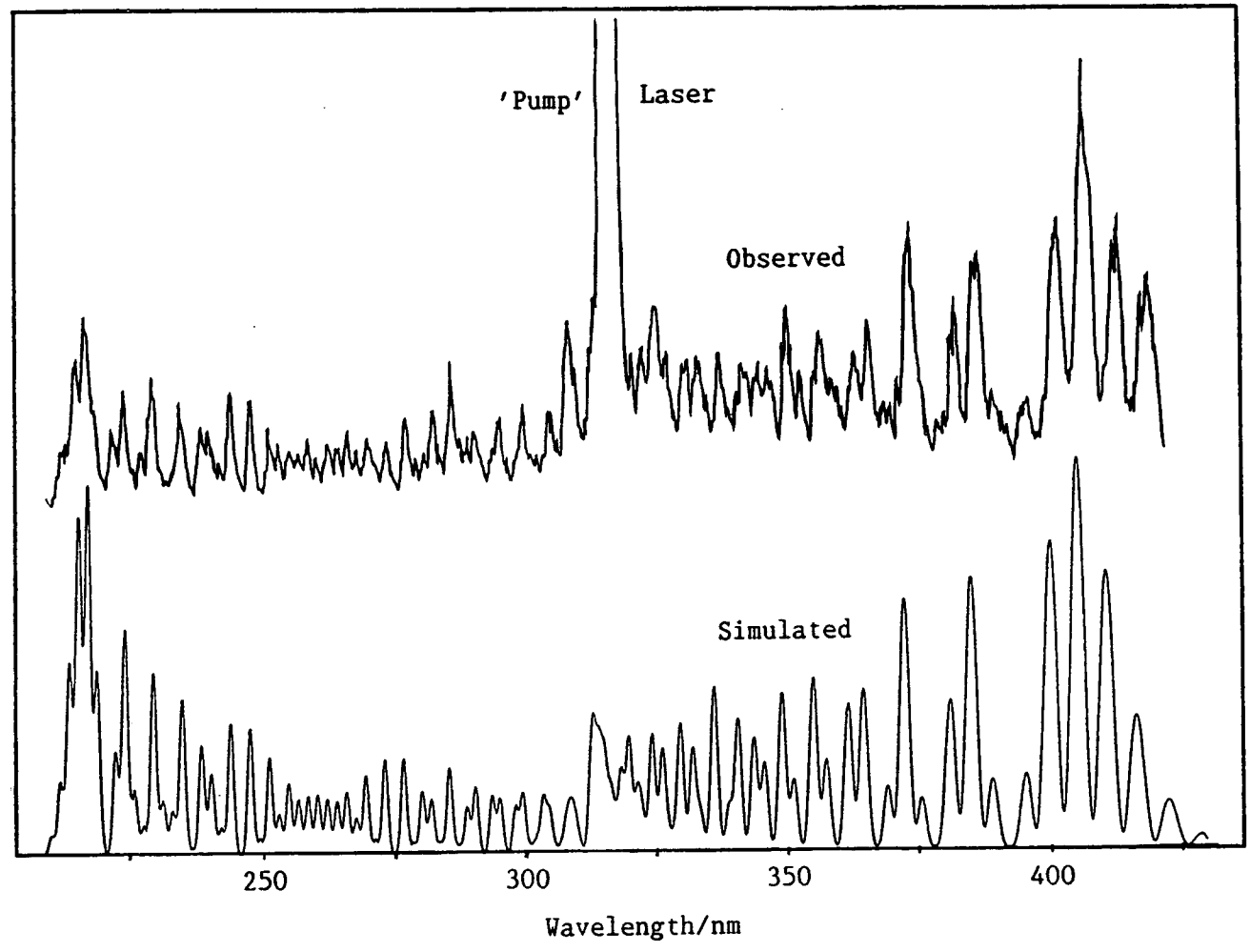

Figure 4.9 - Simulated and observed dispersed fluorescence of $I^{35}Cl$ from the $E_{v',J'}$ = 76,23 level, excited by OODR. ICl pressure = Cl_2 pressure = 1 Torr. Fluorescence was analysed with a resolution of 0.75 nm.

Dispersed fluorescence extending from the bound-bound short wavelength extremum to the bound-free maximum as shown in Figures 4.8 and 4.9 is extremely valuable. Such fluorescence provides information on the ion-pair state over the entire breadth of the potential of the vibrational level excited. Particularly useful is the short wavelength bound-bound fluorescence from the initially excited state to low vibrational levels of the ground state. By successfully simulating the fluorescence in this region the repulsive limb of the ion-pair state can be located.

Consider the fluorescence from $v' = 53$, $J' = 23$ of the $E(0^+)$ state (Figure 4.8) and the manner in which this assists definition of the $E(0^+)$ potential. Two distinct regions are observed in the dispersed fluorescence. A bound-bound portion extending from the blue extremum to around 340 nm and a bound-free portion extending from 340 nm to the long wavelength extremum. Bound-bound fluorescence defines the $E(0^+)$ wavefunction near the inner turning point while the region of the difference potential maximum is defined by the bound-free maximum at 404 nm. A third build-up of intensity is observed, at ~ 340 nm, corresponding to the division between bound-bound and bound-free emission. Fluorescence in this region helps to define the wavefunction at the outer turning point. Thus, the dispersed fluorescence from $v' = 53$ samples the $E(0^+)$ potential across a width of ~ 2.5 Å [9].

Dispersed fluorescence from levels excited by the OODR technique has assisted greatly in characterisation of the $E(0^+)$ ion-pair potential, especially in the position of the repulsive limb.

By comparing the dispersed fluorescence spectra obtained following synchrotron radiation and OODR excitation the advantages of selective excitation can easily be appreciated.

4.6 The $E(0^+)$ Potential

The final $E(0^+)$ ion-pair potential curve was constructed with information from various sources. As discussed earlier, previous to this work the potential was well characterised up to v = 30 by the RKR analysis of Bussieres et al [18]. However, the majority of this thesis is concerned with excitation to vibrational levels above $v \simeq 130$. A potential was sought which could adequately account for the experimental results obtained over a large vibrational range.

The attractive limb of any ion-pair potential is dominated by the Coulombic attraction between the oppositely charged ions with which the state correlates diabatically, in this case $I^+(^3P_2)$ and $Cl^-(^1S)$. Thus, a "Rittner" type attractive limb,

$$V(r) = D_e - C1/r + C3/r^3 - C4/r^4 - C6/r^6$$

(where C1/r represents the charge/charge electrostatic attraction, $C3/r^3$ the charge/quadrupole interaction, $C4/r^4$ the charge/induced dipole term and $C6/r^6$ the induced dipole/induced dipole term) was adopted for the E(0+) potential.

Characterisation of the replusive limb of an ion-pair potential is more awkward. This limb is often represented by a simple exponential term, Aexp(-br), which is subsequently "massaged" until a

good fit to experimental data is observed. However, for the $E(0^+)$ potential the inner repulsive wall above $v' = 30$ was defined by 8 points determined from successful simulation of the OODR dispersed fluorescence and fitted by a spline routine. The latter method is more versatile and also very accurate as the dispersed fluorescence can locate the inner wall to within 0.005Å.

Accurate term values for the $J = 23$ rotational level of selected vibrational levels in the range $v' = 47 - 116$ were obtained from $E(0^+)$ fluorescence excitation spectra. The separations observed between consecutive vibrational levels give information on the width of the potential. The corresponding term values and vibrational spacings of the final $E(0^+)$ potential curve agree, within experimental error, with the OODR data. Comparison of the calculated and observed data is reported by Austin [9].

The final $E(0^+)$ potential was also in good agreement with the experimental data obtained following synchrotron radiation excitation. The dispersed fluorescence from levels populated at 176.0 nm was successfully simulated, as illustrated in Figure 4.4. In higher resolution ($\Delta\lambda = 0.03$ nm) absorption and fluorescence excitation studies, ion-pair vibrational spacing was observed in absorption btween 158 nm and 166 nm (Figure 3.3) and in fluorescence excitation between 172.5 nm and 176.8 nm (Figure 3.6), with average spacing ranging from 53 cm^{-1} to 29 cm^{-1}. The $E(0^+)$ potential reproduces the vibrational spacing in this energy region, within experimental error limits.

The final form of the $E(0^+)$ potential curve is shown in Figure 4.10. The potential is that of a typical ion-pair state. No obvious signs of perburbation are present, even in the region where the $E(0^+)$ ion-pair state crosses the $b_6'(0^+)$ Rydberg state. However, the repulsive inner limb does appear to be rather soft ie. not as steep as expected. This may be due to interactions between the $E(0^+)$ and $f(0^+)$ states and investigation of the $f(0^+)$ state has begun, to determine whether this is the case.

4.7 Physical Quenching of the $E(0^+)$ Ion-Pair State

A preliminary study on quenching of the initially populated ion-pair levels was carried out. It is well known that in the presence of foreign gas a collisional cascade occurs down to the foot of the lowest ion-pair cluster [25]. Strong emission, attributed to the $D'(2) \rightarrow A'(^3\Pi_2)$ system, has been observed by Diegelmann et al for many halogen and interhalogen molecules following electron impact excitation in the presence of buffer gas [26]. It has previously been assumed that the $D'(2)$ state is the lowest ion-pair state since this is where the collisional cascade appears to end. However, in ICl it is known that the $E(0^+)$ state is the lowest ion-pair state [23], although all three states in the lowest cluster, the $E(0^+)$, $\beta(1)$ and $D'(2)$ states, lie within 50 cm^{-1} of one another.

Following synchrotron radiation excitation at 176.0 nm of an ICl/Cl_2 sample with 29 Torr of N_2 added, quenching of the $E(0^+) \rightarrow X(^1\Sigma^+)$ oscillatory continuum is observed as shown in Figure 4.11. The new system with red extremum around 433 nm and extending to the blue has been extensively analysed by Tellinghuisen et al [27] who produced this system by Tesla discharge of ICl in

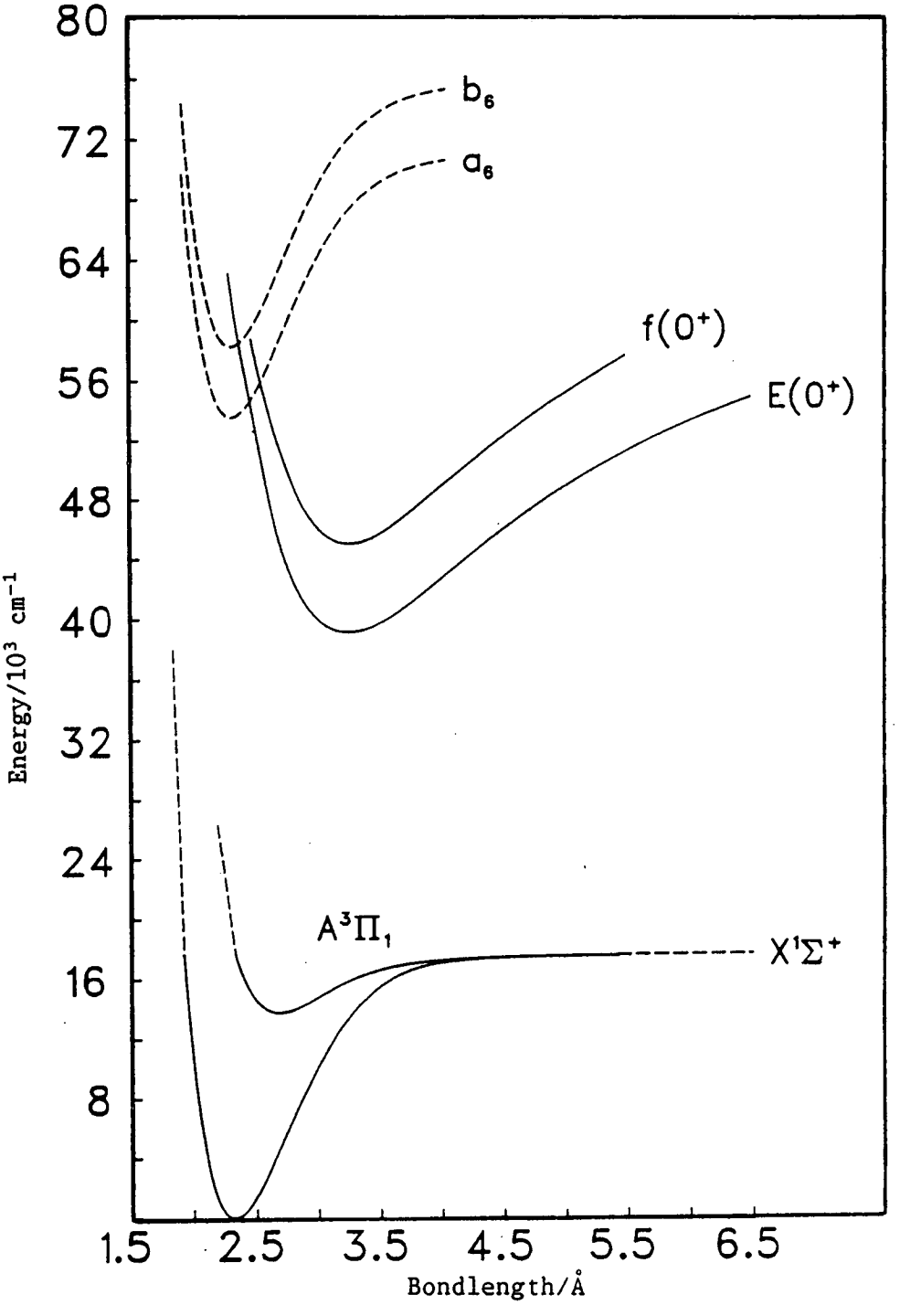

Figure 4.10 - The $E(0^+)$ state and some other known states of ICl. The dashed curves represent extrapolations of the known $X(^1\Sigma^+)$ and $A(^3\Pi_1)$ potentials and approximations of the a_6 and b_6 Rydberg states. For further information on the construction of this potential diagram see Reference 9.

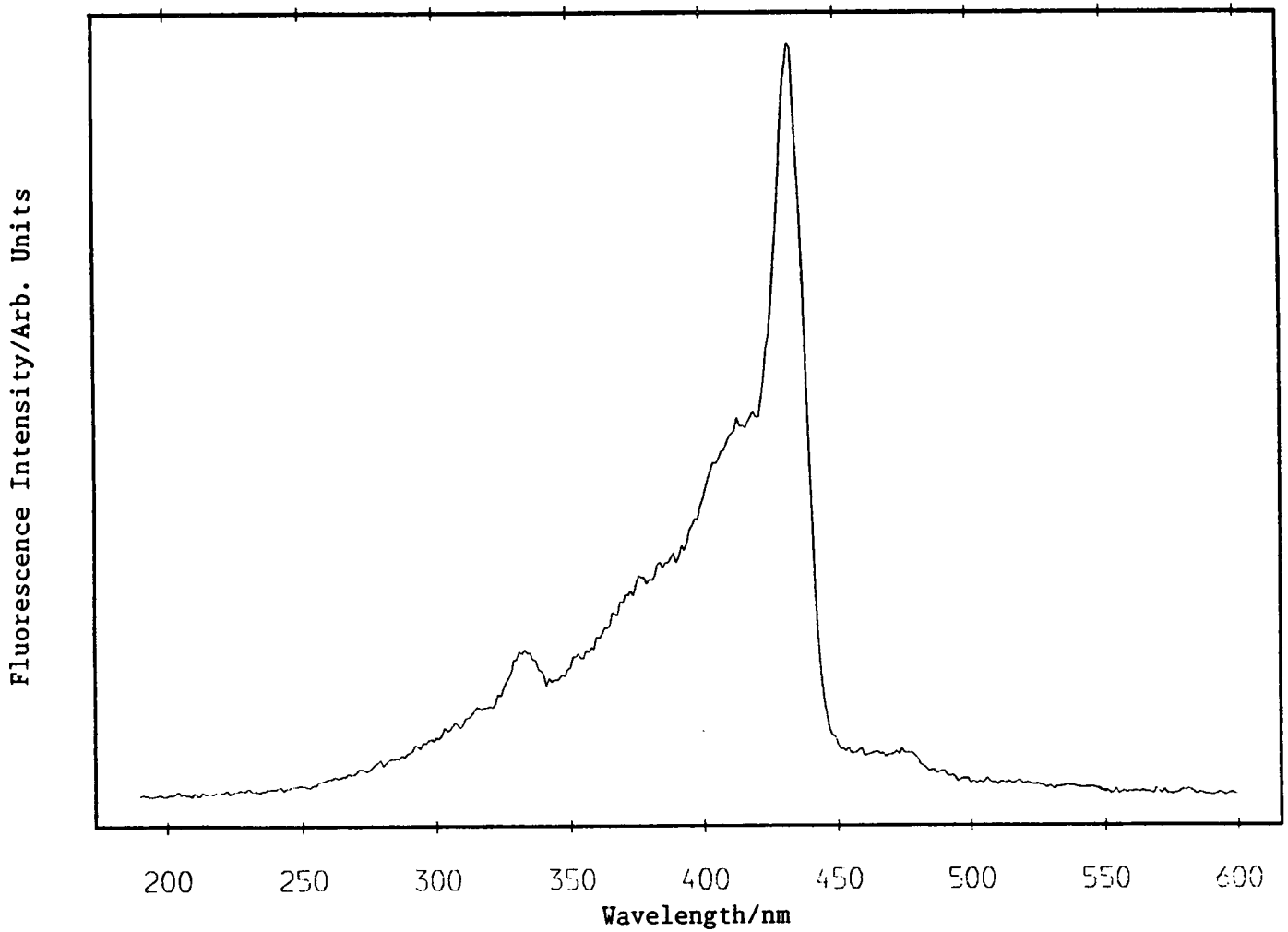

Figure 4.11 - Dispersed fluorescence of ICl and Cl_2 excited at 176.0 nm in the presence of 29 Torr N_2. Fluorescence was excited with a bandpass of 3.0 nm and analysed with 7.5 nm resolution. ICl pressure = Cl_2 pressure = 1 Torr. Fluorescence is not corrected for beam current decay or the response of the detection system.

excess buffer gas. Tellinghuisen has attributed the quenched system mainly to $D'(2) \rightarrow A'(^3\Pi_2)$ bound-bound fluorescence but has also assigned a sizeable portion of the fluorescence, approximately one third, to the $\beta(1) \rightarrow A(^3\Pi_1)$ system. Fluorescence from low vibrational levels, $v' < 2$, of the $E(0^+)$ state was not observed. This cannot be due to thermodynamic factors, as the $E(0^+)$ is the lowest ion-pair state, and must be a result of differing transition probabilities for the various emission systems.

At a N_2 pressure of approximately 30 Torr much of the fluorescence has collapsed into the $D'(2) \rightarrow A'(2)$ and $\beta(1) \rightarrow A(1)$ systems, although at this pressure an underlying contribution from $E \rightarrow X$ around 404 nm may also be present. Further studies over a wide pressure range are necessary to clarify the situation.

A second quenched system is observed around 330 nm, red-shifted from the red extremum of the $f(0^+) \rightarrow X(^1\Sigma^+)$ oscillatory continuum. By analogy with the physical quenching of the $E(0^+)$ state this must correspond to emission from low vibrational levels of the second ion-pair cluster. Molecules initially occupying high vibrational levels of the $f(0^+)$ state will be quenched to the foot of the second cluster. At this point, a population build up occurs as further quenching requires large changes in nuclear position and momentum of the molecules.

REFERENCES

1. R.S. Mulliken, J. Chem. Phys., **55**, 288 (1971).
2. R.S. Mulliken, J. Chem. Phys., **55**, 309 (1971).
3. M.A. MacDonald, Ph.D. Thesis, University of Edinburgh, 1984.
4. D.I. Austin, R.J. Donovan, A. Hopkirk, K.P. Lawley, D. Shaw and A.J. Yencha, Chem. Phys., **118**, 91 (1987),
5. M.A. MacDonald, J.P.T. Wilkinson, C. Fotakis, M. Martin and R.J. Donovan, Chem. Phys. Lett., **99**, 250 (1983).
6. T. Moeller, B. Jordan, P. Gurtler, G. Zimmerer, D. Haaks, J. Le Calve and M.C. Castex, "Spectral Line Shapes, Vol. 2," p.597, Edited by K. Burnett, Walter de Gruyter, Berlin, 1983.
7. D.W. Setser, T.D. Dreiling, H.C. Brashears Jr. and J.H. Kolts, Faraday Discuss. Chem. Soc., **67**, 255 (1979).
8. M.F. Golde, J. Mol. Spectros., **58**, 261 (1975).
9. D.I. Austin, Ph.D. Thesis, University of Edinburgh, 1987.
10. J. Tellinghuisen, J. Mol. Spectrosc., **103**, 455 (1984).
11. J. Tellinghuisen, Advances in Chemical Physics LX, "Photodissociation and Photoionization", p.299, Wiley, 1985.
12. S. Gerstenkorn and P. Luc, "Atlas du spectre d'absorption de la molecule d'iode", CNRS, Paris, 1978.
13. J.C.D. Brand, D. Bussieres and A.R. Hoy, Mol. Phys., **53**, 525 (1984).
14. J.C.D. Brand and A.R. Hoy. J. Mol. Spectrosc., **114**, 197 (1985).
15. J.C.D. Brand, A.R. Hoy and S.M. Jaywant, J. Mol. Spectrosc., **106**, 388 (1984).

16. S.G. Hansen, J.D. Thompson, R.A. Kennedy and B.J. Howard, J. Chem. Soc. Faraday Trans., 2, **78**, 1293 (1982).

17. J.C.D. Brand, D. Bussieres, A.R. Hoy and S.M. Jaywant, Can. J. Phys., **62**, 1947 (1984).

18. D. Bussieres and A.R. Hoy, Can. J. Phys., **62**, 1941 (1984).

19. J.A. Coxon and M.A. Wickramaaratchi, J. Mol. Spectrosc., **79**, 380 (1980).

20. R.D. Gordon and K.K. Innes, J. Chem. Phys., **71**, 2824 (1979).

21. S.J. Harris, W.C. Natzle and C.B. Moore, J. Chem. Phys., **70**, 4215 (1979).

22. M.A.A. Clyne and I.S. McDermid, "Electronically Excited States of Small Molecules" in "Dynamics of the Excited State", p. 1, Edited by K.P. Lawley, Wiley, New York, 1982.

23. J.C.D. Brand, D. Bussieres, A.R. Hoy, S.M. Jaywant and D.B. Miller, Opt. Commun., **48**, 195 (1983).

24. J. Chevaleyre, J.P. Perrot, J.M. Chastan, S. Valignat and M. Broyer, Chem. Phys., **67**, 59 (1982).

25. R.J. Donovan, B.V. O'Grady, L. Lain and C. Fotakis, J. Chem. Phys., **78**, 3727 (1983).

26. M. Diegelmann, K. Hohla, F. Rebentrost and K.L. Kompa, J. Chem. Phys., **76**, 1233 (1982).

27. J.D. Spivey, J.G. Ashmore and J. Tellinghuisen, Chem. Phys. Lett., **109**, 456 (1984).

CHAPTER FIVE

LIFETIME STUDIES OF THE E(0^+) ION-PAIR STATE OF ICl

5.1 Introduction

Zero-pressure radiative lifetimes and quenching rate coefficients have been determined for ICl following excitation at wavelengths above 155 nm. Absorption and fluorescence excitation studies show considerable evidence that perturbations, both homogeneous and heterogeneous, occur between the E(0^+) ion-pair state and neighbouring Rydberg states. By examination of the radiative decay parameters it was hoped that further information could be obtained on these interactions.

In conjunction with the fluorescence excitation spectra three excitation wavelengths were chosen for the time-resolved study; 176.0, 173.8 and 163.4 nm. Excitation at 163.4 nm populates the E(0^+) state in the discrete banded region of the fluorescence excitation where a strong E(0^+) - $b_6'(0^+)$ interaction has been proposed. 176.0 nm radiation excites ICl to a heterogeneously perturbed dip-resonance region while the third excitation wavelength, 173.8 nm, populates an intermediate region situated just above the proposed T_e value of the $b_6'(0^+)$ Rydberg state (57,517cm^{-1}).

To determine the zero pressure radiative lifetimes and absolute quenching rates of the initially excited levels by both ICl and Cl_2, the radiative lifetimes were studied as a function of total pressure and of the sample ICl:Cl_2 pressure ratio.

5.2 Experimental

All time-resolved experiments reported in this work were carried out on station FS13.2 with the SRS operating in single bunch mode. In this mode a single bunch of electrons circulates in the ring with a bunch length of 160 ps and an orbital period of 320 ns. An injection current of ~ 15 mA was typical for single bunch operation.

The experimental apparatus was as described in Chapter Two with lifetime data collected on the fluorescence excitation axis, perpendicular to the beam axis, by a Mullard XP2020Q photomultiplier cooled to -20°C. The collection bandpass was limited by a BG1 filter which transmits photons in the 280 - 480 nm range. The photomultiplier signal was sampled using conventional single photon counting techniques. By time-correlating this signal with the excitation pulse over many excitation cycles a radiative decay of the fluorescence signal with time was obtained, as described more fully in the following section.

An excitation bandpass of 1.35 nm was employed in all experiments.

5.3 Time-Correlated Single Photon Counting and Data Analysis

5.3.1 Time Correlated Single Photon Counting

Lifetime measurement by the time-correlated single photon counting technique depends on the concept that the probability distribution for emission of a single photon following an excitation

pulse is the same as the actual intensity versus time distribution of the radiative decay. By detecting single photon events following a large number of excitation pulses this probability distribution can be built-up. The lifetime data presented here was collected by this method and subsequently analysed by Fluorfit, a weighted non-linear least-squares program available at the SRS, Daresbury Laboratory. Fluorfit fits the observed decays to a multiexponential function, allowing for deconvolution of the excitation pulse profiles.

To ensure that only a single photon is emitted per excitation cycle the ratio of number of pulses detected to number of excitation cycles must be maintained below 0.005. If several photons are emitted from one excitation pulse the probability distribution becomes skewed to shorter lifetimes as only the first photon detected contributes to the observed distribution.

Figure 5.1 shows a schematic diagram of the timing apparatus employed on station FS13 to measure the time interval between detection of a single photon and the excitation pulse. After passing through a constant fraction discriminator (CFD) the photomultiplier pulse acts as the start input for a time-to-amplitude converter (TAC), initiating the charging of a capacitor. Arrival of a timing signal from the storage ring, which is correlated with the excitation pulse, stops the charging ramp in the TAC and outputs a pulse whose amplitude is proportional to the time interval between the start and stop pulses. This signal is then processed by a fast analogue-to-digital converter (ADC) and stored in a multichannel analyser (MCA). For the experimental data presented here, the above procedure was repeated until 10,000 counts were accumulated in the initial decay channel. At

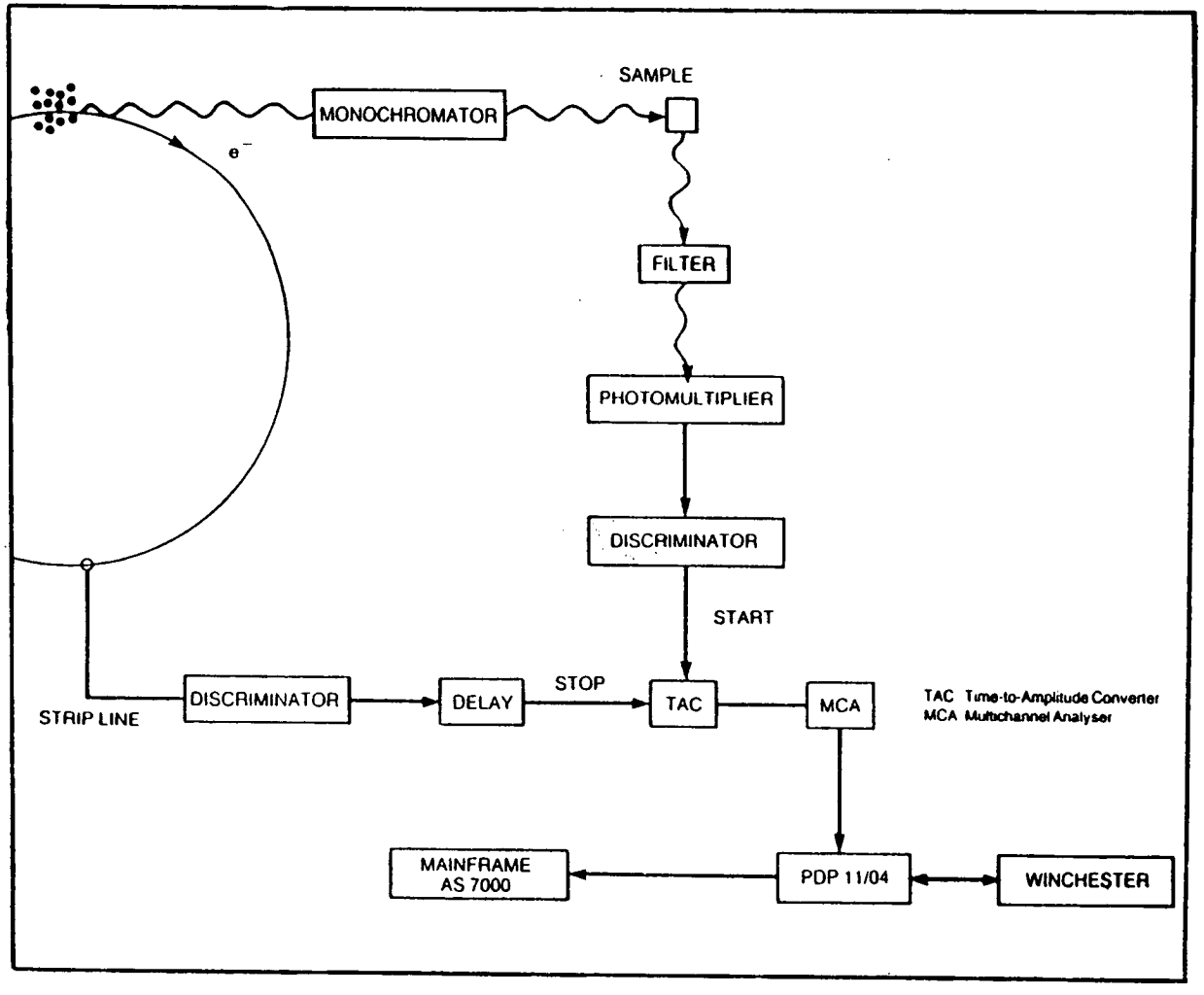

Figure 5.1 – A schematic diagram of the time-correlated single photon counting apparatus employed on station FS13.2 to measure radiative lifetimes.

this point the collected data represents a well defined decay curve. As deconvolution of the pulse profile from the observed decay is necessary, the time profile of the excitation pulse was determined by detecting scattered excitation light (λ = 329 nm) in a similar manner.

The lifetime data was transferred initially to the station PDP11/04 microcomputer and finally on to the NAS (AS7000) mainframe computer for permanent storage and analysis by Fluorfit.

Further information on time-correlated single photon counting can be found in reference 1.

5.3.2 Data Analysis

The lifetime data was fitted by Fluorfit, the non-linear least-squares program mentioned above, to a multiexponential decay function. This yielded the amplitudes and decay constants of the required number of exponentials. In the present data analysis, decay curves were fitted to the least number of exponentials which could adequately describe them.

Problems were encountered on fitting the observed decay around the maximum of the prompt (the excitation pulse profile) for several reasons. Ideally the prompt should be collected at the same wavelength as the fluorescence, ie. around 404 nm for $E(0^+) \rightarrow X(^1\Sigma^+)$ emission, as the temporal response of the photomultiplier is dependent upon the incident wavelength. However, in this study the excitation monochromator (the Seya 0.5 nm) cannot be driven past 330 nm and all excitation pulse profiles were recorded at 329 nm. Secondly, the prompt was obtained from excitation light scattered from the surfaces

of the cell. A more accurate prompt is obtained from a light scatterer which occupies the same volume as that from which fluorescence is observed. These two factors combine to create difficulties in deconvolution of the prompt from the accumulated decay.

Consequently, in this work analysis of the decay curves was begun ten channels after the channel corresonding to the maximum prompt intensity. This method of analysis had little effect on long lifetime components of the decay, ~ 3% change, but did lengthen shorter components considerably, by up to ~ 20%.

5.4 Results

The number of exponentials required to describe the fluorescence decays was found to be a function of excitation wavelength. At 176.0 and 173.8 nm excitation a two exponential fit was sufficient whereas three exponentials were required at 163.4 nm. Typical decays for excitation at the three different wavelengths are shown in Figures 5.2 - 5.4 with the solid line representing the fitted curve and the dotted curves showing the observed fluorescence decays. In each figure the residuals are also displayed and these show that a good fit was achieved over the range specified in the previous section.

As additional Cl_2 was present in all experiments, to suppress I_2 formation, two studies were necessary to separate the ICl and Cl_2 quenching coefficients. Assuming an excited level from which predissociation does not occur, the effective rate constant for loss

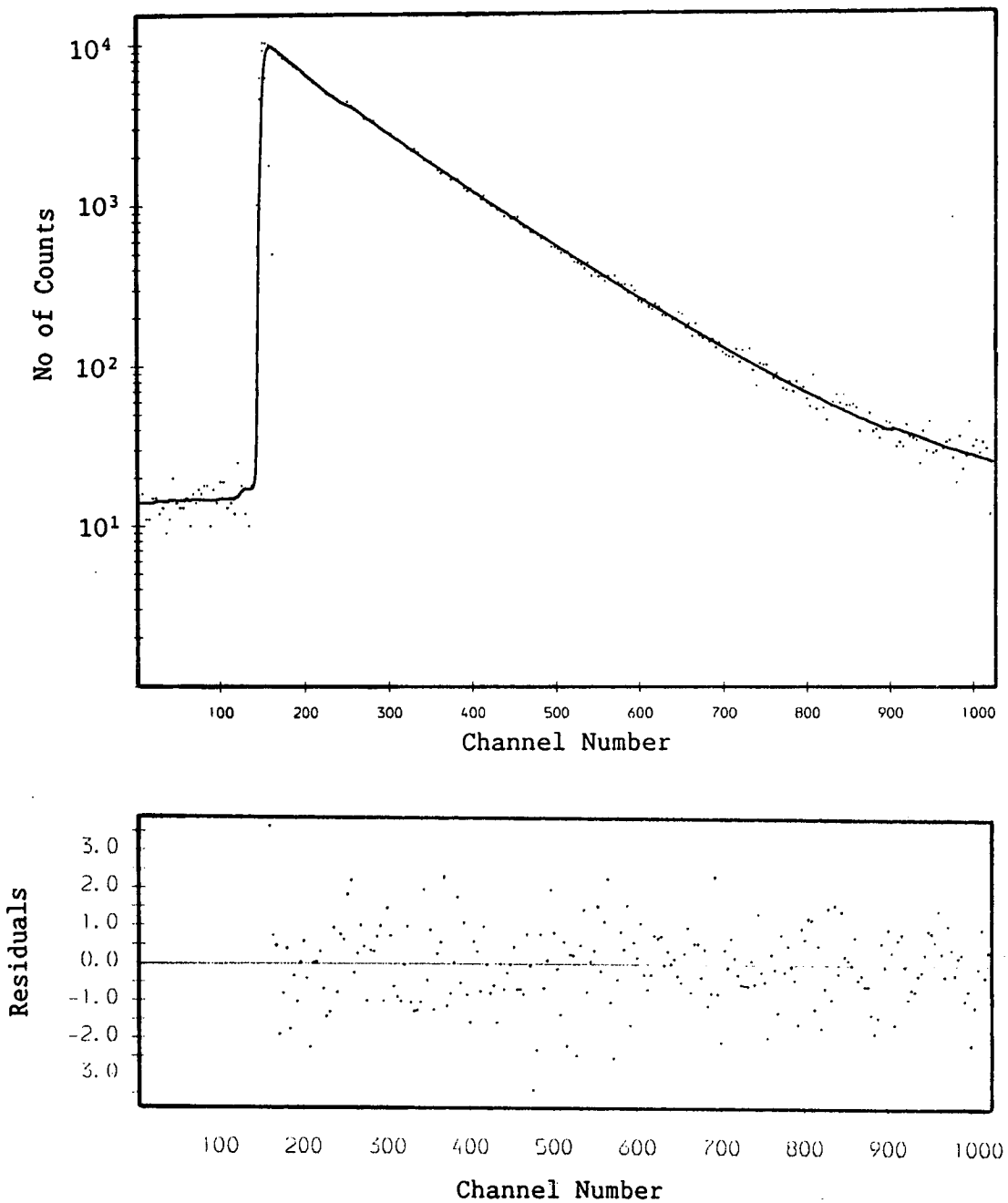

Figure 5.2 - Decay and residuals of ICl fluorescence following excitation at 176.0 nm ($\Delta\lambda$ = 1.35 nm) : the fluorescence decay is fitted to two exponentials. ICl pressure = 344 m Torr, Cl_2 pressure = 688 mTorr, 1 channel = 0.1412 ns.

The subsidiary maxima observed in the decay curves of Figures 5.2-5.4 around channel numbers 270 and 900 are due to an after-pulse from the photomultiplier and a contribution from the booster synchrotron respectively. These maxima also appear in the prompt profile and hence are included in the deconvolution process.

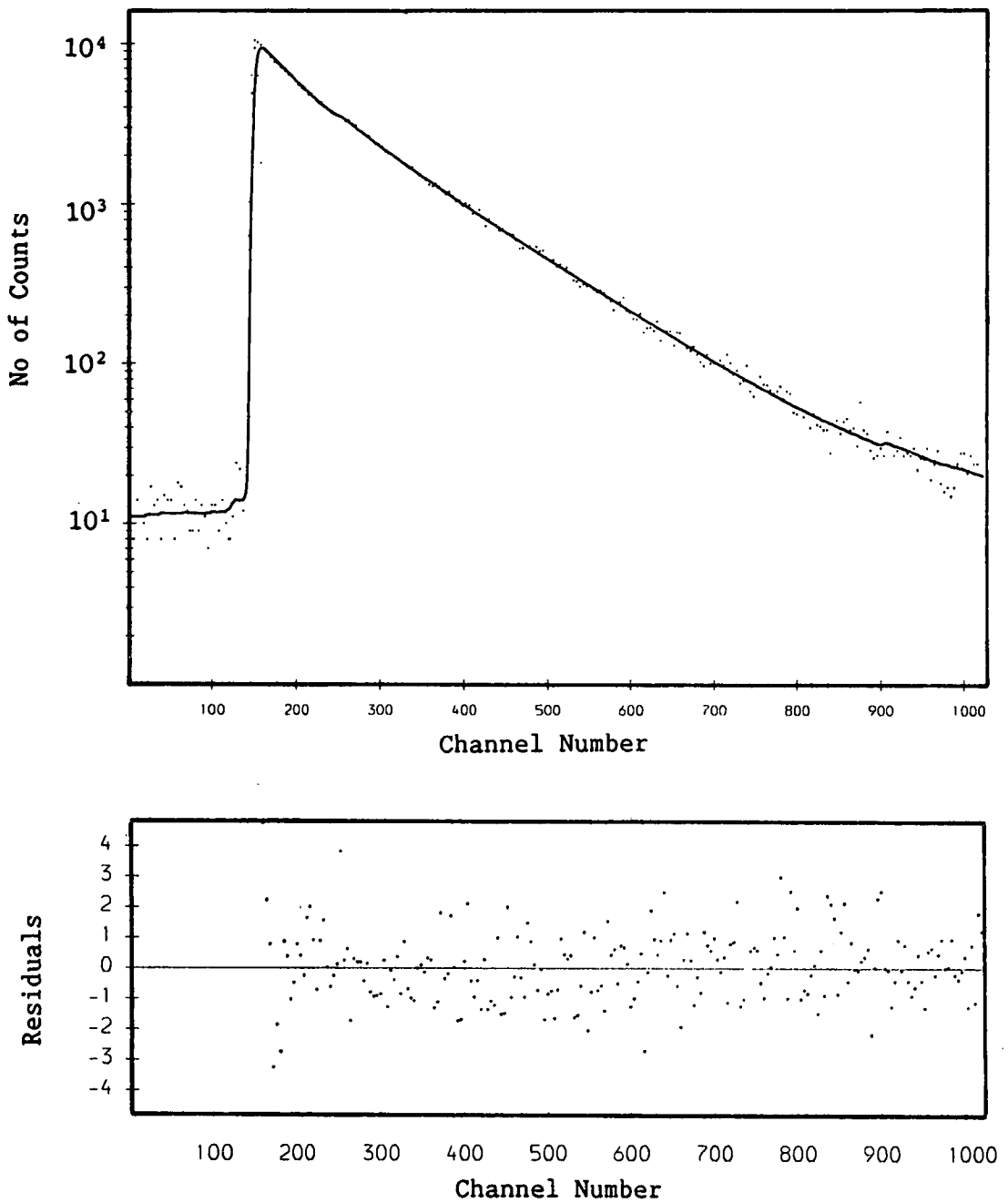

Figure 5.3 - Decay and residues of ICl fluorescence following excitation at 173.8 nm ($\Delta\lambda$ = 1.35 nm) : the fluorescence decay is fitted to two exponentials. ICl pressure = 345 m Torr, Cl_2 pressure = 690 m Torr, 1 channel = 0.1412 ns.

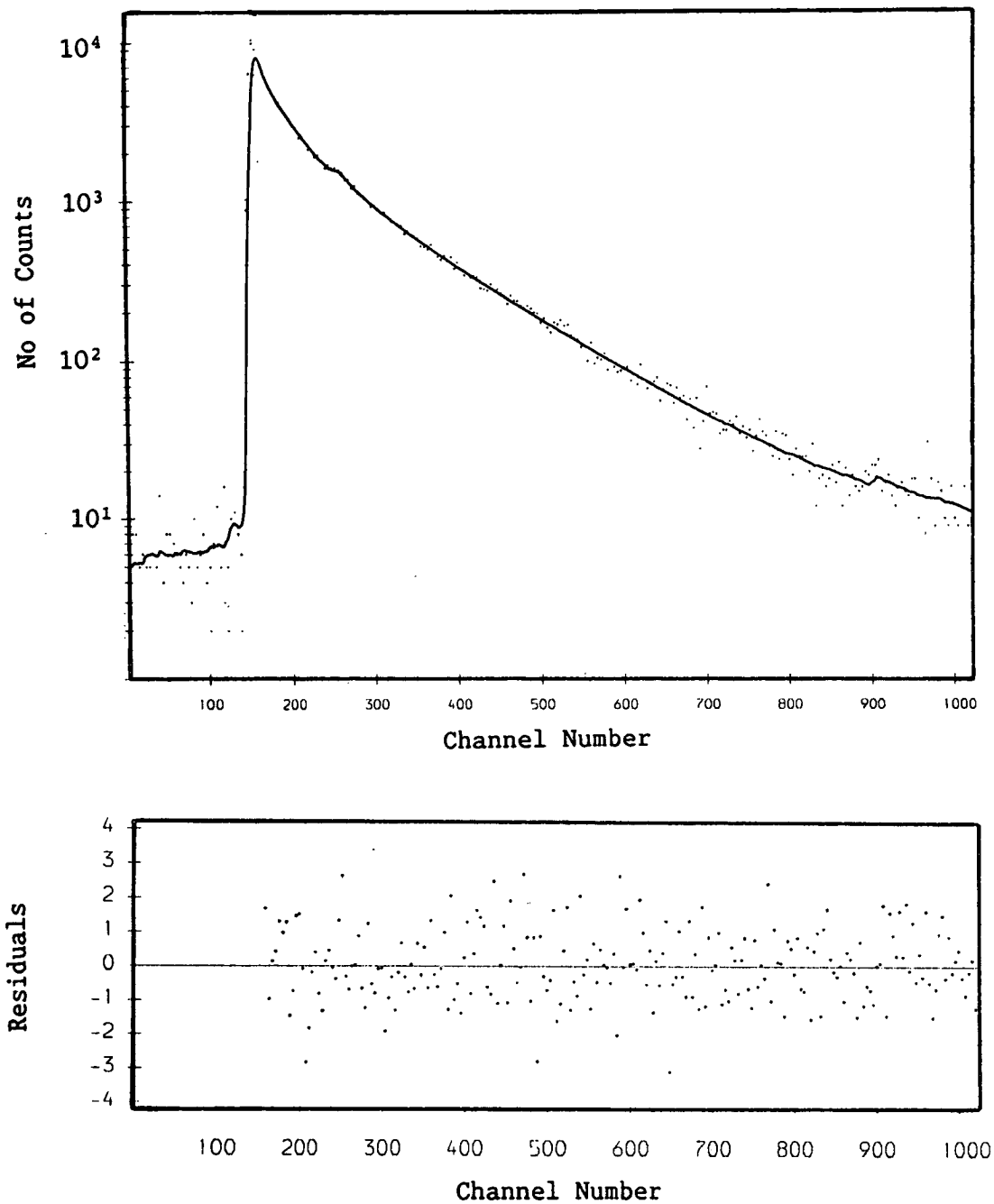

Figure 5.4 - Decay and residuals of ICl fluorescence following excitation at 163.4 nm ($\Delta\lambda$ = 1.35 nm) : the fluorescence decay is fitted to three exponentials. ICl pressure = 347 m Torr, Cl_2 pressure = 694 m Torr, 1 channel = 0.1412 ns.

of initially excited ICl $E(0^+)$ levels, k_{eff}, can be written as:-

$$k_{eff} = k_R + k_{ICl}[ICl] + k_{Cl_2}[Cl_2] \qquad (a)$$

where k_R is the radiative decay coefficient and k_{ICl} and k_{Cl_2} are coefficients for quenching by ICl and Cl_2 respectively. Cl_2 quenching coefficients were determined by measurement of fluorescence lifetimes as a function of Cl_2 pressure, with ICl pressure held constant. The gradients from plots of inverse fluorescence lifetime (k_{eff}) against Cl_2 pressure give k_{Cl_2} directly. ICl quenching rate constants were obtained using the known values of k_{Cl_2} and the gradients of inverse fluorescence lifetime against total pressure plots, where the ICl/Cl_2 sample composition was fixed. Zero pressure radiative lifetimes, $\tau = {}^1/k_R$, were determined by extrapolation to zero pressure of the total pressure variation plots.

Figures 5.5 and 5.6 show the dependence of the inverse long lifetime components upon total pressure and Cl_2 pressure respectively. Good agreement with expression (a) was observed over the entire experimental pressure range in both cases. The pressure dependences of the inverse short lifetime components for the two quenching experiments are shown in Figures 5.7 and 5.8. At higher sample pressures the shorter-lifetime plots deviate from the straight-line fits predicted by expression (a) and only the portion of the data used to calculate the quenching coefficients and zero-pressure radiative lifetimes is displayed. Such deviation is due to the shorter lifetime components becoming less well-defined at higher pressures and more difficult to separate from scattered light

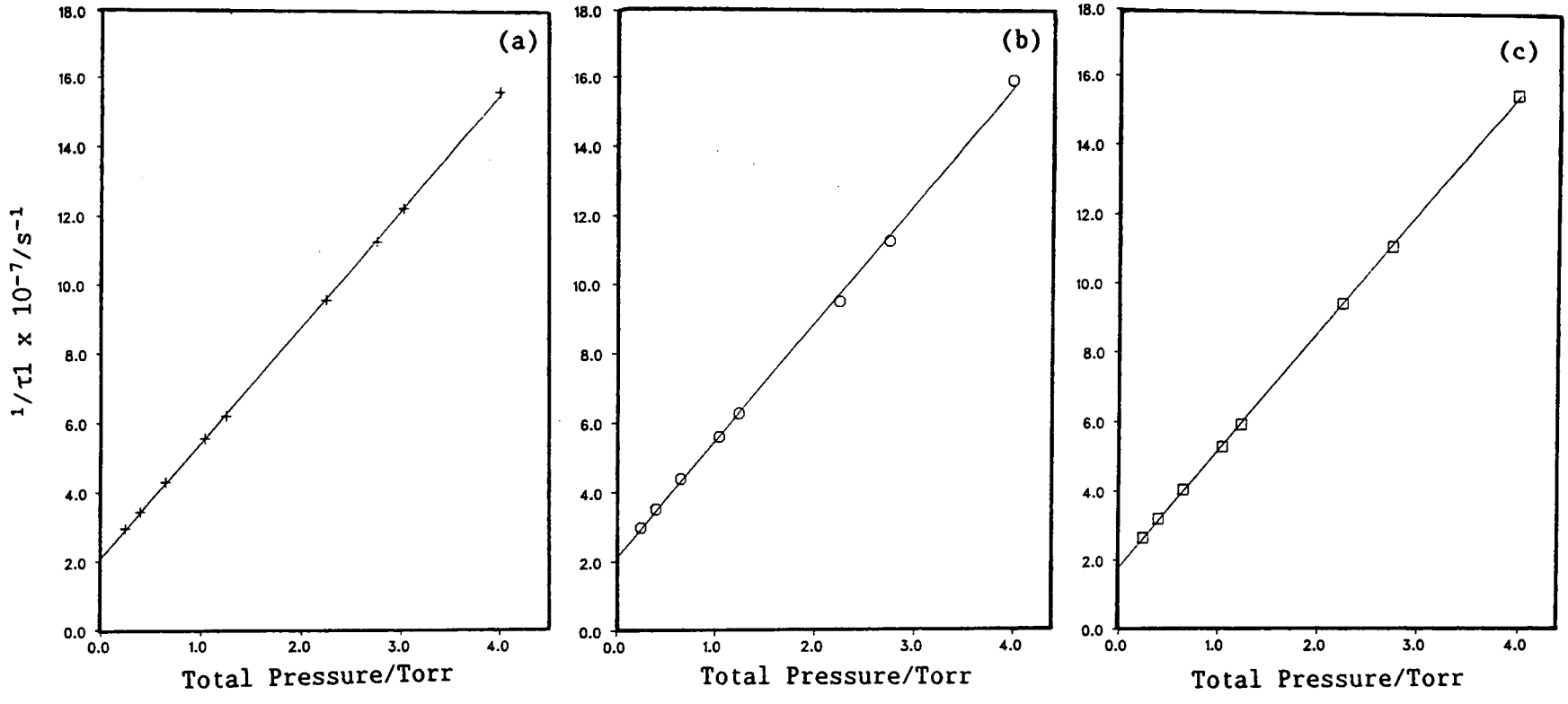

Figure 5.5 - Plots of the inverse long lifetimes ($^1/\tau 1$) versus total pressure for ICl excited at (a) 176.0 nm (b) 173.8 nm and (c) 163.4 nm ($\Delta\lambda$ = 1.35 nm). Ratio of ICl pressure to Cl_2 pressure is 1:2 throughout.

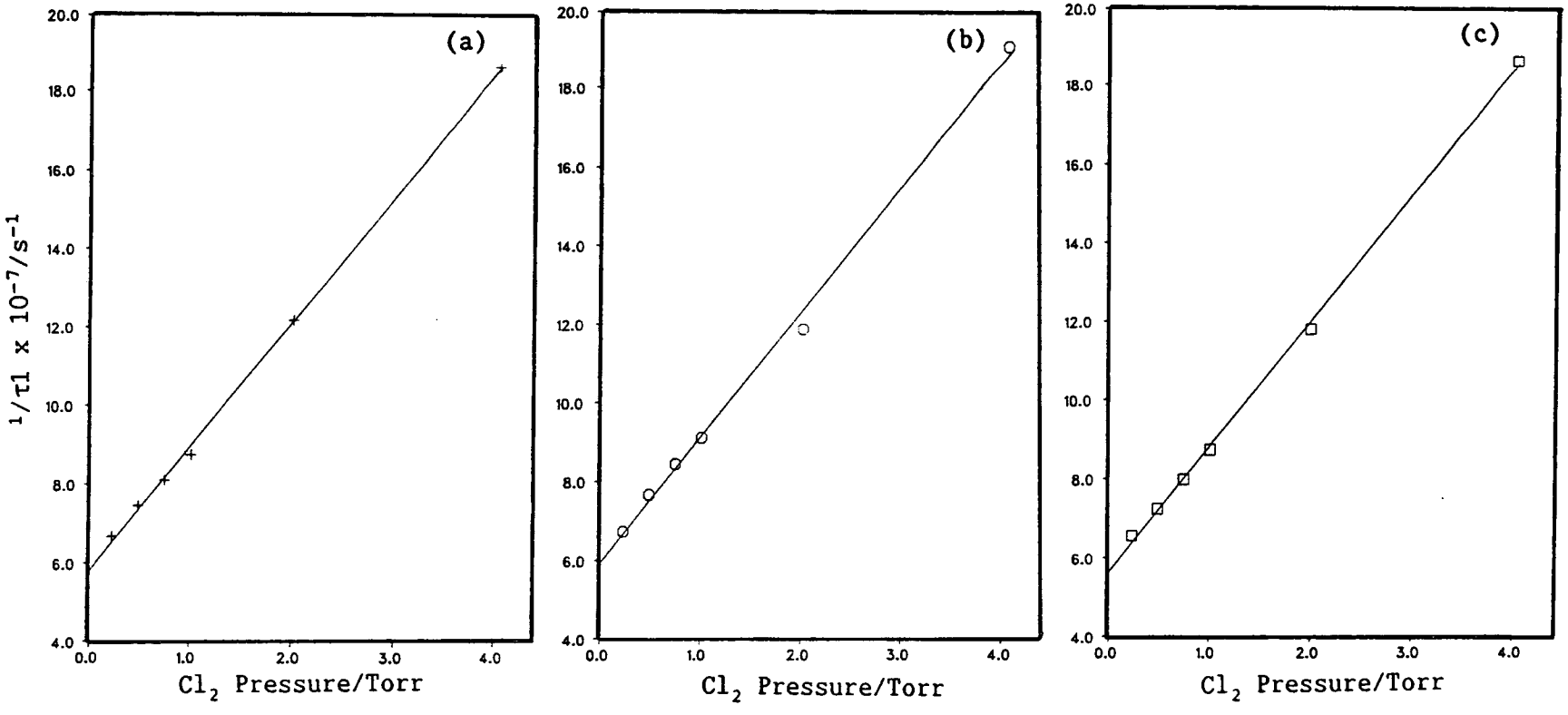

Figure 5.6 - Plots of the inverse long lifetimes ($^1/\tau 1$) versus Cl_2 pressure for ICl excited at (a) 176.0 nm (b) 173.8 nm and (c) 163.4 nm ($\Delta\lambda$ = 1.35 nm). The partial pressure of ICl was held constant throughout at 1.0 Torr.

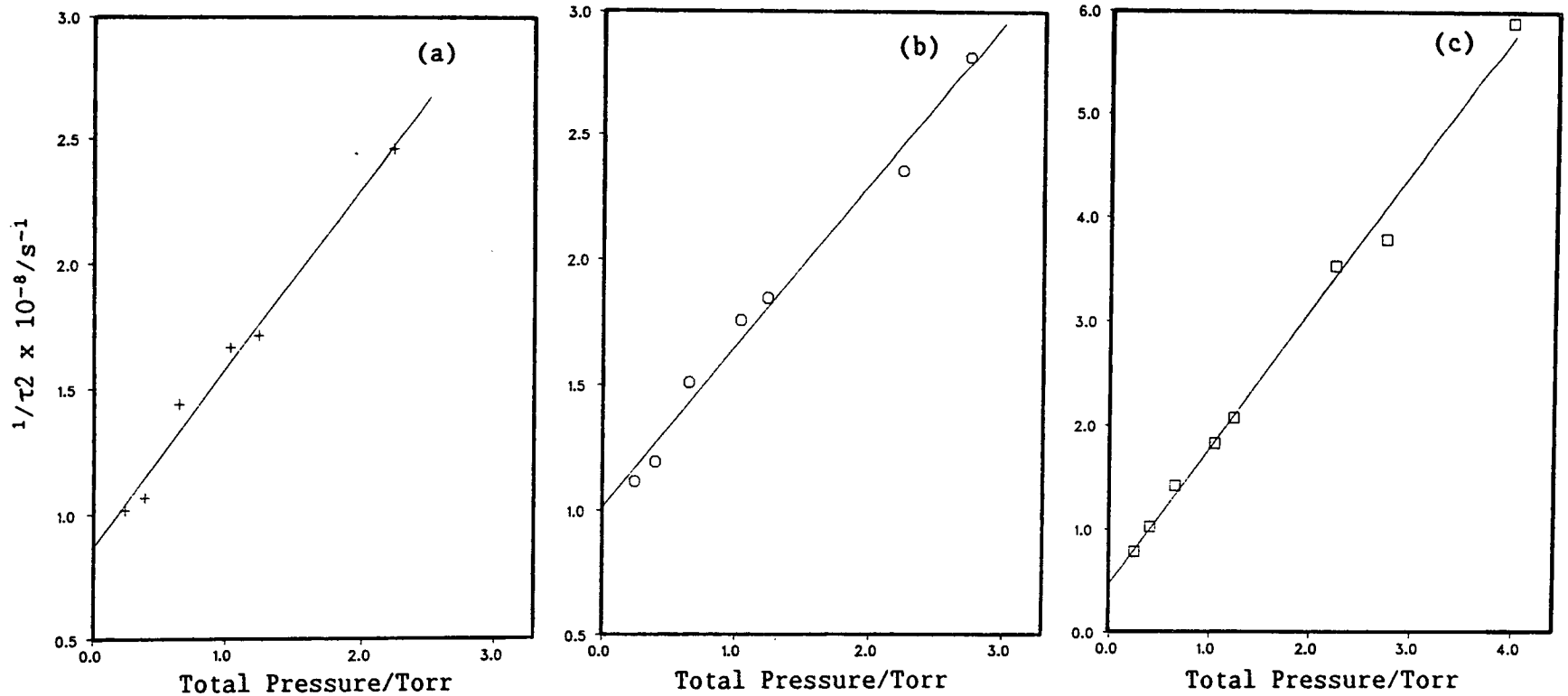

Figure 5.7 - Plots of the inverse short lifetimes ($^1/\tau 2$) versus total pressure for ICl excited at (a) 176.0 nm (b) 173.8 nm and (c) 163.4 nm ($\Delta\lambda$ = 1.35 nm). Ratio of ICl pressure to Cl_2 pressure is 1:2 throughout.

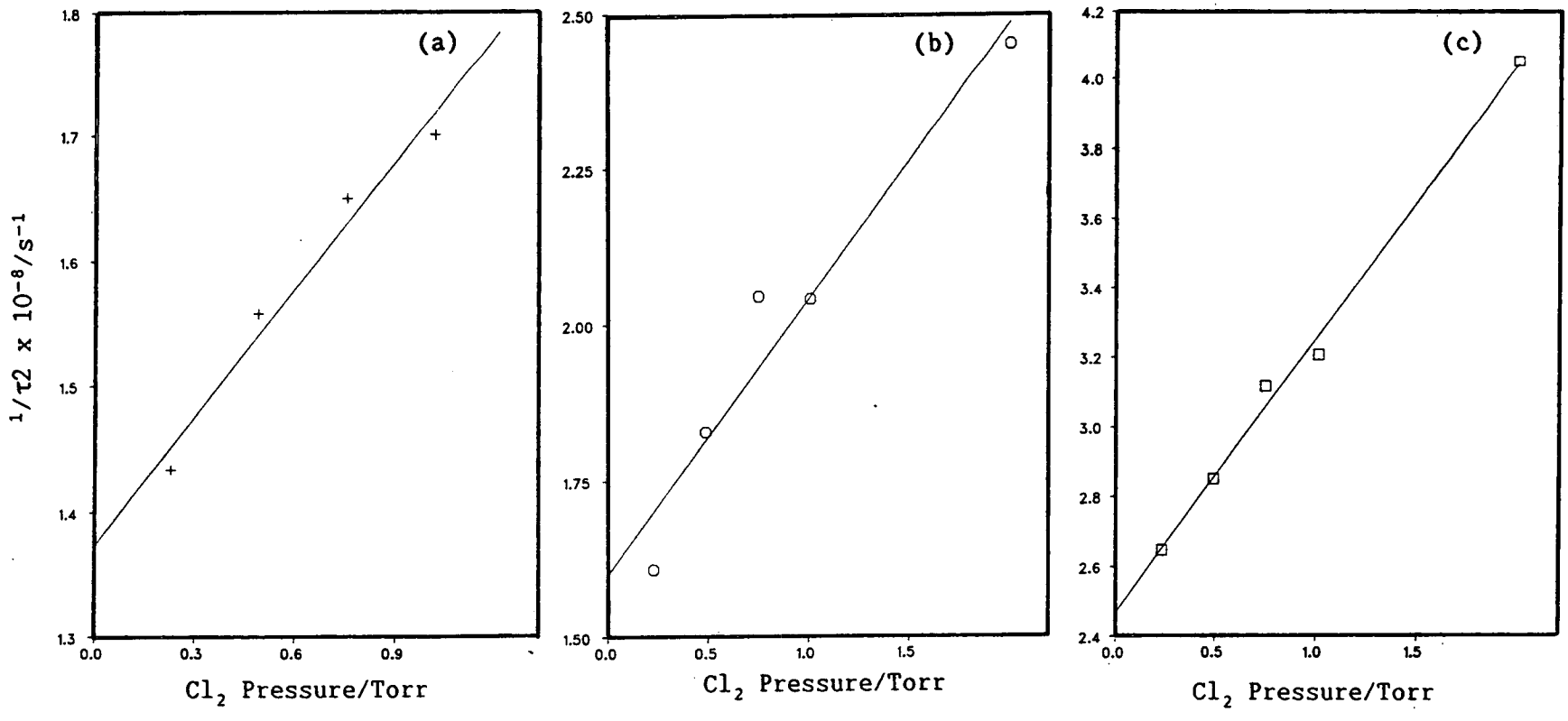

Figure 5.8 - Plots of the inverse short lifetimes ($^1/\tau 2$) versus Cl_2 pressure for ICl excited at (a) 176.0 nm (b) 173.8 nm and (c) 163.4 nm ($\Delta\lambda$ = 1.35 nm). The partial pressure of ICl was held constant throughout at 1.0 Torr.

components around the prompt maximum. The errors involved in the shorter lifetime quenching data are greater than those associated with the long lifetime components and the absolute values given must be treated with caution.

Finally, consider the third and shortest lifetime component observed following excitation at 163.4 nm. This component was found to be short-lived with a magnitude extremely dependent on the channel number at which analysis was begun. Thus, in the results presented here only an upper limit for the zero-pressure radiative lifetime is given. Although short-lived, the third component in the 163.4 nm radiative decays is a necessary and real component as good fits to the observed decays cannot be achieved with a two exponential model.

In Table 5.1 the zero-pressure lifetimes and total pressure quenching coefficients are given for all components of the radiative decays at the three excitation wavelengths. ICl and Cl_2 quenching coefficients are presented in Table 5.2.

TABLE 5.1

LIFETIME AND TOTAL PRESSURE QUENCHING DATA

Excitation Wavelength/nm	τ	τ_o/ns	10^9 k_{TOT}/cm^{3}molecule^{-1}s^{-1}
176.0	τ_1	47.8 ± 7.2	1.01 ± 0.15
173.8	τ_1	47.9 ± 7.2	1.02 ± 0.15
163.4	τ_1	56.3 ± 8.4	1.02 ± 0.15
176.0	τ_2	11.6 ± 2.3	2.16 ± 0.43
173.8	τ_2	9.9 ± 2.0	1.94 ± 0.39
163.4	τ_2	21.0 ± 4.2	3.96 ± 0.79
163.4	τ_3	< 6.0	-

Errors quoted are 1 stand. dev. plus an estimated systematic error to account for method of analysis etc.

TABLE 5.2

ICl AND Cl_2 QUENCHING COEFFICIENTS

Excitation Wavelength/nm	τ	10^9 k_{ICl}/$cm^3 molecule^{-1} s^{-1}$	k_{Cl_2}/$cm^3 molecule^{-1} s^{-1}$
176.0	$\tau 1$	1.12 ± 0.17	(9.51 ± 1.43) x 10^{-10}
173.8	$\tau 1$	1.14 ± 0.17	(9.63 ± 1.44) x 10^{-10}
163.4	$\tau 1$	1.15 ± 0.17	(9.59 ± 1.44) x 10^{-10}
176.0	$\tau 2$	4.42 ± 0.88	(1.03 ± 0.21) x 10^{-9}
173.8	$\tau 2$	3.16 ± 0.63	(1.33 ± 0.27) x 10^{-9}
163.4	$\tau 2$	7.14 ± 1.43	(2.37 ± 0.47) x 10^{-9}

The relative importance of the two lifetimes at 176.0 and 173.8 nm and the two longer lifetimes at 163.4 nm can be gauged by the ratio of the amplitudes (A) of the two components, $A_{\tau 1}/A_{\tau 2}$. The values of this ratio at high and low pressure are listed for the three excitation wavelengths in Table 5.3.

TABLE 5.3

VARIATION OF AMPLITUDE RATIO, $A_{\tau 1}/A_{\tau 2}$, WITH EXCITATION WAVELENGTH AND PRESSURE

Excitation Wavelength/nm	Total Pressure/Torr	$A_{\tau 1}/A_{\tau 2}$
176.0	0.242	1.57
	2.23	3.46
173.8	0.244	1.04
	0.74	2.03
163.4	0.246	0.32
	2.74	0.63

5.5 Discussion

From the multiexponential fits required to describe the radiative decays of ICl following excitation at wavelengths above 155 nm

it is clear that fluorescence does not originate from a single unperturbed ion-pair state. Two lifetimes are indicative of fluorescence from at least two states while a three exponential fit can conceal a large number of underlying decays[2]. To interpret the time-resolved results consideration must be made of the states which can be populated, either by direct absorption or collision, and the interactions which these states undergo.

Consider the lifetime data recorded at 176.0 nm. The long lifetime component ($\tau 1$) of the radiative decay has been assigned to fluorescence from relatively unperturbed levels of the $E(0^+)$ state. The zero-pressure radiative lifetime and quenching coefficients of this component are typical of an ion-pair state from the first cluster; compare with the radiative lifetime of 27 $\pm$ 3 ns for the analogous state of IBr [3]. From dispersed fluorescence at this excitation wavelength it is known that $E(0^+) \rightarrow X(^1\Sigma^+)$ fluorescence is the main emission system lying within the 280 - 480 nm filter bandpass.

Assignment of the second lifetime component ($\tau 2$) is more complex. The excitation bandwidth of 1.35 nm (FWHM) corresponds to ~ 440 cm^{-1} at 176.0 nm excitation, populating at least eight vibrational levels. These levels lie within the region where the $E(0^+)$ state is heterogeneously perturbed by the a_6 (1) Rydberg state leading to the opening of predissociative pathways at positions of higher a_6 (1) vibrational levels. Such levels, situated in the dips of the fluorescence excitation spectrum, will possess shorter lifetimes than the relatively unperturbed $E(0^+)$ levels to which the longer lifetime

component has been assigned. The second, shorter lifetime ($\tau 2$) is therefore attributed to $E(0^+)$ vibrational levels which undergo non-radiative decay.

Caution must be applied when considering absolute values of lifetimes and quenching coefficients obtained following two or more exponential fits. James et al [2] have shown that distributions of more than seven lifetimes can be successfully fit to a two exponential decay law with good fit statistics and randomly scattered residuals. In the present work, considering the number of vibrational levels populated and the change in lifetime on passing from peak to trough in the fluorescence excitation, it is probable that the two exponential fit conceals an underlying range of lifetimes.

Excitation at 173.8 nm produces very similar results to those observed at 176.0 nm. Again a two exponential fit is required with resultant zero-pressure fluorescence lifetimes and quenching constants almost identical to the 176.0 nm parameters.

Turning to 163.4 nm excitation a very different picture emerges. Excitation at this wavelength populates the region of strong, homogeneous interaction between the $E(0^+)$ ion-pair state and the $b_6'(0^+)$ Rydberg state. The differences between the radiative decays following excitation to heterogeneously and homogeneously perturbed portions of the $E(0^+)$ state are immediately obvious on comparison of Figures 5.2 and 5.4 for excitation at 176.0 and 163.4 nm respectively.

At 163.4 nm three exponentials are required to adequately describe the radiative decays. The long lifetime component ($\tau 1$) is comparable to those observed following 176.0 and 173.8 nm excitation, both in terms of zero-pressure radiative lifetimes and quenching coefficients. Consequently this component is assigned as that which describes fluorescence from relatively unperturbed $E(0^+)$ ion-pair levels, ie. from maxima in the fluorescence excitation.

The radiative decay parameters of the intermediate lifetime component ($\tau 2$) are approximately double the corresponding values found for excitation at higher wavelengths. Even so, the $\tau 2$ component at 163.4 nm may still be analogous to the $\tau 2$ components at 173.8 and 176.0 nm. Correlation between the 163.4 nm $\tau 2$ and $\tau 3$ components could easily exist leading to lengthening of the longer-lived component. However, it is not known whether the heterogeneous perturbation between the a_6 (1) and $E(0^+)$ states could realistically be expected to extend as far blue as 163.4 nm. This $\tau 2$ component could also be due to heterogeneous coupling between the $b_6(1)$ and $E(0^+)$ states. No such coupling has been inferred from the observed absorption and fluorescence excitation spectra but it may well be obscured by the strong $E(0^+)$ - $b_6'(0^+)$ interaction.

The third and shortest lifetime component ($\tau 3$) is not observed at other excitation wavelengths suggesting that this component arises as a consequence of the homogeneous coupling between the $E(0^+)$ and $b_6'(0^+)$ states. In the region around 163.4 nm fluorescence is only observed when strong coupling between the two (0^+) states does not occur. The homogeneous interaction leads to a strong predissociative channel opening at positions where the $E(0^+)$ ion-pair and $b_6'(0^+)$ levels come

into resonance, an interaction so strong that the fluorescence quantum yield drops close to zero. The third lifetime component is therefore attributed to fluorescence from vibrational levels which are found in the valleys of the fluorescence excitation spectrum.

Again the absolute values of lifetimes and quenching coefficients must be treated with caution. Moreso in this case, as a three exponential model is required to fit the experimental decays.

The long lifetime component ($\tau 1$) observed following excitation at all three wavelengths has been assigned to fluorescence from mainly unperturbed $E(0^+)$ ion-pair levels. The short lifetime components ($\tau 2$) at 176.0 and 173.8 nm are very similar and indicate the opening of non-radiative pathways through a heterogeneous coupling mechanism. Although excitation at 173.8 nm populates vibrational levels above the proposed T_e value of the $b_6'(0^+)$ state the homogeneous coupling is not strong at this point and no sign of $E(0^+)$ - $b_6'(0^+)$ interaction is observed in the radiative decays. At 163.4 nm the situation is more complex with three component decays observed, illustrating the heavy perturbation of the $E(0^+)$ state in this region. The physical significance of the two shorter components ($\tau 2$ and $\tau 3$) is not clear although it is likely that the $\tau 3$ component represents fluorescence from levels which have a strong, homogeneous predissociation pathway. Due to the multi-exponential fits the absolute values of the radiative decay parameters should be regarded cautiously. However, there is no ambiguity in the number of exponentials required to fit the experimental data or the dependence of this parameter on excitation wavelength.

Before the above conclusions were reached several other candidates for the emitting levels of the shorter lifetime components were eliminated. From Figure 4.3 which shows ICl dispersed fluorescence following excitation at 176.0 nm and 164.0 nm, it is noted that the $f(0^+) \rightarrow X(^1\Sigma^+)$ system at 325 nm also lies within the collection filter bandpass. However, on consideration of the data given in Table 5.3, which compares the relative amplitudes of $\tau 1$ and $\tau 2$ as a function of excitation wavelength and pressure, the $\tau 2$ lifetime components could not be attributed to $f(0^+)$ state fluorescence. Figure 4.3 shows that the ratio of $E(0^+) \rightarrow X(^1\Sigma^+)$ to $f(0^+) \rightarrow X(^1\Sigma^+)$ fluorescence is basically independent of excitation wavelength. However, Table 5.3 shows that $A_{\tau 1} : A_{\tau 2}$ decreases markedly as the excitation wavelength moves to the blue, the shorter lifetime component becoming dominant. Since the $f(0^+) \rightarrow X(^1\Sigma^+)$ fluorescence system does <u>not</u> become stronger to shorter wavelengths the $\tau 2$ component is not assigned to $f(0^+)$ fluorescence. The $f(0^+) \rightarrow X(^1\Sigma^+)$ system only contributes about 5% to the total emission (see Figure 4.3) and makes no noticeable contribution to the fluorescence decays.

Another possible upper state for the $\tau 2$ decay component was the D'(2) ion-pair state which, as discussed in Chapter 4, becomes collisionally populated at higher pressure. However, as the $A_{\tau 1}/A_{\tau 2}$ ratio increases with sample pressure this possibility was discounted.

The multi-exponential decays necessary to fit the experimental data can only be rationalised in terms of fluorescence from $E(0^+)$ vibrational levels which undergo differing degrees and types of perturbation. The lifetime data presented here again illustrates the

interactions which occur between the $E(0^+)$ and a_6 (1), $b_6'(0^+)$ states first deduced from the absorption and fluorescence excitation spectra.

The quenching constants for self and Cl_2 quenching of the $\tau 1$ components are very large and are comparable with the analogous constants of IBr [3]. From these coefficients it appears that the excited ICl molecules are quenched at greater than unit collision frequency. This illustrates once again the width of the ion-pair potentials and their diffuse outer electron structure.

REFERENCES

1. D.V. O'Connor and D. Phillips, "Time-Correlated Single Photon Counting", Academic Press, London, 1984.

2. D.R. James and W.R. Ware, Chem. Phys. Lett., 120, 455 (1985).

3. R.J. Donovan, G. Gilbert, M. MacDonald, J.P.T. Wilkinson, I. Munro and D. Shaw, J. Photochem, 31, 1 (1985).

CHAPTER SIX

REACTIVE AND QUENCHING PATHWAYS OF ICl/Cl_2/RARE GAS MIXTURES FOLLOWING EXCITATION IN THE 130 - 195 nm RANGE

6.1 Introduction

Rare-gas halide excimers are a species of particular interest as lasing occurs on the $B(^1/_2) \rightarrow X(^1/_2)$ transition of many excimers forming the basis of operation for a range of commercially available lasers [1]. Excimer formation has been studied extensively by the reaction of electronically excited rare gas atoms and halogen containing molecules [2 - 5], ie:-

$$Rg^* + RX \rightarrow RgX^* + R + \Delta E,$$

and to a lesser extent by excitation of an XY component:-

$$XY^* + Rg \begin{cases} \rightarrow RgX^* + Y + \Delta E \\ \rightarrow RgY^* + X + \Delta E \end{cases}$$

where XY is a diatomic halogen or interhalogen molecule [6 - 10]. The latter method has the advantage of choice of many vibrationally and electronically excited levels, as opposed to the few atomic Rydberg states available. Depending on the location of the molecular excited states, thresholds for formation of RgX^* can be determined for comparison with thermodynamic thresholds. Synchrotron radiation studies are particularly useful as XY excitation over a broad energy range is easily achieved.

Formation of rare-gas halide excimers occurs by the harpoon mechanism with an electron transferring from rare gas atom to XY molecule and reaction proceeding via a Rg^+ --- XY^- ion-pair surface. The harpoon mechanism was first proposed to describe the main features of alkali metal - halogen reactions with electron transfer from an alkali metal of low ionisation potential to a halogen molecule of high electron affinity [11]: for example, Cs (IP = 3.833 eV) + Cl_2 (EA = 2.50 eV) → CsCl [12, 13]. Rg^* --- XY systems are often considered analogous, as a rare gas atom in its first Rydberg state has the same outer electron configuration and similar ionisation potential as an alkali metal atom : consider the similarities between Xe^* ($^3P_1$) ($5p^56s$, IP = 3.690 eV) and Cs ($5p^66s$, IP = 3.893 eV) [12]. As stated above, much effort has been concentrated in this direction. However, the reaction can proceed equally well by increasing the electron affinity of the electron accepter - the net result of electronic excitation of the XY molecule.

In this work photoexcitation of $ICl/Cl_2/Xe$ mixtures in the 130 - 195 nm range was studied, approaching the ICl + Xe reaction from the molecular excitation angle. Over such a broad energy range excitation occurs to many electronic states although the emphasis is here placed on reaction of ion-pair states above 155 nm. As excitation to the Xe($^3P_1$, 6s) state is observed at 147.0 nm [12] the two reaction pathways, atomic and molecular excitation, were observed. Photoexcitation of $ICl/Cl_2/Kr$ mixtures was also investigated.

The reaction and/or quenching of ICl^* with Xe and Kr was monitored by:-

(i) Dispersing fluorescence in the VUV - UV/VIS regions.

(ii) Collecting fluorescence excitation spectra of the relevant emission systems.

Finally, consider the parallels between RgX^* excimer states and halogen/interhalogen ion-pair states. Three RgX valence states correlate diabatically with ground state halogen and rare gas atoms : the $A(^3/_2)$, $A(^1/_2)$ and $X(^1/_2)$ states. These are repulsive with the exception of the $X(^1/_2)$ state which has a shallow minimum. By contrast, the RgX^* excimer states are all deeply bound and correlate with Rg^+ and X^- ions. These states are typical ion-pair states ie. they are deep, broad, lie at large r_e and cluster together dependent on their asymptotic dissociation limits. The lowest bound excited states, the $B(^1/_2)$ and $C(^3/_2)$ excimer states, lie at approximately the same energy whilst the $D(^1/_2)$ RgX^* state is situated at higher energies. Hay and Dunning [14] have calculated the potential curves for the XeX family, including the XeCl and XeI potentials of interest in this work.

Since the RgX ionic states are deeply bound and the valence states mainly repulsive, bound-free oscillatory continua between the two types of state are observed with lasing action occurring on the $B(^1/_2) \rightarrow X(^1/_2)$ transition.

6.2 Experimental

All ICl - rare gas studies reported here were carried out on station FS13. Dispersed fluorescence spectra were recorded simultaneously on the Acton and Minimate monochromators covering the VUV through UV to visible spectral regions. The fluorescence was detected by an EMI 9883QKA photomultiplier tube in the UV/VIS region and by an EMI G26K314LF tube in the vacuum ultraviolet.

Fluorescence excitation spectra of various emission systems were detected either by a filter-photomultiplier or monochromator-photomultiplier combination, dependent on filter availability. An EMI 9883QKA photomultiplier was employed in all fluorescence excitation experiments.

Three interference filters were used in the course of this work. To detect XeCl $B(^1/_2) \rightarrow X(^1/_2)$ emission, XeI $B(^1/_2) \rightarrow X(^1/_2)$ emission and ICl $D'(2) \rightarrow A'(2)$ fluorescence, filters with peak transmission at 309.4 nm, 254.6 nm and 430.5 nm respectively were employed. Information on the filter bandwidths (FWHM) and peak transmission percentages is given in Table 6.1 while the bandpass of monochromator selected wavelengths is noted alongside the relevant spectra. As the transmission efficiency of a filter is much greater than that of a monochromator, higher resolution fluorescence excitation spectra were obtained for filter-detected transitions.

Table 6.1

Filter Characteristics

Peak Wavelength/nm	FWHM/nm	% Peak Transmission
309.4	12.0	20
254.6	8.1	10
430.5	7.0	57

A full account of the experimental apparatus is given in Chapter Two while further details concerning the collection of dispersed fluorescence can be found in Chapter Four. All dispersed fluorescence spectra are corrected for the relevant response functions unless otherwise stated.

6.3 Reaction of Xe with the ICl Ion-Pair States

The calculated thermodynamic thresholds for formation of XeI and XeCl $B(^1/_2)$ states show that it is energetically feasible for both excimers to be formed by reaction of Xe with the ICl ion-pair states populated by single photon absorption. From the known dissociation energy of ICl (17,366 cm^{-1} [15]) and the zero-point energies of the XeX $B(^1/_2)$ states [4, 16], the formation thresholds for XeI and XeCl $B(^1/_2)$:-

$$E_{thres} = D_o°(ICl) + E(XeX\ B(^1/_2)\ v' = 0),$$

were evaluated as 174.4 nm and 200.5 nm respectively. All ion-pair levels excited in the 158 - 195 nm region possess sufficient energy to react with Xe and form $XeCl^*$ while the area round the XeI^* threshold can be studied.

Figure 6.1 shows the XeCl $B(^1/_2) \rightarrow X(^1/_2)$ excitation function and a typical fluorescence excitation spectrum of ICl UV/VIS fluorescence. Above 158 nm the $XeCl^*$ excitation function closely follows that of the ICl emission whereas at wavelengths less than 158 nm the two spectra differ markedly. In previous chapters it has

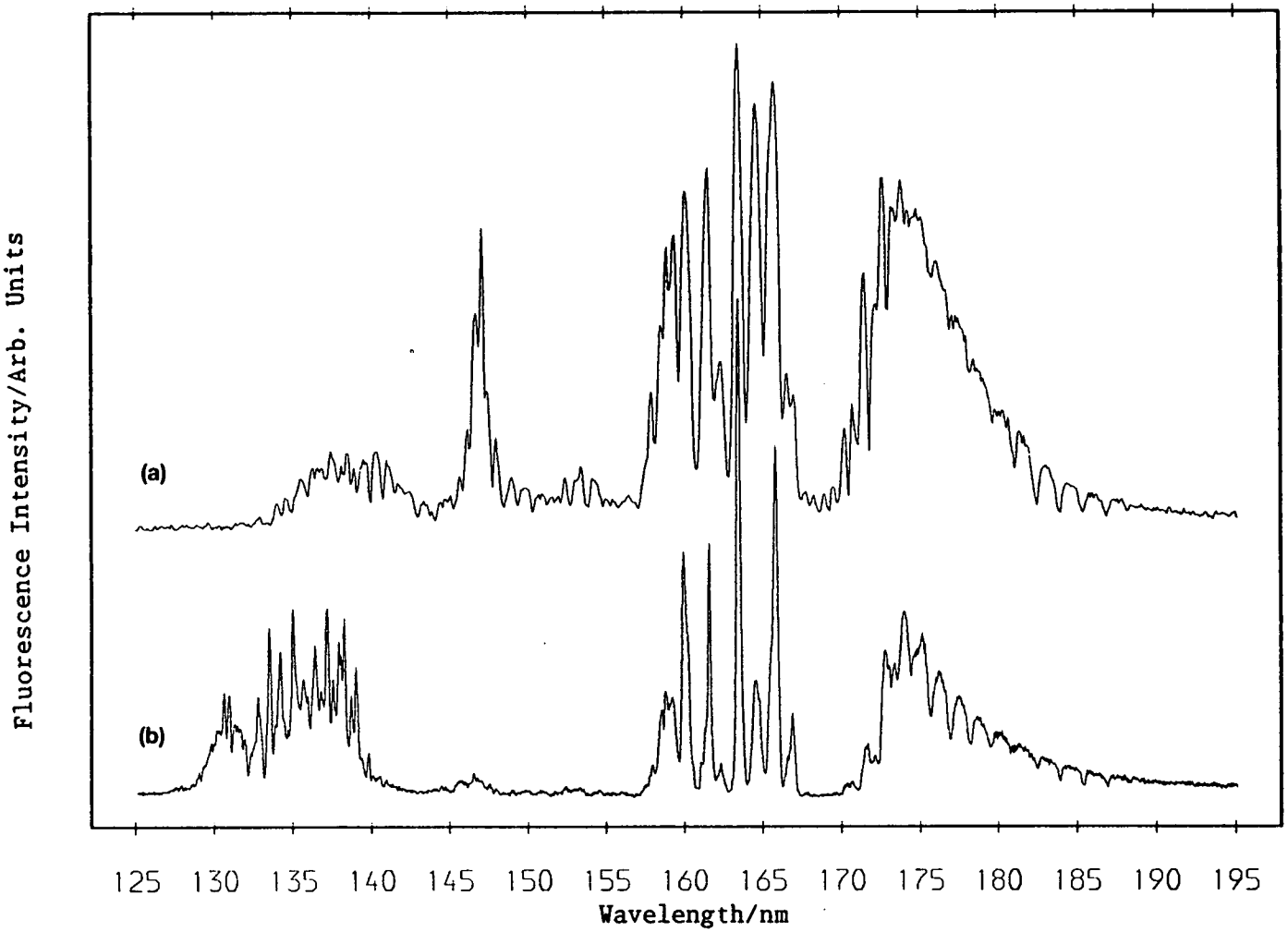

Figure 6.1 - (a) XeCl $B(^1/_2) \rightarrow X(^1/_2)$ excitation function (detected by a 309.4 nm interference filter). $\Delta\lambda$ = 0.2 nm, ICl pressure = 0.86 Torr, Cl_2 pressure = 1.72 Torr, Xe pressure = 25.7 Torr. (b) ICl and Cl_2 fluorescence excitation spectrum. $\Delta\lambda$ = 0.1 nm, ICl pressure = 45 mTorr, Cl_2 pressure = 90 mTorr.

been shown that for λ_{exc} > 158 nm both ion-pair and Rydberg states are populated while shorter wavelength excitation occurs mainly to Rydberg states. Attention is here focussed on the ICl ion-pair - Xe reaction. Analysis of the ICl* - Xe reaction to shorter wavelengths is complicated by the presence of other excited species, such as Xe* and Cl_2*, and will only be considered briefly.

From Figure 6.1 it is clear that, above 158 nm, the reaction ICl* + Xe → XeCl B($^1/_2$) + I proceeds via the ICl ion-pair states.* Reaction with Rydberg states does not occur, as is evident from the minima observed at positions of the $a_6(1)$ and $b_6(1)$ absorption bands. All structure in the ICl* fluorescence excitation spectrum above 158 nm is mirrored by the XeCl* excitation function, except in the 174 - 180 nm region. Here the dip-resonances of the XeCl* spectrum are less pronounced. This effect is a physical one and is the same as that observed for quenching of the ICl E(0^+) state by N_2, discussed in Section 3.9. All ion-pair states populated in the 158 - 195 nm region lie above the thermodynamic limit of 200.5 nm for XeCl B($^1/_2$) formation and threshold for this reaction is not observed.

Figure 6.2 shows the XeI B($^1/_2$) excitation function in the region of exciation to the ion-pair states. The thermodynamic threshold for this reaction is 174.4 nm and accordingly marked reduction of the XeI* quantum yield is observed above 168 nm as the threshold is approached. Determination of the experimental threshold is ambiguous due to the excitation bandpass ($\Delta\lambda$ = 0.3 nm) and the filter bandwidth ($\Delta\lambda$ = 8.1 nm). From Figure 6.2 the experimental threshold was estimated as 182 ± 2 nm. The discrepancy between experimental and calculated thresholds is attributed mainly to

* Although the E(0^+) is the initially populated state the experimental data presented here do not exclude the possibility that a component of the XeCl* and XeI* excimer formation occurs via sufficiently energetic neighbouring ion-pair states, populated by collision induced transfer between the states.

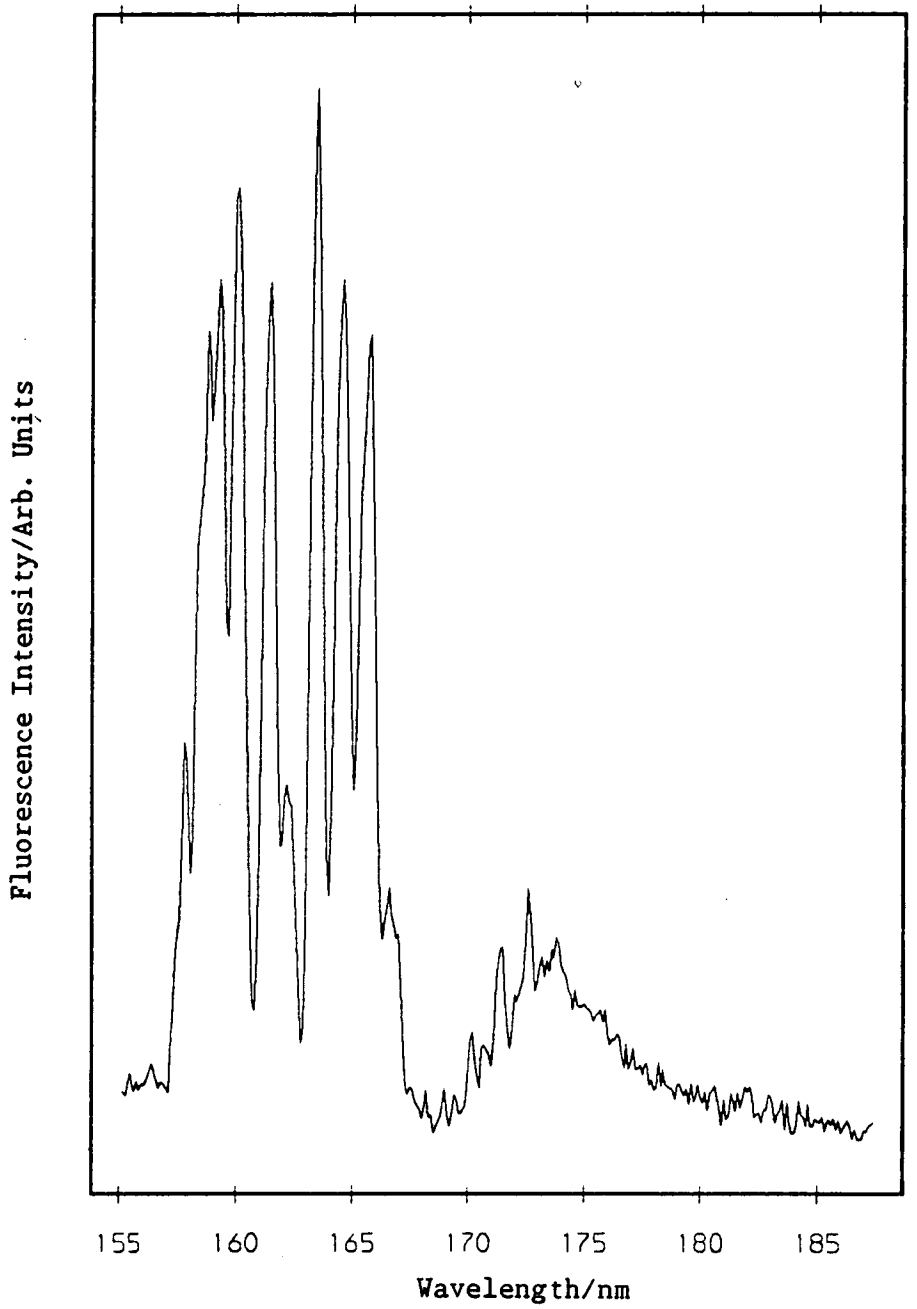

Figure 6.2 - XeI $B(^1/_2) \rightarrow X(^1/_2)$ excitation function (detected by a 254.6 nm interference filter). $\Delta\lambda$ = 0.3 nm, ICl pressure = 0.67 Torr, Cl_2 pressure = 1.33 Torr, Xe pressure = 20.0 Torr.

contributions from the tail of the XeCl $B(^1/_2)$ emission system which lies within the collection filter bandpass. The available thermal energy (517 cm^{-1} at 298K) also serves to blur the reaction onset. Although the experimental threshold cannot be determined precisely it is clear that XeI $B(^1/_2)$ formation occurs from the thermodynamic threshold with no barrier to reaction.

The onset of XeI^* formation is well illustrated by the dispersed fluorescence obtained following excitation at 176.0 nm and 164.0 nm, shown in Figure 6.3. The main exit channel for 176.0 nm excitation is formation of XeCl in the $B(^1/_2)$ state which is monitored by the $B(^1/_2) \rightarrow X(^1/_2)$ transition at 308 nm. The corresponding XeI^* emission at 254 nm is extremely weak, as expected since 176 nm lies just below threshold for XeI $B(^1/_2) \rightarrow X(^1/_2)$: emission is only observed here due to the broad excitation bandpass ($\Delta\lambda$ = 4.5 nm) necessary for detection of dispersed fluorescence. Excitation at 164 nm produces both XeCl and XeI in their $B(^1/_2)$ states although the former remains predominant, in agreement with the branching ratios found in Xe^* + ICl experiments [3].

Following excitation at either wavelength further emission is observed in the 315 - 440 nm region. The fluorescence with maximum at 430 nm is assigned to the D'(2) → A'(2) transition of ICl with the D'(2) state populated by physical quenching of the $E(0^+)$ state. However comparison of D'(2) → A'(2) fluorescence resulting from quenching by similar pressures of N_2 and Xe (see Figure 6.4) shows that other emission systems are also present.

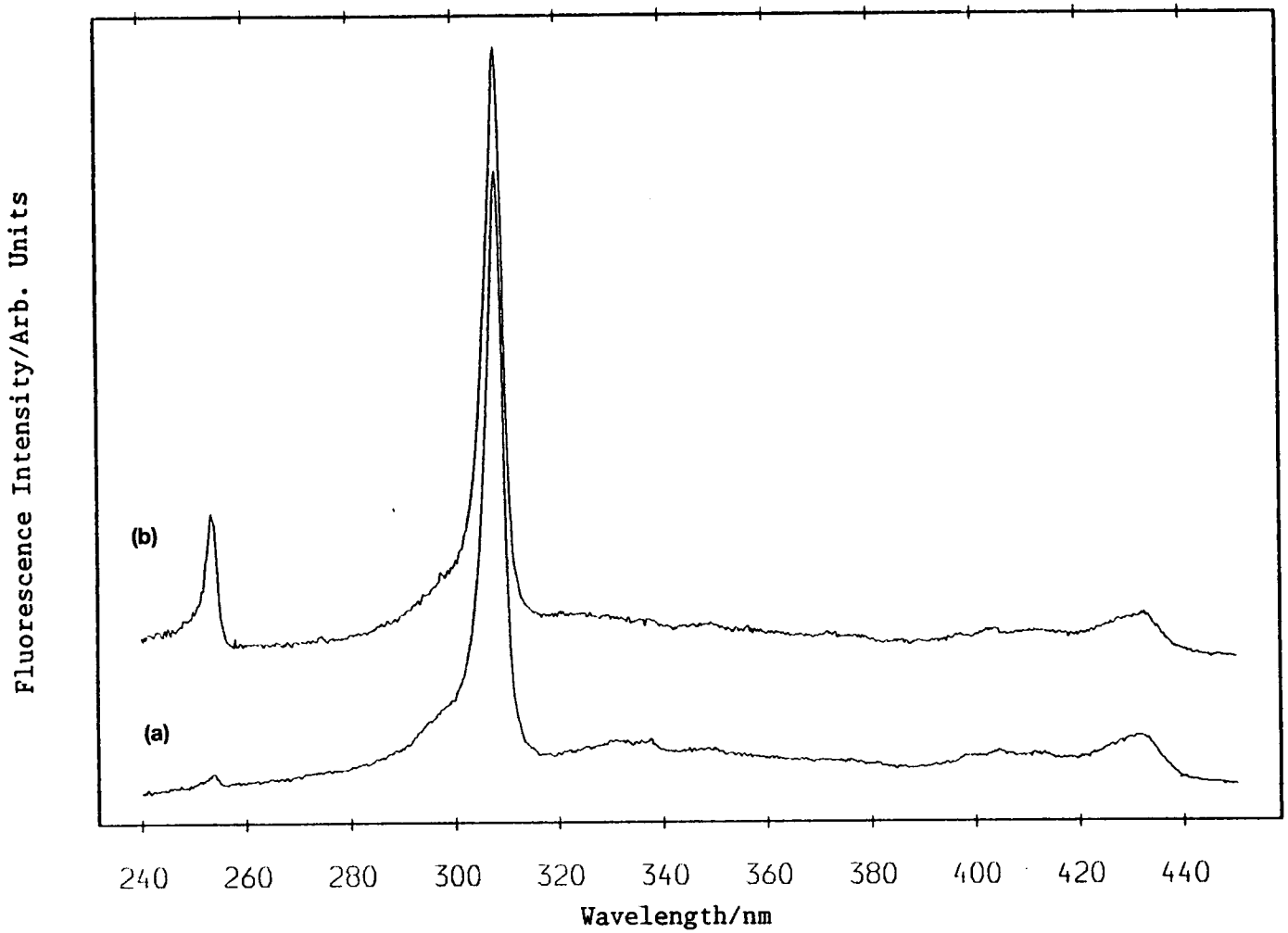

Figure 6.3 - Normalised dispersed fluorescence of $ICl/Cl_2/Xe$ mixtures excited at (a) 176.0 nm and (b) 164.0 nm. Fluorescence was excited with a bandpass of 4.5 nm and analysed with 1.7 nm resolution. ICl pressure = 0.67 Torr, Cl_2 pressure = 1.33 Torr, Xe pressure = 20.0 Torr in both spectra.

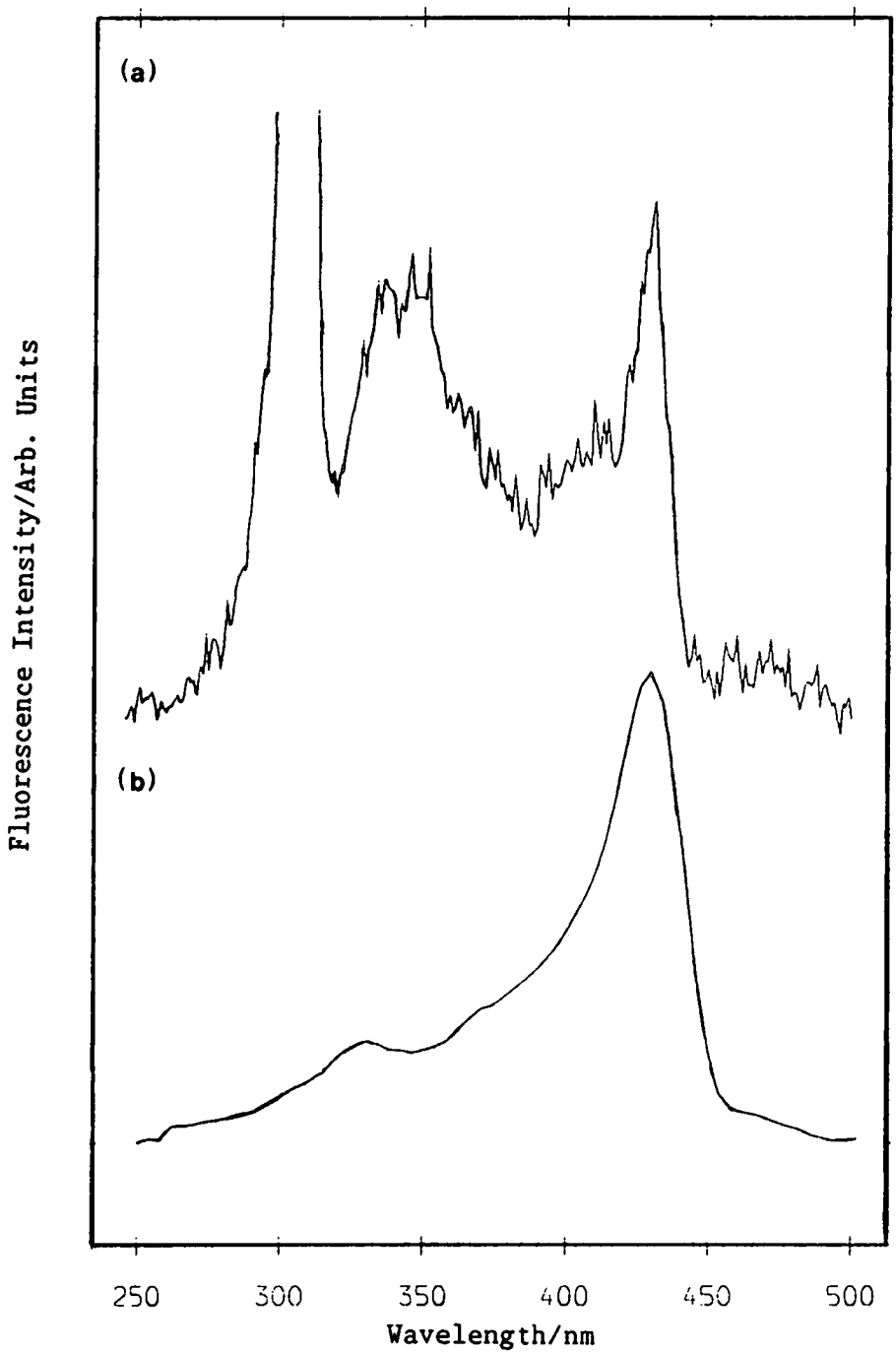

Figure 6.4 - Normalised dispersed fluorescence of (a) $ICl/Cl_2/Xe$ excited at 173.5 nm (ICl pressure = Cl_2 pressure = 1.0 Torr, Xe pressure = 60 Torr, $\Delta\lambda \approx 9$ nm) and (b) $ICl/Cl_2/N_2$ excited at 176.0 nm (ICl pressure = Cl_2 pressure = 1.0 Torr, N_2 pressure = 60 Torr, $\Delta\lambda = 20$ nm). Both spectra were excited with a bandpass of 3.0 nm. Neither is corrected for the response function of the analysing system which was the same in both cases.

From the ab initio calculations of Hay and Dunning [14], five strong ($\Delta\Omega = 0$) rare gas halide transitions are predicted. By far the strongest of these is the $B(^1/_2) \rightarrow X(^1/_2)$ lasing transition. To the red of this system $B(^1/_2) \rightarrow A(^1/_2)$ and $C(^3/_2) \rightarrow A(^3/_2)$ fluorescence occurs while $D(^1/_2) \rightarrow X(^1/_2)$ emission is situated to shorter wavelengths. The final, predicted transition, between the $D(^1/_2)$ and $A(^1/_2)$ states, has a low transition moment for both XeI and XeCl excimers and has not been observed experimentally.

At 176 nm excitation, additional fluorescence must originate from XeCl excited states as negligible amounts of XeI^* are formed. The fluorescence in the 320 - 360 nm region has been assigned to the XeCl $C(^3/_2) \rightarrow A(^3/_2)$ transition. XeCl $B(^1/_2) \rightarrow A(^1/_2)$ fluorescence is also predicted to lie in this region [3] but with a much reduced intensity.

Excitation at 164 nm produces XeI^* and $XeCl^*$ excimers in appreciable quantities. Unlike $XeCl^*$ emission, at low pressures the XeI $B(^1/_2) \rightarrow A(^1/_2)$ and $C(^3/_2) \rightarrow A(^3/_2)$ systems are well resolved, occurring in the 301 - 340 nm and 256 - 301 nm regions respectively [4]. Due to the increase in spin-orbit coupling constant with halogen atom mass the XeI $B(^1/_2) \rightarrow A(^1/_2)$ transition is now the more intense of the two systems. Indeed, following excitation at 164 nm, Figure 6.3 shows a slight increase in intensity in the 312 - 340 nm region which has been attributed to the XeI $B(^1/_2) \rightarrow A(^1/_2)$ system.

Although Figure 6.4 indicates the presence of additional XeX $B(^1/_2) \rightarrow A(^1/_2)$ and $C(^3/_2) \rightarrow A(^3/_2)$ fluorescence, these systems are extremely weak in comparison with the dominant XeX $B(^1/_2) \rightarrow X(^1/_2)$ transitions. This is due, in part, to the strong $B(^1/_2) \rightarrow X(^1/_2)$ transition moments but also to the relatively high sample pressures employed. In general, the XeX $B(^1/_2)$ states have radiative lifetimes in the 20 - 40 ns range whereas the $C(^3/_2)$ state lifetimes are about an order of magnitude larger [16,17]. Thus, at pressures > 0.1 Torr collisional transfer occurs between the close-lying $B(^1/_2)$ and $C(^3/_2)$ states with the shorter-lived $B(^1/_2)$ state making a larger contribution to the fluorescence as pressure increases.

Collisional quenching of the initially excited levels also occurs with high sample pressures, resulting in relatively narrow $B(^1/_2) \rightarrow X(^1/_2)$ emission bands with few bound-free oscillations (see Figure 6.3). The weak $C(^3/_2) \rightarrow A(^3/_2)$ and $B(^1/_2) \rightarrow A(^1/_2)$ systems are much broader due to the more replusive nature of the $A(^3/_2, {}^1/_2)$ states.

6.4 Mechanism of the ICl $E(0^+)$ + Xe Reaction

The reaction $[Rg + X_2]^* \rightarrow RgX^* + X$ proceeds via a $[Rg^+, X_2^-]$ potential energy surface irrespective of the location of the excitation energy. The impetus for the harpoon reaction may be either the low ionisation potential of the Rg^* component or the high electron affinity of the X_2^* component. Variation of the initially excited reactant changes the Rg - X separation at which harpooning occurs thus altering the point at which the complex enters the excited potential surface (as illustrated in the approximate potential energy surfaces

of Donovan et al [18]). The point of entry on the potential surface affects both the products formed and their final energy distributions.

Consider the reaction of ICl^* + Xe $\rightarrow$ $XeCl^*$ + I / XeI^* + Cl

The initial stages of the harpoon mechanism can be easily explained by the changes in electron configuration of the reactants.

The electron configuration of the ICl ground state is $\sigma^2\pi^4\pi^{*4}\sigma^{*0}$ (2440). Excitation to the $E(0^+)$ state is a one electron transfer process resulting in an electron configuration of 1441. This leaves a vacancy in the low lying σ-bonding orbital which increases the electron affinity of the interhalogen molecule (by the energy of the excitation photon) thus facilitating the harpoon reaction. As the ionisation potential of iodine is lower than that of chlorine the electron in the σ^* antibonding orbital is located mainly on the iodine atom.

Harpooning from the closed shell Xe atom then occurs to form an ion-pair, ICl^- ($^2\Sigma^+$, 2441) + Xe^+, with the negative charge at the $^2\Sigma^+$ ground state ion remaining on the iodine. Due to the net antibonding configuration of the ICl^- component and the Coulombic attraction between the two oppositely charged ions the ICl^- bond begins to stretch. As reaction proceeds and the bond stretches the electron density migrates from the iodine towards the chlorine atom (since the lowest ICl^- asymptotic dissociation limit is I and Cl^- [19]). This process is aided by the large equilibrium internuclear

bondlengths of the high ICl $E(0^+)$ vibrational levels which are accessed in a single photon experiment. As the $E(0^+)$ state dissociates asymptotically to $I^+(^3P_2)$ and $Cl^-(^1S)$, charge migration has already begun at large internuclear separations, enhancing the formation of [I --- Cl^- --- Xe^+]. Consequently, XeCl* formation is preferred to XeI* formation, as witnessed in Figure 6.3 where the ratio of XeCl to XeI $B(^1/_2) \rightarrow X(^1/_2)$ emission is approximately 4.4:1 (λ_{exc} = 164 nm). The spectra in Figure 6.3 have been corrected for the response function of the dispersion system but not for the XeCl and XeI $B(^1/_2) \rightarrow X(^1/_2)$ transition moments. Since Hay and Dunning calculated that these transition moments are similar (2.76 D for XeCl $B(^1/_2) \rightarrow X(^1/_2)$ and 2.07 D for the corresponding XeI transition [14]) this should not significantly affect the observed ratio.

Further experiments are necessary to determine if the preference for XeCl* formation is a function of excitation wavelength. The branching ratio may vary with the total energy available above the formation thresholds of the excimers. However, as a similar result has been found in Xe^* $(^3P_2)$ + ICl experiments [3], it is likely that XeCl* formation is always preferred; in accord with the mechanism outlined above.

XeI* formation is thought to occur only when a Xe atom collides with the iodine end of the ICl molecule at small impact parameters [18]. The ICl^- ion is formed initially in the $^2\Sigma^+$ (2441) state but must undergo mixing with excited ICl^- states for XeI* formation to take place. Mixing of the ICl^- states is induced by the electric field of the approaching Xe^+ ion. The $^2\Pi_{1/2}$ (2432) and $^2\Pi_{3/2,1/2}$ (2342) ICl^- states all possess the correct dissociation

characteristics (I^- + Cl) for the reaction to exit by a XeI^* channel [19]. This channel is preferred over the more normal route of charge migration to the chlorine atom due to the large bulk of the iodine atom which blocks the passage of the Xe atom around the ICl molecule.

A preliminary account of the ICl $E(0^+)$ + Xe reaction above 158 nm has already been published [20] but even with the higher resolution ($\Delta\lambda_{exc}$ = 0.3 nm) study presented here the experimental XeI^* reaction threshold can only be determined to within 4 nm. For more accurate experimental thresholds the initial state of the excited halogen/inter-halogen molecule must be defined more precisely as in the I_2 $f(0^+)$ + Xe study of Donovan et al [21] where optical-optical double resonance (OODR) excitation prepares the I_2 molecule in a known rovibrational level. However, even in their work the collision energy was not well defined as the experiment was conducted in a static cell at 300K. Jouvet et al [22] have defined the reagent conditions even more stringently by direct excitation of X_2--- Rg van der Waals complexes in a supersonic beam expansion. Such work contains much information on the dynamics of the reaction.

However, synchroton radiation excitation of such systems should not be dismissed since sources such as the SRS provide valuable information over a broad excitation range and have been the origin of much elegant work : such as determination of the ordering of the B, C states of RgX excimers by the time-resolved experiments of Le Calve et al [23].

6.5 Photoexcitation of $ICl/Cl_2/Xe$ Mixtures at Wavelengths Below 158 nm

In contrast to the region above 158 nm, Figure 6.1 shows that below 158 nm the XeCl $B(^1/_2)$ action spectrum does not follow that of ICl^* fluorescence. Three $XeCl^*$ excitation systems are observed; centred around 152 nm, 147 nm and 140 nm, whereas in ICl/Cl_2 samples fluorescence only occurs following excitation below 140 nm. The two systems at 152 nm and 147 nm have no analogue in the ICl^* fluorescence excitation whilst the third system at 140 nm is a completely different shape.

The dispersed fluorescence spectra of $ICl/Cl_2/Xe$ mixtures following excitation at 152 nm, 147 nm and 140 nm are shown in Figure 6.5. The UV-VIS traces are shown in Figure 6.5 (a) and the VUV-UV traces in Figure 6.5 (b). Consider initially the 152 nm system. In the UV-VIS spectrum of Figure 6.5-C three distinct peaks are observed; the XeCl and XeI $B(^1/_2) \rightarrow X(^1/_2)$ excimer transitions at 308 nm and 254 nm respectively and a third, weaker system around 282 nm. To the red of the XeCl $B(^1/_2)$ band further weak emission occurs which may be assigned to the $B(^1/_2) \rightarrow A(^1/_2)$ and $C(^3/_2) \rightarrow A(^3/_2)$ transitions discussed in Section 6.3. There also appears to be a very slight contribution from the ICl $D'(2) \rightarrow A'(2)$ system around 430 nm but this is much reduced in intensity when compared with the same system excited at higher wavelength.

Excitation at 147 nm produces a very similar spectrum in the UV-VIS region although fluorescence is not detected to the red of the XeCl $B(^1/_2) \rightarrow X(^1/_2)$ band. The three bands monitored above are again

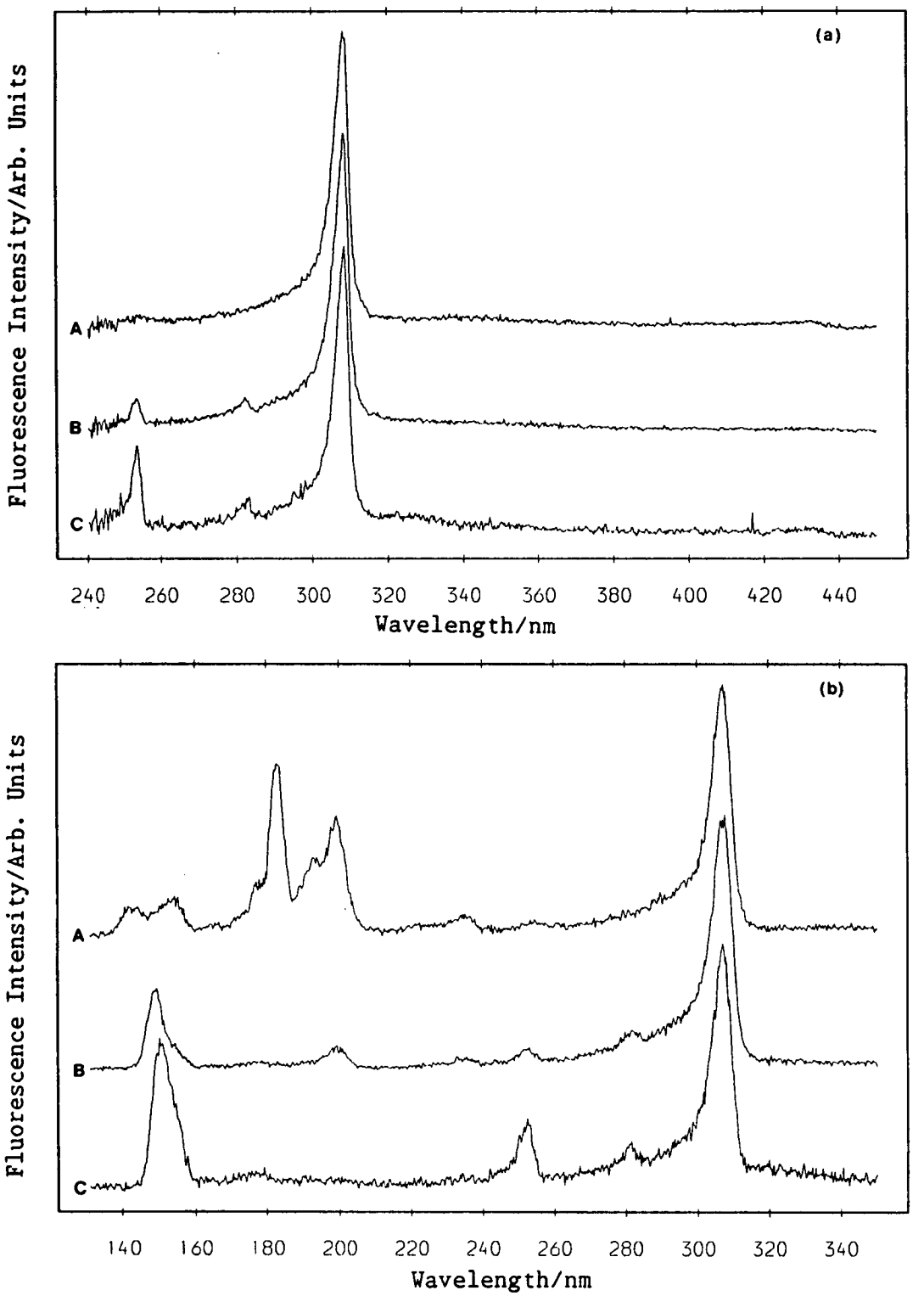

Figure 6.5 - Normalised dispersed fluorescence of $ICl/Cl_2/Xe$ mixtures following excitation at A - 140.3 nm, B - 147.0 nm and C - 152.4 nm. Fluorescence was excited with a bandpass of 4.5 nm in all cases. The UV-VIS fluorescence, shown in (a), was analysed with 1.7 nm resolution and the VUV-UV fluorescence, (b), by 4.0 nm resolution. ICl pressure = 0.67 Torr, Cl_2 pressure = 1.33 Torr and Xe pressure = 20.0 Torr.

observed. The XeCl $D(^1/_2) \rightarrow X(^1/_2)$ system at 235 nm [3] is also observed in the VUV-UV spectrum of Figure 6.5-B. As the resonant $^3P_1^\circ \leftarrow {}^1S$ (6s - 5p) Xe transition occurs at 147.0 nm [12] and since ICl^* emission is not observed at this wavelength, excimer formation has been attributed to reactions of the Xe ($^3P_1$) atom with ICl and Cl_2.

From experiments of Setser et al [2, 24], it is known that the Xe^* (6s, $^3P_1$) reactivity parallels that of the more extensively studied Xe^* (6s, $^3P_2$) metastable atom. Comparison between the Xe^* (6s, $^3P_2$) results of Donovan et al [18] and direct photoexcitation of the Xe^* (6s, $^3P_1$) atom is therefore valid, although the differing pressure regimes must be considered.

In both sets of experiments it was found that the excitation transfer channel (formation of the D'(2) state) was negligible in comparison with the results from the ICl^* + Xe reaction. In the present work, the XeCl: XeI branching ratio is much higher than the 2.3 value of Kolts et al [3] due to the twofold excess of chlorine in the reaction mixture.

Finally consider the system centred around 140 nm (see Figure 6.5). Formation of the XeCl excimer now dominates with only the slightest indication of a peak around 254 nm. The region below 200 nm is congested and closely resembles the dispersed fluorescence of an ICl/Cl_2 mixture excited in the absence of Xe (see Figure 4.14). Cl_2 ($1\ ^1\Sigma_u^+ \rightarrow X\ ^1\Sigma_g^+$) bound-free fluorescence is sited at wavelengths below 200 nm with the bound-bound portion of the same transition at the blue end of the spectrum. The intense peak at 182 nm corresponds

to the $^4P_{5/2}$ - $^2P^o_{3/2}$ atomic transition with the excited iodine atoms produced by predissociation of ICl Rydberg states.

Formation of XeI* is almost zero and even assignment of the small peak around 254 nm is ambiguous since unquenched Cl_2^* emission also occurs in this region [25]. Very little fluorescence is observed to the red of the XeCl* $B(^1/_2) \rightarrow X(^1/_2)$ band with only a suggestion of ICl $D'(2) \rightarrow A'(2)$ fluorescence around 430 nm.

The reaction following excitation at 140 nm is essentially that of ground state Xe and Cl_2 in the 1 $^1\Sigma_u^+$ excited state. Reaction with ICl* does not occur as the Rydberg states populated in this region are predissociated and a two-body collision of I* + Xe will not produce XeI*. The small quantities of ICl $D'(2)$ present must be produced by the process:-

$$ICl + h\nu \rightarrow I^* + Cl$$

and

$$I^* + ICl \rightarrow ICl\ D'(2) + I$$

as discussed in Section 3.10. However, even this process is quenched by the presence of ~ 20 Torr Xe. By contrast, it is interesting to note that the Cl_2 (1 $^1\Sigma_u^+ \rightarrow X\ ^1\Sigma_g^+$) system is not quenched by $P_{Xe} \simeq 20$ Torr. Witness the similarities between the VUV traces of Figures 3.15 and 6.5. On addition of high pressures of foreign gas ($P_{Ar} > 30$ Torr) quenching of the Cl_2 (1 $^1\Sigma_u^+ \rightarrow X\ ^1\Sigma_g^+$) system has been observed with intersystem crossing to the 2 $^3\Pi_g$ state taking place [7]. Strong 2 $^3\Pi_g \rightarrow 1\ ^3\Pi_u$ emission at 258 nm, the Cl_2 lasing

transition, then occurs. This process is analogous to collisional transfer of the ICl $E(0^+)$ state to the $D'(2)$ state and subsequent ICl $D'(2) \rightarrow A'(2)$ emission. As discussed above, excitation of the $ICl/Cl_2/Xe$ sample at 140.3 nm, results in Cl_2 ($1\ ^1\Sigma_u^+ \rightarrow X\ ^1\Sigma_g^+$) fluorescence below 200 nm with no sign of fluorescence from the Cl_2 $2\ ^3\Pi_g$ state at 258 nm. Lifetime studies of the Cl_2 $1\ ^1\Sigma_u^+$ state give a radiative lifetime of ~ 3 ns [26]. At the total sample pressure of 22 Torr employed in this work it appears that the excited Cl_2 molecules either radiate before collision with Xe or react on every collision to produce $XeCl^*$, with negligible branching to the Cl_2 intersystem crossing channel.

Returning to the fluorescence observed following 152 nm and 147 nm excitation. In both cases an unassigned peak was observed around 282 nm. This band does not correspond to any XeI^* or $XeCl^*$ system, nor can it be attributed to ICl^* or Cl_2^* fluorescence. 282 nm is, however, the wavelength at which the XeBr $B(^1/_2) \rightarrow X(^1/_2)$ transition occurs. The effects of BrCl contamination in absorption have already been noted in Figure 3.4. Figure 6.6 shows the $BrCl/Cl_2$ fluorescence excitation spectrum in the 130 - 175 nm region. BrCl systems are observed around both 147 nm and 152 nm and, indeed, small levels of BrCl contamination can be seen in the 140 - 155 nm region of the ICl/Cl_2 fluorescence excitation spectrum of Figure 6.1. Consequently, the peak at 282 nm has been assigned to XeBr $B(^1/_2)$ fluorescence as a result of Br_2 contamination of the sample cell.

The situation following excitation of an $ICl/Cl_2/Xe$ mixture below 158 nm is more complex than for excitation wavelengths > 158 nm, with each system following a different reaction pathway. Reaction via

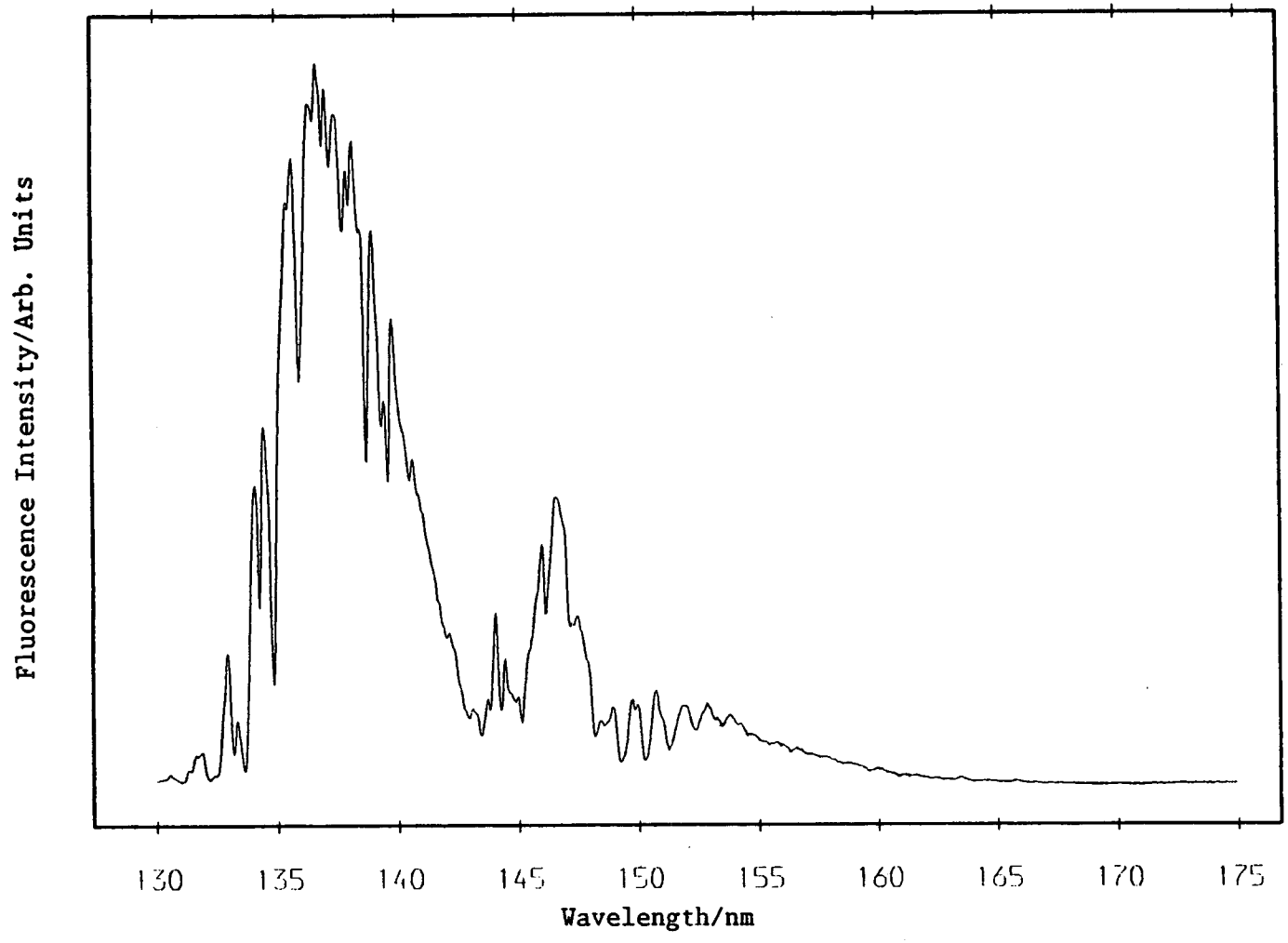

Figure 6.6 - BrCl and Cl_2 fluorescence excitation spectrum (200 - 600 nm detection). Excitation wavelength resolution, $\Delta\lambda$ = 0.2 nm. BrCl pressure = 18 mTorr, Cl_2 pressure = 212 mTorr.

the 140 nm system proceeds via an excited Cl_2 state ie. Cl_2 1 $^1\Sigma_u^+$ + Xe → XeCl* + Cl with the ICl* molelcules predissociating and taking no part in reaction. 147 nm excitation produces Xe ($^3P_1$) Rydberg atoms which react with ICl and Cl_2 and also any BrCl molecules present.

The pathway for reaction following 152 nm excitation is unknown. Figure 6.5 shows that XeI*, XeCl* and XeBr* excimers are formed. Reaction does not proceed by excited Xe* as the $^3P_1$ state is the first single-photon accessible Rydberg state of Xe. The ICl molecule must be involved as both XeI and XeCl excimers are formed. However, it appears that all ICl excited states in this region are predissociated since fluorescence is not observed in the VUV, UV or visible spectral regions (see Figure 3.16). This leaves the possibility of a photon-assisted reaction of ICl --- Xe collision pairs. Such a phenomenon has been reported for laser assisted reactions of both ICl and Cl_2 [27 - 29] with Xe but it is doubtful whether the photon flux of a synchrotron radiation source is sufficient for this to be a feasible proposition. XeBr* formation is observed at this wavelength presumably by reaction of BrCl* with Xe since BrCl* states are known to fluoresce in this region (see Figure 6.6).

Other questions such as the shape of the low wavelength system and the width of the 'atomic' Xe ($^3P_1$) transition at 147.0 nm must also be considered.

The low wavelength system around 140 nm is essentially a Cl_2*/Xe fluorescence excitation spectrum. Contributions from the ICl

states excited by 128 - 133 nm radiation are not observed. However, on comparison with the Cl_2 fluorescence excitation spectra of Moeller et al [30] the system appears to be red shifted. This may be a function of the ICl/Cl_2 pressure employed and pressure dependent studies are required.

A more detailed study of the photoexcitation of $ICl/ICl_2/Xe$ mixtures below 158 nm is necessary to determine the nature of the reaction following 152 nm excitation and to correlate the $XeCl^*$ action spectrum with that of ICl/Cl_2 fluorescence excitation. The present results show that no:-

$$ICl^* + Xe \longrightarrow \begin{cases} XeCl^* + I \\ XeI^* + Cl \end{cases}$$

channels are present in this excitation region. The differences between reaction proceeding by the ICl $E(0^+)$ state and the Xe ($^3P_1$) state illustrate the effect of accessing different regions of the excited potential energy surface.

6.6 Photoexcitation of $ICl/Cl_2/Kr$ Mixtures in the 125 - 195 nm Region

A brief study on the reactions and quenching of ICl and Cl_2 by Kr was also carried out. The reaction thresholds for formation of KrCl in the $B(^1/_2)$ state by reaction of Kr with Cl_2 ($D_o° = 19{,}997\ cm^{-1}$ [31]) and ICl ($D_o° = 17{,}366\ cm^{-1}$ [14]) are 153.7 nm and 160.2 nm

respectively, assuming a KrCl $B(^1/_2) \rightarrow X(^1/_2)$ transition of 222.0 nm [32]. Thus the majority of the ICl $E(0^+)$ levels above 158 nm are not sufficiently energetic for reaction to occur while reaction of the lower wavelength Cl_2 system has been previously reported [6, 26].

Figure 6.7 shows an excitation spectrum of the KrCl $B(^1/_2) \rightarrow X(^1/_2)$ transition at 222 nm. The resolution of this spectrum is poor since a secondary monochromator (the Acton VM-502) was employed to detect fluorescence and the excitation bandwidth had to be increased to 3.1 nm.

The $KrCl^*$ excitation spectrum is very similar to that of $XeCl^*$ with the exception of the atomic Xe system around 147 nm. The corresponding Kr transition is found at 123.6 nm [33] and lies below the CaF_2 cut-off (128 nm). Dispersed fluorescence following 176 nm excitation (Figure 6.8) shows that no $KrCl^*$ is formed at this wavelength as expected. The spectrum is essentially that of quenched ICl $E(0^+)$ fluorescence as discussed in Section 4.7 with the bound-bound fluorescence at 222 nm contributing to the action spectrum of Figure 6.7. Excitation at 142 nm (Figure 6.9) reveals a spectrum very similar to that of the $ICl/Cl_2/Xe$ mixture (λ_{exc} = 140 nm, Figure 6.5-A), although the KrCl $B(^1/_2) \rightarrow X(^1/_2)$ transition at 222 nm is now observed instead of the $XeCl^*$ transition at 308 nm. The ICl molecule again takes no part in the reaction due to ICl^* predissociation.

Dispersion of fluorescence following excitation from 150 nm to 160.2 nm (the $KrCl^*$ formation threshold) was not possible due to low levels of fluorescence. It is noted that the 152 nm excitation

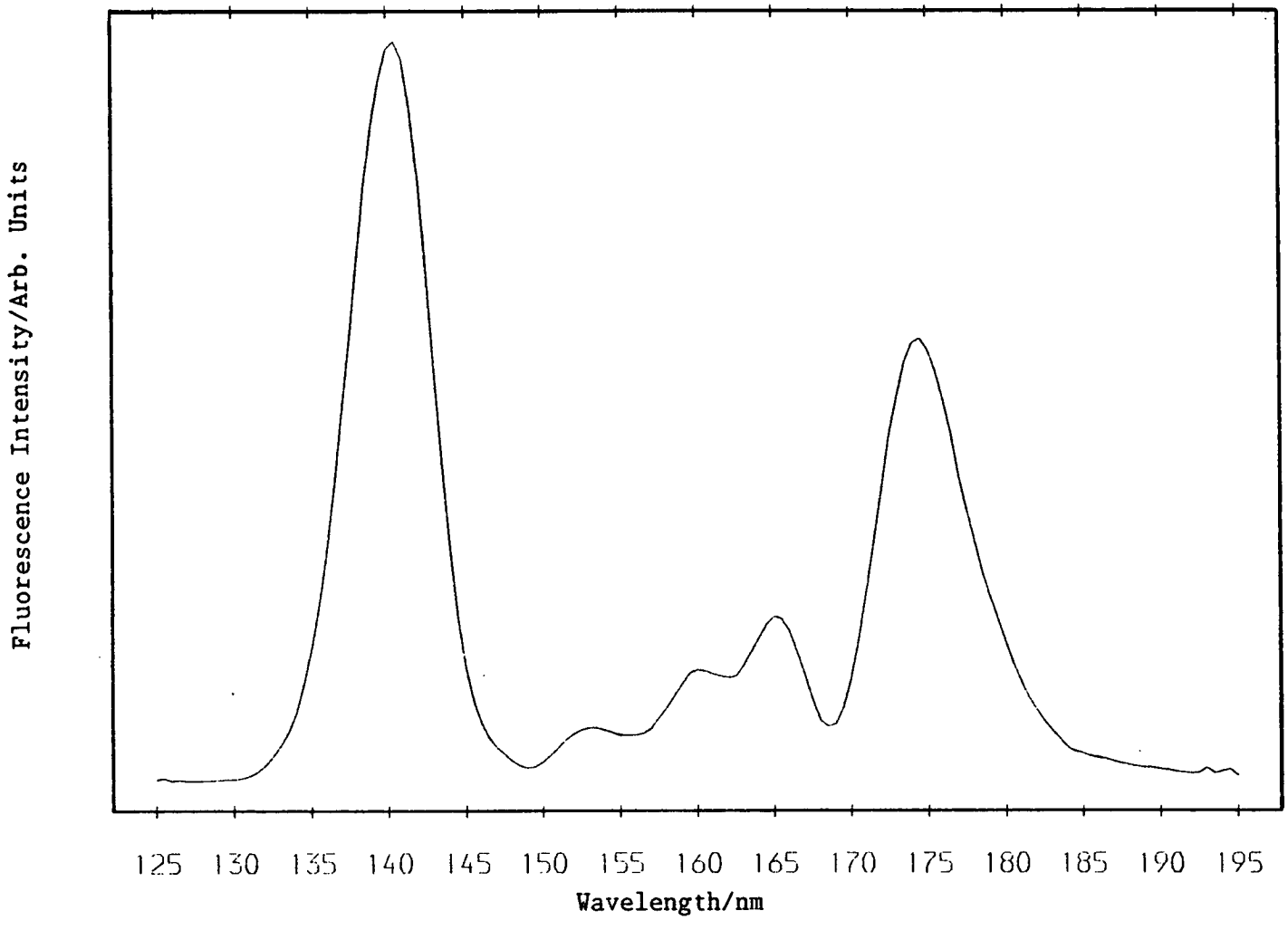

Figure 6.7 - Fluorescence excitation of the KrCl $B(^1/_2) \rightarrow X(^1/_2)$ band at 222 nm ($\Delta\lambda$ = 12.0 nm). Excitation wavelength resolution, $\Delta\lambda$ = 3.2 nm. ICl pressure = 0.65 Torr, Cl_2 pressure = 1.31 Torr, Kr pressure = 19.3 Torr.

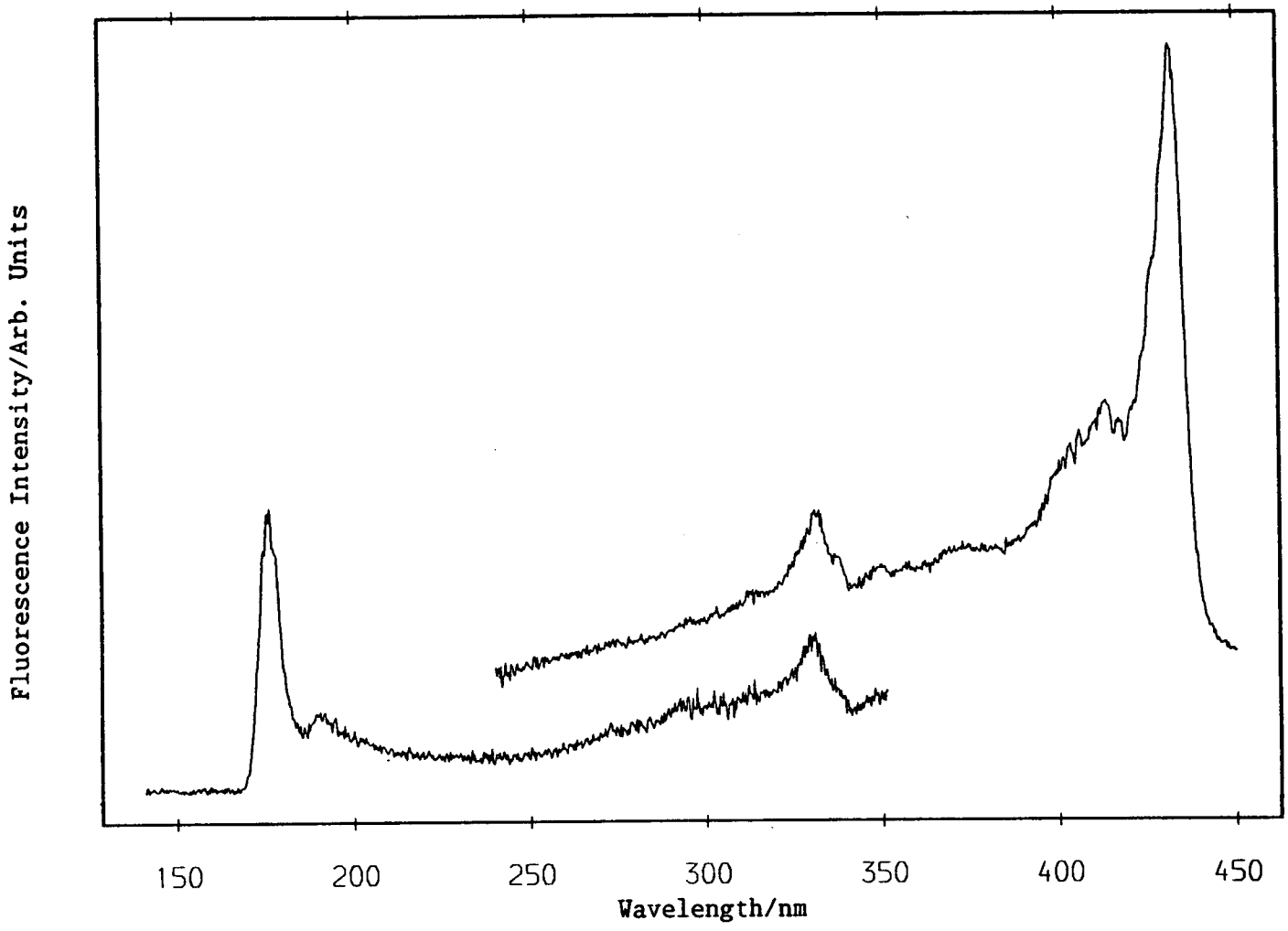

Figure 6.8 - Dispersed fluorescence of an $ICl/Cl_2/Kr$ mixture following excitation at 176.0 nm ($\Delta\lambda$ = 4.5 nm). The UV-VIS fluorescence (upper trace, $\Delta\lambda$ = 1.7 nm) is corrected for the response function of the detection system but the VUV-UV fluorescence (lower trace, $\Delta\lambda$ = 4.0 nm) is not. ICl pressure = 0.63 Torr, Cl_2 pressure = 1.25 Torr, Kr pressure = 39.5 Torr.

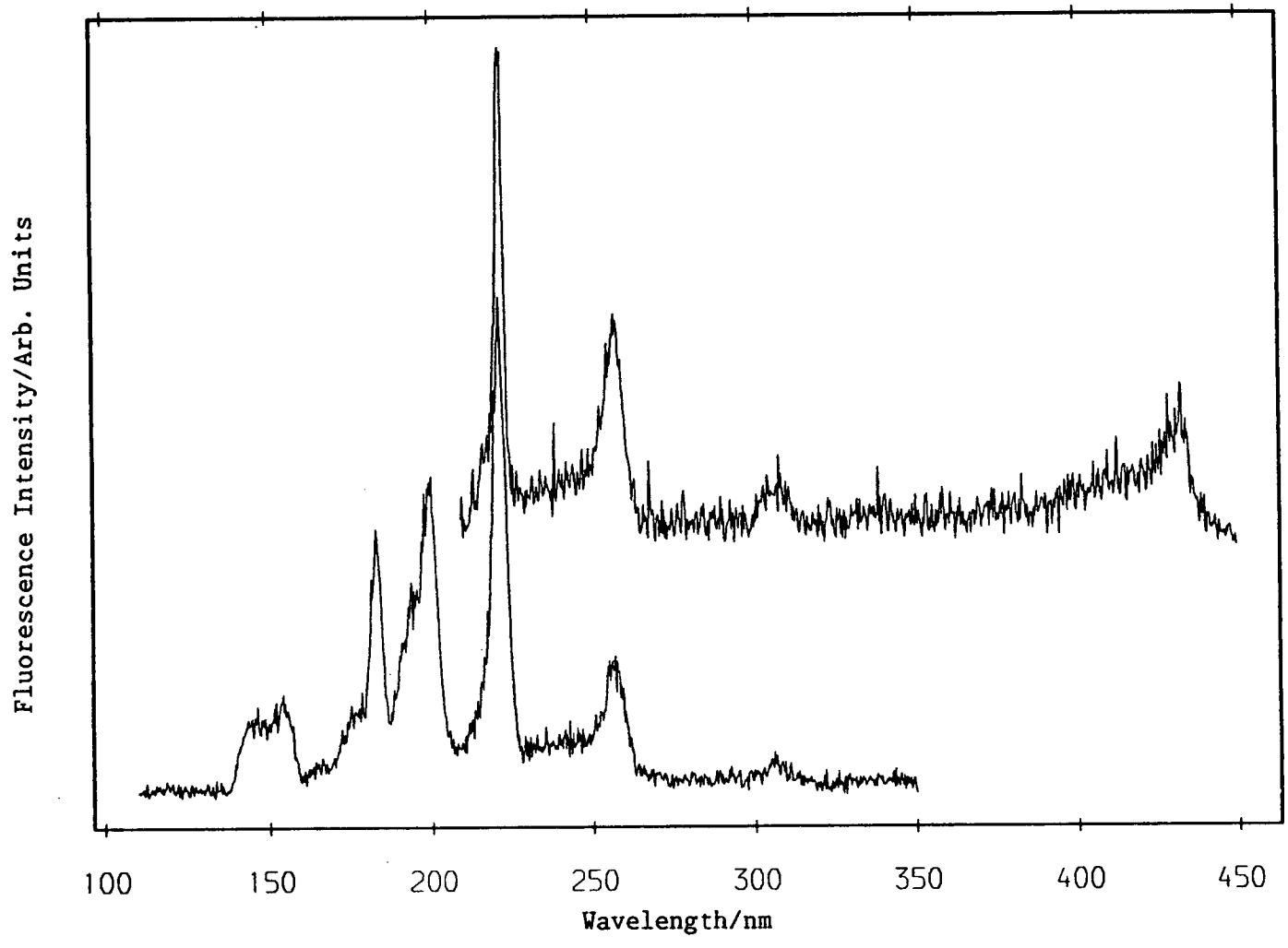

Figure 6.9 - Normalised dispersed fluorescence of an $ICl/Cl_2/Kr$ mixture following excitation at 142.0 nm ($\Delta\lambda$ = 4.5 nm). The UV-VIS fluorescence was analysed with 1.7 nm resolution and the VUV-UV by 4.0 nm resolution. Neither spectrum is corrected for the response function of the analysing system.

system is still present and it would be interesting to ascertain whether $KrCl^*$ is formed by excitation of this system.

Excitation of $Kr/ICl/Cl_2$ mixtures produces similar results to the $Xe/ICl/Cl_2$ system which has been studied in more detail. However, in this case the ICl ion-pair states (primarily the $E(0^+)$ state) are not well-positioned for the study of the $KrCl^*$ formation threshold.

REFERENCES

1. "Excimer Lasers" in "Topics in Applied Physics", Vol. 30, Edited by C. Rhodes, Springer-Verlag, Berlin, Heidelberg, New York, 1979.
2. D.W. Setser, T.D. Dreiling, H.C. Brashears Jr. and J.H. Kolts, Faraday Discuss. Chem. Soc., **67**, 255 (1979).
3. J.H. Kolts, J.F. Velazco and D.W. Setser, J. Chem. Phys., **71**, 1247 (1979).
4. K. Tamagake, D.W. Setser and J.H. Kolts, J. Chem. Phys., **74**, 4286 (1981).
5. T.D. Dreiling and D.W. Setser, J. Chem. Phys., **75**, 4360 (1981).
6. M.C. Castex, J. Le Calve, D. Haaks, B. Jordan and G. Zimmerer, Chem. Phys. Lett., **70**, 106 (1980).
7. T. Moeller, B. Jordan, G. Zimmerer, D. Haaks, J. Le Calve and M.C. Castex, Z. Phys. D-Atoms, Molecules and Clusters, **4**, 73 (1986).
8. J.P.T. Wilkinson, M. MacDonald and R.J. Donovan, Chem. Phys. Lett., **101**, 284 (1983).
9. B.V. O'Grady and R.J. Donovan, Chem. Phys. Lett., **122**, 502 (1985).
10. N.K. Bibinov and J.P. Vinogradov, Opt. Spectrosc., **59**, 191 (1985).
11. D.R. Herschbach, Adv. Chem. Phys., **10**, 319 (1966).
12. C.E. Moore, "Atomic Energy Levels", NBS Circular 467, Vol. III, U.S. Bureau of Commerce, Washington, D.C., 1958.
13. U. Ross, T. Schulze and H-J Meyer, Chem. Phys. Lett., **121**, 174 (1985).

14. P.J. Hay and T.H. Dunning, J. Chem. Phys., **69**, 2209 (1978).

15. G.W. King and R.G. McFadden, Chem. Phys. Lett., **58**, 119 (1978).

16. A. Sur, A.K. Hui and J. Tellinghuisen, J. Mol. Spectrosc., **74**, 465 (1979).

17. G. Inoue, J.K. Ku and D.W. Setser, J. Chem. Phys., **80**, 6006 (1984).

18. R.J. Donovan, P. Greenhill, M.A. MacDonald, A.J. Yencha, W.S. Hartree, K. Johnson, C. Jouvet, A. Kvaran and J.P. Simons, Faraday Discuss. Chem. Soc., **84**, Paper 12 (1987).

19. G.H. Kwei and D.R. Herschbach, J. Chem. Phys., **51**, 1742 (1969).

20. J.P.T. Wilkinson, E.A. Kerr, K.P. Lawley, R.J. Donovan, D. Shaw, A. Hopkirk and I. Munro, Chem. Phys. Lett., **130**, 213 (1986).

21. R.J. Donovan, A.J. Holmes, P.R.R. Langridge-Smith and T. Ridley, J. Chem. Soc., Faraday Trans. 2, **84**, 541 (1988).

22. C. Jouvet, M. Boivineau, M.C. Duval and B. Soep, J. Phys. Chem., **91**, 5416 (1987).

23. J. Le Calve, M.C. Castex, B. Jordan, G. Zimmerer, T. Moeller and D. Haaks, "Photophysics and Photochemistry above 6eV", p. 639, Elsevier, Amsterdam, 1985.

24. H.C. Brashears Jr. and D.W. Setser, J. Phys. Chem., **84**, 224 (1980).

25. T. Moeller, B. Jordan, P. Gurtler, G. Zimmerer, D. Haaks, J. Le Calve and M.C. Castex, "Spectral Line Shapes, Vol. 2," p. 597, Edited by K. Burnett, Walter de Gruyter, Berlin, 1983.

26. J. Le Calve, M.C. Castex, D. Haaks, B. Jordan and G. Zimmerer, Nuovo Cimento, **63 B**, 265 (1981).

27. D.W. Setser and J. Ku, "Photophysics and Photochemistry above 6eV", p. 621, Elsevier, Amsterdam, 1985.

28. J.K. Ku, G. Inoue and D.W. Setser, J. Phys. Chem., **87**, 2989 (1983).

29. H.P. Grieneisen, H. Xue-Jing and K.L. Kompa, Chem. Phys. Lett., **82**, 421 (1981).

30. T. Moeller, B. Jordan, P. Gurtler, G. Zimmerer, D. Haaks, J. Le Calve and M.C. Castex, Chem. Phys., **76**, 295 (1983).

31. A.E. Douglas and A.R. Hoy, Can. J. Phys., **53**, 1965 (1975).

32. J.R. Murray and H.T. Powell, Appl. Phys. Lett., **29**, 252 (1976).

33. H. Okabe, "Photochemistry of Small Molecules, " Wiley, New York, 1978.

Appendix I

Courses and Conferences Attended

In accordance with the regulations of the University of Edinburgh, the Department of Chemistry, the following lectures and lecture courses were attended over the period of three years.

Courses

Lasers

Mass Spectrometry

RKR Theory

Non-Linear Least Mean Squares Methods

Theoretical Methods

Molecular Electronics

One Week Course on Fortran Programming

Attendance at Laser and Molecular Beam Group Meetings, 1984 - 1987

Summer Schools and Workshops

Attendance at one week of the 30th Scottish Universities Summer School of Physics on Synchrotron Radiation Research, University of Aberdeen, 1985.

SERC Sponsored Short Course on Gas Kinetics, University of Cambridge, 1985.

Workshop on Fluorescence Lifetime Spectroscopy, Edinburgh Instruments Ltd., 1986.

Conferences and Meetings

9th International Symposium on Gas Kinetics, University of Bordeaux, 1986.

XIth International Symposium on Molecular Beams, University of Edinburgh, 1987.

Gas Kinetics Group Meetings:

- University of Leicester, 1985.
- University of Cambridge, 1985.
- University of Edinburgh, 1987.

APPENDIX II

PUBLISHED PAPERS

Journal of Photochemistry, 31 (1985) 149 - 155

VACUUM UV FLUORESCENCE EXCITATION SPECTRUM OF ICl USING SYNCHROTRON RADIATION

ELINOR KERR, MICHAEL MacDONALD†, ROBERT J. DONOVAN and JEREMY P. T. WILKINSON

Department of Chemistry, University of Edinburgh, West Mains Road, Edinburgh EH9 3JJ (Gt. Britain)

DAVID SHAW and IAN MUNRO

Science and Engineering Research Council Daresbury Laboratory, Daresbury, Warrington WA4 4AD (Gt. Britain)

(Received March 25, 1985; in revised form May 25, 1985)

Summary

The fluorescence excitation spectrum of ICl in the region 160 - 200 nm has been recorded using tunable synchrotron radiation. The dominant absorption features in this region involve transitions to Rydberg states but the main fluorescence (for $\lambda \geq 200$ nm) is from ion pair states.

1. Introduction

Until quite recently very little was known about the ion pair states of halogen and interhalogen molecules. However, there has been considerable recent interest following the discovery that they have rather unusual chemical and spectroscopic properties [1 - 10].

From a chemical viewpoint they are of interest because of their high reactivity [1 - 4]; they are known to react with noble gas atoms [4] and to be capable of breaking some of the strongest chemical bonds (*e.g.* the carbon—fluorine bond) [3]. From a spectroscopic viewpoint, ion pair states are of interest because of the extensive oscillatory continuum emission to which they generally give rise [5 - 10].

We have previously reported [2, 7 - 10] work on the ion pair states of I_2, IBr and Br_2. However, despite considerable efforts we have, until now, failed in attempts to excite the ion pair states of ICl using single-photon techniques. In previous attempts we have used an ArF laser (193 nm), a commercial fluorometer ($\lambda \geq 190$ nm), an intense mercury lamp (184.9 nm) and an F_2 laser (157 nm). These failures surprised us in view of the relative

†Present address: Department of Chemistry, University of Denver, University Park, Denver, CO 80208, U.S.A.

0047-2670/85/$3.30

ease with which the other halogen ion pair states could be excited and we therefore decided to make a systematic fluorescence excitation study using tunable synchrotron radiation. This study has revealed that the most intense fluorescence results from excitation between 160 and 180 nm, which is a region poorly covered by conventional line sources. Our work serves to illustrate the very great advantages associated with using a continuously tunable synchrotron radiation source.

2. Experimental details

All experiments were carried out using beam line 12 at the Science and Engineering Research Council Daresbury Synchrotron Source. Radiation from the storage ring was dispersed using a Spex 1500 SP Czerny–Turner monochromator. Samples of ICl were contained in conventional Spectrosil fluorescence cells (cross section, 1 cm^2) fitted with a greaseless tap. These cells were then mounted in an evacuable chamber which allowed absorption and fluorescence spectra to be monitored simultaneously. Absorption spectra were recorded using a screen coated with sodium salicylate to convert vacuum UV radiation to wavelengths suitable for monitoring with a conventional photomultiplier (EMI 6256B). Undispersed fluorescence was monitored at right angles to the excitation beam using a quartz-windowed photomultiplier (Mullard PM2020Q) outside the evacuable box (*i.e.* fluorescence was observed for 650 nm $\geqslant \lambda \geqslant$ 185 nm).

3. Results

The absorption spectrum of ICl in the region 160 - 200 nm is shown in Fig. 1. The two sets of Rydberg bands previously reported by Venkateswarlu [11] are clearly seen between 190 - 180 nm and 175 - 165 nm. The sloping background on which the strong Rydberg peaks are superimposed is due mainly to the change in monochromator throughput I_0 with wavelength.

The absorption spectra of Cl_2 and I_2 were also recorded, for comparison, as ICl exists in equilibrium with both these molecules. Cl_2 does not show any structured absorption in this region; however, I_2 exhibits strong Rydberg absorption below 175 nm. Thus, in order to suppress I_2, excess Cl_2 was added to all samples of ICl.

A fluorescence excitation spectrum of ICl, in the region 159 - 195 nm, is shown in Fig. 2. The most intense fluorescence is observed for excitation between 172.5 and 182.5 nm. The banded structure observed between 180 and 189 nm and between 170 and 175 nm is due to absorption by ICl (absorption by ICl strongly reduces the intensity of the excitation beam before it traverses the region from which fluorescence is observed, *i.e.* the sample is optically thick). This point has been confirmed by running spectra at lower pressures of ICl; as the pressure of ICl is reduced the sample becomes

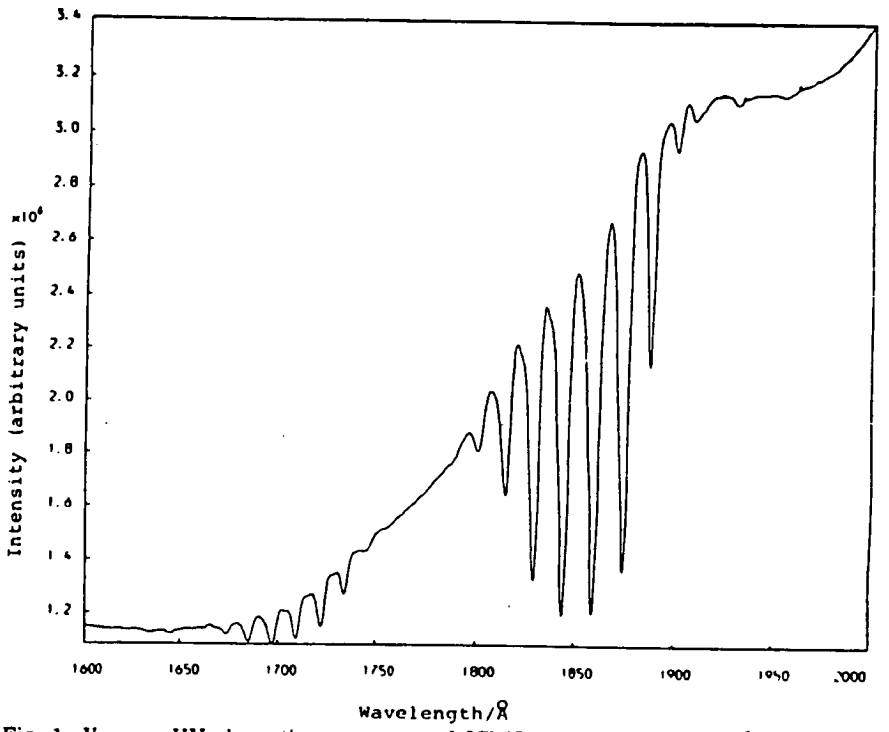

Fig. 1. Vacuum UV absorption spectrum of ICl ($P_{ICl} = P_{Cl_2}$ = 268 N m^{-2}; path length, 1 cm; resolution, 3 Å).

optically thin and the banded structure becomes much weaker relative to the fluorescence. The structure observed between 174 and 178 nm persists even at low pressures of ICl and is therefore not due to optical thickness of the sample.

There is a distinct break in the fluorescence excitation spectrum between 171 and 168 nm with a second highly structured system observed below 168 nm down to the limit of the Spectrosil–quartz cut-off (160 nm). It should be noted that the spectrum shown in Fig. 2 has not been corrected for the change in incident light intensity with wavelength: this is approximately 30% less below 168 nm compared with that at 175 nm. Thus the peak intensity for the fluorescence system below 168 nm is approximately equal to that of the peak at 175 nm. The second fluorescence excitation system appears to be quite sensitive to quenching by ICl and/or Cl_2 since the intensity of this system, relative to that at longer wavelengths, declines rapidly for halogen pressures above 133 N m^{-2}. The separation between the peaks corresponds to the vibrational frequency of the Rydberg states in this region; however, the *structure* in this region does not change with the partial pressure of ICl and is not therefore due to the effect of optical thickness.

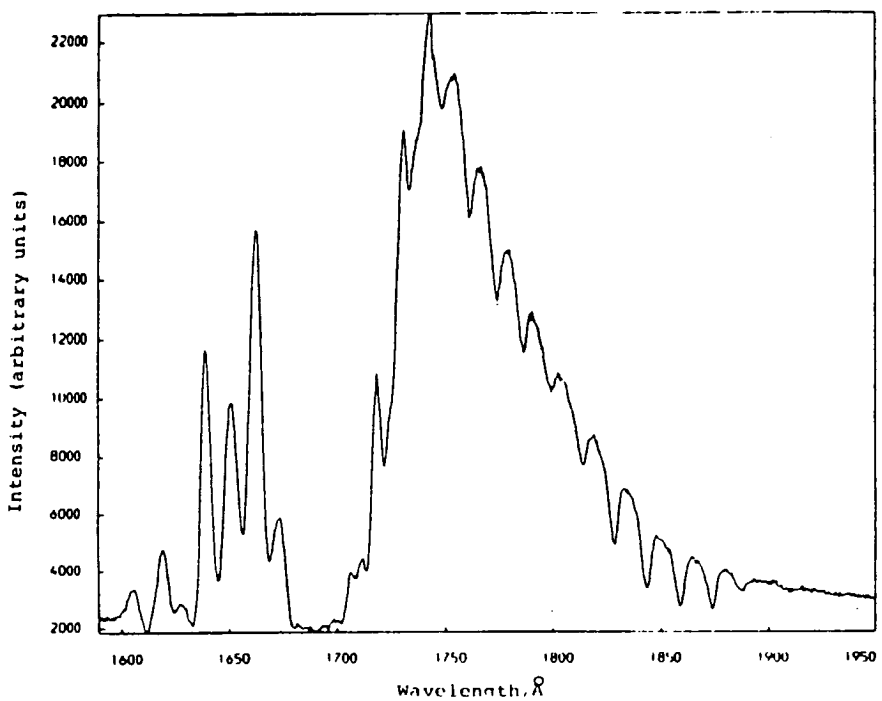

Fig. 2. Vacuum UV fluorescence excitation spectrum of ICl ($P_{ICl} = P_{Cl_2} = 133$ N m^{-2}). The spectrum has not been corrected for the variation with wavelength of the incident light intensity.

Fluorescence excitation spectra were also recorded following the addition of N_2 as a quenching gas up to a total pressure of 12 kN m^{-2}. As the pressure of N_2 was increased the total fluorescence intensity (for excitation wavelengths between 160 and 190 nm) also initially increased up to about 8 kN m^{-2} N_2, after which the intensity decreased. In these experiments no attempt was made to disperse the fluorescence and thus the photomultiplier registered emission from both the initially populated states and any other states populated during collisional cascade processes [10], provided that these states emitted in the region 185 - 650 nm. However, the intensity increase was not uniform and the bands between 160 and 170 nm increased in intensity more rapidly than the broad system at longer wavelengths (Figs. 2 and 3 should be compared). Furthermore, the relative intensities of some of the bands within the 160 - 170 nm system changed with pressure and there appear to be at least two electronic systems which behave differently in this region.

The increase in total fluorescence (about 30%) with increasing pressure of N_2 is probably due to pressure broadening of the absorption spectrum.

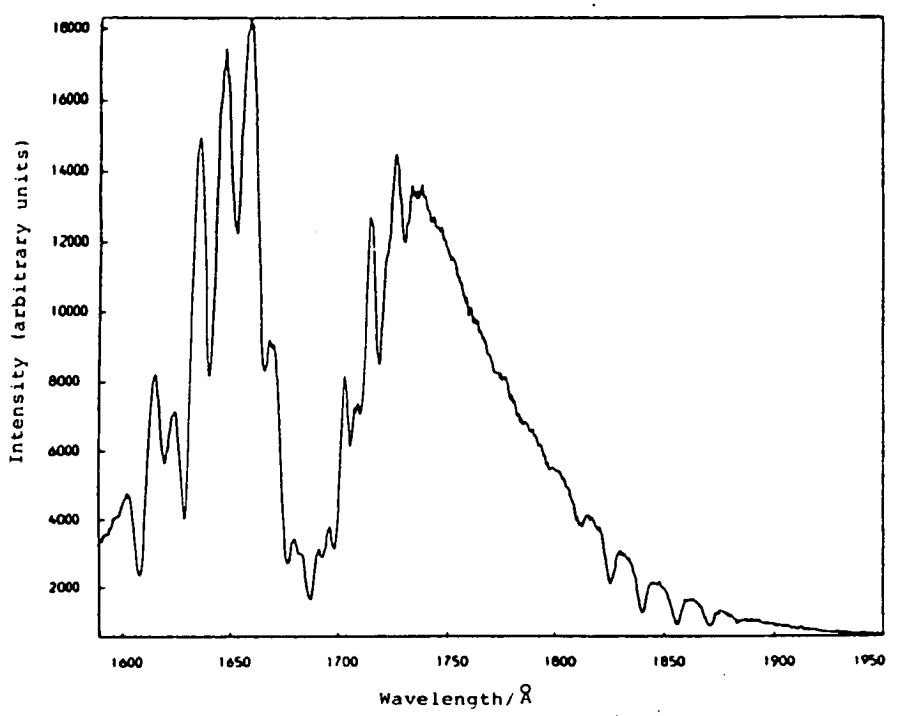

Fig. 3. Vacuum UV fluorescence excitation spectrum of ICl in the presence of a large excess of N_2 ($P_{ICl} = P_{Cl_2} = 133$ N m^{-2}; $P_{N_2} = 12.3$ kN m^{-2}). The spectrum has not been corrected for the variation with wavelength of the incident light intensity.

This has been observed previously with I_2 where the effect has been studied in some detail [12].

By comparison with previous work on halogen ion pair states [2, 4, 8, 10] we would expect collisions with N_2 to induce efficient interstate transfer and cascading with the eventual population of the lowest state within the ion pair manifold; this state would then be expected to radiate to lower valence states.

4. Discussion

It is clear from this study that the Rydberg states, which dominate the absorption spectrum of ICl in the region 165 - 190 nm, do not give rise to fluorescence at $\lambda \geqslant 190$ nm, as the excitation spectrum does not exhibit the structure observed in absorption. The spectra reported by Venkateswarlu [11] suggest that these Rydberg states are predissociated. No rotational structure is observable in the published spectra; however, it is still possible for discrete structure to exist close to some of the band origins, where the

rotational structure is dense and difficult to resolve. Our results show clearly that the first Rydberg system is completely predissociated and that this is probably also the case for the second Rydberg system. Fluorescence from this second system could occur below our detection limit and some doubt therefore remains as to whether or not fluorescence can take place from this second system.

The structure observed on the second fluorescence excitation system (160 - 170 nm) suggests that the upper state is a Rydberg state. However, Venkateswarlu [11] has reported a strong and densely structured absorption system in this region which must be due to an upper ion pair state; unfortunately no analysis of this spectrum was given. It would appear that the ion pair state is strongly perturbed by a close-lying Rydberg state and that interference between the two states results in the pronounced structure observed in the fluorescence excitation spectrum. The intensity changes observed when N_2 is added as a quenching gas also suggest that more than one electronic state is involved in this region.

Several ion pair states are known in the region of interest [13] and transitions to two of these states (0^+ and 1) in the lowest cluster, correlating with $I^+(^3P_2)$ and $Cl^-(^1S_0)$, are fully allowed. Both states are expected to lie close in energy to one another and, as a result of the large change in equilibrium internuclear separation between the ground state and the ion pair states, high vibrational levels should be populated in the absorption process. The fluorescence is therefore expected to be predominantly of the bound free type (*i.e.* oscillatory continuum fluorescence). Further work to examine the dispersed fluorescence is therefore desirable and the present work shows that excitation could be achieved using the atomic lines of nitrogen at 174 nm.

5. Conclusions

We have recorded the first fluorescence excitation spectrum of ICl in the vacuum UV and have shown that at least three upper states are involved in the fluorescence. These states all show behaviour characteristic of ion pair systems; however, the states excited in the region 160 - 170 nm probably have mixed Rydberg and ion pair parentage. Further work, at higher resolution, on the absorption spectrum of ICl in the vacuum UV, together with work on the dispersed fluorescence, is clearly desirable.

Acknowledgments

We thank the Science and Engineering Research Council for support of this research and for use of facilities at the Daresbury Laboratory. We also thank the referee for several helpful comments.

References

1 L. C. Glasgow and J. E. Willard, *J. Phys. Chem.*, *77* (1973) 1585.
2 R. J. Donovan, B. V. O'Grady, L. Lain and C. Fotakis, *J. Chem. Phys.*, *78* (1983) 3727.
3 Z. Yun-Wu, W. Fuss and K. L. Kompa, *J. Photochem.*, *23* (1983) 311.
4 J. P. T. Wilkinson, M. MacDonald and R. J. Donovan, *Chem. Phys. Lett.*, *101* (1983) 284.
5 R. S. Mulliken, *J. Chem. Phys.*, *55* (1971) 309.
6 J. Tellinghuisen, *Chem. Phys. Lett.*, *29* (1974) 359.
7 M. MacDonald, J. P. T. Wilkinson, C. Fotakis, M. Martin and R. J. Donovan, *Chem. Phys. Lett.*, *99* (1983) 250.
8 M. MacDonald, R. J. Donovan and M. C. Gower, *Chem. Phys. Lett.*, *97* (1983) 72.
9 K. P. Lawley, M. MacDonald, R. J. Donovan and A. Kvaran, *Chem. Phys. Lett.*, *92* (1982) 322.
10 M. Martin, C. Fotakis, R. J. Donovan and M. J. Shaw, *Nuovo Cimento Soc. Ital. Phys., B, 63* (1981) 300.
11 P. Venkateswarlu, *Can. J. Phys.*, *53* (1975) 812.
12 B. V. O'Grady, to be published.
13 J. C. D. Brand, D. Bussieres, A. R. Hoy, S. M. Jaywart and D. B. Miller, *Opt. Commun.*, *48* (1983) 195.

FORMATION OF XeCl($B\ ^2\Sigma_{1/2}$) AND XeI($B\ ^2\Sigma_{1/2}$) BY REACTION OF ELECTRONICALLY EXCITED ICl WITH Xe

J.P.T. WILKINSON, E.A. KERR, K.P. LAWLEY, R.J. DONOVAN
Department of Chemistry, University of Edinburgh, West Mains Road, Edinburgh EH9 3JJ, UK

D. SHAW, A. HOPKIRK and I. MUNRO
SERC Daresbury Laboratory, Daresbury, Warrington WA4 4AD, UK

Received 14 July 1986

Tunable synchrotron radiation has been used to excite the ion-pair states of ICl and to study their reactions with Xe. Strong fluorescence from both XeCl($B\ ^2\Sigma_{1/2}$) and XeI($B\ ^2\Sigma_{1/2}$) has been observed and their excitation functions are reported.

1. Introduction

The ion-pair states of the halogens are known to undergo efficient collisional-energy transfer *within* their ion-pair manifold. Rapid cascading to the lowest ion-pair state occurs and cross sections for collisional transfer by the rare gases are typically 50 Å^2 [1].

In a few cases reactive channels leading to electronically excited rare gas halide species have been observed. We have previously reported the observation of fluorescence from XeBr($B\ ^2\Sigma_{1/2}$) from the reaction

$$IBr(E0^+) + Xe \rightarrow XeBr(B\ ^2\Sigma_{1/2}) + I$$

and the formation of XeI($B\ ^2\Sigma_{1/2}$) in the analogous reaction between $I_2(D0_u^+)$ and Xe [2,3]. In the latter case the threshold for reaction was also determined and it was shown that reaction occurs with little, or possible zero, activation energy. Similar reactions have been observed between excited states of Cl_2 and some of the rare gases [4,5].

A low-resolution study of some of the luminescence produced following vacuum ultraviolet excitation of Xe/ICl mixtures has been reported previously by Bibinov and Vinogradov [6]. In the present work we report a study of the chemiluminescent reactions that occur between the ion-pair states of ICl and Xe, and the excitation functions for the formation of both XeCl($B\ ^2\Sigma_{1/2}$) and XeI($B\ ^2\Sigma_{1/2}$).

2. Experimental

All experiments were carried out at the SERC synchrotron radiation source at the Daresbury Laboratory. Two ports were used to record the spectra, high aperture 12 (HA12) and vacuum ultraviolet 13 (VUV13): similar results were obtained in both cases. Since the arrangements were somewhat different for each port some further details will be given.

The experimental arrangement on HA12 used samples of ICl/Cl_2/Xe which were contained in a conventional 1 cm^2 cross section Spectrosil fluorescence cell. The cell was mounted at the centre of an evacuable chamber into which the output of the synchrotron was passed after dispersion by a Spex 1500 Czerny–Turner (0.75 m) monochromator (usable resolution, 0.04 nm).

The arrangement for VUV13 was similar to that on HA12 but the synchrotron radiation was dispersed using a 0.5 m Seya monochromator before passage into the sample chamber (the Spectrosil fluorescence cell was dispensed with in these experiments). The somewhat poorer resolution (0.1 nm) of the Seya monochromator on VUV13, compared

0 009-2614/86/$ 03.50

to the Czerny–Turner on HA12, was more than offset by the greater throughput of radiation on VUV13 particularly at shorter wavelengths.

For both HA12 and VUV13 the detection systems were essentially the same. Fluorescence was collected at right angles to the excitation beam using a suitably filtered Mullard XP2020Q (HA12) or EMI9883QA (VUV13) photomultiplier which was mounted outside the evacuated chamber. The excitation spectra for the rare gas halides were run using either narrow-band interference filters or a Spex Minimate monochromator, on the fluorescence axis, in order to isolate the spectral range of interest. VUV absorption spectra were recorded by using a sodium salicylate fluorescence screen to convert the VUV radiation to a wavelength suitable for detection using a conventional photomultiplier. None of the spectra presented here have been corrected for the wavelength response of the monochromator or detection system.

3. Results and discussion

A fluorescence excitation spectrum of ICl is shown in fig. 1. The excited states which give rise to this fluorescence have been identified as ion-pair states: we have recently succeeded in dispersing this fluorescence and have observed clear oscillatory continuum structure [7] which confirms the ion-pair assignment. It should be noted that a pressure of Cl_2 equal to, or in some cases twice, that of ICl was added to all samples, in order to suppress the small amount of I_2 which is present in equilibrium with ICl: the presence of even small amounts of I_2 would give rise to a rich fluorescence spectrum following optical excitation in the region studied here [8].

Addition of Xe to ICl/Cl_2 mixtures quenches the primary fluorescence and results in the formation of $XeCl(B\ ^2\Sigma_{1/2})$ as shown in fig. 2: formation of $XeI(B\ ^2\Sigma_{1/2})$ is also observed for excitation below $\lambda = 168$ nm. By monitoring the emission at 308 nm,

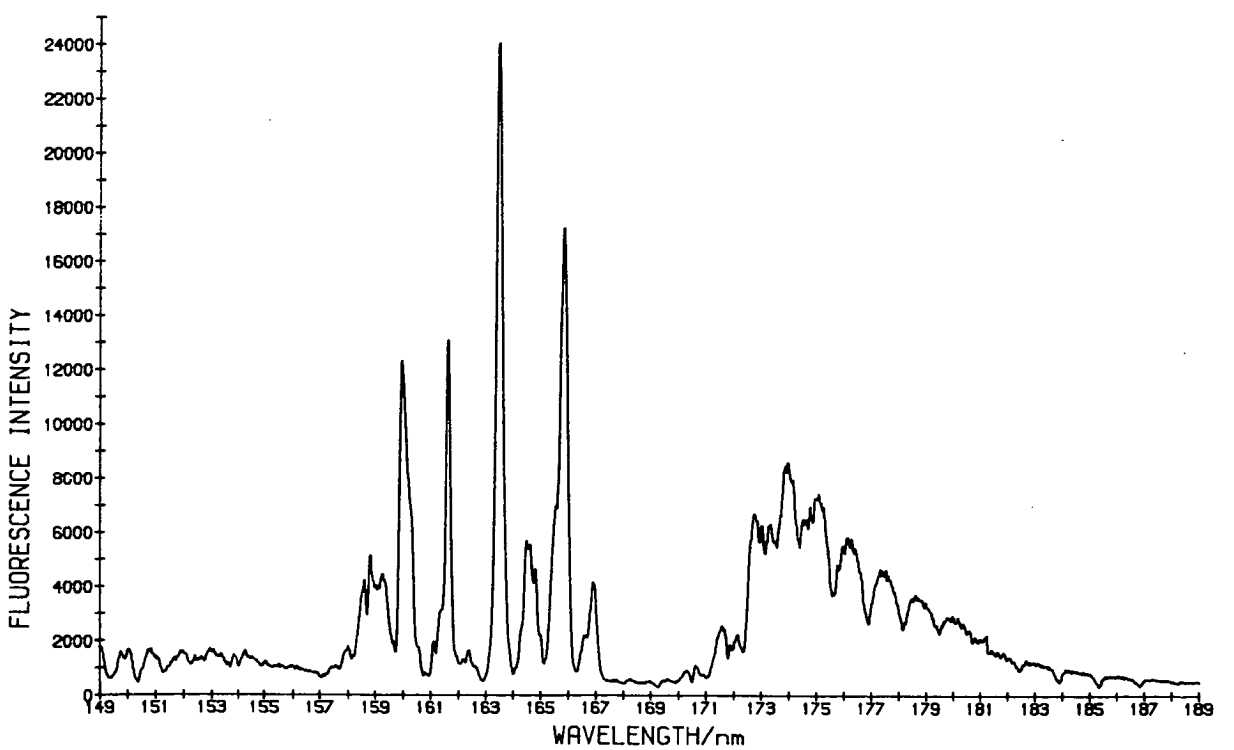

Fig. 1. Fluorescence excitation spectrum for ICl in the 150–190 nm region. ($P_{ICl} = 9$ N m^{-2}, $P_{Cl_2} = 18$ N m^{-2}.)

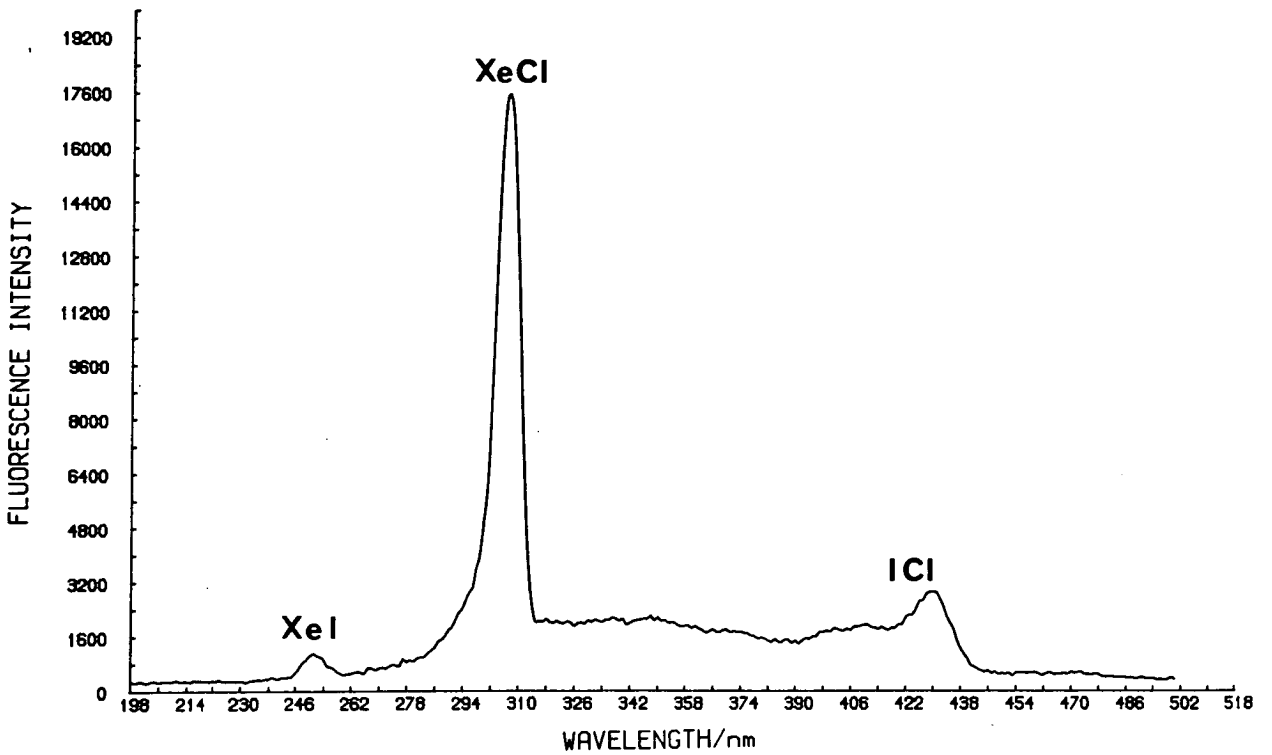

Fig. 2. Emission spectrum from $ICl/Cl_2/Xe$ mixture excited at 165 ± 2 nm. ($P_{ICl} = P_{Cl_2} = 133$ N m^{-2}, $P_{Xe} = 5.3$ kN m^{-2}.)

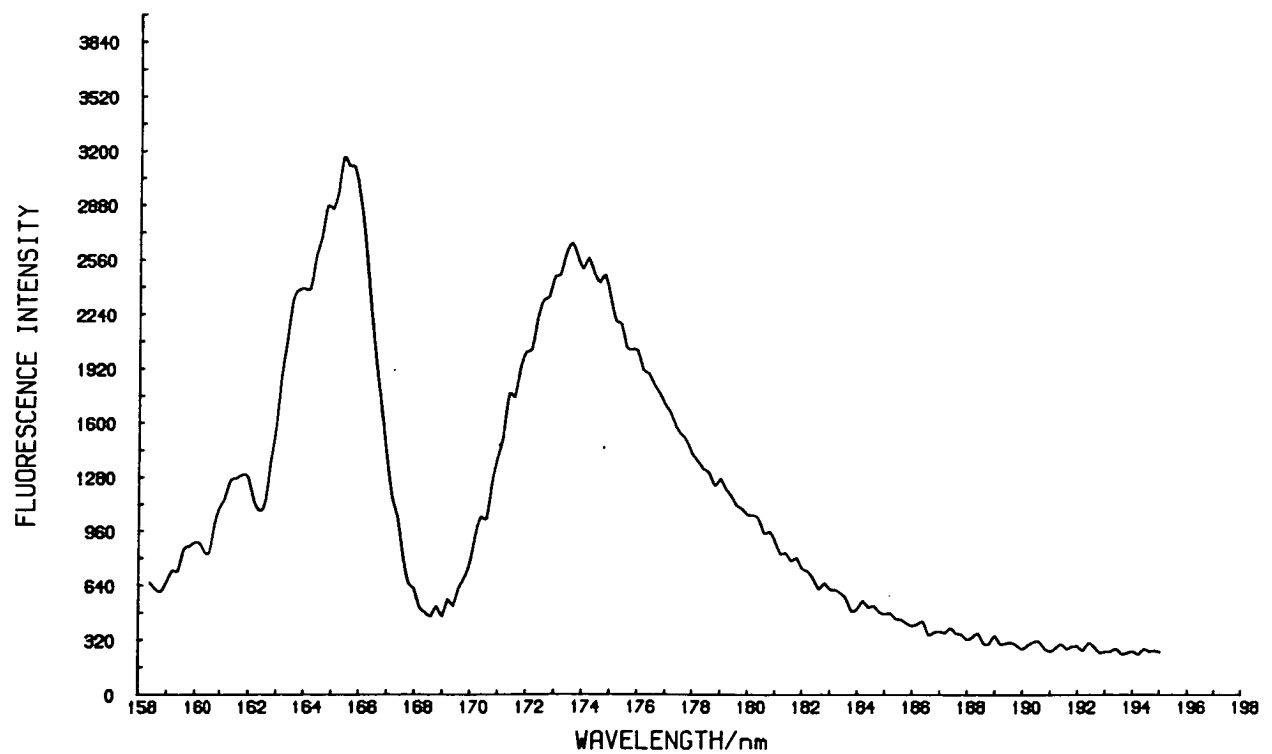

Fig. 3. XeCl($B\ ^2\Sigma_{1/2} \rightarrow X\ ^2\Sigma_{1/2}$) excitation function. ($P_{ICl} = P_{Cl_2} = 133$ N m^{-2}, $P_{Xe} = 5.3$ kN m^{-2}.)

due to XeCl($B\ ^2\Sigma_{1/2} \rightarrow X\ ^2\Sigma_{1/2}$), while scanning the synchrotron radiation over the region 190–160 nm, an excitation spectrum for XeCl($B\ ^2\Sigma_{1/2}$) formation is generated, and this is shown in fig. 3. A comparison of figs. 1 and 3 shows that the XeCl($B\ ^2\Sigma_{1/2}$) excitation spectrum is very similar to the ion-pair fluorescence excitation spectrum when due allowance is made for the lower resolution used to collect the XeCl($B\ ^2\Sigma_{1/2}$) data. The thermodynamic threshold for XeCl($B\ ^2\Sigma_{1/2}$) formation is 200 nm, however absorption by ICl is negligible at this wavelength and the apparent threshold for XeCl ($B\ ^2\Sigma_{1/2}$) formation coincides with the onset of absorption by the ion-pair state of ICl at 190 nm. It is clear that the Rydberg states of ICl in this region do not react: they appear to be predissociated [9] and their lifetimes are probably too short for fluorescence or collisional processes to be important.

The thermodynamic threshold for XeI($B\ ^2\Sigma_{1/2}$) formation is 174 nm, and weak XeI($B\ ^2\Sigma_{1/2} \rightarrow X\ ^2\Sigma_{1/2}$) emission is seen at this wavelength (fig. 4). However, it can be seen from fig. 1 that this threshold wavelength coincides with a steep drop in the fluorescence excitation spectrum and it is clear that ion-pair absorption is negligible in the region 173–168 nm. Furthermore, some emission from ICl itself falls within the bandpass of the 251 nm interference filter ($\Delta\lambda = 2$ nm) used in this work, and the excitation function should therefore be treated with some caution in the region 170–175 nm. A steep rise in the excitation function is observed below 1168 nm which coincides with strong resonance structure in the fluorescence excitation spectrum. It should be noted that the chemiluminescence from XeI($B\ ^2\Sigma$) is more intense than it would appear from fig. 2, as the response of the monochromator used in this work declines rapidly below 300 nm.

The dominant ion-pair state absorption by ICl at long wavelengths ($\lambda > 170$ nm) is assigned as $E0^+ \leftarrow X0^+$, from the work of Brand et al. [10]: the

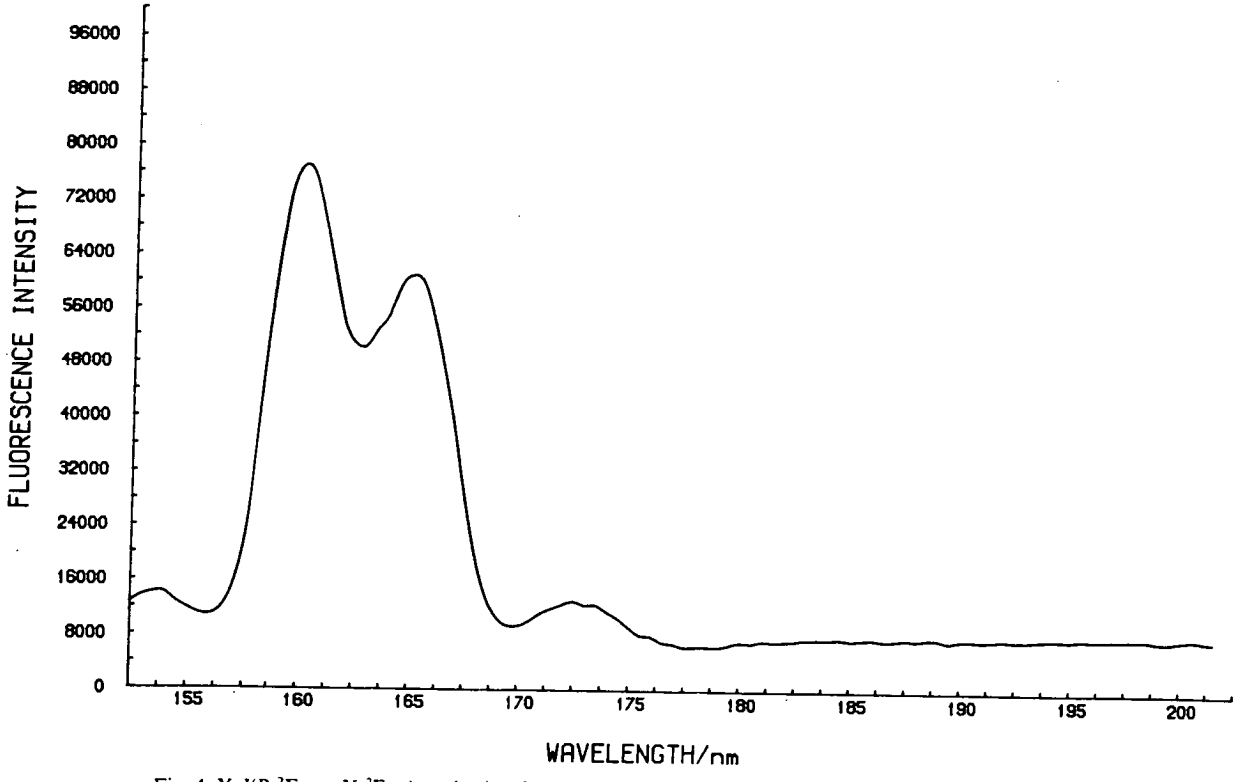

Fig. 4. XeI($B\ ^2\Sigma_{1/2} \rightarrow X\ ^2\Sigma_{1/2}$) excitation function. ($P_{ICl} = 29$ N m^{-2}, $P_{Cl_2} = 81$ N m^{-2}, $P_{Xe} = 875$N m^{-2}.)

$E0^+$ state belongs to the lowest cluster of ion-pair states which correlate asymptotically with $I^+(^3P_2)$ and $Cl^-(^1S_0)$. We have previously suggested that the sharp resonance structure in the region 160–170 nm is associated with a state of mixed Rydberg and ion-pair character, and the present observations lend further support to this proposal.

The mechanism for reaction of $ICl(E0^+)$ with Xe must involve the charge-transfer potential surface which correlates with ICl^- and Xe^+. The ion-pair state will have a large effective electron affinity and during collision an electron will be transferred from Xe into the hole in the bonding σ orbital on ICl. If a strictly linear approach is assumed, so that Ω is conserved, the adiabatic pathway to reaction can be pictured as follows. An electron is transferred at long range thus [#]:

$$ICl(E, 1441, \Omega=0) + Xe(m_J=0)$$
$$\rightarrow ICl^-(2441, \Omega=1/2) + Xe^+(^2P_3, m_J=1/2) .$$

The ICl^- bond begins to stretch rapidly with incipient formation of $I(^2P_{3/2}) + Cl^-$. The incoming Xe^+ then picks up the Cl^- and formation of XeCl* proceeds smoothly, without any barrier, passing through one avoided crossing on leaving the charge transfer surface in the exit channel, to form XeCl(B, $\Omega=1/2$): the I atom is left in the required lower $^2P_{3/2}$ state. It is seen that the XeCl C state is not accessible in this collinear approach. We note that the potential-energy surface as a whole is dominated by electrostatic forces, especially at close separations of the three atoms and this would lead to a pronounced minimum in the surface around the linear configuration ($I–Cl^–Xe^+$) so that non-collinear trajectories would be funneled into linear configurations.

If, in contrast, the Xe approaches from the I end of $ICl(E0^+)$ the same initial electron transfer occurs, but the (2441) state so formed has the wrong dissociation characteristics (to $I+Cl^-$) for formation of XeI*. However, the electric field of the approaching Xe^+ ion induces strong mixing of the (2441) and (1442) ICl^- states (which are related by a one-electron transfer) until the latter, having the right dissociation characteristics to I^-+Cl, dominates. The reaction then proceeds as before and the whole path is traced out over a surface that is continuous (no seams or intersections) with that leading to $XeCl^*+I$.

There is an exact analogy with the reactions

$$Cs+ICl(X) \rightarrow CsI+Cl ,$$
$$\rightarrow CsCl+I .$$

Once again, approach from the Cl or the I end results in the formation of the same electronic state of ICl^- (2441), which, to correlate with CsI must be mixed with the (1442) configuration.

In summary, we have shown that the low lying ion-pair states of ICl react with the ground state of Xe, to yield both $XeCl(B\ ^2\Sigma_{1/2})$ and $XeI(B\ ^2\Sigma_{1/2})$. The use of tunable synchrotron radiation has allowed excitation functions for the formation of both of these excited rare gas halide species to be determined.

[#] The original occupancy is designated ($i\ j\ k\ l$) to signify $(\sigma^i\pi^j\pi^{*k}\sigma^{*l})$.

Acknowledgement

We thank the SERC for use of the synchrotron radiation facility at the Daresbury Laboratory.

References

[1] M. Martin, C. Fotakis, R.J. Donovan and M.J. Shaw, Nuovo Cimento B63 (1981) 300;
R.J. Donovan, B.V. O'Grady, L. Lain and C. Fotakis, J. Chem. Phys. 78 (1983) 3727.

[2] M. MacDonald, J.P.T. Wilkinson, C. Fotakis, M. Martin and R.J. Donovan, Chem. Phys. Letters 99 (1983) 250.

[3] B.V. O'Grady and R.J. Donovan, Chem. Phys. Letters 122 (1985) 503.

[4] M.C. Castex, J. le Calvé, D. Haaks, B. Jordan and G. Zimmerer, Chem. Phys. Letters 70 (1980) 106.

[5] T. Ishiwata, A. Tokunaga and I. Tanaka, Chem. Phys. Letters 112 (1984) 356.

[6] N.K. Bibinov and I.P. Vinogradov, Opt. Spectry. 59 (1985) 191.

[7] R.J. Donovan, E. Kerr, J.P.T. Wilkinson, D. Austin, K.P. Lawley, D. Shaw and A. Hopkirk, to be published.

[8] R.J. Donovan, B.V. O'Grady, K. Shobatake and A. Hiraya, Chem. Phys. Letters 122 (1985) 612.

[9] P. Venkateswarlu, Can. J. Phys. 53 (1975) 812.

[10] J.C.D. Brand, U.D. Deshpande, A.R. Hoy and S.M. Jaywant, J. Mol. Spectry. 100 (1983) 416.